MICROWAVE IMAGING USING A TUNABLE REFLECTARRAY ANTENNA AND SUPERRADIANCE IN OPEN QUANTUM SYSTEMS

By

Amin Tayebi

A DISSERTATION

Submitted to
Michigan State University
in partial fulfillment of the requirements
for the degree of

Electrical Engineering—Doctor of Philosophy
Physics—Doctor of Philosophy

2017

ABSTRACT

MICROWAVE IMAGING USING A TUNABLE REFLECTARRAY ANTENNA AND SUPERRADIANCE IN OPEN QUANTUM SYSTEMS

By

Amin Tayebi

Theory, experiment, and computation are the three paradigms for scientific discoveries. This dissertation includes work in all three areas. The first part is dedicated to the practical design and development of a microwave imaging system, a problem mostly experimental and computational in nature. The second part discusses theoretical foundations of possible future advances in quantum signal transmission.

In part one, a new active microwave imaging system is proposed. At the heart of this novel system lies an electronically reconfigurable beam-scanning reflectarray antenna. The high tuning capability of the reflectarray provides a broad steering range of $\pm 60^{\circ}$ in two distinct frequency bands: S and F. The array, combined with an external source, dynamically steers the incoming beam across this range in order to generate multi-angle projection data for target detection. The collected data is then used for image reconstruction by means of time reversal signal processing technique. Our design significantly reduces cost and operational complexities compared to traditional imaging systems. The inclusion of the beam scanning array and the utilization of a single source, eliminates the need for a costly array of transceiver antennas and the involved switching circuitry. In addition, unlike conventional setups, this system is not constrained by the dimensions of the object under test. Thus the inspection of large objects, such as extended laminate structures, composite airplane wings and wind turbine blades becomes possible. Experimental results of detection of various dielectric targets as well as anomalies within them, such as defects and metallic impurities, are presented.

The second part includes the theoretical consideration of three different problems: quantum transport through two different nanostructures, a solid state device suitable for quantum computing and spherical plasmonic nanoantennas and waveguides. These three physically different systems are all investigated within a single quantum theory; the effective non-Hermitian Hamiltonian framework. The non-Hermitian Hamiltonian approach is a convenient mathematical formalism for the description of open quantum systems. This method based on the Feshbach projection formalism provides an alternative to popular methods such as the Feynman diagrammatic techniques and the master equation approach that are commonly used for studying open quantum systems. It is formally exact but very flexible and can be adjusted to many specific situations.

One bright phenomenon emerging in the situation with a sufficiently strong continuum coupling in the case when the number of open channels is relatively small compared to the number of involved intrinsic states is the so-called superradiance. Being an analog of superradiance in quantum optics, this term stands for the formation in the system of a collective superposition of the intrinsic states coherently coupled to the same decay channel.

The footprint of superradiance in each system is investigated in detail. In the quantum transport problem, signal transmission is greatly enhanced at the transition to superradiance. In the proposed solid state charge qubit, the superradiant states effectively protect the remaining internal states from decaying into the continuum and hence increase the lifetime of the device. Finally, superradiance provides us a tool to manipulate light at the nanoscale. It is responsible for the existence of modes with distinct radiation properties in a system of coupled plasmonic nanoantennas: superradiant states with enhanced and dark modes with extremely damped radiation. Furthermore, similar to the quantum case, energy transport through a plasmonic waveguide is greatly enhanced.

To my parents: Mo and Feri.

ACKNOWLEDGMENTS

> Progress is impossible without change, and those who cannot change their minds cannot change anything.
>
> *George Bernard Shaw*

To all those who have helped shape and develop my thinking, keeping my mind open to new ideas and approaches, you have my deepest appreciation.

I must first thank Michigan State University for its commitment to quality education and state of the art, nationally recognized science programs. MSU's campus was my first experience of life in the U.S. and I'll always remember a sense of acceptance and respect for all students, no matter their origin. My advisors and committee members have been key sounding boards throughout my graduate studies and I want to thank them for their distinct roles in my development.

Professors Satish and Lalita Udpa, you were the inception of making my dream of pursuing a PhD a reality. I must first and foremost thank you for accepting me into your program and making me a part of your ever-growing NDE family, of which I know I'll feel included in for many years to come. Despite your many endeavors and administrative duties, you both always made time to meet with me and guide me along the path to success.

To Professor Vladimir Zelevinksy, I will be forever grateful that you accepted me as a dual-PhD student, allowing me to enter into an entirely new world and develop a fresh passion for physics. Not only have you been an inspiring mentor, you have become a lifelong friend. Your guidance in the field of physics over the last six years has permanently transformed my way of thinking. I thank you and your wife, Vera for your continual support, companionship and endless supply of chocolate.

Professors Edward J. Rothwell and Prem Chahal, I cannot thank you both enough for

your open availability and willingness to discuss any problems I ran into. Your guidance and counsel has been invaluable to me and instrumental in my growth as an engineer. To Professor Alexander Volya, thank you for providing me with your notes and allowing me to use your slides in carrying on your work. To my labmates in the NDE lab, I will greatly miss our comradery and daily interactions. I have enjoyed getting to know and work with each of you in and outside of the lab. Scott Rice, thank you for the late nights and many hours you have put in helping me on the Plasmonics project. I truly appreciate your distinct approach and persistence when working on the problem.

Finally, to my family, I owe everything to you for where I am today. To my mother, Feri, and my father, Mo, thank you for the many sacrifices you made on my behalf. Mom, you spent countless hours making sure I could focus solely on school, which set me on this path toward attaining my PhD. Dad, I will always admire and aspire to have your courage and vision in life. To my brother, Ali, thank you for teaching me high school math when I was in elementary school and initiating my love of numbers, also for being everything a big brother should be. To my sister, Asal, who has always been a loving big sister, thank you for sharing your outlook on life and your continued support.

To my best friend and partner, Alicia, thank you for your love and encouragement despite all the stress of graduate school. I am excited for the next chapter of our lives and the many happy years we have to come.

TABLE OF CONTENTS

LIST OF TABLES

LIST OF FIGURES

Part 1

Introduction

Theory, experiment, and computation are the three paradigms for scientific discoveries. This dissertation includes work in all three areas. In the first part of this thesis, a problem with mostly experimental and computational nature is considered. Part one is dedicated to the design and development of a novel microwave imaging system. The applications of microwave imaging range from breast cancer detection to non-destructive testing of dielectric materials. Medical imaging is one field in which microwaves have gained significant attention, particularly due to the ever increasing number of breast cancer diagnoses around the world. Microwave imaging techniques are known to be a promising candidate for early breast cancer detection due to the high contrast in dielectric properties of malignant and healthy breast tissues at microwave frequencies. Another application in which microwave imaging plays an important role is in the non-destructive evaluation of composite materials and laminate structures. Such materials are gradually replacing traditional metallic counterparts due to their versatility and superior mechanical properties such as light weight and superior strength. With their increasing use in structures, comes the necessity of a robust method for inspection. Microwaves have proven to be a successful candidate. In light of this, the first part of the thesis presents a novel microwave imaging system suitable for medical applications and the inspection and detection of anomalies in dielectric materials. The design, simulation and fabrication process of the components of the system are described in detail in this part.

The second part of the thesis includes the theoretical consideration of various quantum systems. With recent advances in nanotechnology, quantum mechanics has come more closer than ever to problems with real-world applications. One ultimate driving force in this area is evidently the quest for the realization of quantum computers. Quantum computers, are believed to have a significant impact on our lives. Their computing power is expected to greatly exceed that of classical computers, network security will vastly improve and simulation of

physical systems with much larger scales would become possible. Therefore there has been a significant effort over the last two decades to design, simulate and fabricate components of quantum computers and develop theories for better describing such devices. In light of this developments, the second part of the thesis is dedicated to a quantum theory that is convenient for studying such devices. The effective non-Hermitian Hamiltonian method is formally exact but very flexible and can be adjusted to many specific situations. In part two, this framework is utilized to consider nanodevices from three different fields: quantum transport, solid state quantum computing and plasmonic nanoantennas and waveguides. The derivation of the theory and its applications to the three problems are discussed in detail in the second part .

Part 2

Microwave Imaging Using an Electronically Tunable Reflectarray Antenna

Light brings us the news of the Universe.

William Henry Bragg

Chapter 1

Introduction

1.1 A Brief History of Imaging

Human curiosity and want for a greater understanding of the universe have led to the invention of a great many imaging instruments used for observation of the unknown. Optical devices were the first type of instrument used by humans in order to enhance observation. Even though it is believed that the oldest optical lens, a crystal called the Nimrud lens, may have been used as a magnifying glass about 2700 years ago, it wasn't until the 10th century that we studied lenses in a scientific context. Ibn Sahl (c. 940-1000), a Persian mathematician, physicist and engineer, was one of the early leaders in the field of optics. His theoretical and experimental work, such as the discovery of the law of refraction, now commonly known as "Snell's law", formed the basis for the study of optical devices for scientists to come. An important breakthrough in the optical industry was made by the famous Dutch spectacle makers, Zacharias Jansen and his father Hans. Their experiment of placing several lenses in a tube resulted in one of the great discoveries of the 1590's, the compound microscope.

In parallel, instruments were being developed to better observe the night sky. The first telescope was built in 1608 by Hans Lippershey, a German-Dutch glass maker. Over many years, both microscopes and telescopes significantly improved. Electron microscopes being used today have achieved resolutions of up to 50 pm and magnifications of up to 10 million. Likewise, telescopes have greatly increased their capacity and have made imaging of distant galaxies possible. Recently, a galaxy 13.1 billion light-years from earth was imaged by the Hubble telescope.

The discovery of X-rays in 1895, by German physicist Wilhelm Röntgen, began a new era in imaging technology for non-destructive evaluation (NDE) applications. Physicians quickly realized the power of X-ray imaging in medical applications. Radiographs, images produced on a sensitive film utilizing X-rays, provided means of skeletal evaluation of patients. Later, a new imaging technique exploiting X-rays, called computed tomography (CT) was developed. CT is capable of producing detailed cross-sectional (tomographic) images of the human body. Yet another advancement of significant impact was the development of magnetic resonance imaging (MRI). Because of the extraordinary contributions to the field of medical imaging by both CT and MRI, each received the Nobel prize in Medicine and Physiology, in 1979 and 2003 respectively. It is important to mention that the application of X-ray is not limited to medical imaging; X-ray imaging is widely used in the non-destructive testing (NDT) of various industrial components and structures such as circuit boards, concrete, metal parts, et cetera.

Despite the rapid speed in the development and wide-spread use of X-ray imaging after its discovery, the long-term risks of repeated exposure to radiation only began to be studied in the late 1940's [1]. X-ray machines were popular in many industries and were occasionally used as a gimmick to attract customers. Many American shoe stores provided X-ray machines

for their customers, enabling them to see the skeletal structure of their feet. This practice was determined to be extremely risky in the 1950's and began to be phased out. The danger of prolonged radiation exposure is now well understood. Due to the harmful nature of X-ray ionizing radiation, many scientists started to search for a less hazardous alternative imaging technique. English physicist and physician John Wild, commonly known as the father of medical ultrasound, made an important breakthrough in 1949 when he utilized ultrasonic energy to assess the thickness of bowel tissue. As in the case of X-rays, ultrasound imaging quickly became widely popular. Today, physicians utilize ultrasound technology to visualize various tissues, listen and look at fetuses in utero, and to view heart function (echocardiogram). Ultrasound imaging is also being vastly used for NDE purposes such as structure health monitoring, material characterization and flaw detection. Despite its popularity, ultrasonic technology has one main disadvantage, the requirement of a couplant in order to effectively couple sound waves to the desired medium. In addition, porous materials do not allow for an efficient propagation of acoustic signals.

Next we consider an imaging technique utilizing electromagnetic microwaves, which has the benefit of being harmless while also outperforming X-ray and ultrasonic approaches in certain applications.

1.2 Microwave and Millimeter Wave Imaging

Generally, Microwaves are defined as electromagnetic waves with wavelengths ranging from one millimeter to one meter, corresponding to frequencies from 300 GHz to 300 MHz, respectively. A more precise definition was proposed by IEEE; according to IEEE standard 521, microwaves cover a frequency range from 1 GHz to 110 GHz and millimeter waves

cover the range of 110 GHz to 300 GHz. Nevertheless, compared to other frequency bands, microwaves have properties such as propagation in air with very low attenuation. In general, atmospheric attenuation of electromagnetic waves above 1 GHz increases rapidly with increase in frequency with isolated resonances due to the presence of oxygen and water molecules in air [2, 3]. This makes microwaves suitable for long distance applications such as communications and the detection of flying objects. Similarly, in dielectric materials microwaves have a larger penetration depth compared to higher frequencies, such as terahertz, and provide better resolution compared to lower frequency bands. It is important to mention that the microwave frequency band corresponds to photons with energies ranging from 1.24 μeV at 300 Mhz to 1.24 meV at 300 GHz, which when compared to X-ray radiation, makes them virtually harmless and safe for a greater number of applications.

The properties mentioned above make microwaves an invaluable tool for imaging, with many applications varying from breast cancer detection [4] to machine vision and robotics [5]. Medical imaging is one field in which microwave imaging has gained significant attention, particularly due to the ever increasing number of breast cancer diagnoses around the world. In 2015, in the United States alone, it was estimated that 292,130 women were diagnosed with invasive or carcinoma in situ types of breast cancer [6]. Thus, there is an urgent need to develop a more reliable and effective detection system. Microwave imaging is known to be a promising candidate for early breast cancer detection [7] due to its ability to differentiate with high contrast, the dielectric properties of malignant and healthy breast tissue. Normal breast tissue has a relative dielectric constant of about 4.5 at 10 GHz, whereas the dielectric constant of cancerous tissue is approximately 10 times more [8]. For X-rays however, the contrast between tumor and normal tissue is low. A maximum ratio of 1.7 between the attenuation coefficients of breast tumors and healthy tissues occurs at photon energies of 20

keV [9, 10]. Similarly, ultrasound suffers from poor contrast ratio. The maximum ratio of attenuation coefficients between cancerous and normal breast tissues is only about 2.5 [11]. This allows microwave imaging to potentially surpass X-ray mammography and ultrasonic instruments in breast cancer detection. Another area in which microwave imaging has been widely applied is in the NDT of low loss dielectrics and composite materials, where traditional eddy current based approaches fail. This is because Eddy currents can be induced only in materials with high conductivity and therefore are only useful in the inspection of metallic materials. Moreover, unlike Eddy current testing, which can only be used for surface and near surface flaw detection, microwaves are capable of propagating deep into dielectrics. Therefore the detection of anomalies deep inside materials is possible with microwaves. A detailed overview and discussion of the advances in microwave NDT can be found in [12].

Next, some of the drawbacks of traditional microwave imaging systems are discussed along with a proposal for an alternative setup.

1.3 A New Design: Mirror-Based Microwave Imaging

Traditional microwave imaging using tomographic reconstruction methods, involves the illumination of a region of interest (ROI) at different angles from 0° to 360° and collection of scattered field data around the test object. These projections are then used to reconstruct the ROI by means of an appropriate inverse problem method such as full-wave inverse scattering and diffraction tomography based techniques. However, the conventional microwave setup has a number of drawbacks in practical implementation. A traditional system needs an array of costly transceivers to be placed all around the object [13–18]. This requires complicated circuitry to accommodate transceiver switching for projection data acquisition.

The conventional system also requires antenna compensation algorithms and an increased of number of antennas in order to obtain higher resolution.

A new prototype for an active microwave imaging system is presented in this thesis that greatly reduces design and operational complexities compared to traditional systems. This work was inspired by a number of papers from Arunachalam et al. [19–21], where a system employing a continuous deformable reflective surface, or *mirror*, was investigated in a theoretical framework. Fig. 1.1 shows the schematic of the mirror-based imaging system. The setup uses a single source instead of a transceiver array of source elements, which greatly reduces the overall cost. The source is coupled to a continuously conformable mirror that is used to generate meaningful projections by steering the incident beam into various angles. The scattered field is then measured by a receiver antenna array and used for image reconstruction. This design eliminates the need for complicated antenna switching circuitry. Moreover, the test object need not be enclosed in a gantry to generate a 360° projection data set and hence there is no constraint on object dimensions. Therefore, imaging of larger dielectric materials such as laminate structures and airplane wings would be possible. The proposed system is highly scalable and also has potential for various medical applications including breast cancer detection.

Although the theoretical studies demonstrated the feasibility of the concept, there were two main challenges that must be overcome for practical implementation. The first challenge is the realization of the deformable mirror. The second is image reconstruction from limited view projections. Since projections are not taken from all angles, reconstruction becomes a more challenging task. These key issues are briefly addressed here and again in more detail in the following chapters of the thesis.

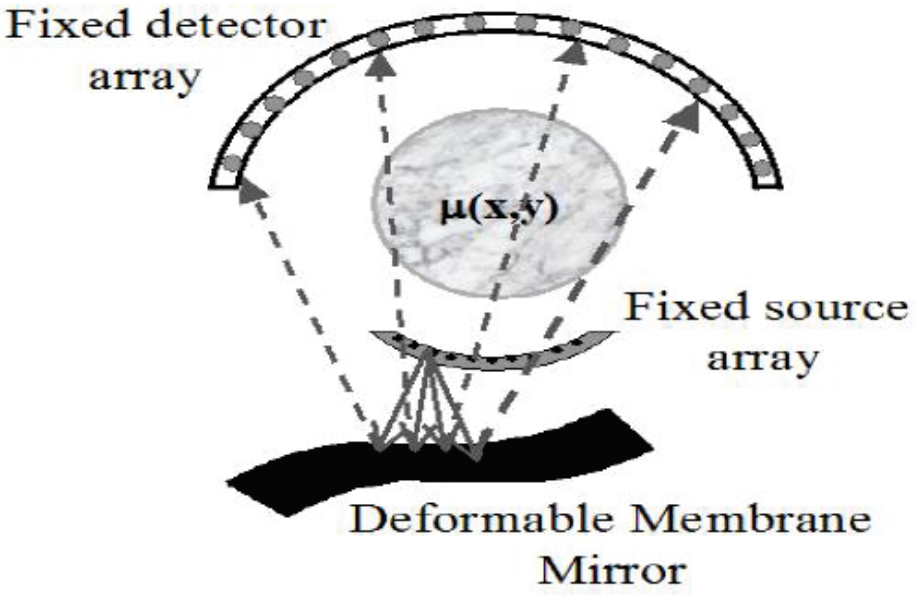

Figure 1.1: Schematic of the proposed microwave imaging system [19].

1.3.1 Deformable Mirror

In the theoretical study by Arunachalam et al. [21] several options were suggested for realizing the active mirror. Some of the designs include the use of segmented, continuous thin-plate, monolithic and membrane mirrors. The advantages and disadvantages of each of the mirror designs were discussed in [21]. It is important to ensure that the mirror is capable of steering the incident beam into various angles in order to generate information rich, unique measurements. A thin plate conformable mirror was chosen in [21] and optimal mirror shapes for beam steering were studied.

In reality however, using a thin metal plate as the mirror proved to be extremely challenging. In this case, mechanical actuators with translational and rotational degrees of freedom are required in order to alter the mirror shape. Also, the mirror has to be under constant tension in order to maintain surface flatness. This makes precise shaping (deformation) of

the thin metal plate difficult. In addition, changing the configuration of the mirror in order to steer the beam into different angles using mechanical motion would be slow. For these reasons we have adopted a fully electronically controllable mirror; a reflectarray antenna.

A reflectarray antenna is an array of radiating elements illuminated by an external source. The elements of the array possess distinct radiation characteristics. The properties of the individual cells are determined in such a way that the field reflected from the surface of the array has a desired radiation pattern. The properties of the elements of the array can be dynamically manipulated by electric means. This yields the so-called reconfigurable reflectarray antenna, where one can exploit features such as beam steering.

Tunable reflectarrays are excellent candidates for implementing the proposed mirror. The mirror utilized in our system is a dual-band tunbale reflectarray antenna with a high tuning capability. The array provides a broad steering range of $\pm 60^{\circ}$. The beam is steered across this range and the scattered field is recorded to be used for image reconstruction. The electric mirror not only eliminates all mechanical parts, it also significantly reduces the time needed to switch between steering angles. The design and fabrication of the array is discussed in Chapter 2.

1.3.2 Image Reconstruction

Due to the interaction of the electromagnetic field with the test object, the scattered filed contains information about the object. Therefore the projection data collected by the receiver array is used to solve the inverse scattering problem i.e. reconstructing the image of the object being tested. The inverse scattering problem is in principle ill-posed. In our case, the situation becomes even more challenging because projection measurements do not provide a full 360° view around the test object. With limited access to the object and decreased angular

coverage, advanced image reconstruction schemes are required. Several techniques have been developed in order to handle the so-called limited angle scenario. The most popular methods are model-based (full-wave) approaches, diffraction tomography approaches such as filtered back-propagation and Fourier inversion algorithms, and the time reversal signal processing technique. In this thesis, in order to realize the first prototype of the new imaging setup, the use of the time reversal technique is chosen. This method, which relies on the time reversal invariance property of the wave equation, allows us to detect and pinpoint any scatterer located in the region of interest (ROI). Details of the image reconstruction process are discussed in Chapter 3.

1.4 Organization

The design, simulation, fabrication and measurement of the reconfigurable reflectarray antenna is explained in Chapter 2. The concept of reflectarrays is introduced in the beginning of this chapter. Various means of achieving tunability are explained. Next, a brief summary of the theory of reflectarrays is provided. Since the most important component of any reflectarray is its unit cell, the main section of this chapter is on the design, measurement and testing of a single element of the array. Finally, a 10x10 array is fabricated and experimental results of the measurement of radiation patterns from the array are presented. Chapter 3 describes the time reversal image reconstruction technique in detail. The chapter begins with a brief introduction to inverse problems and various methods of image reconstruction. A finite difference time domain (FDTD) code is developed to solve Maxwell's equations numerically. The concept of time reversal is then validated using computer simulation. Chapter 4 presents experimental results obtained using the prototype of the imaging setup. Two experiments

conducted in order to evaluate the detection capabilities of the system are discussed. The capability of the system to detect anomalies within dielectric materials is also demonstrated. Specifically two types of anomalies are considered in this chapter: defects and metallic impurities. It is shown that the system can accurately detect both anomaly types. Part 4 includes the conclusion and future directions.

> It's of no use whatsoever ... this is just an experiment that proves Maestro Maxwell was right − we just have these mysterious electromagnetic waves that we cannot see with the naked eye. But they are there.
> I do not think that the wireless waves I have discovered will have any practical application.
>
> *Heinrich Hertz*

Chapter 2

The Reflectarray Antenna

2.1 Introduction

The reflectarray antenna, first introduced in 1963 by Berry et al., can be thought of as a reflecting surface where elements in the array determine the reflection properties of the surface [22]. The amplitude and phase change between the incident and the reflected fields, at any point on the surface of the reflectarray, are determined by the elements of the array. Similar to antenna arrays, in order to achieve the desired radiation pattern, proper phase shift has to be assigned to each element of the array, which can be done by appropriately choosing the parameters of individual elements. An array of variable-length, open-ended waveguides was used by Berry et al. in [22] to demonstrate the reflectarray principle.

Later, with the advent of microstrip technology and the extension to microstrip arrays, reflectarrays became easier to build. The behavior of a microstrip array is defined by its

printed resonating elements. First generation microstrip reflectarrays as seen in the work of Javor et al., comprised patch elements with variable-length transmission lines attached to the patches where the reflection from the open end of the line determined the phase shift of the element [23]. Rectangular patches of variable lengths are used in the paper by Pozar and Metzler [24] since the reflection phase changes with the length of the patch. A variety of microstrip reflectarrays have been developed using other radiating elements, such as variable-length crossed dipoles by Kelkar [25] and rotated patches by Huang and Pogorzelski [26], that lead to circularly-polarized reflectarrays.

Research on reflectarrays continued to advance with the introduction of dual-band reflectarrays, in which each unit cell comprises two different elements, each accountable for radiating in one of the bands. Crossed-dipoles of variable sizes printed on a single layer in the work of Kelkar [25], patches of variable sizes on two stacked layers in the paper by Encinar [27] and double ring elements used by Huang et al. in [28] are all examples of dual-band reflectarray antennas.

An extra dimension of versatility is added to this group of antennas by their ability to dynamically adjust element scattering properties in order to alter the radiation pattern, and thereby produce tunable reflectarrays. Reconfigurable elements are achieved via several techniques. In the paper by Inam and Ismail [29] a pin diode is incorporated in the unit cell; the ON and OFF states of the diode alter the electrical length of the element and hence provide tunability. Beam shaping is achieved by means of RF MEMS in the work of Bayraktar et al. [30]. Technologies using liquid crystals [31], ferroelectric materials [32] and graphene [33] have been used as well. A recent review on the advantages and disadvantages of different technologies can be found in the paper of Hum and Perruisseau-Carrier [34]. These techniques can be combined with dual-band unit cells to produce tunable dual-band

reflectarrays. In [35] by Guclu et al. and in [36] by Moghadas et al. two tunable dual-band unit cells based on RF MEMS are proposed as reflectarray antennas, though the array has not yet been built.

Beam steering using high impedance surfaces (HIS) is a relatively new and fascinating area in the field of reflectarrays. A varactor tunable HIS element is presented in the paper by Mias and Yap [37]. Despite their promising performance, the size of the periodic element is often much smaller than the operating wavelength, therefore more elements are required on the surface of the array. This leads to an increase in the cost and complexity of the array.

In this thesis varactor diodes are used to create tunable array elements, since they can be easily incorporated into the unit cell and are more cost-effective, and more reliable, than the previously mentioned techniques. Recent developments in unit cells that exploit varactor diodes for phase adjustability have shown promising results [38], [39]. The unit cell introduced by Hum et al. [38], which uses two varactor diodes, is capable of providing a phase shift of up to 320°. Using two varactors per unit cell is not only costly, but the biasing circuit fabricated on the reflecting surface of the antenna increases loss and lowers the scattering amplitude. In the paper by Rodrigo et al. [39], frequency tunability is achieved using a single varactor, but at the cost of a lower phase change of 270°, and the additional need for two RF switches and corresponding complexity of fabrication.

In the following sections, a dual-band metamaterial-inspired unit cell is introduced that uses a single varactor diode to dynamically adjust the phase of the reflected electric field in the two frequency bands [40–42]. The unit cell is modeled and analyzed, and the results are used to design a reflectarray antenna. Finally, a prototype of the antenna is constructed, and the subsequent measurements are used to verify the predicted properties of the proposed antenna.

2.2 The Theory of Reflectarrays

Several techniques have been used for the analysis of reflectarrays. Numerical methods, such as finite difference time domain (FDTD) and finite element method (FEM) modeling, described in the works of Cadoret et al. [43] and Bradi et al. [44] respectively, provide accurate results, although they are time and computation expensive. In this thesis, similar to the paper by Berry et al. [22], a simple yet effective theory based on the concept of impedance surfaces is utilized.

Consider the infinitely large reflectarray shown in Fig. 2.1. For simplicity, it is assumed that the incident field is a plane wave normal to the reflectarray and linearly polarized along the y-axis. This is a good approximation when the reflectarray feed is far away from the surface of the array or is capable of generating plane waves, such as with lensed horn antennas. Under this assumption the electric field on the surface of the array is expressed as

$$\vec{E}_i = E_0 e^{-jkd} \hat{y}, \tag{2.1}$$

where E_0 is the amplitude of the wave, $k = 2\pi/\lambda_0$ is the wavenumber corresponding to the free space wavelength λ_0, and d is the distance of the source from the array.

Exploiting the concept of surface impedance, introduced by Schelkunoff [45], the reflected electric field is

$$\vec{E}_r = \Gamma(x, y)\vec{E}_i, \tag{2.2}$$

where Γ is the reflection coefficient at (x, y) on the surface of the array as given by

$$\Gamma(x, y) = \frac{Z_s(x, y) - \eta_0}{Z_s(x, y) + \eta_0}. \tag{2.3}$$

Here η_0 is the free space impedance of plane waves and Z_s is the surface impedance at point (x, y). The parameter Z_s projects the effects of various phenomena, such as absorption, radiation, and scattering that occur in the region $z \leq 0$, and projects them onto the surface $z = 0$.

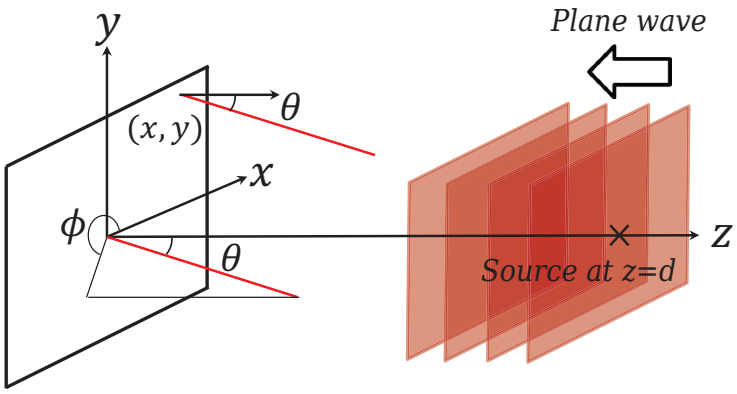

Figure 2.1: Reflectarray geometry.

Assuming the reflectarray is lossless and passive, the surface impedance is purely reactive such that

$$Z_s = jX_s \tag{2.4}$$

An appropriate expression for X_s is derived in section 2.3.2, where the equivalent circuit of the unit cell is introduced. For now, it is sufficient to assume that $X_s \geq 0$; $X_s = 0$ occurs in the case of a perfectly reflecting surface (short circuit).

Using (2.3) and (2.4), the reflected electric field on a plane infinitesimally close to the surface of the array is

$$\vec{E}_r = \frac{jX_s(x, y) - \eta_0}{jX_s(x, y) + \eta_0} E_0 e^{-jkd} \hat{y}. \tag{2.5}$$

Two limiting cases are of practical interest. First, when $X_s \ll \eta_0$ a surface with properties similar to a perfect electrical conductor (PEC) is produced, and the surface reflects out of

phase ($\Gamma \approx e^{j\pi}$). Second, when $X_s \gg \eta_0$ a *high impedance surface* is produced. This is also called an *artificial magnetic conductor* since the surface acts similar to a perfect magnetic conductor (PMC), reflecting the wave back in phase ($\Gamma \approx e^{j2\pi}$).

In general, (2.5) can be written as

$$\vec{E}_r = E_0 e^{-j\{(2\tan(\frac{X_s(x,y)}{\eta_0})+kd\}}\hat{y}, \tag{2.6}$$

and thus the phase of the reflected field is

$$\Phi(x,y) = -2\tan\left(\frac{X_s(x,y)}{\eta_0}\right) - kd. \tag{2.7}$$

The first term in (2.7), the so-called "reflection phase", is the phase difference between the incident and reflected fields at the surface of the array, and is solely due to the presence of the reflectarray. The second term is due to the propagation of the wave from the source to the reflecting surface. With other kinds of incident waves, such as spherical waves, this term requires a different expression, which is of course a function of position on the reflectarray.

It is obvious from (2.7) that the properties of the surface, and hence X_s, can be changed in order to assign different phase shifts to different points on the array. As a result, one can form a desired radiation pattern by properly selecting the surface impedance at each point on the array. For instance, in order to obtain the maximum of the scattered field in the direction (θ,ϕ) shown in Fig. 2.1, the reflected waves should constructively interfere at a point far away from the surface along those angles. This criterion leads to

$$\Phi(x,y) + k\sin\theta(x\sin\phi + y\cos\phi) - \Phi(0,0) = 2n\pi, \tag{2.8}$$

where n is an integer number. Using (2.7), the phase criterion across the array can be written in terms of X_s as

$$-2\left\{\tan\left(\frac{X_s(x,y)}{\eta_0}\right)-\tan\left(\frac{X_s(0,0)}{\eta_0}\right)\right\}+k\sin\theta=2n\pi. \tag{2.9}$$

In microstrip reflectarrays, printed radiating elements are used to manipulate the surface impedance and hence generate the proper phase shift across the array needed to produce the desired beam shape. It is not possible to practically measure the reflection phase at each point on the surface of the reflectarray, so the average phase over a unit cell is used as a design parameter. The design of a single unit of the array is explained in the next section.

2.3 Analysis of The Unit Cell

Reflection phase, reflection efficiency, and the bandwidth of the element are the most important features of a unit cell used in a reflectarray antenna [46]. In this thesis, the focus is mainly on the reflection phase properties of the unit cell. However, the reflection efficiency and the bandwidth will be briefly addressed.

In order to achieve a dual-band, phase-adjustable element with a wide reflection phase range and a high reflection efficiency, an appropriate geometry must be considered. The proposed unit cell is shown in Fig. 2.2. The geometry of the unit cell was inspired by a double square loop frequency selective surface (FSS), which perfectly blocks the incident electromagnetic wave at its two resonance frequencies [49]. In this work, the inner loop is replaced by a square patch since the square patch provides wider bandwidth. This improves the scattering properties of the unit cell. Hence, the proposed unit cell consists of a square

patch centered in a square ring along with a varactor diode placed across the gap between the ring and the square patch to provide phase adjustability. A tunable dual-band unit cell based on square loops is studied in [50] in the context of electromagnetic band-gap structures. The unit cell has the advantage of tuning each band independently. However, using six capacitors and inductors per unit cell increases the complexity of the structure.

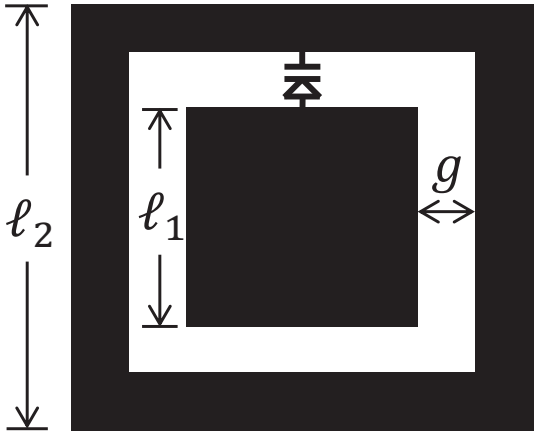

Figure 2.2: Geometry of the unit cell.

The unit cell is analyzed in two ways – with the aid of a commercial full wave solver (ANSYS HFSS), and by using an equivalent circuit model. In both cases it is assumed that the unit cell is printed on a square substrate of side p (the periodicity of the unit cell) with a conducting ground on the reverse side. Although it is assumed here that the incident wave is a plane wave normal to the unit cell, so as to simplify the derivation of the equivalent circuit parameters, in principle the problem can be solved for TE or TM fields at arbitrary incidence.

2.3.1 Full Wave Simulation

The commercial full wave simulator ANSYS HFSS was used to analyze the scattering properties of the unit cell. Since waveguides are convenient for measuring the reflection and transmission coefficients, the unit cell was located inside a fictitious square waveguide and periodic boundary conditions used to model the array by infinitely replicating the unit cell. As a result, mutual interactions between the neighboring unit cells are taken into account.

The unit cell was designed to operate within S band (2.6-3.95 GHz) and F band (4.9-7.05 GHz). The geometry parameters were optimized in order to maximize the reflection coefficient and the phase change over the two bands. The periodicity of the unit cell, and thus the dimension of the square waveguide, was chosen to be 22 mm. The other parameters are $\ell_2 = 18$ mm, $\ell_1 = 12$ mm and $g = 1$ mm. The substrate is 1.575 mm thick with a metal plane on the back, and the dielectric constant is set to unity. This last assumption is made in order to simplify the equations derived in the next section.

A varactor diode with a dynamic range of 0.1-0.6 pF is placed across the gap to achieve tunability. Two key points have to be considered in order to properly incorporate the varactor diode into the unit cell. First, it is crucial that the diode offers an appropriate range of capacitances, otherwise it will dominate or be dominated by the intrinsic parameters of the unit cell. Second, the diode should be connected in a way that the polarity of the diode is aligned with the polarization of the incident electric field. The presence of the diode breaks the symmetry of the structure. Therefore, unlike conventional double-square-loop elements, the unit cell no longer provides dual-polarized operations. However, the symmetrical structure of the unit cell does suppress cross polarization effects [38]. These two points will be visited in the investigation of the equivalent circuit model.

Fig. 2.3 shows the reflection phase (2.7) as a function of frequency for different values of the varactor capacitance. The reflection phase has a range of almost 360°, indicating high tuning ability. Moreover, two resonant frequencies can be observed. The higher resonant frequency is mainly due to the square patch, and the lower resonant frequency is largely due to the ring. This indicates that the array has the potential to steer the beam within two distinct frequency bands. Furthermore, the unit cell has the advantage of having stable performance over a wide range of incident angles 0-45° [53].

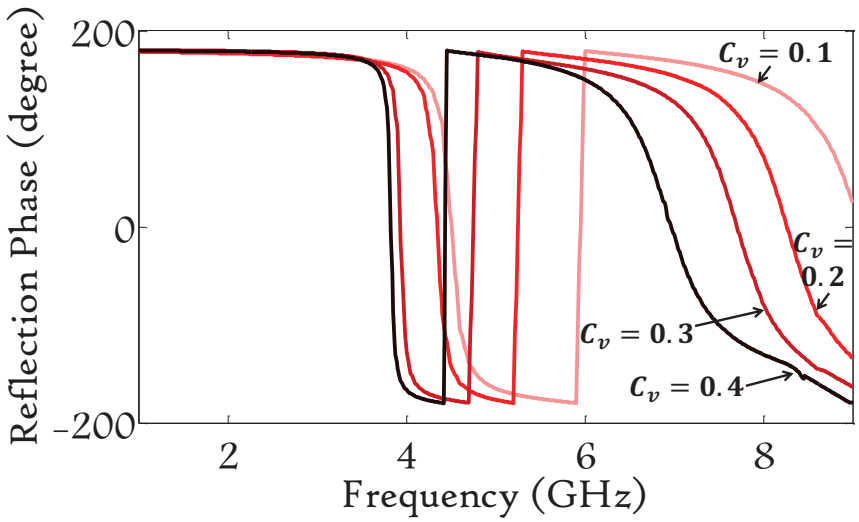

Figure 2.3: Reflection phase for different varactor capacitance values, C_v(pF).

Plots of the reflection phase as a function of the capacitance for both frequency bands are shown in Fig. 2.4. It is clear that the phase reaches its maximum and minimum at the low and high values of the varactor capacitance (C_v) respectively. This suggests that the dynamic capacitance range of the diode has to be carefully chosen in order to maximize the phase shift produced by the unit cell. Notice that the parameters of the unit cell are designed in such a way that a single diode is capable of changing the reflection phase in the two bands simultaneously.

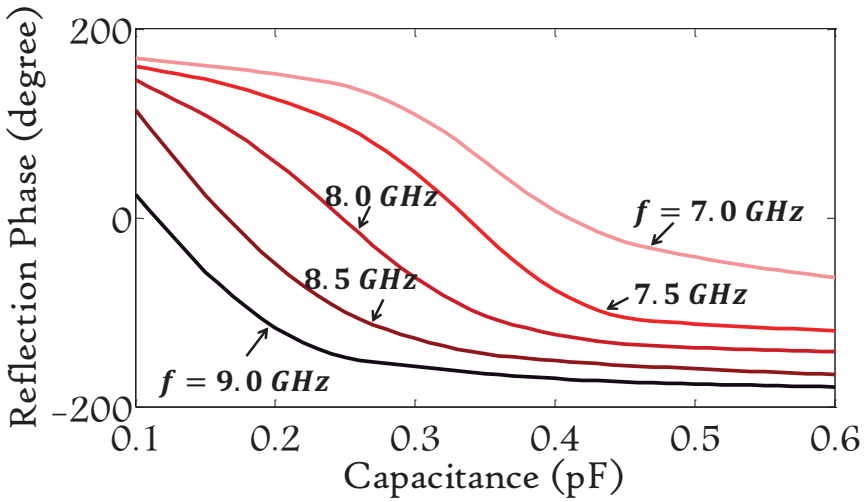

(a)

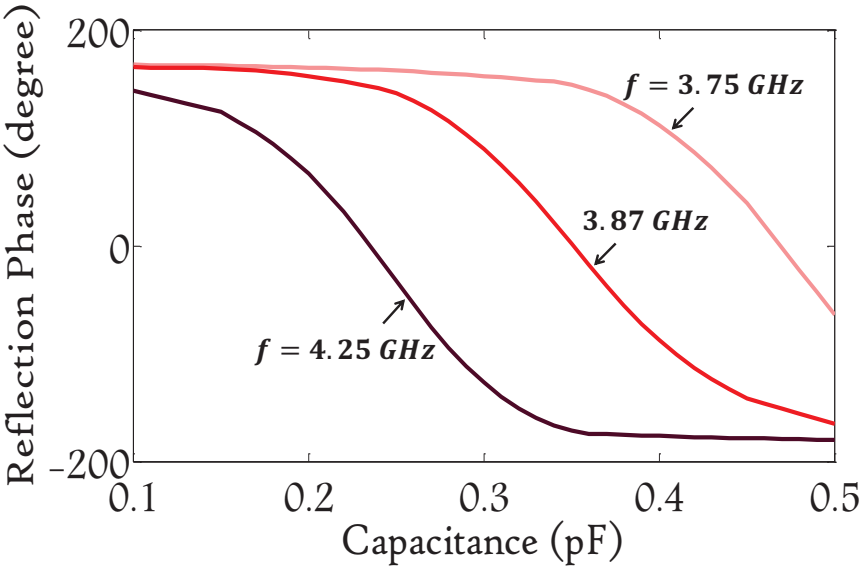

(b)

Figure 2.4: Reflection phase at different frequencies in (a) the higher frequency band and (b) the lower frequency band.

A good way to envision the role of the diode in changing the reflection phase is the 2D plot of the reflection coefficient on a surface near the unit cell [47]. The magnitude and phase of the reflection coefficient of the electric field on a plane located 0.1 mm above the surface of the unit cell is shown in Fig. 2.5. Note that the reflection phase given in Fig. 2.3 and Fig. 2.4 can be interpreted as the phase of the average reflection coefficient at each

point on this surface. To obtain Γ on the surface, two simulations are required, one with the unit cell inside the waveguide in order to calculate the total electric field, and one without the unit cell in order to calculate the incident field. The scattered field is calculated in the post processing stage by subtracting the incident field from the total field, and finally Γ is calculated with the aid of (2.2). The incoming wave is polarized along the y-axis (parallel to the diode polarity), and hence the magnitude and phase of the x and z components of the electric field are not considered. The magnitude and phase of the reflection coefficient of the y component of the electric field at 8.0 GHz with $C_v = 0.2$ pF are shown in Fig. 2.5(a). As expected, the main contribution to the scattered field is from the two radiating edges of the square patch. Consequently, the reflection phase is greatly influenced by the phase at the radiating edges, and is approximately equal to it. In Fig. 2.5(a) this phase is equal to 62°, which matches with the corresponding curve in Fig. 2.4(a). Fig. 2.5(b) shows the magnitude and phase of the reflection coefficient of the y component electric field at 4.25 GHz with $C_v = 0.2$ pF. It is obvious that the main contribution to the scattered field is from the two edges of the ring, so that again the phase of the two edges of the ring defines the final phase of the reflection coefficient. This phase is equal to 75° and matches with Fig. 2.4(b). Note that for both frequencies the phase of the reflection coefficient at the center of the unit cell, is equal to 180°. This is because the edge effects are minimal at the center, thus the center behaves similar to a PEC.

2.3.2 Equivalent Circuit Model

One of the objectives of studying an FSS is the evaluation and optimization of the transmission and reflection coefficients of the incident wave with the help of an appropriate model [48]. Modeling an FSS using equivalent circuits is a well-known technique, which not only provides

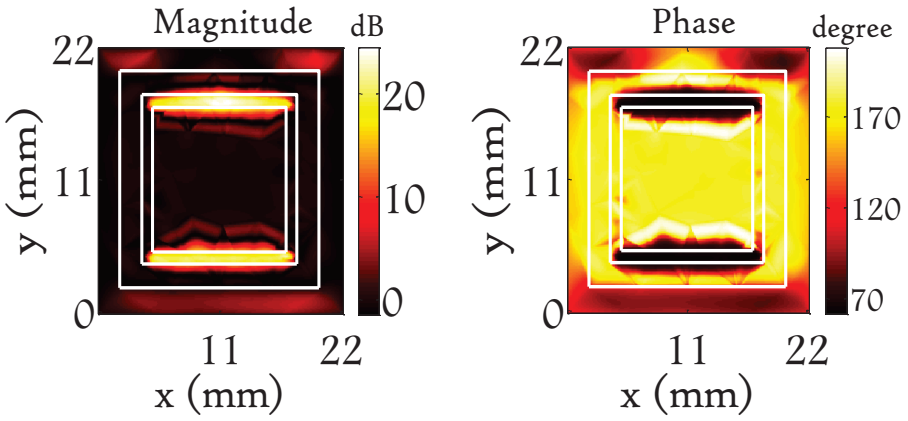

(a)

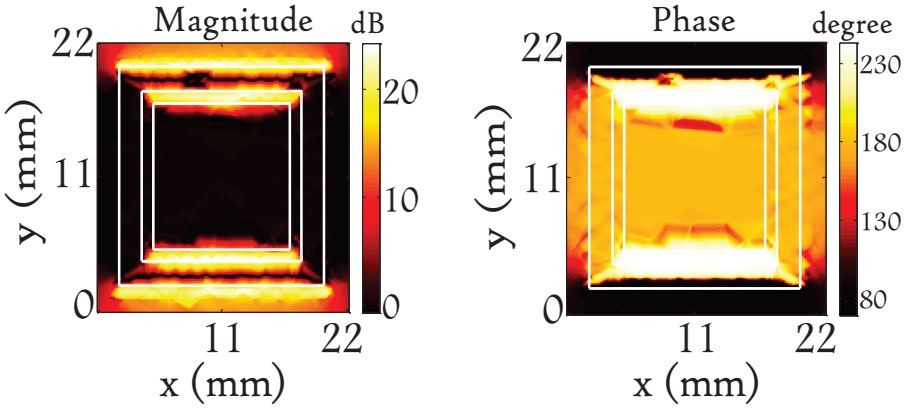

(b)

Figure 2.5: Magnitude and phase of the reflection coefficient of the y component of the electric field on a plane 0.1 mm above the surface of the unit cell at (a) 8.0 GHz and C_v=0.2 pF and (b) 4.25 GHz and C_v=0.2 pF. The layout of the unit cell is shown with white lines.

fast and accurate results but also reveals the physics of the problem. The first attempt in modeling an FSS with equivalent circuits can be found in the work of Marcuvitz [51] where two simple cases of a field incident on an infinite array of metallic strips is considered. If the strips are parallel to the electric field, the surface can be modeled with a single inductor; if the strips are parallel to the magnetic field, the surface can be modeled with a single capacitor. Equivalent circuits of more complicated geometries such as square loops [52], gridded-square elements [53], double-square loops [53]- [54] and Jerusalem crosses [55] can

be found by combining these two type of strips.

Fig. 2.6(a) shows the double loop geometry and its corresponding equivalent circuit [54]. The model consists of two shunt LC circuits representing the outer and inner loops. It is easy to see that the limiting case of the double loop, described by $w_1 = \ell_1/2$, lends itself well to the proposed unit cell, Fig. 2.6(b). One can modify the equivalent circuit of a double loop structure to achieve a model for the proposed unit cell as shown in the right panel of Fig. 2.6(b). For a TEM incident wave, the normalized values of the inductances and the capacitances of the equivalent circuit shown in Fig. 2.6(a) are given by [54]

$$\begin{aligned}
\frac{X_{w_1}}{\eta_0} &= \frac{\omega L_{w_1}}{\eta_0} = X_1 \frac{\ell_1}{p}, \\
\frac{X_{w_2}}{\eta_0} &= \frac{\omega L_{w_2}}{\eta_0} = 2\frac{X_2 X_3}{X_2 + X_3}\frac{\ell_2}{p}, \\
B_{g_1}\eta_0 &= \omega C_{g_1}\eta_0 = \frac{B_1 B_2}{B_1 + B_2}\frac{\ell_1}{p}, \\
B_{g_2}\eta_0 &= \omega C_{g_2}\eta_0 = \frac{3}{4}B_2\frac{\ell_2}{p}.
\end{aligned} \tag{2.10}$$

Here X_1, X_2, X_3, B_1 and B_2 in (2.10) are given by

$$\begin{aligned}
X_1 &= F(p, 2w_1, \lambda), \\
X_2 &= F(p, w_2, \lambda), \\
X_3 &= F(p, w_1, \lambda), \\
B_1 &= 4F(p, g_1, \lambda), \\
B_2 &= 4F(p, g_2, \lambda),
\end{aligned} \tag{2.11}$$

where $F(p, x, \lambda)$ has a general form of

$$F(p, x, \lambda) = \frac{p}{\lambda}\left[\ln \csc\left(\frac{\pi x}{2p}\right) + G(p, x, \lambda)\right]. \tag{2.12}$$

Here $G(p, x, \lambda)$ is a correction factor given by

$$G(p, x, \lambda) = \frac{1}{2}\frac{(1-\beta^2)^2[2C(1-\beta^2/4) + 4C^2\beta^2]}{(1-\beta^2/4) + 2C\beta^2(1+\beta^2/2-\beta^4/8) + 2C^2\beta^6} \tag{2.13}$$

where

$$\beta = \sin\left(\frac{\pi x}{2p}\right) \tag{2.14}$$

and

$$C = \frac{1}{\sqrt{1-(p/\lambda)^2}} - 1 \tag{2.15}$$

The model accurately predicts the behavior of a double loop as long as w_1, w_2, g_1, and g_2 are all much less than p, and $p < \lambda$.

The values of the inductances and capacitances of the unit cell equivalent circuit can be found using (2.10)-(2.15). In addition, the effect of the substrate, the metal plate on the back, and the varactor diode should be taken into account. The substrate is treated as a transmission line with a length equal to the thickness of the substrate, while the ground plate provides a short circuit at the end of the line. Hence the impedance seen at the surface due to the substrate is

$$Z_1 = j\eta_0 \tan(\beta d), \tag{2.16}$$

where η_0 is the free space impedance, $\beta = 2\pi f\sqrt{\mu_0\epsilon_0}$ is the phase constant at frequency f, ϵ_0

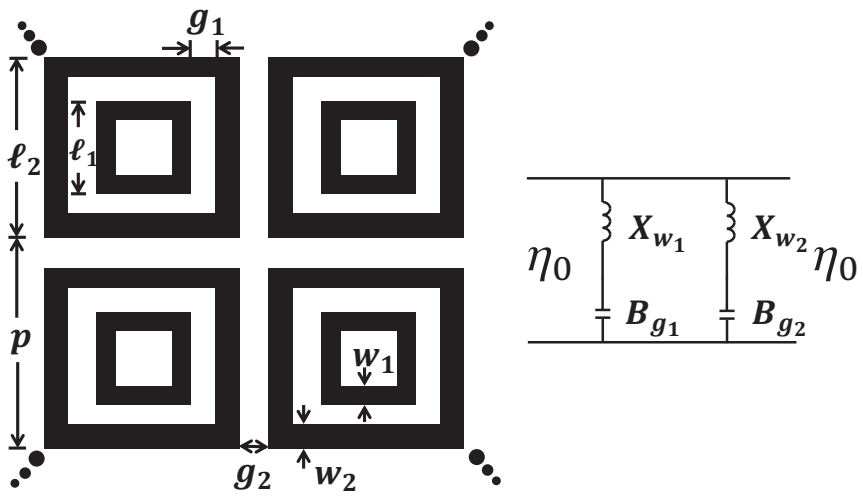

(a)

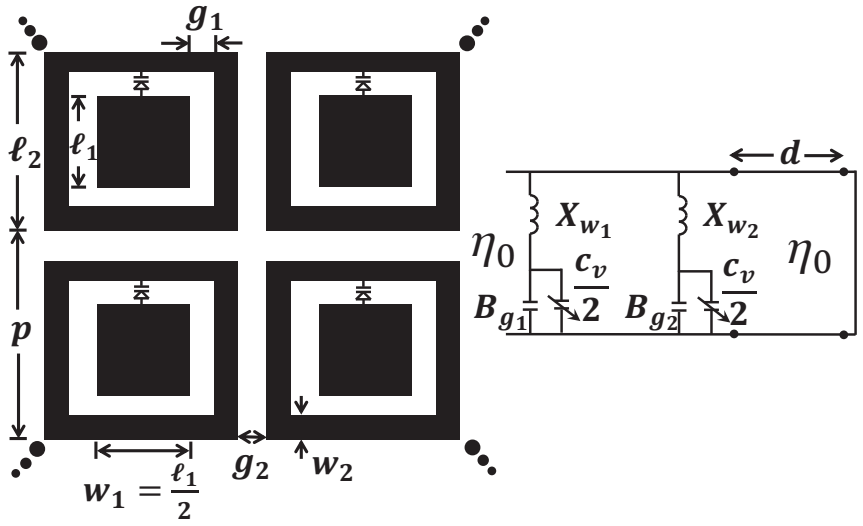

(b)

Figure 2.6: (a) Geometry of a double square loop and the equivalent circuit of an infinite array of double square loops. (b) Geometry of the proposed unit cell derived from a double square loop with $w_1 = \ell_1/2$ and the corresponding equivalent circuit.

and μ_0 are the free space permittivity and permeability respectively, and d is the thickness of the substrate. The effect of the varactor diode is taken into account by assuming that the diode almost equally shifts the two resonant frequencies, and thus it equally affects the outer loop and the patch. It is clear that the diode polarity should be along the incident electric field. This configuration minimally perturb the intrinsic inductances of the unit cell.

The surface impedance (see eqs. 2.3 and 2.4) of the array can be calculated as

$$Z_s = \eta_0/Y_s = \eta_0/(Y_1 + Y_2 + Y_3) \tag{2.17}$$

The quantity Y_s is the normalized surface admittance. Y_1, Y_2 and Y_3 are the normalized admittances corresponding to the substrate (eqn. 2.16), the ring and the patch respectively, and are given by

$$\begin{aligned} Y_1 &= 1/Z_1, \\ Y_2 &= \frac{j(B_{g_2} + B_{C_v}/2)}{1 - X_{w_2}(B_{g_2} + B_{C_v}/2)}, \\ Y_3 &= \frac{j(B_{g_1} + B_{C_v}/2)}{1 - X_{w_1}(B_{g_1} + B_{C_v}/2)}, \end{aligned} \tag{2.18}$$

where $B_{C_v} = \eta_0 w C_v$ is the normalized reactance of the capacitor.

Notice that since there is no lossy element in the circuit, Z_s is purely reactive. Once the surface impedance is known, the phase of the reflection coefficient can be calculated as shown in (2.3),

$$\phi = \Im\left\{\ln\frac{Z_s - \eta_0}{Z_s + \eta_0}\right\} \tag{2.19}$$

The reflection phase predicted by the circuit is shown in Fig. 2.7. The parameters are the same as in the previous section. A good agreement can be seen between the phase predicted by the circuit (Fig. 2.7) and predicted by HFSS (Fig. 2.3). Note that with the dimensions mentioned, the condition $w_1 \ll p$ still holds. It is seen that the addition of C_v shifts the resonance frequency of the structure.

It is worth mentioning that, in principle, the effect of dielectric substrates can be taken into account in various ways. In [56]- [57] the frequency axis is scaled by a factor of $1/\sqrt{\epsilon_r}$. In [49] the effect of the dielectric properties is incorporated in the equivalent susceptances

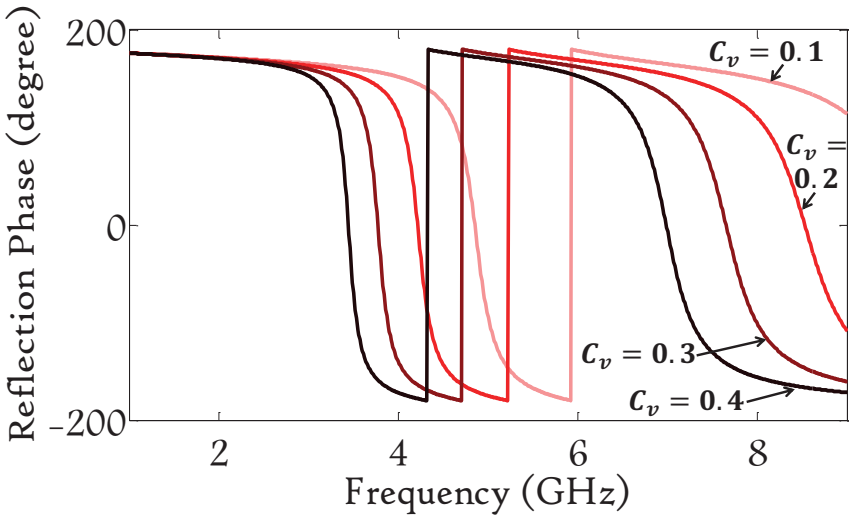

Figure 2.7: Reflection phase curves for different capacitance values, C_v(pF), predicted by the equivalent circuit model.

given in (2.11). Although the dielectric properties have not been considered so far, in the next section where simulation and experimental results are compared the substrate properties are taken into account.

2.3.3 Measurements

Since the higher and lower resonance frequencies of the structure lie in the F (4.9-7.05 GHz) and S (2.6-3.95 GHz) frequency bands respectively, two waveguides were used to experimentally validate the simulated results. Two prototypes based on the aperture sizes of the waveguides were fabricated to completely fill the waveguide cross sections; see Fig. 2.8(a). The unit cells with the dimensions provided in section 2.3.1, were fabricated on a 1.575 mm thick RT/Duroid 5880 substrate with ϵ_r of 2.2 and $\tan\delta = 0.0009$. The biasing circuit for the varactor diode, shown in Fig. 2.8(b), consists of a resistor R=10 MΩ and a capacitor C=1000 pF, and prevents the structure from coupling to the bias line, bypassing the RF noise from the power source. Vias are used in order to preserve a high reflection efficiency.

This eliminates the need to use wires and circuitry on the front side of the unit cell, which would perturb the scattered field. The appropriate placement of the vias and the biasing components was determined by investigating the surface current distribution on the structure using HFSS. The regions with relatively low surface currents were considered and different combinations of the vias located in these areas were implemented and compared. The best configuration was chosen to produce minimum impact on the performance of the resonant structure. One via close to the center of the square patch is connected to the ground plane, while another via is placed slightly below the bottom edge of the square ring, thus creating enough space for mounting the resistor on the ring.

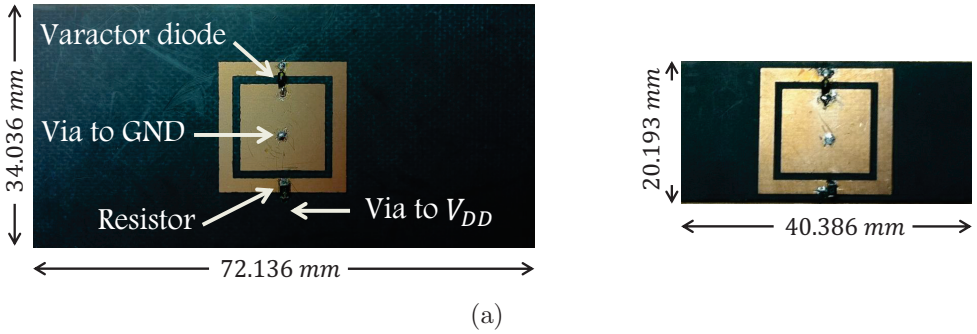

(a)

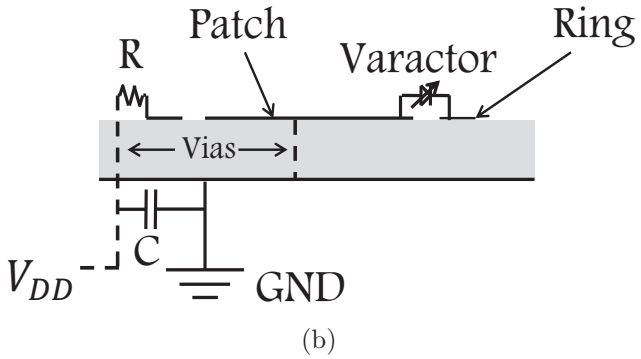

(b)

Figure 2.8: (a) Unit cells. Left: S-band. Right: F-band. (b) Side-view schematic of the biasing circuit.

A GaAs hyperabrupt varactor diode (Aeroflex Metelics MGV100-20) with a practical dynamic tuning range of $C_v = 0.18 - 2.0$ pF (corresponding to the voltage range $28 - 0.5$ V)

is used, since the diodes have both low parasitic parameters and low power dissipation. The series resistance of the diode is 3 Ω and the parasitic inductance is 0.4 nH.

In order to properly analyze the behavior of the unit cell inside the two waveguides, one has to consider two key differences from the model described in the previous sections. First, since the S-band and F-band unit cells have different periodicities, the equivalent infinite arrays generated by imaging into the waveguide walls have different unit cell spacings. This spacing is also different from the initial design (p in sections 2.3.1 and 2.3.2). This alters the scattering properties, shifts the resonance frequencies, and as a result the reflection phase curves are shifted. Second, real waveguides do not support TEM modes. The dominant propagating mode is TE_{10}, which is a superposition of two plane waves bouncing between the waveguide walls, at angle θ with respect to the main symmetry axis of the waveguide. The angle θ for the TE_{10} mode is given as [58]

$$\theta = \sin^{-1}\left(\frac{\lambda_0}{2a}\right) \tag{2.20}$$

where λ_0 is the free space wavelength and $2a$ is the cutoff wavelength of the TE_{10} mode, where a is the dimension of the longer side of the rectangular waveguide cross section. For the S-band and F-band waveguides, at their central frequencies, $\theta = 39.38^\circ$ and $\theta = 38.40^\circ$, respectively. These deviations from the original model considered in the previous section have to be incorporated and the simulation model has to be altered correspondingly before comparing the simulation results with the measurements.

Fig. 2.9(a) shows the measured reflection phase of the F-band unit cell with a varactor diode biased under various voltages. The applied voltage varies from 0.5 V to 28 V (with 0.5 V increments) corresponding to a capacitance range of 2.0 pF to 0.18 pF. Simulations

of the unit cell under the same capacitance conditions as the experiment were performed, and the phase responses are shown in Fig. 2.9(b). It is seen that good agreement of the phase response between measurement and simulation is achieved, and the unit cell is able to provide excellent phase shift capability over a wide frequency range. A maximum phase range of 335° is achieved experimentally at 5.30 GHz, and acceptable phase tuning ability over a wide frequency band of 5.0 GHz to 6.25 GHz can still be obtained. Note that the reflection phases are different from the unit cell with a TEM incident wave, which are shown in Fig. 2.3 and Fig. 2.7. This suggests that the oblique incidence together with larger periodicity has shifted the resonance frequency.

Fig. 2.10(a) and Fig. 2.10(b) show the measured and simulated magnitude of the reflection coefficient respectively, with the same biasing configuration as in Fig. 2.9. As the simulation predicts, the measured return loss of the unit cell decreases as the voltage increases. For an applied voltage larger than 8 V, a return loss that is less than 5 dB can be achieved, which implies a potential high reflection from the unit cell.

Both experimental and simulated results of phase and return loss of the S-band unit cell are provided in Fig. 2.11 and Fig. 2.12. It can be seen from Fig. 2.11 that parallel results between simulation and experiment are achieved and a maximum phase range of 340° is reached at 3.49 GHz . Note that the phase responses are for a voltage range of 5 V to 28 V (with 1 V increments) or an equivalent capacitance range of 0.38 pF to 0.18 pF. Reflection phase for a lower biasing voltage or higher capacitance can still be obtained. However, discontinuous variations of the phase responses are observed, which make the unit cell under these configurations not suitable for beam steering purposes. This issue can be explained as follows. From (2.12), the value of different elements in the equivalent circuit of Fig. 2.6(b) are proportional to $1/\lambda$, and thus the intrinsic capacitance of the unit cell is lower in the

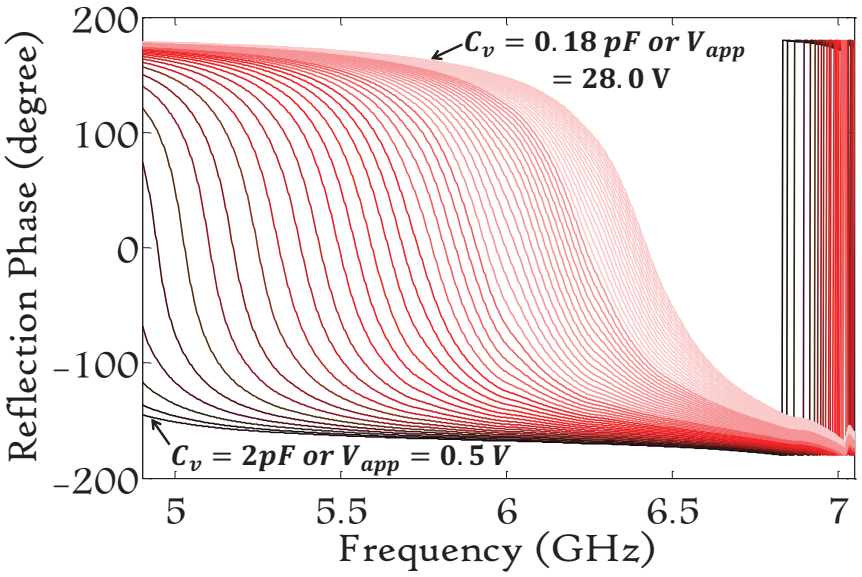

(a)

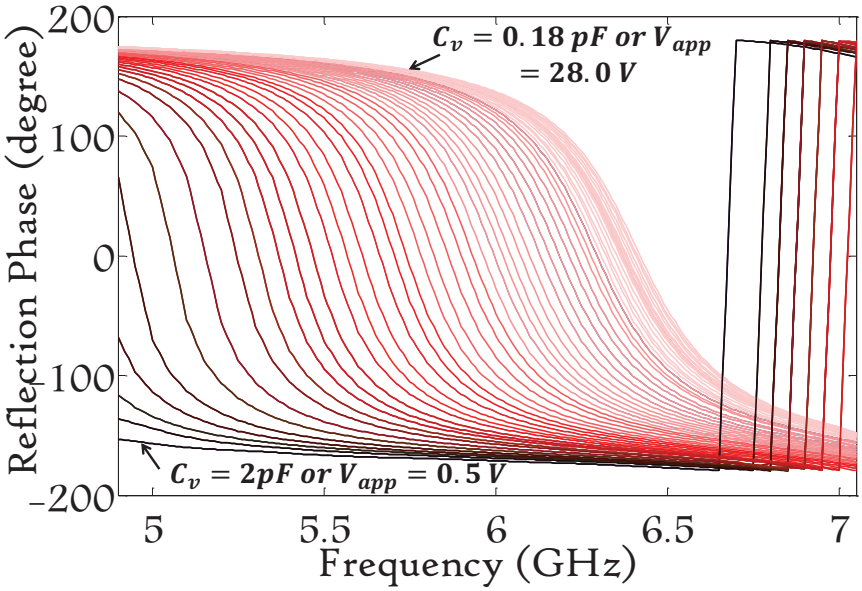

(b)

Figure 2.9: Reflection phase of the F-band unit cell as a function of frequency for different voltages (or equivalently C_v) (a) experiment (b) simulation.

S-band. As a result, for voltages lower than 5 V, the capacitance of the varactor diode dominates the intrinsic capacitance of the unit cell, and therefore interrupts the continuous phase variations of the unit cell. In addition, in contrast to the wide frequency range at F-band, the operating bandwidth for this unit cell is relatively narrow. This is due to the

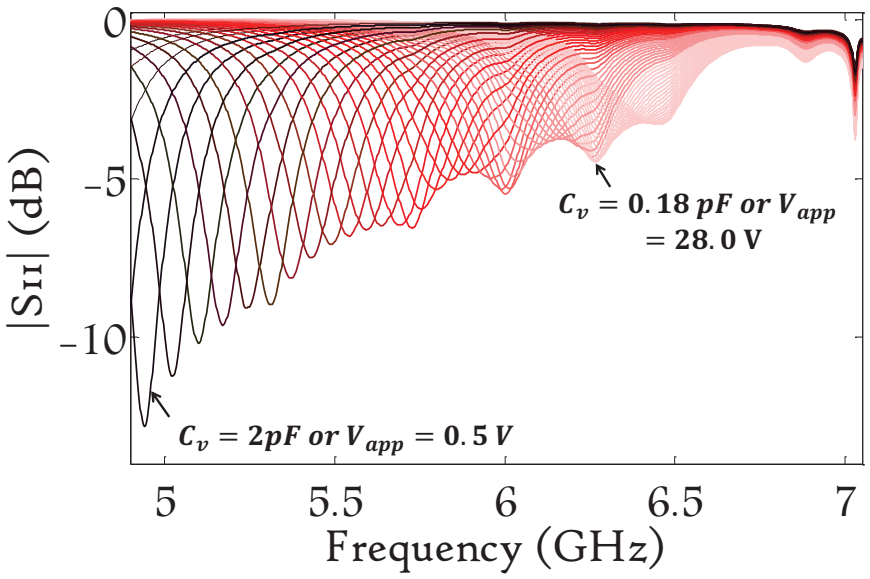

(a)

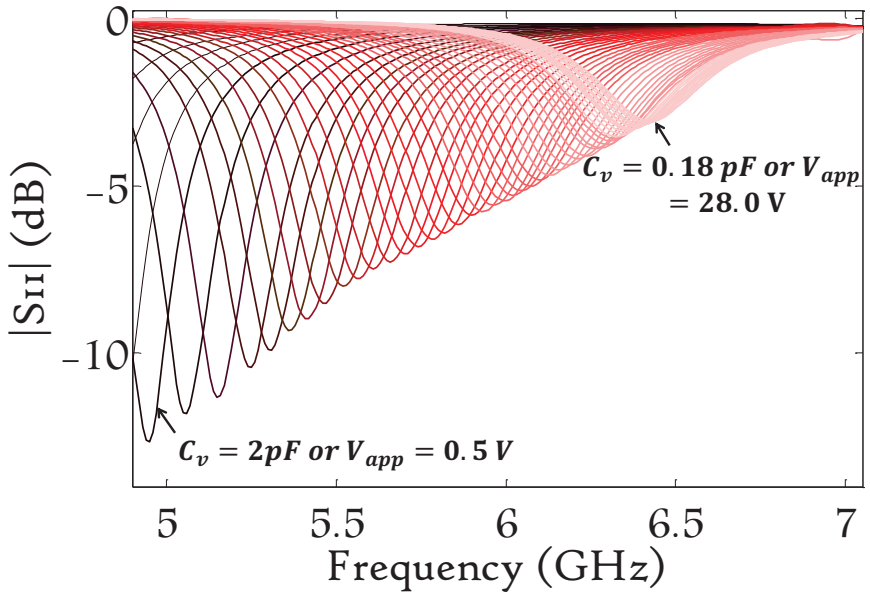

(b)

Figure 2.10: Magnitude of the reflection coefficient of the F-band unit cell as a function of frequency for different voltages (a) experiment (b) simulation.

narrow bandwidth nature of the square ring structure.

Fig. 2.12 shows the magnitude of the reflection coefficient. Reasonable agreement is seen between simulation and measurement. Note that the S-band unit cell exhibits a lower reflection than the F-band unit cell. This is because of the higher loss of the ring compared

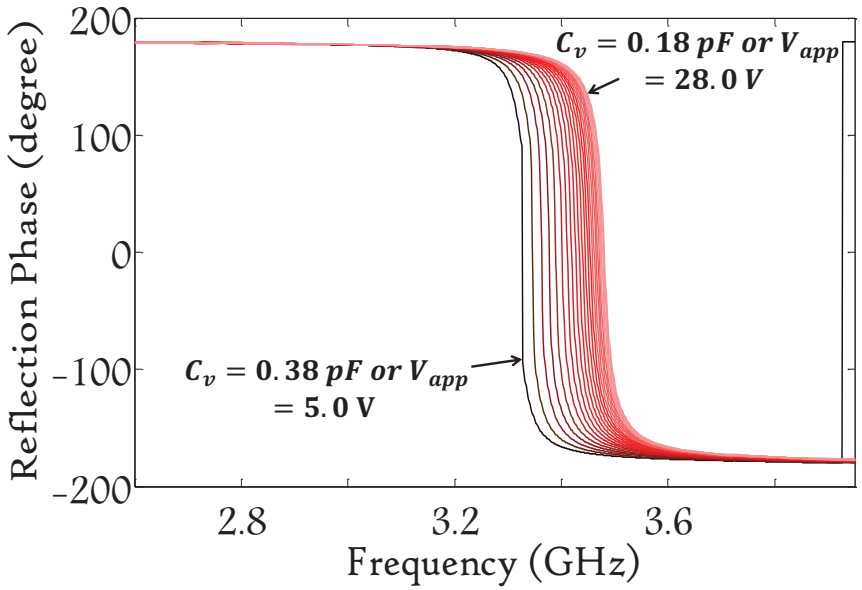

(a)

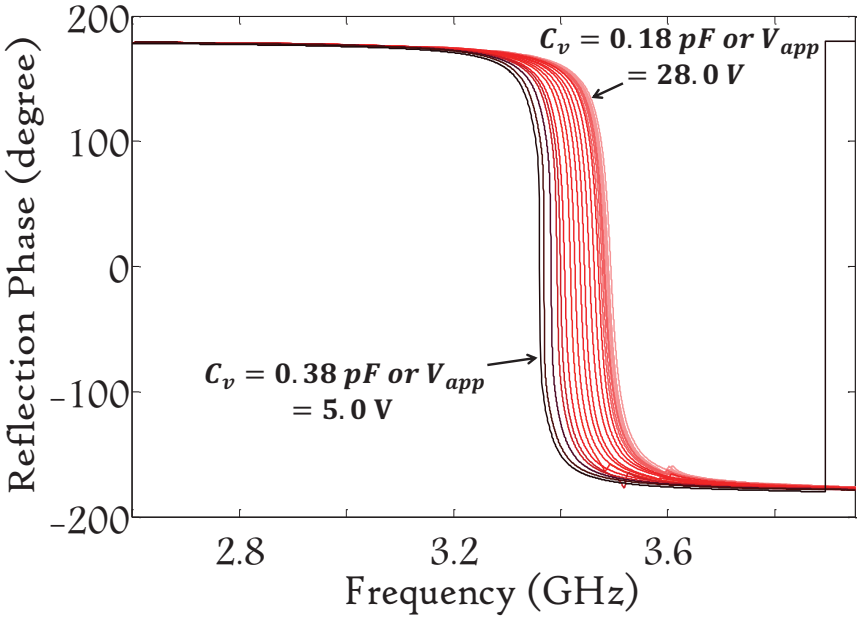

(b)

Figure 2.11: Reflection phase of the S-band unit cell as a function of frequency for different voltages (or equivalently C_v) (a) experiment (b) simulation.

to that of the square patch. In addition, the larger periodicity of the S-band unit cell affects the efficiency negatively.

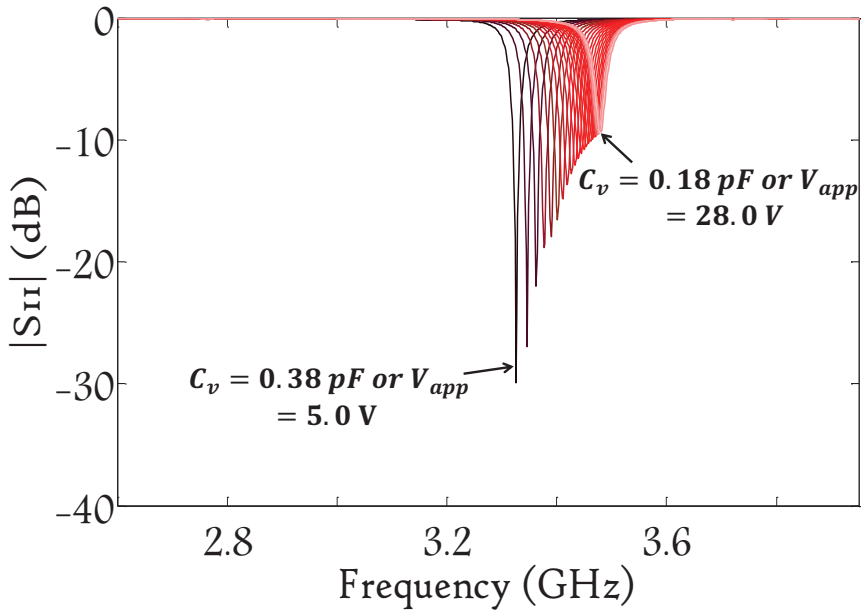

(a)

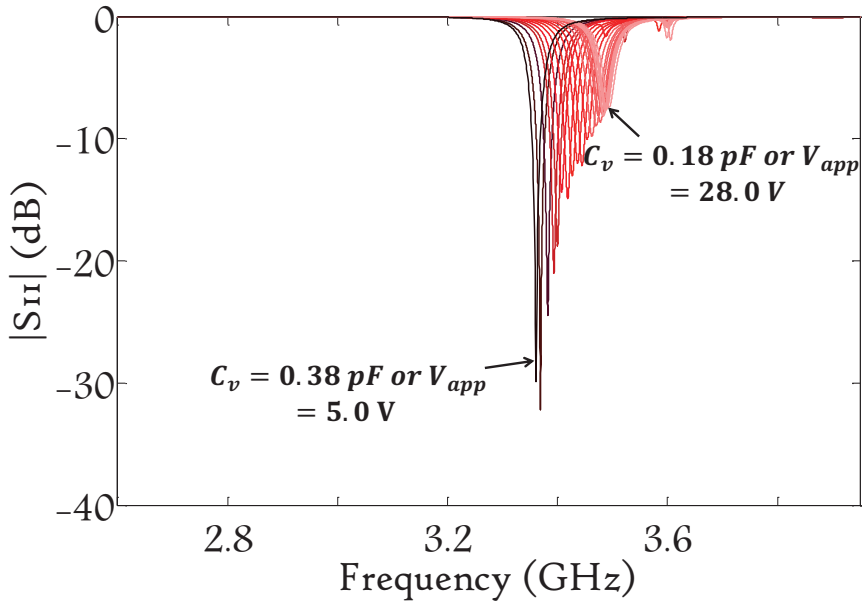

(b)

Figure 2.12: Magnitude of the reflection coefficient of the S-band unit cell as a function of freqeuncy for different voltages (a) experiment (b) simulation.

2.4 Fabricated Reflectarray

A 10x10 element reflectarray antenna was fabricated based on the proposed unit cell design. See Fig. 2.13. The dimensions and periodicity of the unit cell, described in section 2.3.1,

correspond to a square array of 220 mm x 220 mm. The substrate and the biasing circuit used in the full array are the same as that used in the single unit cell prototype described in section 2.3.3. The biasing network for the varactor was fabricated on an additional substrate and glued behind the ground plane of the array. With this prototype, instead of controlling each unit cell individually to achieve a 3-D steerable beam, only the 2-D beam steering ability is investigated. Therefore, each column of the reflectarray is biased with the same voltage. Hence, ten digital voltage regulators were used to accurately bias the array elements.

A bistatic measurement was performed using an arch range at Michigan State University [59] in order to measure the radiation pattern. TEM-horn antennas were connected to an Agilent E5071c network analyzer to measure the transmission coefficients S_{21}. Dielectric lenses were placed in front of the horn antennas to generate a focused beam with uniform phase. At 3 GHz and 6 GHz, the diameters of the beam are approximately 43 cm and 31 cm respectively. Note that in the lower frequency band, the beam size is larger than the array, which may cause a reduction in the measured S_{21}. Moreover, diffraction at the edge of the antenna will also bring a further reduction in the total transmitted power.

The VNA was calibrated from 1.5 GHz to 7.5 GHz with 1601 frequency points. The calibration of the measurement system was then conducted by finding the system response. The response of the system was calculated by considering the canonical problem of scattering off a metal sphere. The response function was obtained by comparing the experimental results with the analytical solution (Mie theory) of the scattering problem. The antenna array was mounted on a sheet of Styrofoam and placed at the center of the arch range. The arch range has a radius of 3.53 m. The center of the array was adjusted to be at the same height as the horn antennas. The array and the transmitter were kept stationary and the direction of the incident wave was adjusted to be perpendicular to the surface of the array.

Fig. 2.13 shows the experiment setup with the antenna in place. The full radiation pattern of the antenna can be measured by moving the receiving antenna (the antenna on the right in Fig. 2.13) along the arch rail. It is important to mention that, due to the large profile of the dielectric lens, the receiving and transmitting antennas cannot be co-located. Therefore, a gap in the antenna pattern appears from approximately -15° to 15°. However, this gap does not affect the measurement at 0° for the co-polarization component.

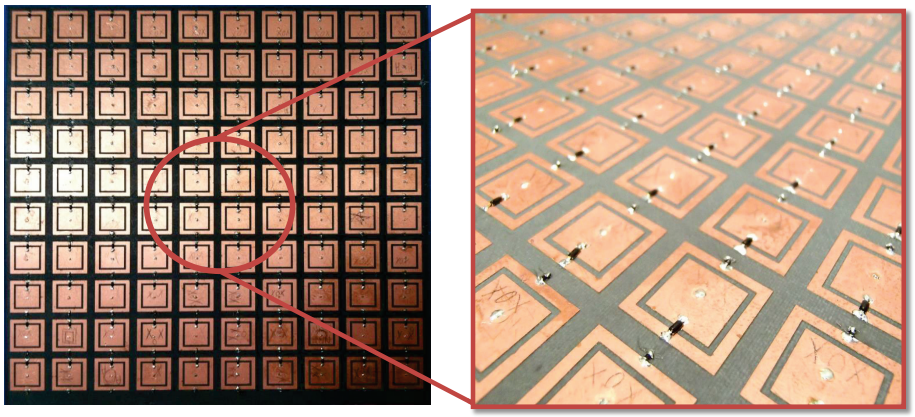

(a)

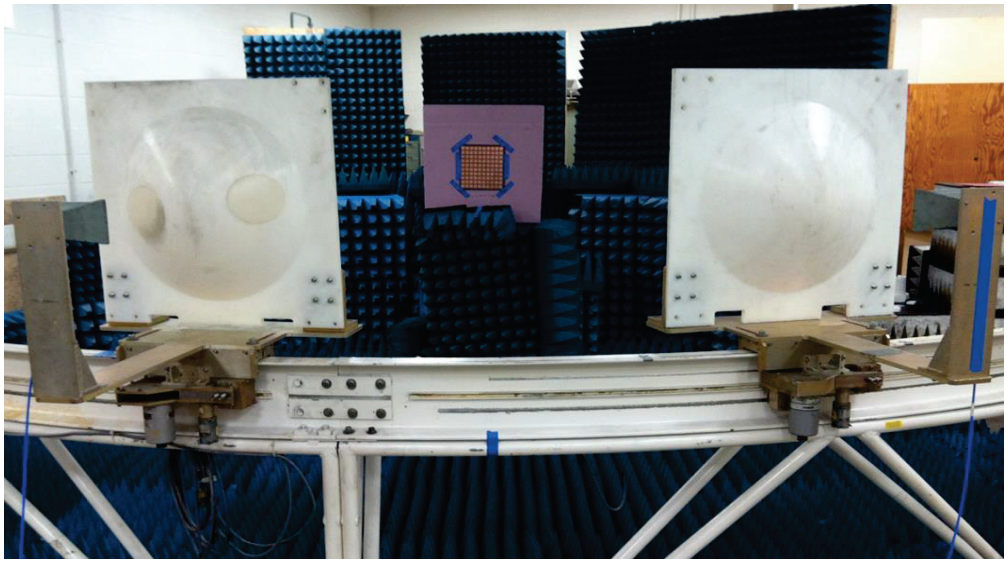

(b)

Figure 2.13: (a) Close-up view of the reflectarray (b) Experimental setup for bistatic measurement with reflectarray at the center of the arch.

Different voltage configurations were applied to the reflectarray in order to steer the main beam in multiple directions. Fig. 2.14 shows four different cases were the beam is steered onto the angles 0°, 30°, 45° and 60° at 6.12 GHz (in the higher frequency band). The values in each plot are normalized so that the maximum of the transmission coefficient, S21, is equal to 1 or 0 dB. We define the reflection efficiency of the array as the ratio of the maximum of the transmission coefficient of the array to that of a metal plate. The metal plate of the same dimensions as the reflectarray was manually rotated in order to steer the beam in the same angle as the array.

When the array is not biased, the measured pattern is similar as that of the metal plate, with the main beam reflected at 0°. The triangular shape of the main beam is due to the described large profile of the receiving and transmitting antennas. At 30°, reflection efficiency, the gain difference between the beam reflected by the array (red curve) and the one reflected by the metal plate (black curve) is -2.9 dB. At 45°, the gain difference between the main lobes is -3.2 dB and at 60° is -4.2 dB. The increase of the power loss for beams steered at large angles is expected and is observed in [38]. This is because the overall return loss of the unit cells under the voltage combination for large steering angles is greater than that of smaller steering angles. In addition, It is obvious that the beam can be deflected into negative angles by simply reversing the applied voltage. This results in an effective beam tuning range of 120°. It was observed that for the voltage configuration applied, within 6-6.2 GHz, the gain reduction is less than 1.5 dB for any steering angles below 60°. This behavior indicates that the phase relationships are maintained in a narrow-band interval. Therefore, a new voltage configuration should be applied to steer the beam in a different frequency range.

In addition to the co-polarization radiation pattern (when the transmitter and the receiver

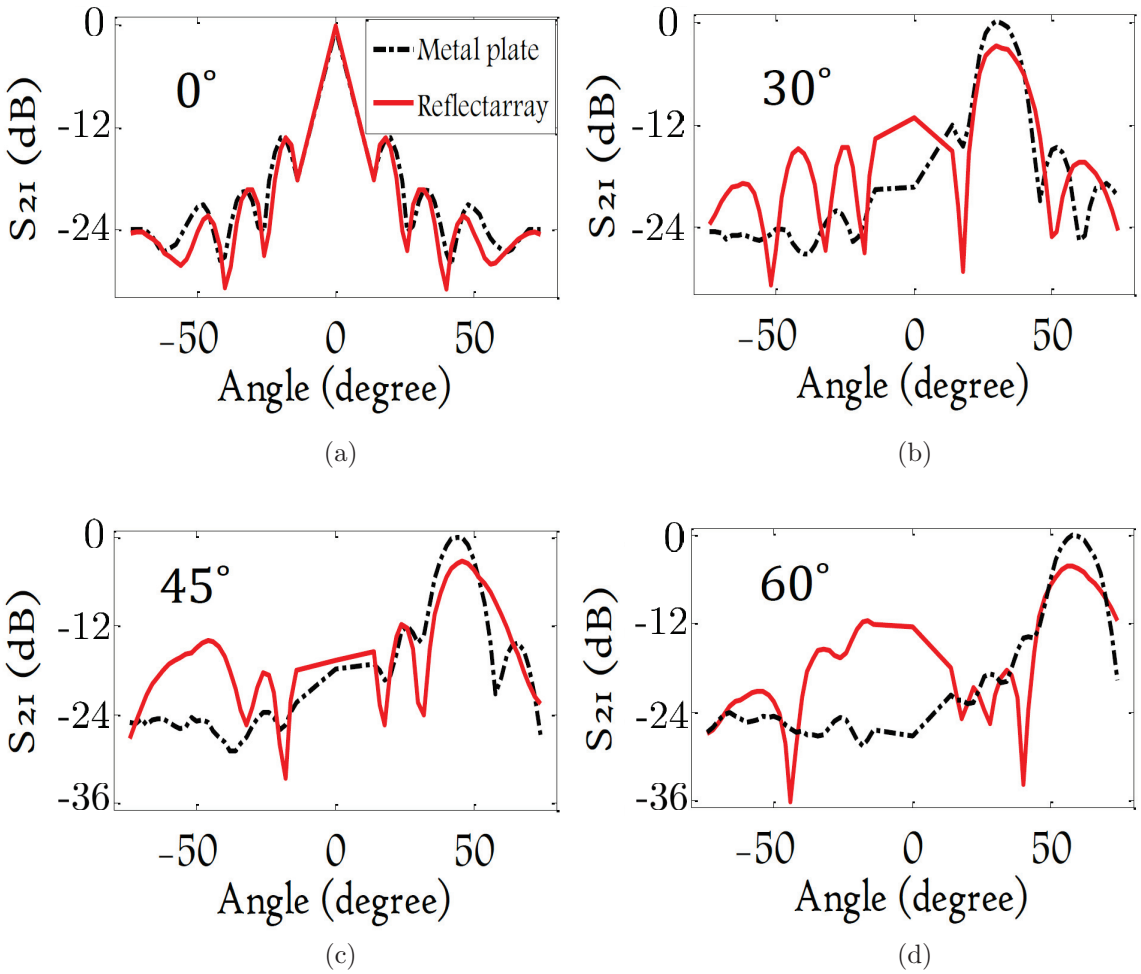

Figure 2.14: Beam steering into (a) 0°, (b) 30°, (c) 45° and (d) 60° at 6.12 GHz. The red and black curves correspond to beam steering using the reflectarray and metal plate, respectively.

have the same polarization), it is important to measure the cross-polarization pattern as well. The cross-polarization component is the component of the electric field orthogonal to the main polarization. The cross-polarization pattern was measured by rotating the receiver horn antenna by 90°. The normalized radiation pattern is shown in Fig. 2.15. The cross polarized component is expected to be low as explained in section 2.3.1. At the beam peak, the cross polarized component is at least 19 dB lower for all steering angles.

Fig. 2.16 shows beam steering at 3.38 GHz (in the lower frequency band). Similar to the

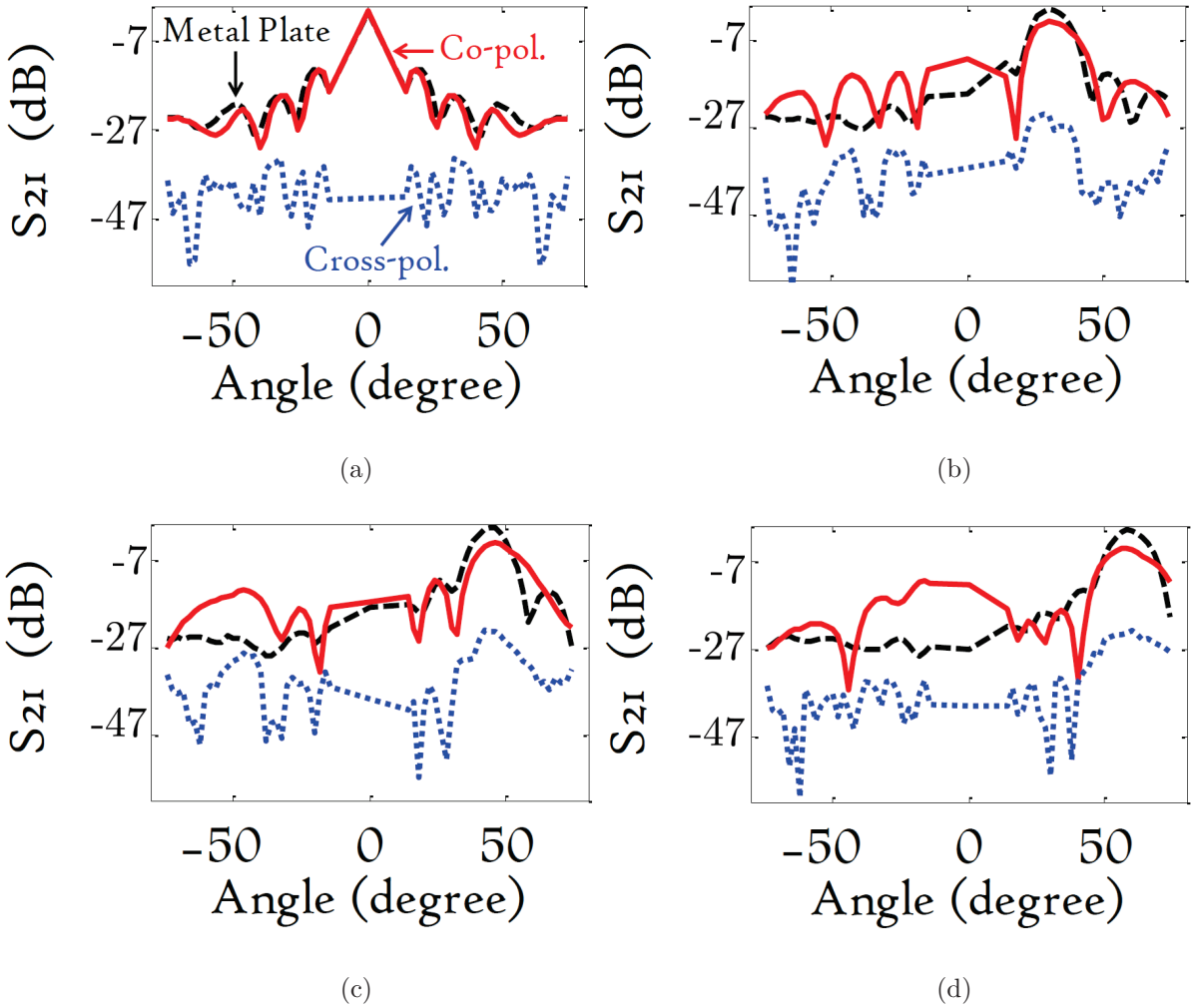

Figure 2.15: Beam steering into (a) 0°, (b) 30°, (c) 45° and (d) 60° at 6.12 GHz with the cross polarized component. The red and black curves correspond to beam steering using the reflectarray and metal plate, respectively. The blue curve is the cross polarization component.

previous case, the values in each plot are normalized to the maximum. Since the unit cell is more lossy (see section 2.3.3) the efficiency of the array is in general lower in this frequency band. However, the beam could still be deflected up to almost 60°.

As in the case of steering at higher frequency, when the array is turned off it behaves similarly to a metal plate. Note that the maximum of the main beam has been decreased in comparison to the measurements at 6.12 GHz. This is due to the fact that the incident beam

is more focused at higher frequencies and hence a larger portion of the power is reflected by both the array and the metal plate. The key element in evaluating efficiency of the array is the relative difference between the metal plate and array. The efficiency is -4.15 dB, -4.25 dB and -4.8 dB at 30°, 45° and 60°, respectively. To the best of our knowledge, such high beam steering in a dual-band tunable reflectarray has not yet been reported in literature. In general, a higher cross polarization component is observed in the S-band (see Fig. 2.17). A difference of at least 8 dB between the two polarizations is observed at the beam peak at all steering angles. Compared to the F-band, the operating frequency range is relatively narrow. This is expected as seen in the measurement of the unit cell in the S-band which indicates the narrow-band nature of such a structure.

Voltage configurations for steering the beam into different angles are given in Table 2.1. Notice the sawtooth shape of the applied voltage for all angles. This voltage variation helps to apply a gradient of the reflection phase across the array. For larger steering angles the phase gradient is larger as expected.

Voltage configurations for beam steering (Volts)						
column	30° F-band	45° F-band	60° F-band	30° S-band	45° S-band	60° S-band
1	20.2	15.0	14.5	19.1	17.5	20.9
2	13	5.9	11.8	14.2	13.6	16.9
3	9.3	5	26.5	13.8	13.5	15.0
4	6.5	15.3	12.9	13.6	13.0	5.1
5	20.4	12.1	6.0	13.3	5.8	20.5
6	14.2	5.0	15.0	5.2	18.0	16.6
7	11	15.8	11.7	17.8	13.7	14.0
8	6.6	11.5	26.4	17.9	13.4	7.0
9	20.8	6.6	13.9	17.8	12.7	20.4
10	15.2	16.9	7.2	17.7	6.1	14.2

Table 2.1: Voltage applied to each column for various steering angles

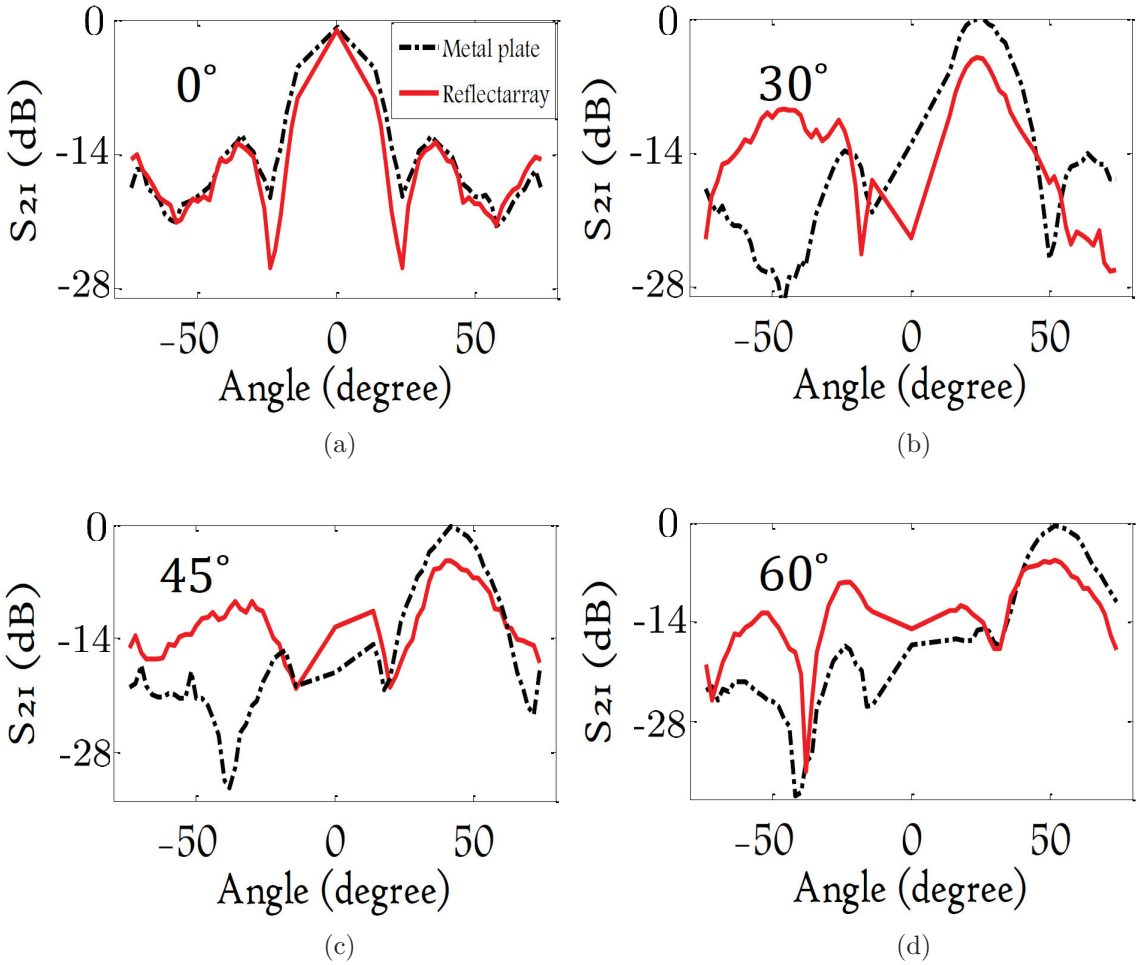

Figure 2.16: Beam steering into (a) 0°, (b) 30°, (c) 45° and (d) 60° at 3.38 GHz. The red and black curves correspond to beam steering using the reflectarray and metal plate, respectively.

2.5 Discussion

This chapter presents the design of a unit cell with tuning ability over a wide range of phase. The unit cell operates at two frequency bands and requires only one varactor diode to dynamically alter the phase of the scattered field. This significantly reduces the manufacturing cost of the array compared to more complicated systems that require multiple varactors. The unit cell was evaluated using both full-wave simulations and equivalent circuit modeling. The equivalent circuit provides a simple description of the unit cell in terms of passive circuit

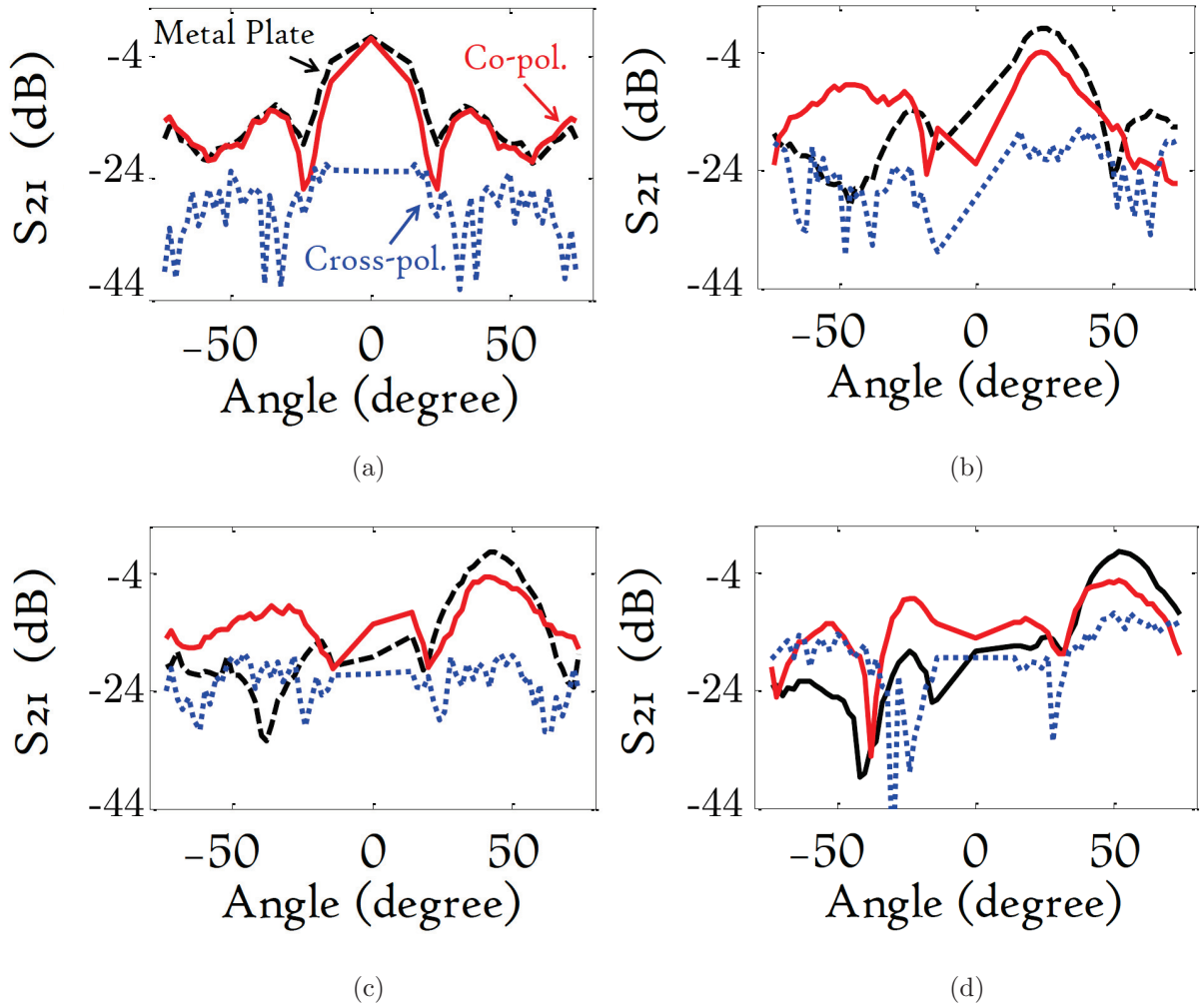

Figure 2.17: Beam steering into 0°, 30°, 45° and 60° at 3.38 GHz with the cross polarized component. The red and black curves correspond to beam steering using the reflectarray and metal plate, respectively. The blue curve is the cross polarization component.

elements, and requires far less computation time compared to the full wave simulations. The unit cell was evaluated experimentally by placing it into a waveguide and measuring the reflection coefficient. A maximum phase shift of 335° was achieved in the upper band, and 340° in the lower band.

The proposed unit cell is scalable and it can operate at other frequency bands by simply scaling its dimensions. In order to demonstrate this point, we scale the unit cell (see Fig. 2.2) by a factor of 10. Thus, the parameters of the scaled unit cell are: $p = 220$ mm,

$\ell_2 = 180$ mm, $\ell_1 = 120$ mm and $g = 10$ mm. The distance between the unit cell and the ground plane is also scaled by a factor of 10. Therefore the thickness of the substrate is $d = 15.75$ mm. To only consider the phase response of the unit cell and not dielectric effects, similar to the unit cell discussion in sections 2.3.1 and 2.3.2, the dielectric constant of the substrate is set to unity. The equivalent model in section 2.3.2 is used (see Fig. 2.6) to predict the behavior of the scaled unit cell as a function of frequency. Fig. 2.18 shows the reflection phase of the unit cell for different capacitance values. As expected, the higher and lower resonant frequencies are both scaled by a factor of 0.1 (compare with Fig. 2.7) and a large phase range is provided in both bands. Consequently the unit cell can be properly scaled in order to operate at the desired frequency band.

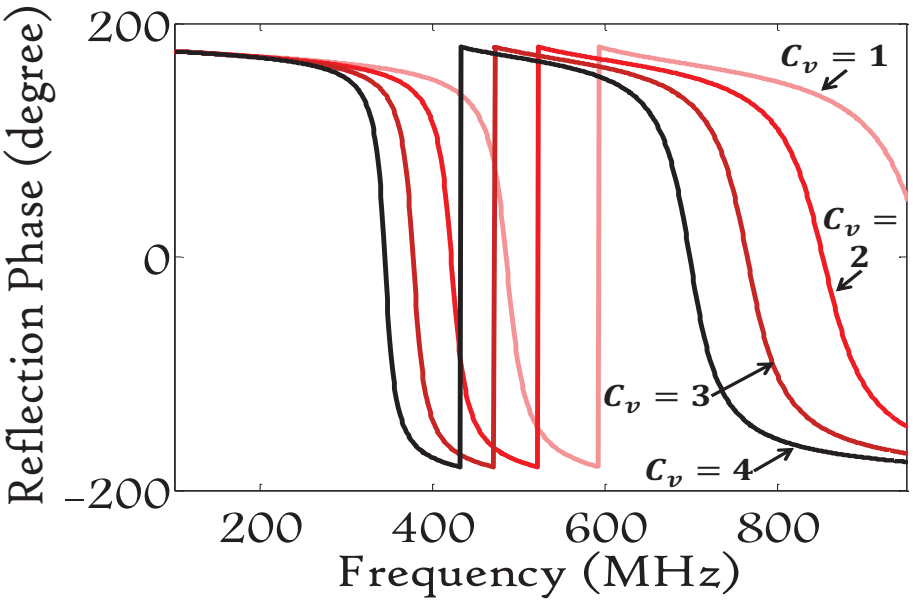

Figure 2.18: Reflection phase curves for a unit cell scaled by a facotor of 10 for different capacitance values, C_v(pF), predicted by the equivalent circuit model.

The 10x10 reflectarray built using the proposed unit cell shows excellent steering capabilities. The beam can be deflected up to $\pm 60^\circ$ in both frequency bands. This steering range has not yet been reported in literature. This unit cell design can be expanded to a larger

scale to allow for a greater range of steering capabilities. Moreover, by individually biasing each unit cell, dynamic 3-D beam steering should be achievable. This is left for future study.

Symmetry, as wide or as narrow as you may define its meaning, is one idea by which man through the ages has tried to comprehend and create order, beauty and perfection.

Hermann Weyl

Chapter 3

Time Reversal Imaging

3.1 Inverse Problems and Reconstruction Methods

An inverse problem is one in which a set of measurements is used in order to predict the causes that produced an observed outcome. Some examples of this method are the calculation of Earth's density using the measured strength of its gravitational field, X-ray imaging using projection data, and flaw profiling using the measured voltage of eddy current probes in non-destructive testing.

Inverse problems are generally ill-posed i.e. they are not well-posed problems [60]. A well-posed problem satisfies the following requirements:

- Existence of a solution
- Uniqueness of the solution

- Continuity of the solution

The last condition means that the function should change continuously with a change in the initial conditions. Inverse problems are typically ill-posed [61] and therefore special attention is required for solving this class of problems.

In this work, for the purpose of imaging, we are interested in the inverse electromagnetic scattering problem. The problem is to find the spatial distribution of the scatterers and their electrical properties (ϵ and μ) using the measured scattered field. This is known as image reconstruction. The inverse scattering problem is ill-posed mainly due to the lack of measured data. Often, the electric field is measured on 1D or 2D scan at discrete intervals. However, in order to have a well-posed problem, both the magnitude and phase of the electric field are required over the continuum of the domain. Many methods have been developed in order to counter the ill-posed aspects of the problem. One such instance is image reconstruction using diffraction tomography [62–67]. This method is even capable of reconstructing electrical properties of scatterers in highly ill-posed conditions due to limited angular coverage of the object [68–71].

In this thesis, we use the time reversal signal processing method for reconstruction purposes. This approach is model based and therefore requires a forward solver. Because we are only interested in detecting targets and not extracting their properties, no iteration is required. In what follows, time reversal imaging is explained in detail. Additionally, the forward FDTD solver is developed and used for the demonstration of the concept of time reversal.

3.2 Fundamentals of Time Reversal Signal Processing

It is known that the classical electromagnetic theory is invariant under the time reversal transformation. In order to see this, consider the electromagnetic wave equation describing the propagation of the electric field in a loss-less medium

$$\Big(\nabla^2 - \frac{1}{c^2}\frac{\partial^2}{\partial t^2}\Big)\vec{E}(\vec{r},t) = 0, \tag{3.1}$$

where ∇ is the vector Laplacian operator, c is the speed of light in the medium and $\vec{E}(\vec{r},t)$ is the electric field. Under the time reversal transformation, i.e. $t \to -t$, the wave equation (3.1) stays invariant and holds its form. Consequently, if $\vec{E}(\vec{r},t)$ is a solution to the equation, $\vec{E}(\vec{r},-t)$ is a solution as well. Notice, the symmetry is violated if the medium is lossy. This is because the presence of loss introduces a first order time derivative in (3.1) and hence the wave equation is no longer invariant under the time reversal transformation.

The time reversal symmetry has a significant practical implication. If one measures the electric field emitted from a source via an antenna array, time reverses the received signals and re-emits them back, the electric field focuses at the initial source of radiation. In a case where there are scatterers present in the medium, they act as secondary sources and the re-emitted time-reversed signals focus at the locations of the scatterers. Therefore, this property can be successfully used as a reconstruction scheme in order to detect and pinpoint scatters in a medium. This approach is known as time reversal imaging and it has been vastly used as a powerful imaging technique. In [72], Bellomo et al. introduce a new radar system utilizing time reversal imaging. It has been experimentally shown that the time-reversed signals focus on the target. Through-the-wall target localization has been demonstrated using the time reversal MUSIC method in the work of Zhang et al. [73]. Time reversal microwave imaging

with random configurations of transmitters or receivers is studied by Razavian et al. in [74]. In [75] by Kosmas et al., the feasibility of microwave breast cancer detection using time reversal algorithms is investigated. Time reversal microwave techniques were also utilized for NDT of laminates and composite materials in the work of Reyes-Rodrigueaz et al. [76]. The application of the time reversal symmetry is not limited to imaging however; in the paper by El Sahmarany et al. [77], time reversal is used for fault detection in wire networks.

In this work, time reversal imaging is the main reconstruction scheme used in order to detect and identify the location of scatterers. Next, we develop a forward solver, i.e. a scheme to numerically solve Maxwell's equations. The solver is then used in order to prove and demonstrate the time reversal concept using computer simulations.

3.3 Finite Difference Time Domain (FDTD)

Over the past few decades many numerical methods have been developed in order to solve Maxwell's equations in different media and for various geometries. Finite Element Method (FEM), Method of Moments (MoM) and Finite Difference Time Domain (FDTD) are among the most popular numerical techniques. A natural choice here would be FDTD because the reconstruction technique is essentially performed in the time domain. Starting with Maxwell's equations, and applying the finite difference approximation, the main equations used for the FDTD simulations are derived in this section.

3.3.1 Maxwell's Equations

Maxwell's equations are partial differential equations that describe the behavior of electric and magnetic fields. Assuming there are no sources in the medium, in the SI units they have

the following form

$$\nabla \cdot \vec{\mathcal{D}}(t) = 0, \tag{3.2}$$

$$\nabla \cdot \vec{B}(t) = 0, \tag{3.3}$$

$$\nabla \times \vec{\mathcal{E}}(t) = -\frac{\partial \vec{B}(t)}{\partial t}, \tag{3.4}$$

$$\nabla \times \vec{H}(t) = \frac{\partial \vec{\mathcal{D}}(t)}{\partial t}, \tag{3.5}$$

where $\vec{\mathcal{E}}$ is the electric field intensity (units of V/m), $\vec{\mathcal{D}}$ is the electric flux density (units of C/m^2), $\vec{H}$ is the magnetic field intensity (units of A/m) and $\vec{B}$ is the magnetic flux density (units of Wb/m^2). Furthermore $\vec{\mathcal{E}}$ and $\vec{\mathcal{D}}$ and also $\vec{H}$ and $\vec{B}$ are related through the constitutive equations

$$\vec{\mathcal{D}}(t) = \epsilon_0 \epsilon_r \vec{\mathcal{E}}(t), \tag{3.6}$$

$$\vec{B}(t) = \mu_0 \mu_r \vec{H}(t), \tag{3.7}$$

where ϵ_0 (μ_0) is the permittivity (permeability) of free space and ϵ_r (μ_r) is the relative permittivity (permeability) of the medium.

For convenience, we normalize the electric field by defining a new variable $\vec{E}(t)$

$$\vec{E}(t) = \sqrt{\frac{\epsilon_0}{\mu_0}} \vec{\mathcal{E}}(t) = \frac{1}{\eta_0} \vec{\mathcal{E}}(t) \tag{3.8}$$

where η_0 is the free space impedance. Accordingly, we modify $\vec{\mathcal{D}}$ by defining a new variable

$$\vec{D}(t) = \frac{1}{\sqrt{\epsilon_0 \mu_0}} \vec{\mathcal{D}}(t) = c \vec{\mathcal{D}}(t) \tag{3.9}$$

here c is the speed of light in free space. Now, rewriting the two curl equations in (3.4) and (3.5) in terms of $\vec{E}$ and $\vec{D}$, we have

$$\nabla \times \vec{E}(t) = -\frac{\mu_r}{c}\frac{\partial \vec{H}(t)}{\partial t}, \tag{3.10}$$

$$\nabla \times \vec{H}(t) = \frac{1}{c}\frac{\partial \vec{D}(t)}{\partial t}, \tag{3.11}$$

Notice that these equations are independent of ϵ_r. Moreover, the materials used for imaging in this thesis are not magnetic materials, i.e. μ_r=1. The independence of these two equations from material properties simplify our numerical calculations discussed in the next section.

The new constitutive relation is

$$\vec{D}(t) = \epsilon_r \vec{E}(t) \tag{3.12}$$

Next, we write the explicit equations for the two curl equations in (3.10) and (3.11) and the modified constitutive relation (3.12) using the Cartesian coordinate system. Furthermore, we assume that the material has a diagonal relative permittivity and permeability tensor. Therefore the only non-zero components of μ_r are μ_{xx}, μ_{yy} and μ_{zz} and similarly for ϵ_r.

We have for equation (3.10)

$$C_x^E = -\frac{\mu_{xx}}{c}\frac{\partial H_x}{\partial t}, \tag{3.13}$$

$$C_y^E = -\frac{\mu_{yy}}{c}\frac{\partial H_y}{\partial t}, \tag{3.14}$$

$$C_z^E = -\frac{\mu_{zz}}{c}\frac{\partial H_z}{\partial t}, \tag{3.15}$$

where C_i^E is the i'th component of the curl of the electric field i.e.

$$C_x^E = \frac{\partial E_z}{\partial y} - \frac{\partial E_y}{\partial z}, \tag{3.16}$$

$$C_x^E = \frac{\partial E_x}{\partial z} - \frac{\partial E_z}{\partial x}, \tag{3.17}$$

$$C_x^E = \frac{\partial E_y}{\partial x} - \frac{\partial E_x}{\partial y}. \tag{3.18}$$

Similarly for equation (3.11) we have

$$C_x^H = \frac{1}{c}\frac{\partial D_x}{\partial t}, \tag{3.19}$$

$$C_y^H = \frac{1}{c}\frac{\partial D_y}{\partial t}, \tag{3.20}$$

$$C_z^H = \frac{1}{c}\frac{\partial D_z}{\partial t}, \tag{3.21}$$

where

$$C_x^H = \frac{\partial H_z}{\partial y} - \frac{\partial H_y}{\partial z}, \tag{3.22}$$

$$C_x^H = \frac{\partial H_x}{\partial z} - \frac{\partial H_z}{\partial x}, \tag{3.23}$$

$$C_x^H = \frac{\partial H_y}{\partial x} - \frac{\partial H_x}{\partial y}, \tag{3.24}$$

Finally, for (3.12) we have

$$D_x = \epsilon_{xx} E_x, \tag{3.25}$$

$$D_y = \epsilon_{yy} E_y, \tag{3.26}$$

$$D_z = \epsilon_{zz} E_z. \tag{3.27}$$

Next we exploit the finite difference approximation in order to numerically solve the equations (3.13)-(3.15), (3.19)-(3.21) and (3.25)-(3.27).

3.3.2 Finite Difference Approximation

In order to calculate the electric and magnetic fields in Maxwell's equations, the derivatives in the differential equations are approximated by a linear difference equation. In this thesis, the so called central difference approximation is used. Consider a real one dimensional function, $f(x)$, which is analytic over $\Omega = (a, b)$. $f(x)$ can be approximated by a discrete valued function

$$f_i = f(x_i) \quad i = 1, 2, ..., N, \tag{3.28}$$

where x_i's are the grid points and N is the number of the grids. The grid is assumed to be uniform with the sampling interval represented by $\Delta x = (b - a)/N$.

We now introduce the forward and backward differences as approximations for the derivative of $f(x)$ at grid point x_i. The forward difference is

$$\Big(\frac{df}{dx}\Big)_i^F \approx \frac{f_{i+1} - f_i}{\Delta x}, \tag{3.29}$$

and the backward difference is

$$\Big(\frac{df}{dx}\Big)_i^B \approx \frac{f_i - f_{i-1}}{\Delta x}. \tag{3.30}$$

Both approximations in (3.29) and (3.30) are accurate only up to the first order in Δx. In order to come up with a better approximation, we first write the complete expansion for

both the forward and backward differences. For the forward difference we have

$$\Big(\frac{df}{dx}\Big)_i^F = \frac{f_{i+1} - f_i}{\Delta x} - \frac{\Delta x}{2}\Big(\frac{d^2 f}{dx^2}\Big)_i - \frac{\Delta x^2}{6}\Big(\frac{d^3 f}{dx^3}\Big)_i + ..., \tag{3.31}$$

and for the backward difference we have

$$\Big(\frac{df}{dx}\Big)_i^B = \frac{f_i - f_{i-1}}{\Delta x} + \frac{\Delta x}{2}\Big(\frac{d^2 f}{dx^2}\Big)_i - \frac{\Delta x^2}{6}\Big(\frac{d^3 f}{dx^3}\Big)_i + ... \tag{3.32}$$

Now we add (3.31) and (3.32) together. Consequently

$$\Big(\frac{df}{dx}\Big)_i^C = \frac{f_{i+1} - f_{i-1}}{2\Delta x} - \frac{\Delta x^2}{6}\Big(\frac{d^3 f}{dx^3}\Big)_i + ... \tag{3.33}$$

From this, one can approximate the derivative with a truncation error of $\mathcal{O}(\Delta x)^2$. Therefore, we define the central difference approximation as

$$\Big(\frac{df}{dx}\Big)_i^C \approx \frac{f_{i+1} - f_{i-1}}{2\Delta x}. \tag{3.34}$$

This approximation is used in order to numerically evaluate the time derivatives and curl equations derived in the previous section. In addition, in order to discretize the continuous electric and magnetic fields, we adopt the popular Yee grid scheme [78]. Fig. 3.1 shows the schematic of a grid cell. This specific configuration of the electric and magnetic fields in the cell has many advantages. It can be shown that the electric and magnetic fields are both divergenceless. Therefore equations (3.2) and (3.3) are naturally satisfied. Moreover, using the central difference approximation becomes easier with this configuration.

In addition to space, time has to be descritized as well. We assume that the electric

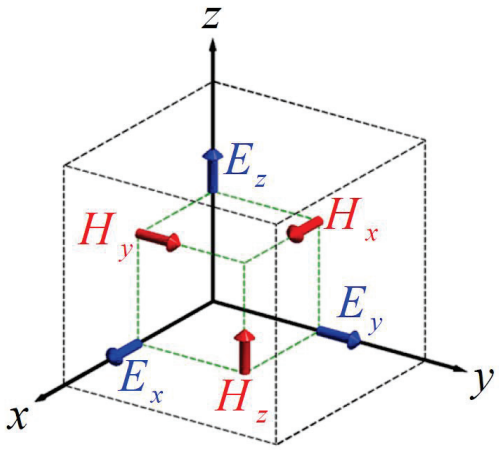

Figure 3.1: Yee grid cell.

field exists in integer time steps i.e. $0, \Delta t, 2\Delta t, ...$, where Δt is the time step. However, the magnetic field is assumed to exist on half-integer time steps i.e. $\Delta t/2, t + \Delta t/2, 2t + \Delta t/2....$ Consequently, each component of the fields requires four indices, (i, j, k) representing the cell location and t representing time.

We now write the descritized expressions for the curl terms in (3.16)-(3.18)

$$C_x^E\Big|_t^{i,j,k} = \frac{E_z\Big|_t^{i,j+1,k} - E_z\Big|_t^{i,j,k}}{\Delta y} - \frac{E_y\Big|_t^{i,j,k+1} - E_y\Big|_t^{i,j,k}}{\Delta z}, \tag{3.35}$$

$$C_y^E\Big|_t^{i,j,k} = \frac{E_x\Big|_t^{i,j,k+1} - E_x\Big|_t^{i,j,k}}{\Delta z} - \frac{E_z\Big|_t^{i+1,j,k} - E_z\Big|_t^{i,j,k}}{\Delta x}, \tag{3.36}$$

$$C_z^E\Big|_t^{i,j,k} = \frac{E_y\Big|_t^{i+1,j,k} - E_y\Big|_t^{i,j,k}}{\Delta x} - \frac{E_x\Big|_t^{i,j+1,k} - E_x\Big|_t^{i,j,k}}{\Delta y}. \tag{3.37}$$

Using (3.35)-(3.37), the finite difference approximation of Faraday's equation in (3.13)-

(3.15) is then

$$C_x^E\Big|_t^{i,j,k} = -\frac{\mu_{xx}\Big|^{i,j,k}}{c}\ \frac{H_x\Big|_{t+\Delta t/2}^{i,j,k} - H_x\Big|_{t-\Delta t/2}^{i,j,k}}{\Delta t}, \tag{3.38}$$

$$C_y^E\Big|_t^{i,j,k} = -\frac{\mu_{yy}\Big|^{i,j,k}}{c}\ \frac{H_y\Big|_{t+\Delta t/2}^{i,j,k} - H_y\Big|_{t-\Delta t/2}^{i,j,k}}{\Delta t}, \tag{3.39}$$

$$C_z^E\Big|_t^{i,j,k} = -\frac{\mu_{zz}\Big|^{i,j,k}}{c}\ \frac{H_z\Big|_{t+\Delta t/2}^{i,j,k} - H_z\Big|_{t-\Delta t/2}^{i,j,k}}{\Delta t}. \tag{3.40}$$

In a similar way, we can approximate Ampere's law. We first calculate the curl expressions in (3.22)-(3.24)

$$C_x^H\Big|_{t+\Delta t/2}^{i,j,k} = \frac{H_z\Big|_{t+\Delta t/2}^{i,j,k} - H_z\Big|_{t+\Delta t/2}^{i,j-1,k}}{\Delta y} - \frac{H_y\Big|_{t+\Delta t/2}^{i,j,k} - H_y\Big|_{t+\Delta t/2}^{i,j,k-1}}{\Delta z}, \tag{3.41}$$

$$C_y^H\Big|_{t+\Delta t/2}^{i,j,k} = \frac{H_x\Big|_{t+\Delta t/2}^{i,j,k} - H_x\Big|_{t+\Delta t/2}^{i,j,k-1}}{\Delta z} - \frac{H_z\Big|_{t+\Delta t/2}^{i,j,k} - H_z\Big|_{t+\Delta t/2}^{i-1,j,k}}{\Delta x}, \tag{3.42}$$

$$C_z^H\Big|_{t+\Delta t/2}^{i,j,k} = \frac{H_y\Big|_{t+\Delta t/2}^{i,j,k} - H_y\Big|_{t+\Delta t/2}^{i-1,j,k}}{\Delta x} - \frac{H_x\Big|_{t+\Delta t/2}^{i,j,k} - H_x\Big|_{t+\Delta t/2}^{i,j-1,k}}{\Delta y}. \tag{3.43}$$

$$\tag{3.44}$$

Ampere's law in (3.19)-(3.21) becomes

$$C_x^H\Big|_{t+\Delta t/2}^{i,j,k} = \frac{1}{c}\,\frac{D_x\Big|_{t+\Delta t}^{i,j,k} - D_x\Big|_{t}^{i,j,k}}{\Delta t}, \tag{3.45}$$

$$C_y^H\Big|_{t+\Delta t/2}^{i,j,k} = \frac{1}{c}\,\frac{D_y\Big|_{t+\Delta t}^{i,j,k} - D_y\Big|_{t}^{i,j,k}}{\Delta t}, \tag{3.46}$$

$$C_z^H\Big|_{t+\Delta t/2}^{i,j,k} = \frac{1}{c}\,\frac{D_z\Big|_{t+\Delta t}^{i,j,k} - D_z\Big|_{t}^{i,j,k}}{\Delta t}. \tag{3.47}$$

Finally, the descritized constitutive relation (3.25)-(3.27) is

$$D_x\Big|_{t}^{i,j,k} = \left(\epsilon_{xx}\Big|^{i,j,k}\right) E_x\Big|_{t}^{i,j,k}, \tag{3.48}$$

$$D_y\Big|_{t}^{i,j,k} = \left(\epsilon_{yy}\Big|^{i,j,k}\right) E_y\Big|_{t}^{i,j,k}, \tag{3.49}$$

$$D_z\Big|_{t}^{i,j,k} = \left(\epsilon_{zz}\Big|^{i,j,k}\right) E_z\Big|_{t}^{i,j,k}. \tag{3.50}$$

3.3.2.1 Reduction to Two Dimensions

For simplicity, we assume a two dimensional scenario i.e. all the physical objects are infinitely extended and uniform in one dimension (here, we choose the z-direction). Mathematically, we require $\frac{\partial}{\partial z} = 0$. Moreover, we assume that the wave produced by the source is of TM_z type. This means that there is no magnetic field in the z-direction, or $\vec{H}.\hat{z} = 0$. As we will see in the next chapter, these are realistic assumptions seeing that the targets used in the experiment are uniform and long with respect to the wavelength of the wave. Also, the horn antennas used in the experimental setup are linearly polarized, therefore we simply choose our coordinate system so that the z-direction coincides with the generated electric field.

Consequently, the condition for $\vec{H}.\hat{z} = 0$ is satisfied. With these assumptions we can greatly simplify the equations derived in the previous section. For a two dimensional problem and a TM_z source, the curl expressions (3.35)-(3.37) in Faraday's law become

$$C_x^E\Big|_t^{i,j} = \frac{E_z\Big|_t^{i,j+1} - E_z\Big|_t^{i,j}}{\Delta y}, \tag{3.51}$$

$$C_y^E\Big|_t^{i,j} = -\frac{E_z\Big|_t^{i+1,j} - E_z\Big|_t^{i,j}}{\Delta x}. \tag{3.52}$$

Therefore, for Faraday's law (3.38)-(3.40) we have

$$C_x^E\Big|_t^{i,j} = -\frac{\mu_{xx}\Big|^{i,j}}{c}\ \frac{H_x\Big|_{t+\Delta t/2}^{i,j} - H_x\Big|_{t-\Delta t/2}^{i,j}}{\Delta t}, \tag{3.53}$$

$$C_y^E\Big|_t^{i,j} = -\frac{\mu_{yy}\Big|^{i,j}}{c}\ \frac{H_y\Big|_{t+\Delta t/2}^{i,j} - H_y\Big|_{t-\Delta t/2}^{i,j}}{\Delta t}. \tag{3.54}$$

Similarly, the curl equations in (3.41)-(3.43) become

$$C_z^H\Big|_{t+\Delta t/2}^{i,j} = \frac{H_y\Big|_{t+\Delta t/2}^{i,j} - H_y\Big|_{t+\Delta t/2}^{i-1,j}}{\Delta x} - \frac{H_x\Big|_{t+\Delta t/2}^{i,j} - H_x\Big|_{t+\Delta t/2}^{i,j-1}}{\Delta y}. \tag{3.55}$$

Consequently for Ampere's law in (3.45)-(3.47), we have

$$C_z^H\Big|_{t+\Delta t/2}^{i,j} = \frac{1}{c}\ \frac{D_z\Big|_{t+\Delta t}^{i,j} - D_z\Big|_t^{i,j}}{\Delta t}. \tag{3.56}$$

Finally, the constitutive relation in equations (3.48)-(3.50) reduces to

$$D_z\Big|_t^{i,j} = \Big(\epsilon_{zz}\Big|^{i,j}\Big) E_z\Big|_t^{i,j}. \tag{3.57}$$

Equations (3.51)-(3.57) are our main FDTD expressions. The expressions can be easily implemented in order to simulate wave propagation in different media. It is important to mention that in order to avoid non physical propagation of the wave, the so called Courant stability condition should be satisfied. The stability condition is

$$c\ \Delta t < \frac{1}{\sqrt{\frac{1}{\Delta x^2} + \frac{1}{\Delta y^2} + \frac{1}{\Delta z^2}}}. \tag{3.58}$$

The condition assures that the wave cannot propagate faster than the speed of light.

3.3.2.2 Source

There are different ways to introduce a source in the computational domain. For instance, there are hard and soft sources. A hard source is simply enforcing a point in the grid to have a particular value at each time interval i.e.

$$E_z\Big|_t^{i,j} = S(t), \tag{3.59}$$

where $S(t)$ is the desired source as a function of time. Even though this is easy to implement, it has the disadvantage of not being transparent to waves in the medium. The hard source acts like a perfect electric conductor and causes scattering of other incoming waves. In this

thesis, a so called soft source is used. A soft additive source is defined as

$$E_z\Big|_{t+\Delta t}^{i,j} = E_z\Big|_{t}^{i,j} + S(t). \tag{3.60}$$

Contrary to hard sources, soft sources are transparent and therefore incoming waves can pass through the source without any scattering.

For simulation purposes we use a Gaussian pulse, defined as

$$S(t) = A_0 \; exp\Big[- \frac{(t-t_0)^2}{\tau^2} \; \Big]. \tag{3.61}$$

where A_0 is the amplitude, t_0 is associated with delay, and τ is a parameter related to the bandwidth of the source. In order to see this, we compute the Fourier transform of (3.61)

$$S(f) = \int_{-\infty}^{\infty} dt S(t) e^{-i2\pi ft} = \sqrt{\pi} A_0 \; B \; e^{-i2\pi ft_0} \; exp\Big[- \frac{\pi^2 f^2}{B^2} \Big], \tag{3.62}$$

where $B = 1/\tau$ is the bandwidth of the input signal.

3.3.2.3 Boundary Conditions

Because the boundaries of the computational domain are truncated, an artificial reflection of the waves at the boundaries is created. In order to prevent this phenomena, we can introduce loss at the boundaries of the computational domain. Moreover, the absorbing boundaries are impedance matched at all frequencies and for any angle of incidence. Following [80] we implement the uniaxial perfectly matched layer (PML) by modifying the permittivity and permeability matrices in the absorbing boundaries. This is achieved by introducing a new

matrix, M. The modified parameters, ϵ_N and μ_N are

$$\epsilon_N = \epsilon_0 M \tag{3.63}$$

$$\mu_N = \mu_0 M \tag{3.64}$$

where M is

$$\begin{bmatrix} \frac{M_y M_z}{M_x} & 0 & 0 \\ 0 & \frac{M_x M_z}{M_y} & 0 \\ 0 & 0 & \frac{M_x M_y}{M_z} \end{bmatrix}$$

here M_x, M_y and M_z are defined as follows

$$M_x(x) = 1 + \frac{\sigma(x)}{i\omega\epsilon_0}; \qquad \sigma(x) = \frac{\epsilon_0}{2\Delta t}\Big(\frac{x}{L_x}\Big)^3, \tag{3.65}$$

$$M_y(y) = 1 + \frac{\sigma(y)}{i\omega\epsilon_0}; \qquad \sigma(y) = \frac{\epsilon_0}{2\Delta t}\Big(\frac{y}{L_y}\Big)^3, \tag{3.66}$$

$$M_z(z) = 1 + \frac{\sigma(z)}{i\omega\epsilon_0}; \qquad \sigma(z) = \frac{\epsilon_0}{2\Delta t}\Big(\frac{z}{L_z}\Big)^3. \tag{3.67}$$

L_x, L_y and L_z are the thickness of the PML boundaries in the x, y and z directions. It is clear from (3.65)-(3.67) that the conductivity terms are responsible for the loss in the boundaries. Moreover, these terms increase gradually, resulting in the further reduction of the reflection.

3.4 Computer Simulation of Time Reversal Imaging

In this section it is shown how time reversal imaging works using the FDTD solver. The goal is to demonstrate how the properties of the time reversal technique allow us to detect scattering objects in a medium. In general, the demonstration can be divided into four steps. First is to define the geometry of the problem i.e. the properties of the medium and scattering objects, the location of the source and the receivers, and the dimensions of the computational domain. The second step is to measure the so called background signal. For this, all the scattering objects are removed from the medium. The source radiates and the radiated field is measured by the receivers. In the third step, the scattering objects are present. In this case, the measured field radiated by the source, contains information about the scattering objects. The background signal is then subtracted from this field in order to obtain the perturbation fields due to the scatterer. In the final step, this field is time reversed and re-radiated back into the medium. The re-emitted signal focuses on the scattering objects in the medium. Detection is possible through this focusing. There are several ways to find the location of the target. Here we use two approaches. One is to calculate the "Entropy" of the waves. The minimum of the entropy provides us the exact moment of focusing. The entropy is defined as [79]

$$H(t) = \frac{\left[\sum_{i,j} \left(E_t^{i,j}\right)^2\right]^2}{\sum_{i,j} \left(E_t^{i,j}\right)^4}, \tag{3.68}$$

where t is the time frame and i, j are grid numbers. Here, the summation is over the entire computational domain. Another way to pinpoint the object is to calculate the energy that

passes through each point over the entire computational time T. The energy is defined as

$$W(i,j) = \sum_{t=0}^{T} \left| E_t^{i,j} \right|^2. \tag{3.69}$$

In what follows we consider three cases. First, we demonstrate that in the absence of scatterers, the time-reversed waves focus on the source. In the second and third cases, we demonstrate detection of one and two scattering objects, respectively. For all three cases, the computational domain is 0.5 m x 0.5 m and the medium is assumed to be air, therefore $\epsilon_r = \mu_r = 1$.

3.4.1 Case I: Free Space - Focusing on Source

In this case, there is no scattering object present in the medium. Therefore, the time-reversed background signal should focus on the source location. The input to the source is a Gaussian wave function defined in (3.61) with amplitude $A_0 = 1$, bandwidth $B = 1/\tau = 10\pi$ GHz and delay time $t_0 = 30\tau$. The source is located at $x = 0.1250$ m and $y = 0.1250$ m as shown in Fig. (3.2). Eight receivers are located on an arc of a circle centered at $x = 0$ and $y = 0$ with radius 0.5 m. The angular separation between the receivers is 6°. The total computational time is 2.36 ns. This is the time required for the wave to traverse the longest path, the diagonal, of the computational domain. Fig. (3.2) shows the amplitude of the electric field, E_z, propagating towards the receivers at $t = 1.17$ ns.

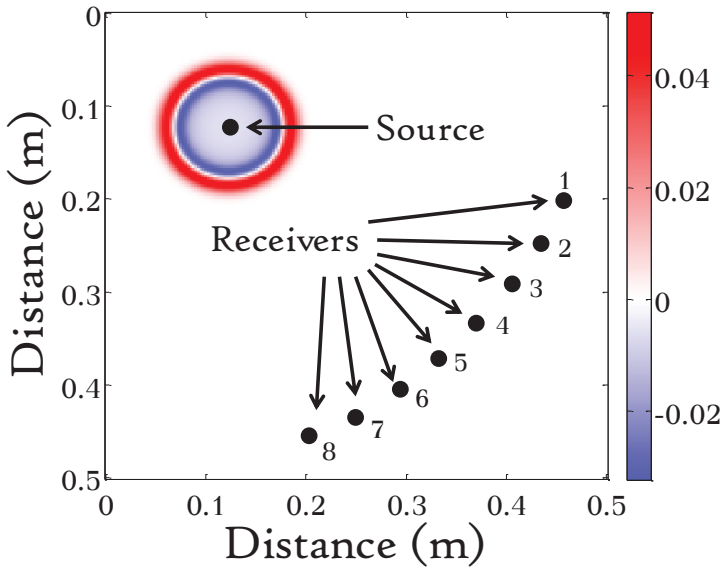

Figure 3.2: Forward propagation of the electric field at $t = 1.17$ ns. The eight black dots represent the location of the recievers.

The electric field is depicted at a later time instance in Fig. 3.3. Notice, that due to absorption in the PML region, there is no artificial reflection from the boundaries of the computational domain. Also, the amplitude of the wave has decreased due to $1/r^2$ propagation loss.

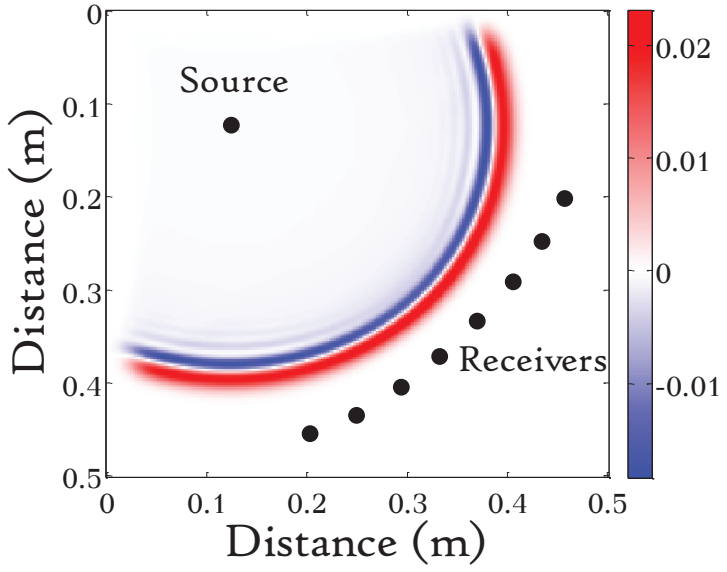

Figure 3.3: Forward propagation of the electric field at $t = 1.94$ ns.

We let the simulation run for a sufficiently long time i.e. until most of the wave is absorbed by the PML boundaries. The measured electric field at the receivers are shown in Fig. 3.4.

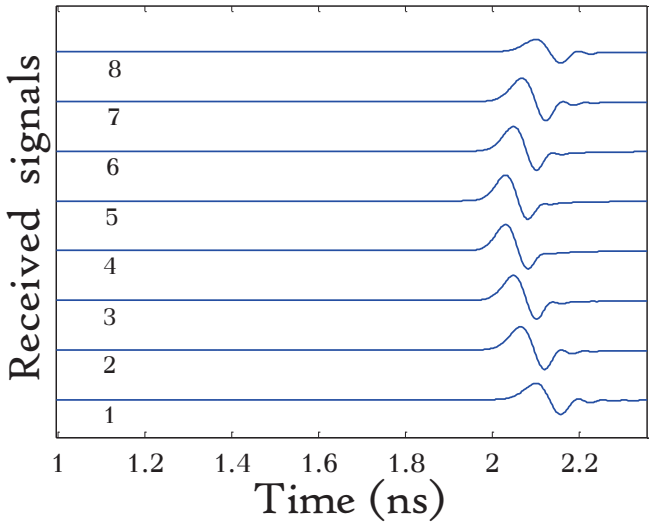

Figure 3.4: Received signals at the recievers. The numbering corresponds to the eight receivers shown in Fig. 3.2.

The received signals are then time reversed and re-emitted into the medium. Now the receivers act like new sources. The back propagation of the time reversed signals at time instance $t = 0.65$ ns is shown in Fig. 3.5.

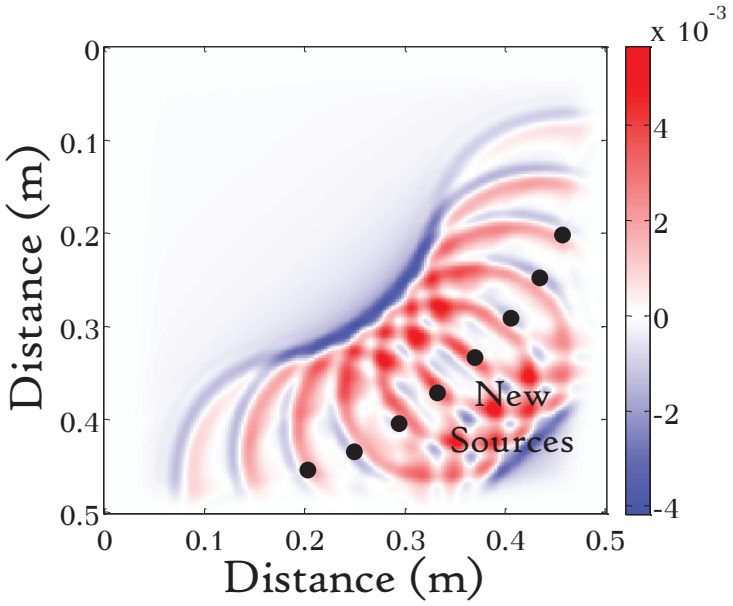

Figure 3.5: Back propagation of time reversed fields at $t = 0.65$ ns.

Again we let the simulation run for a adequately long time. In order to pinpoint the location of any scattering object we use the entropy defined in (3.68). The entropy plot is shown in Fig. 3.6.

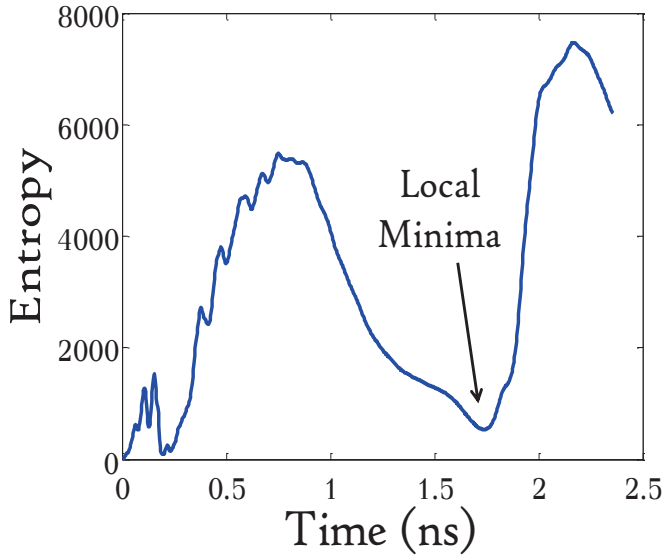

Figure 3.6: Entropy of the electric field calculated in accordance to eqn. 3.68.

The minimum in the entropy corresponds to the time instance where the back propagating

waves focus on the location of the scatterer. Since there was no scattering object present in this case, the time-reversed waves focus on the location of the initial source. The electric field is shown at $t = 1.75$ ns in Fig. 3.7. It is apparent that the fields are constructively interfering at the location of the initial source, shown with the black dot.

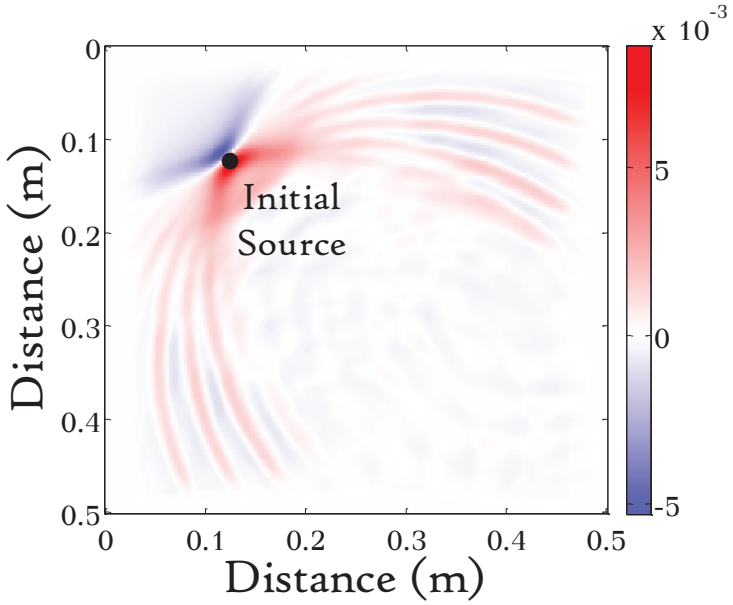

Figure 3.7: Focusing of time-reversed back propagated waves on the location of the initial source at $t = 1.75$ ns. This time instance correspond to the minimum of the entropy plot in Fig. 3.6.

As mentioned, another way to pinpoint the location of targets is to use the energy plot. The energy was calculated according to eqn. 3.69 and is shown in Fig .3.8.

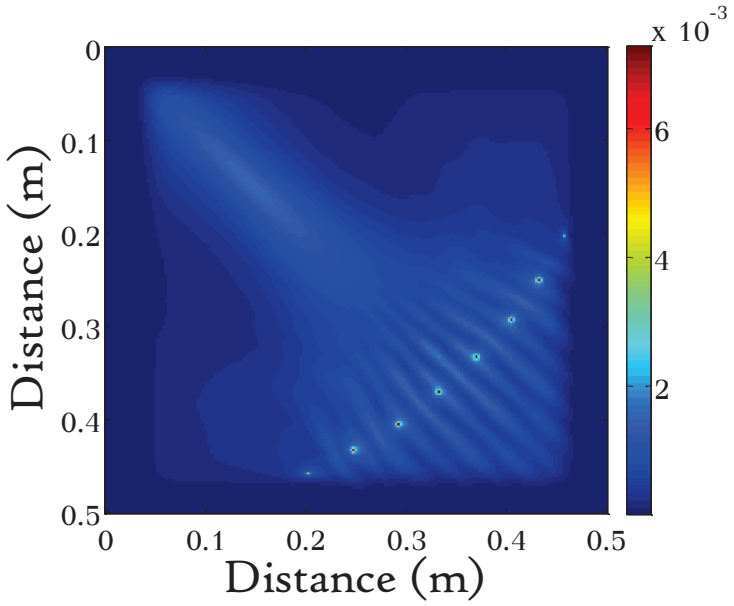

Figure 3.8: Energy plot of the backpropagated waves calculated accoridng to eqn. 3.69. The eight bright points in the figure correspond to the sources.

However, since the maximum of the energy plot occurs at the location of the sources, it is hard to see the focused energy on the initial source location. This focusing is due to the convergence of time-reversed signal at the initial source. In Fig. 3.9 the energy of a smaller region of the computational domain is shown. The bright points are excluded from the region and therefore the focused energy on the source can be easily observed. The black dot in the figure corresponds to the real location of the initial source.

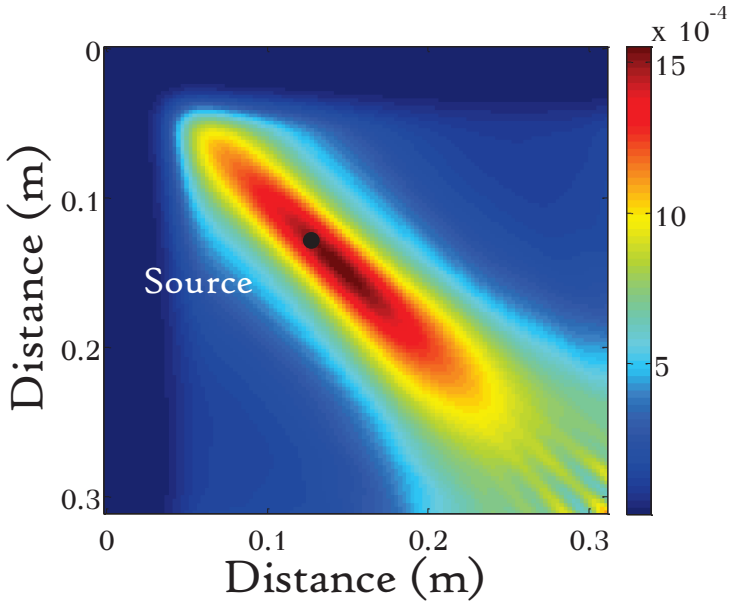

Figure 3.9: Energy plot of the back propagated waves zoomed in the location of the intial source.

The stretched out pattern of the focused power in the figure is due to the limited angle coverage of the receivers. If the receivers were located along a full circle, the focused energy would be circular rather than elliptical pattern.

3.4.2 Case II: Single Scatterer

Now we consider the case of a single scatterer in the medium. The scatterer is assumed to be a circular dielectric of radius 1 cm and relative dielectric constant of 3. The target is located at $x = 0.09$ m and $y = 0.15$ m and the source is located at $x = 0.075$ m and $y = 0.075$ m. Similar to the previous case, the bandwidth of the input Gaussian signal is $B = 1/\tau = 10\pi$ GHz. The delay parameter t_0 is set to 6τ. The receivers are located in the same position as in the previous case. And as before, the first step is to store the background signal. The second step is to measure the field in the presence of the target. Fig. 3.10 shows the electric field propagating from the source towards the receivers. The distortion in the wave front is

due to the interaction of the field with the scatterer (black circle in the figure).

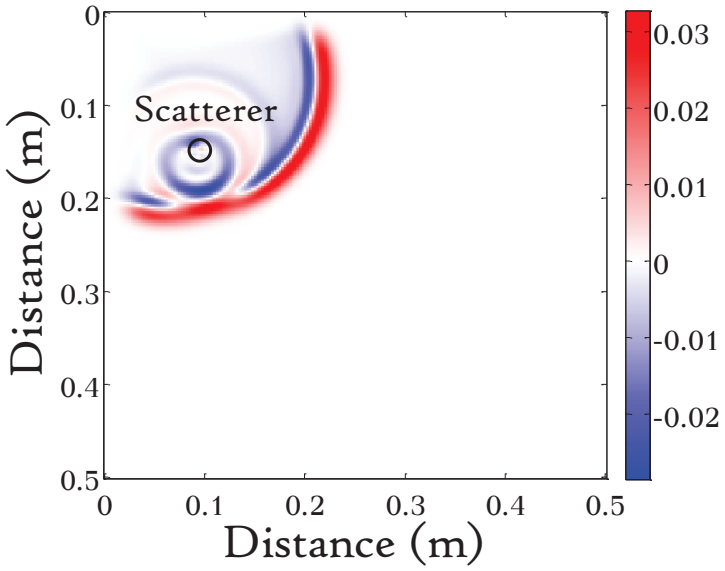

Figure 3.10: Forward propagation of the electric field at $t = 0.67$ ns. The presence of the scatterer, shown with the black circle, causes distortion in the propagating wave. The relative permittivity of the target is 3.

The scattered field is then calculated, time-reversed and re-emitted back through the medium. The entropy of the wave at each time instance is shown in Fig. 3.11. The local minimum indicated in the figure corresponds to the time instance of focusing.

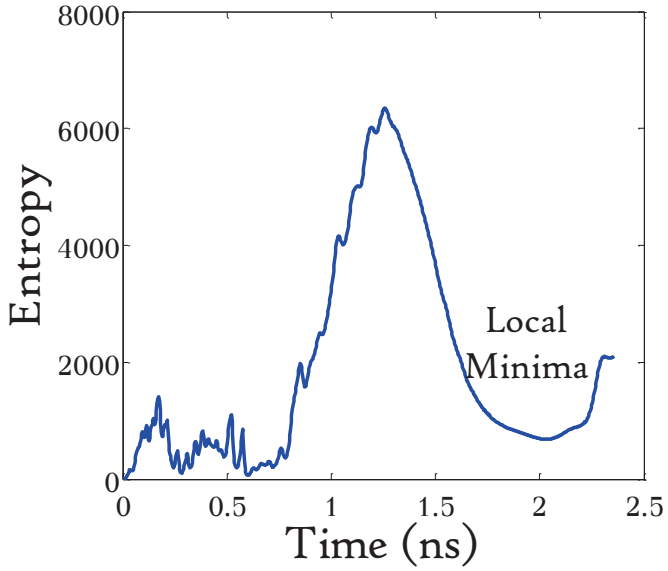

Figure 3.11: Entropy of the electric field as a function of time. The local minimum time instance corresponds to the focusing of the waves.

Fig. 3.12 shows the electric field at the time instance of minimum entropy, $t = 2.03$ ns. As expected the re-radiated fields are focused on the location of the scatterer.

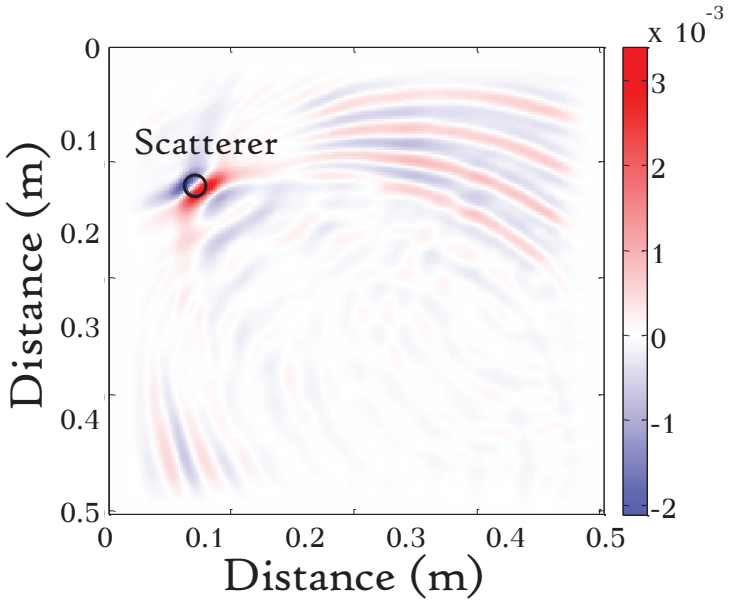

Figure 3.12: Focusing of time-reversed back propagated waves on the location of the scatterer at $t = 2.03$ ns. This time instance correspond to the minimum of the entropy plot in Fig. 3.11.

Using the aforementioned energy plot is an alternative approach for detecting the scatterer. The energy plot is shown in Fig. 3.13. The sources are excluded from the plotted region due to their high power intensity. The black circle in the figure corresponds to the true location of the target. As it can be seen, the energy is focused in the vicinity of the scatterer.

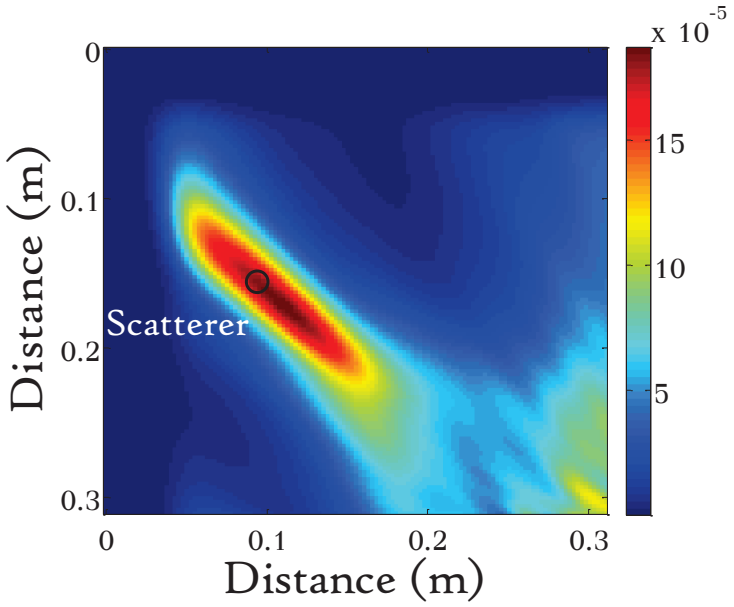

Figure 3.13: Energy plot of the back propagated waves zoomed in the location of the scatterer. The black circle corresponds to the true location of the scatterer.

3.4.3 Case III: Two Scatterers

In the final case we consider the presence of more than one scatterer. Target one is a circular dielectric with a radius of 0.5 cm, positioned at $x = 0.09$ m and $y = 0.15$ m. Target two is an elliptical dielectric with semi-major axis of 1 cm and semi-minor axis of 0.5 cm, located at $x = 0.25$ m and $y = 0.20$ m. Both targets have a relative dielectric constant of 4.1. The configuration of the receivers, along with the source parameters and location, is the same as cases I and II. We first need to calculate the scattered field. For this, the background signal

has to be subtracted from the total field in the presence of scatterers. Fig. 3.14 shows the electric field interacting with the first scatterer. The disturbance in the field is due to this interaction. Fig. 3.15 shows the field a few moments later when the wave front has reached the second scatterer. The field finally reaches the receivers and the scattered field can be easily calculated.

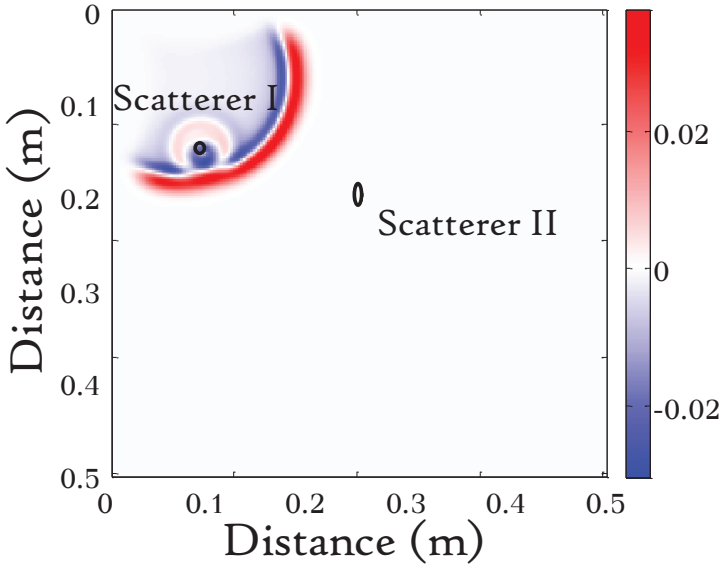

Figure 3.14: Forward propagation of the electric field at $t = 0.56$ ns when the wave front reaches the first scatterer.

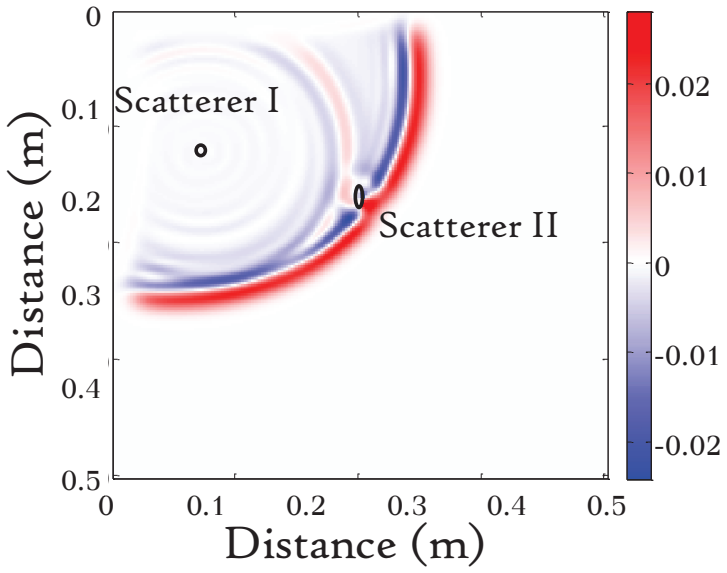

Figure 3.15: Forward propagation of the electric field at $t = 0.99$ ns when the wave front reaches the second scatterer.

We again calculate the entropy of the re-emitted waves. The entropy is shown in Fig. (3.18). The two local minima correspond to the time instances that the wave is focused on the location of the two scatterers. Clearly the first minima corresponds to the focusing on the elliptical scatterer and the second minima corresponds to the circular scatterer.

Fig. (3.17) corresponds to the time instance of the first local minimum in the entropy plot ($t = 1.44$ ns). The waves are clearly focused on scatterer two.

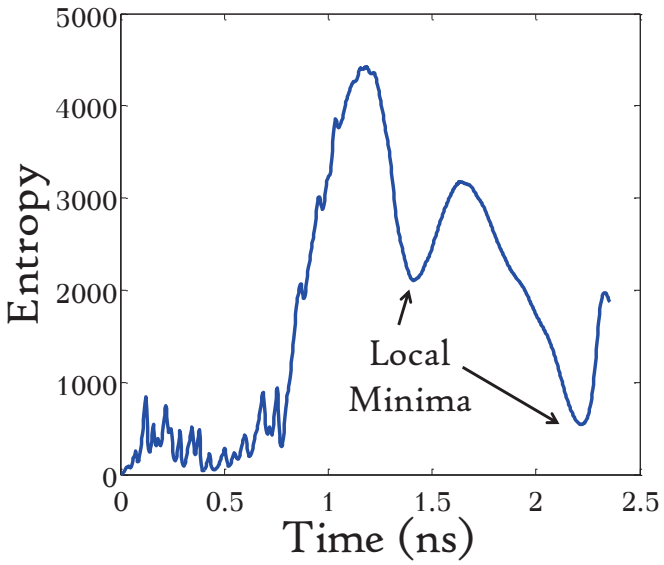

Figure 3.16: Entropy of the electric field as a function of time. The two local minima correspond to the time instances that the field focuses on the location of the two scatterers in the medium.

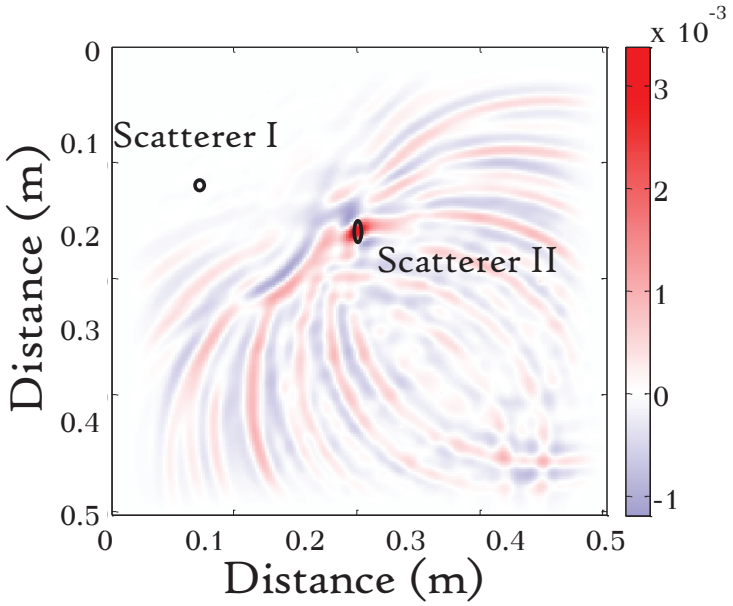

Figure 3.17: Focusing of time-reversed back propagated waves on the location of scatterer two at $t = 1.44$ ns. This time instance corresponds to the first local minima of the entropy plot in Fig. 3.16.

Fig. (3.17) shows the back propagated electric field a few moments later, at $t = 2.2$. The time instance corresponds to the time instance of the second local minimum in the entropy.

The waves are focused on scatterer one.

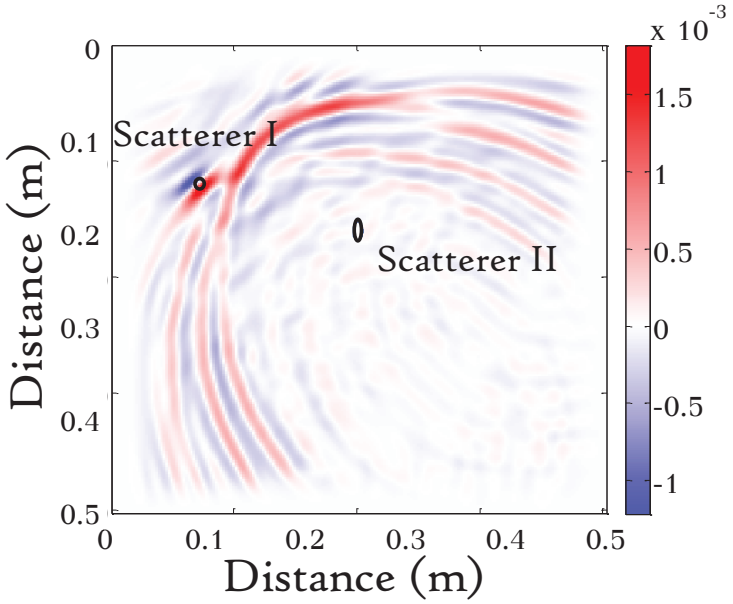

Figure 3.18: Focusing of time-reversed back propagated waves on the location of scatterer one at $t = 2.2$ ns. This time instance corresponds to the second local minima of the entropy plot in Fig. 3.16.

Again, the alternative approach for detection is using the energy plot. The energy plot is shown in Fig. 3.19. Because the elliptical scatterer is larger, the scattered field associated to this target is larger compared to the field associated with the smaller scatterer. Consequently, the indication corresponding to the elliptical scatterer has higher intensity.

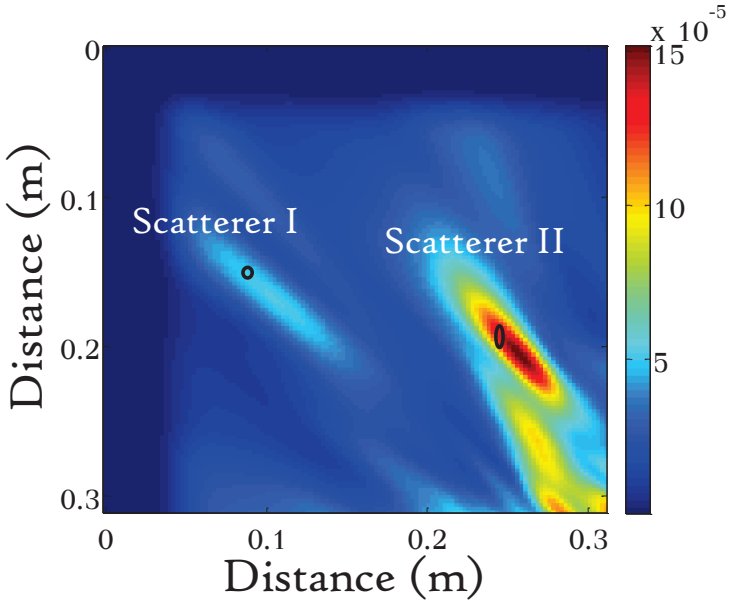

Figure 3.19: Energy plot of the back propagated waves zoomed in the location of the two scatterers. The black circle and ellipse in the figure correspond to the true location of the circular and elliptical scatterers, respectively.

An experiment is a question which science poses to Nature, and a measurement is the recording of Nature's answer.

Max Karl Ernst Ludwig Planck

Chapter 4

Experimental Setup and Results

A prototype of the proposed microwave imaging system was built using the reflectarray antenna and the arch range at Michigan State University [59, 81]. The setup is very similar to the one used for measuring the radiation pattern of the reflectarray described in Chapter 2. Here we briefly describe the experimental setup. Fig. 4.1 depicts the schematic of the system. The reflectarray antenna, mounted on a Styrofoam sheet, was located at the center of the arch range, which has a radius of 3.53 m. The center of the arch range is also chosen to be the origin of the polar coordinate system used throughout the experiment (see Fig. 4.1). The line normal to the array corresponds to $\theta = 0$ and the curved arrow shows the direction in which θ increases. An H-1498 series broadband horn antenna was placed on the arch rail facing the reflectarray and was used as the source. A dielectric lens was placed in front of the antenna in order to create a focused plane wave beam. Moreover, the transmitter was aligned with the center of the reflectarray and the incident beam was

directed to be perpendicular to the surface of the array. Both the array and the transmitter were kept stationary throughout the experiment. The reflectarray antenna steered the beam into different angles, sweeping the region of interest, and the scattered field was measured by a receiver antenna. An identical horn antenna was used as the receiver. The transmitter and the receiver were both connected to an Agilent E5071c network analyzer, calibrated from 1.5 GHz to 7.5 GHz with 1601 frequency points. The receiver antenna was moved along the arch rail in order to measure the transmission scattering parameter S_{21}. The white dots in Fig. 4.1 represent locations were a reading was taken. Measurements were taken every two degrees from $\theta = -74°$, represented by the left-most dot, to $\theta = 74°$, represented by the right-most dot. Due to the large size of the focusing lens of both the transmitter and the receiver, measurements could not be taken from $\theta = -14°$ to $\theta = 14°$. The measured signals at each position were calibrated using the response of the system. The system response was calculated in accordance to [59], by considering the canonical problem of scattering off a metal sphere.

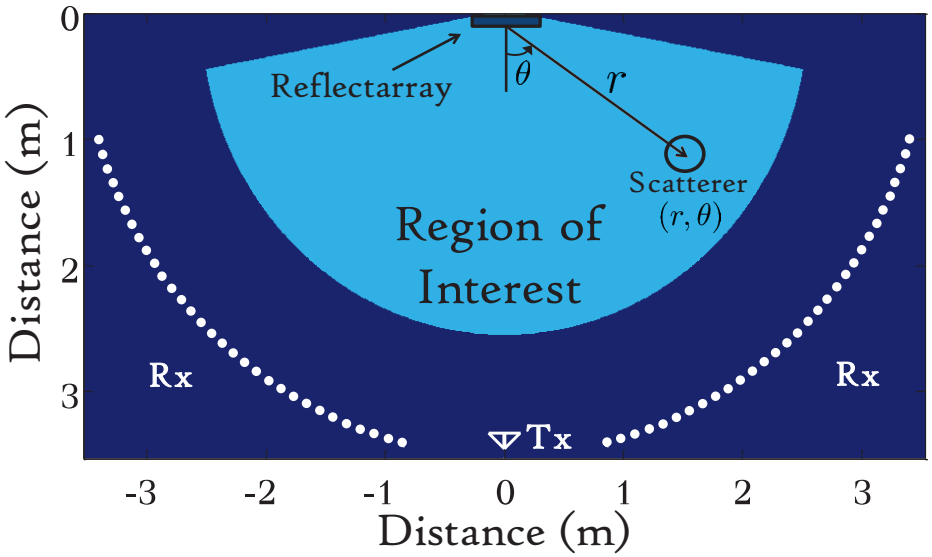

Figure 4.1: Schematic of the microwave imaging setup.

For each angle at which the beam was steered, the background (free space) field was measured to be used as a reference. This reference was later subtracted from field measurements of different scatterer configurations in order to obtain the respective scattered fields. Since the measurements were performed in the frequency domain, the resulting scattered field was mapped back to the time domain using Fourier transform. Next, these signals were time reversed and re-radiated back using in-house finite difference time domain (FDTD) simulation software. As explained in Chapter 3, the propagating time-reversed signals focus on the scatterers in the medium and hence detect and locate the targets. Similar to [76, 82], the electric field energy density (in units of $\frac{1}{2}\epsilon_0$) was calculated using the expression

$$W(\vec{r}) = \sum_{t=0}^{T} |\vec{E}(\vec{r}, t)|^2, \tag{4.1}$$

where $\vec{E}$ is the electric field at point $\vec{r}$ and time t, and T is the total simulation time. $W(\vec{r})$ can be interpreted as the accumulated energy at each point $\vec{r}$ during backpropagation. In all experiments performed, the scattering objects were sufficiently tall so that the problem was considered to be two dimensional. Also, the region of interest where the image is reconstructed is a 100-inch radius circular sector shown in Fig. 4.1. The area near the sources has been excluded from the ROI because of the high energy concentration and possible masking of target indications.

Two experiments were performed in order to demonstrate the feasibility of the proposed system.

4.1 Experiment I: Single Scatterer

In the first experiment, the reflectarray was set to deflect the beam at the fixed angle of 45°. A cylindrical acetal (polyoxymethylene) with dielectric constant of 2.74 and dissipation factor of tanδ= 0.006 at room temperature was used as a target [83]. The cylinder had a diameter of 4 inches and a height of 12 inches and was located at $\theta = 45°$. Measurements were taken of the cylinder placed at three different distances from the center of the array; 40, 60 and 80 inches. For each case, the energy image was reconstructed according to equation 4.1. Fig. 4.2 shows the reconstructed image without any further processing for the three different cases. As expected, the indication associated with the target is stretched out. This is because the measurements of the scattered field were not taken from all possible angles. This pattern was also observed in the paper by Rodriguez et al. [74,76]. The figure indicates that the intensity of the scattered field reduces as the object is placed farther away from the reflectarray antenna. This is due to path loss and divergence of the beam as the field propagates through space. The maximum intensity in Fig. 4.2(a), when the target 40 is inches from the array, is almost an order of magnitude greater than the maximum intensity in Fig. 4.2(c), where the target is located 80 inches away from the array. A similar experiment was performed using a metal plate. The plate was rotated manually to deflect the beam to 45°. It was observed that the artifacts seen in the energy figures were removed. This suggests that the artifacts in the images are due to the limited bandwidth of the steered electric field. A metal plate would reflect the entire frequency band of 1.5-7.5 GHz. Compared to the metal plate, the reflectarray has a relatively narrow bandwidth and therefore it generates more artifacts in the images. This hypothesis is under further investigation.

In order to evaluate the accuracy of our system, it is assumed that the maximum intensity

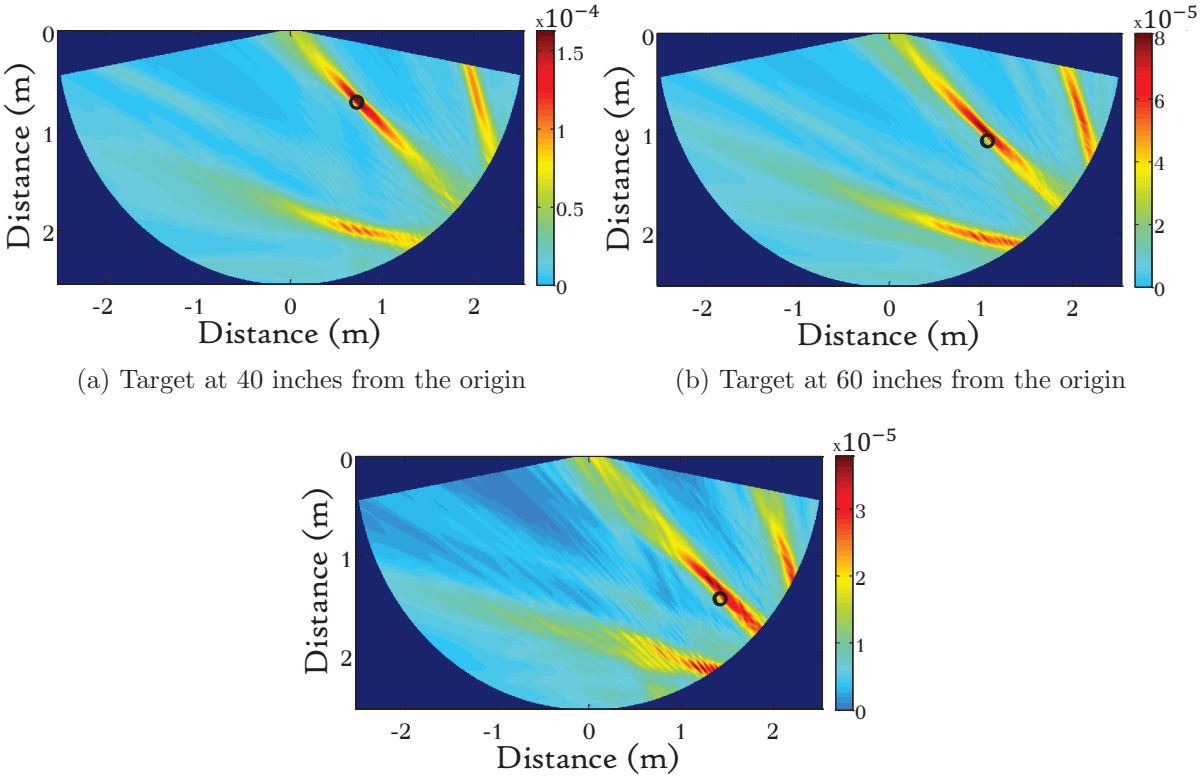

(a) Target at 40 inches from the origin

(b) Target at 60 inches from the origin

(c) Target at 80 inches from the origin

Figure 4.2: Energy image of the three configurations in experiment one. The target was placed at three different distances from the center of the array. The black circle corresponds to the actual position of the scatterer.

point in the image corresponds to the center of the cylindrical scatterer. Then the relative error in detection is defined as:

$$\epsilon = \frac{|\vec{r}_{det} - \vec{r}_{act}|}{r_{roi}}, \tag{4.2}$$

where $\vec{r}_{det}$ is the highest intensity point in the image, $\vec{r}_{act}$ is the actual location of the dielectric center and r_{roi} is the radius of the ROI which is equal to 100 inches. Table 4.1 shows the detection error calculated for different target positions. The results indicate that the error increases as the target moves away from the reflectarray. When the target is close to the array the error is less than 1%, however, it increases to about 9% when the target is located at 80" from the center. The results match with the theoretical predictions by Born

and Wolf [84]. They have shown that the radial resolution is proportional to $\lambda\left(\frac{\ell}{a}\right)^2$, where λ is the central frequency of the pulse, ℓ is the distance of the object from the source and a is the length of the receiver array. Radial resolution is proportional to power, therefore for objects placed far from the source, as the power decreases, detection error increases.

Target distance from reflectarray (inch)	Detection error (ϵ)
40	9.4e-04
60	0.0471
80	0.0933

Table 4.1: Detection error calculated for different positions of the dielectric cylinder.

4.2 Experiment II: Two Scatterers - Beam Scanning

The second experiment was designed to demonstrate the beam scanning ability of the system. Two cylindrical dielectrics of diameters 2.25 and 6 inches were located at $(r, \theta) = (40", -30^\circ)$ and $(r, \theta) = (60", 45^\circ)$, respectively. The cylinders were both 3 feet long and made of acetal. In order to scan the region of interest, the beam was steered into various angles, starting from -60° to $+60^\circ$ in 15-degree increments, excluding $\pm 15^\circ$ due to the large profile of the lenses (see Chapter 2). At each steering angle the scattered field was measured along the arch rail. Similar to the previous experiment, the field was time-reversed and re-radiated back into the medium using computer simulation. Finally the energy image was plotted in order to detect and locate the scatterers in the ROI. The results are shown in Fig. 4.3. The beam is steered to -60° and -45°, corresponding to Fig. 4.3(a) and Fig. 4.3(b), respectively. In both cases, the target located at $(r, \theta) = (40", -30^\circ)$ is detected. This is due to the side

lobes of the reflectarray (see Fig. 2.14 in Chapter 2). Fig. 4.3(c) shows the case where the main beam is steered to -30° and consequently passes through the target. In this case the interaction is maximized and hence, compared to the two previous cases, the target has a much stronger indication in the energy image. Similar to the first experiment, when there is maximum interaction, artifacts are more visible in the image. Fig. 4.3(d) corresponds to the case where the beam is reflected to 0°. In this case, both scatterers are detected. In the last three cases, where the main beam is deflected into $+30^\circ$, $+45^\circ$ and $+60^\circ$, only the bigger dielectric cylinder located at $(r, \theta) = (60", +45^\circ)$ is detected. However, the strongest indication of the target appears when the beam is steered to $+45^\circ$ which also results in stronger artifacts in the energy image.

In order to evaluate the accuracy of detection when the beam is steered into different angles, the relative error is calculated (see Table 4.2). As expected, the error is at a minimum (equal or below 5%) when the main beam passes through the object and increases otherwise. Tables 4.1 and 4.2 indicate that detection error is smaller for larger scatterers due to a bigger scattered field. In addition, the error decreases for targets closer to the reflectarray. This is due to a more focused beam in closer proximity to the array.

4.3 Experiment III: Dielectric Anomalies - Defects and Metallic Impurities

This section demonstrates the capability of the proposed microwave imaging system to detect anomalies within dielectrics. Two types of anomalies are considered: defects and metallic impurities. For each type, a cylindrical dielectric sample was prepared. The samples both have a radius of 2 inches and are 12 inches tall (see Fig. 4.4). The first sample contains an

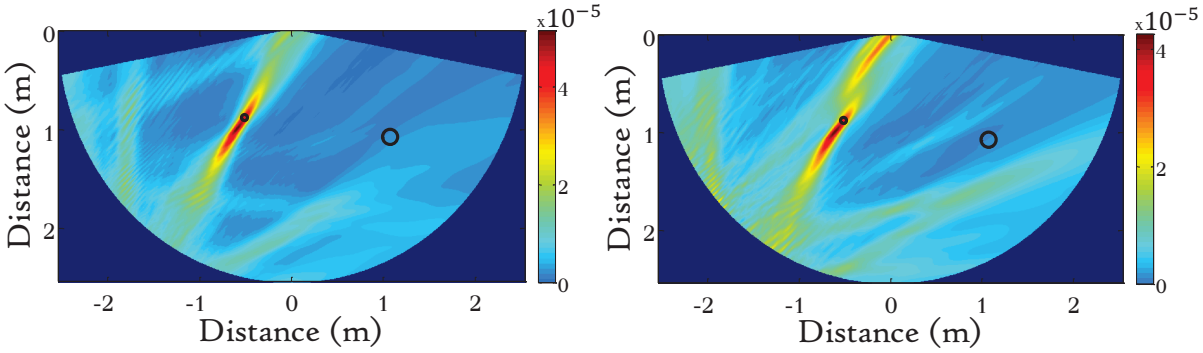

(a) Beam steered to $-60°$

(b) Beam steered to $-45°$

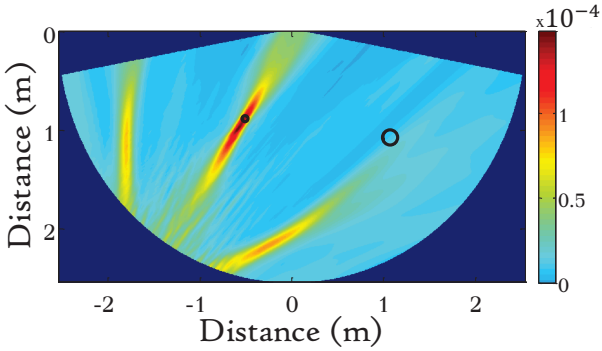

(c) Beam steered to $-30°$

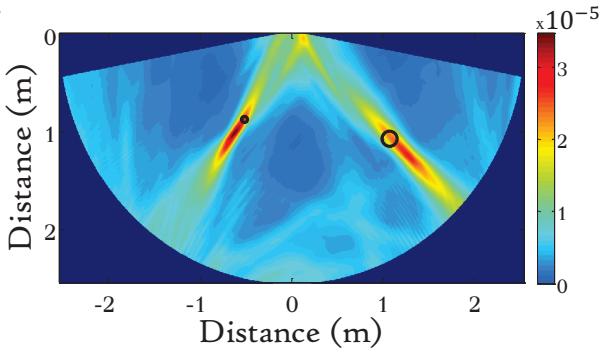

(d) Beam steered to $0°$

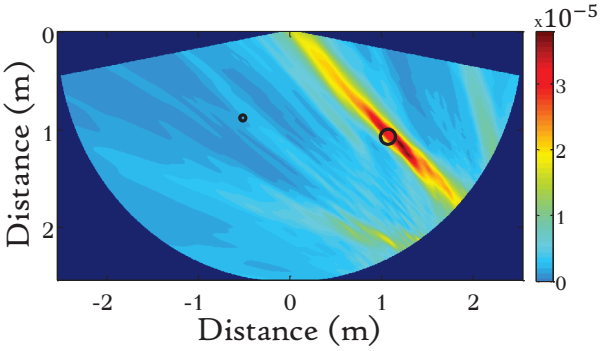

(e) Beam steered to $+30°$

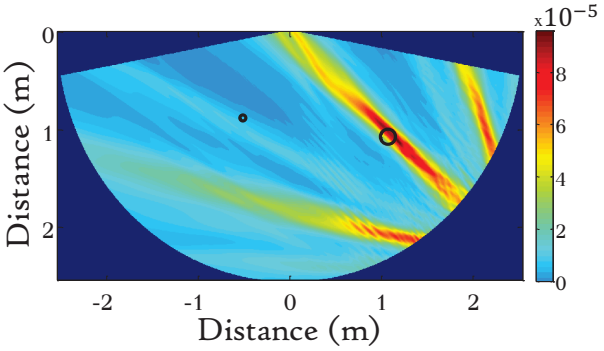

(f) Beam steered to $+45°$

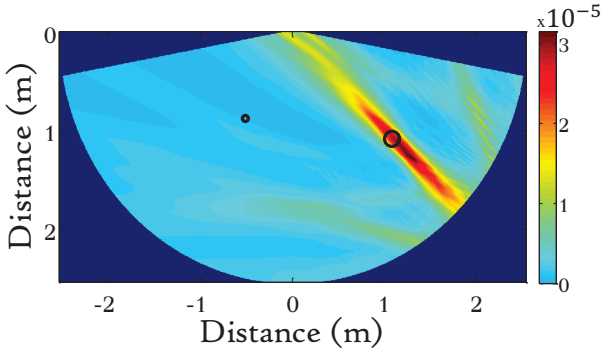

(g) Beam steered to $+60°$

Figure 4.3: Energy image for different steering angles in experiment two. The black circles correspond to the actual positions of the scatterers.

Steering angle (degree)	Detection error (ϵ) 2.25" diameter cylinder	Detection error (ϵ) 6.0" diameter cylinder
-60	0.0535	ND
-45	0.0592	ND
-30	0.0505	ND
0	0.0699	0.1046
30	ND	0.0565
45	ND	0.0401
60	ND	0.1141

Table 4.2: Detection error calculated for different steering angles. ND indicates that the target was not detectable at the particular steering angle.

axial defect along the axis of the cylinder. The defect is 1-inch-deep and 1.75 inches wide. The second sample, resembling cases of metallic impurities within dielectric materials [85], was affixed with a 2-inch-wide thin layer of copper tape along its main axis. The two samples were examined one at a time, each located at $(r, \theta) = (40", 45^\circ)$. The main beam was also steered to 45° in order to achieve maximum interaction. To find the defect contribution, the signal from a healthy sample was recorded and subtracted from the signals of the targets with anomalies. This ensures that the resulting scattered field contains only contributions from the anomaly.

The calculated energy images for the cylinder with defect are shown in Fig. 4.5 and Fig. 4.6. Two configurations were considered with the defect centered along $\theta = 45^\circ$. In the first case the defect was facing the arch rail, Fig. 4.5(a), and in the second case, the defect was 180°-rotated to face the beam scanning array, Fig. 4.6(a). The red arrows in the figures indicate the location of the defect. It is apparent that the location of maximum intensity in the energy image changes as the cylinder is rotated, implying high detection accuracy of the system.

Figure 4.4: Dielectric samples with different types of anomalies. The left sample contains a 1.75-inch-wide and 1-inch-deep axial defect. The second sample contains a 2-inch-wide piece of copper tape along its main axis.

The calculated energy images for the cylinder with copper anomaly are shown in Fig. 4.7 and Fig. 4.8. Two cases were considered again; the copper tape facing the arch rail in the first case and the beam scanning array in the second case (sample was 180 degrees rotated). The copper indication in the energy images moves clearly as the sample is rotated indicating the sensitivity of the system with respect to the location of the anomaly.

Similar to the previous experiments, we calculate the detection error given by (4.2) for Fig. 4.5, Fig. 4.6, Fig. 4.7 and Fig. 4.8. For the sample with defect, $\vec{r}_{act}$ is the centroid or the geometric center of the defect and for the other sample, the center of the copper tape is considered as $\vec{r}_{act}$. For all cases $\vec{r}_{det}$ is the pixel with maximum intensity in the energy image and r_{roi} is 100 inches. The results are given in Table 4.3.

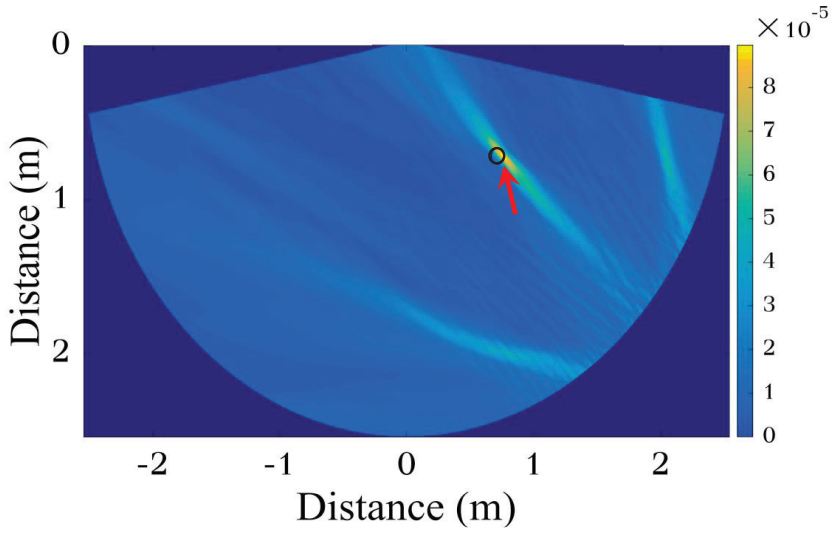

(a)

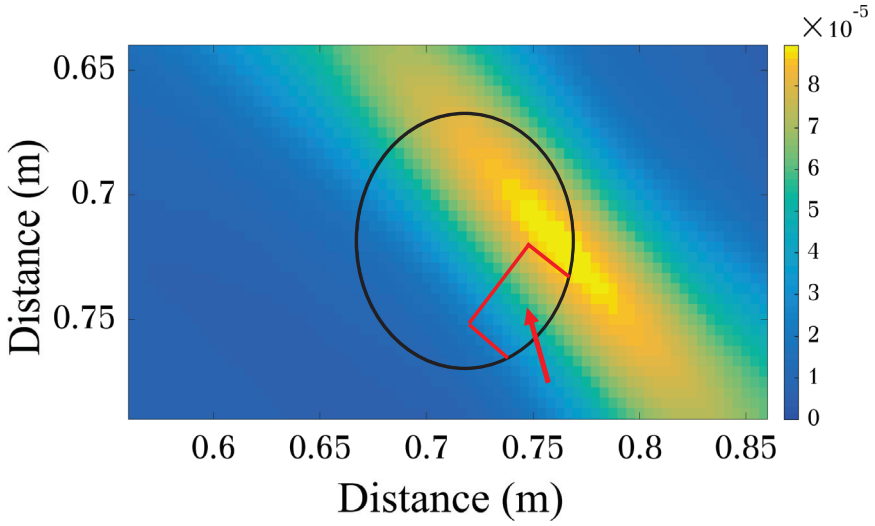

(b)

Figure 4.5: (a) Calculated energy image of the backpropagating waves for the dielectric sample with defect facing the arch rail (b) close-up view. The red arrows point to the location of the defect.

Table 4.3 indicates that both anomalies can be detected with high accuracy. However, the defected cylinder generates a stronger scattered field and therefore is detected more accurately. It is interesting that compared to Table 4.2, the error values shown in Table 4.3, are in general smaller. This is because the time reversal signal processing approach is mainly

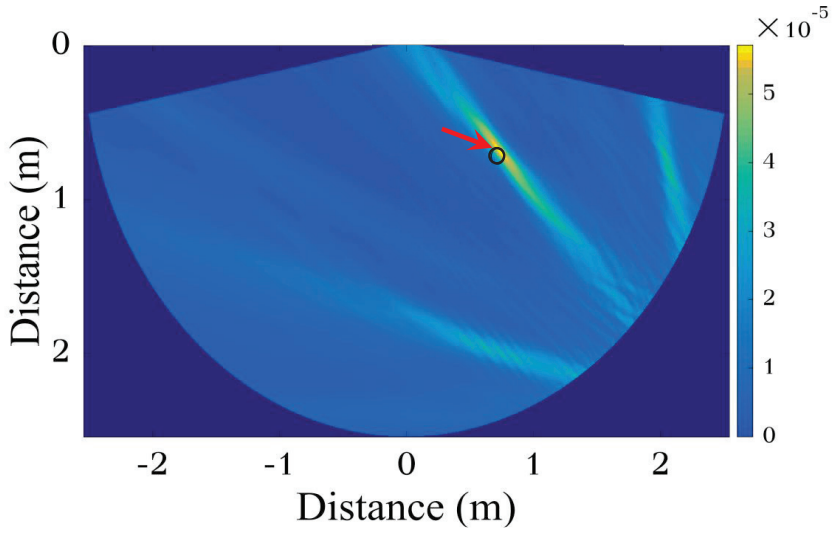

(a)

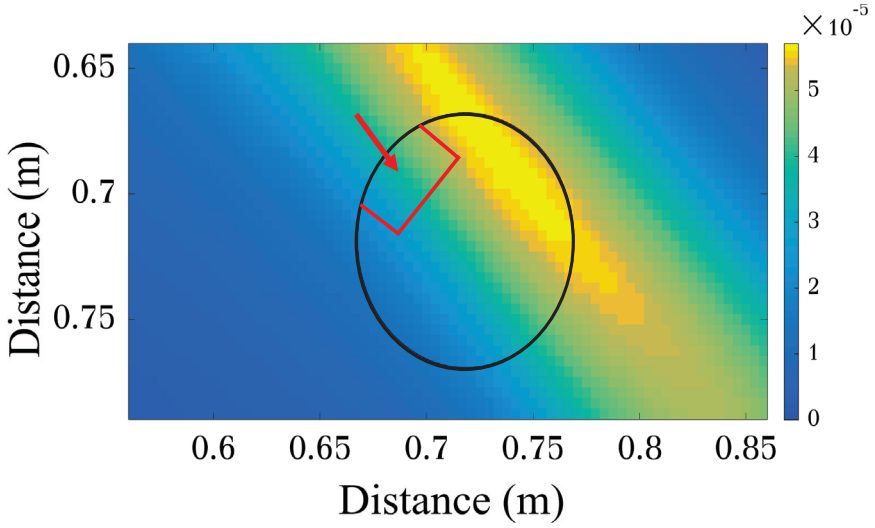

(b)

Figure 4.6: (a) Calculated energy image of the backpropagating waves for the dielectric sample with defect facing the beam scanning array (b) close-up view. The red arrows point to the location of the defect.

for detecting point-like scatterers [86]. Indeed, the anomalies considered in this work, both the defect and copper strip, are more representative of a point source than the dielectric cylinders in the previous section.

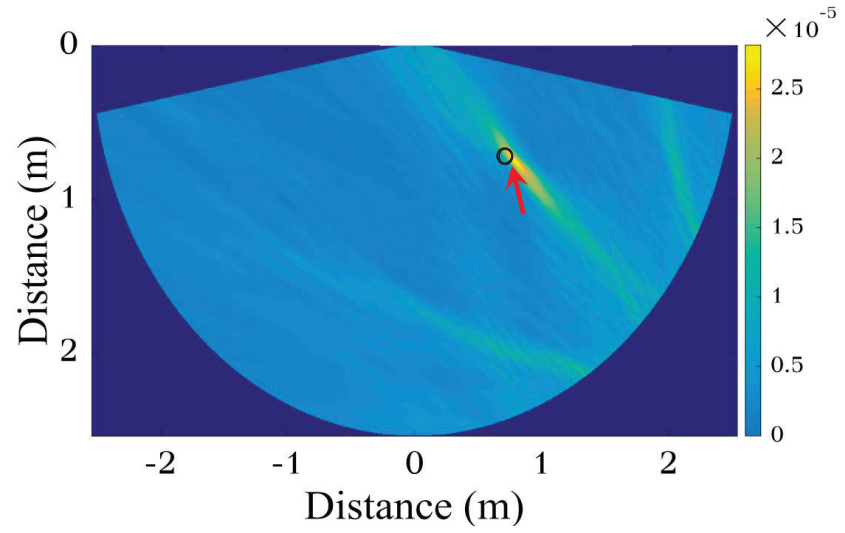

(a)

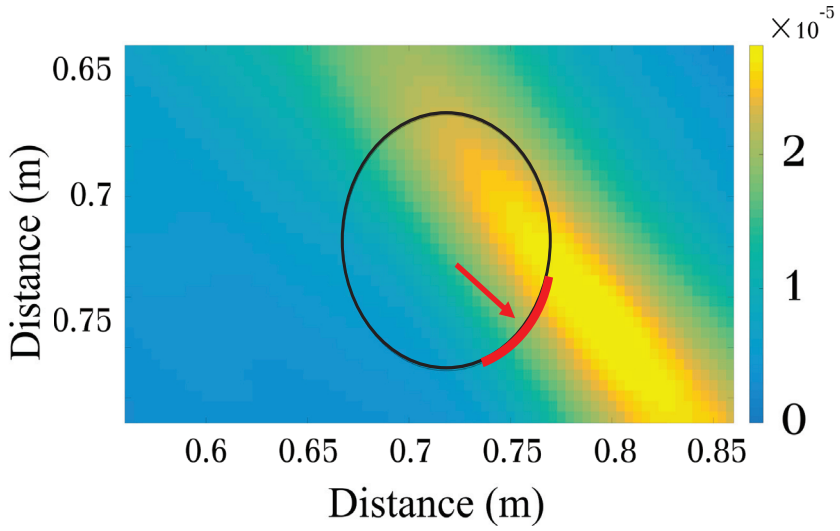

(b)

Figure 4.7: (a) Calculated energy image of the backpropagating waves for the sample with copper anomaly when the copper tape is facing the arch rail (b) close-up view. The red arrows point to the location of the copper anomaly.

Defect orientation	Detection error (ϵ) Sample with defect	Detection error (ϵ) Sample with copper
Facing receiver	0.012	0.015
Facing array	0.015	0.045

Table 4.3: Detection error calculated for the two dielectric samples with anomalies.

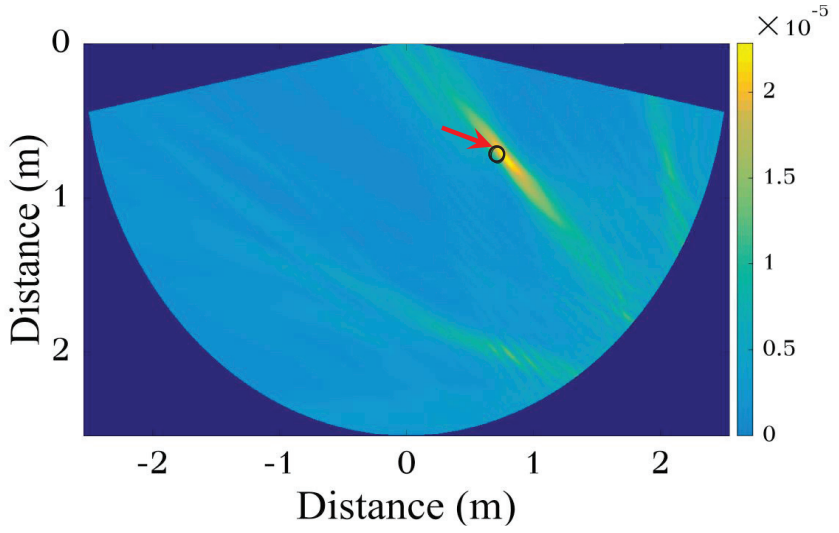

(a)

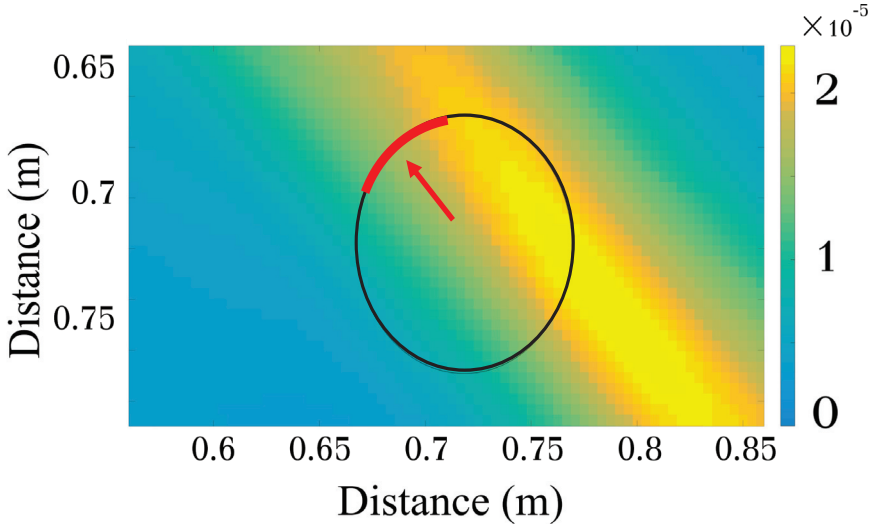

(b)

Figure 4.8: (a) Calculated energy image of the backpropagating waves for the sample with copper anomaly when the copper tape is facing the arch rail (b) close-up view. The red arrows point to the location of the copper anomaly.

Part 3

Superradiance in Open Quantum Systems

Physics is like sex: sure, it may give some practical results, but that's not why we do it.

Richard Phillips Feynman

Chapter 5

Introduction

5.1 Open Quantum Systems

Open quantum systems are currently the research focus of many physicists in various subfields. The main driving force in this direction is evidently the quest for new developments in quantum informatics. Another area with significant recent achievements related to openness of a quantum system is nuclear physics, where the understanding of structure and reactions of loosely bound nuclei far from stability requires the correct unified treatment of the bound states and continuum. Cold atoms in traps and optical lattices can give rise to new effects of coupling, entanglement and transfer of information. Solid-state micro- and nano-devices, including Josephson junctions and spintronics, are probably the most developed arrangements of this type. Fig. 5.1 depicts two examples of the aforementioned open quantum systems, an unstable nucleus and a quantum wire attached to leads.

From a general point of view, in all cases we have to deal with a mesoscopic system [1] of interacting constituents that serves as a guide for the transmission of a quantum signal. The system can have intrinsic degrees of freedom which can be excited and deexcited by the signal. The coupling to the external world is realized through a certain amount of channels characterized by the asymptotic quantum numbers of emitted particles or quanta and the final state of the system. Each channel has an energy threshold where it becomes open and connects to the environment. In the absence of decoherence through external noise or a heat bath, the transmission at given energy is described by the unitary scattering matrix in the space of channels open at this energy. All these features are common for numerous loosely bound or marginally stable mesoscopic systems and play a key role in determining their main observable properties.

A convenient mathematical formalism for the description of such systems is given by the effective non-Hermitian Hamiltonian; this method, based on the Feshbach projection formalism, is formally exact but very flexible and can be adjusted to many specific situations. This approach provides an alternative to popular methods such as the Feynman diagrammatic techniques and the master equation that are commonly used for studying open quantum systems. The suggested method, being practically simpler, reveals new physics, including the sharp redistribution of decay widths and the emergence of short-lived superradiant states and long-lived trapped states for sufficiently strong coupling to the continuum.

Using the non-Hermitian Hamiltonian framework, three different problems are considered in this thesis. Even though the systems are physically distinct, the emergence of superradiant states as a result of interaction with the external world is the common thread between all

[1] Mesoscopic physics is concerned with matter in intermediate length scales, between elementary particles and macroscopic objects. Mesoscopic systems can contain a relatively large number of particles, however, in contrast with macroscopic systems, material properties are defined by individual quantum states and not the average over their ensemble.

three cases. An overview of these three problems and the thesis organization is given in the next section.

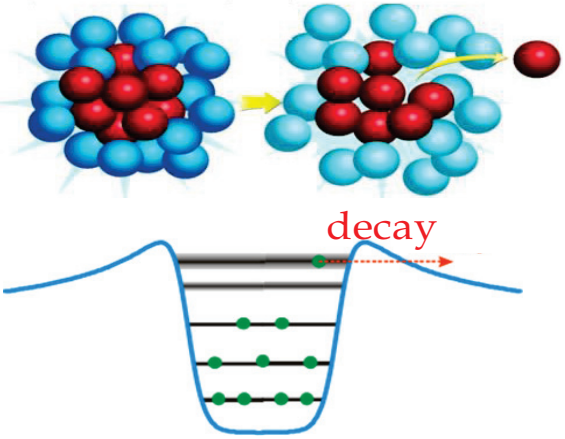

(a)

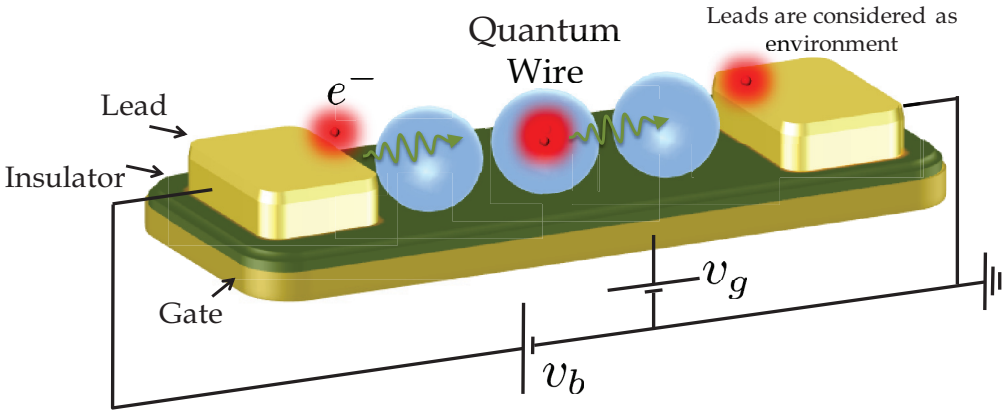

(b)

Figure 5.1: Examples of open quantum systems: (a) an unstable nucleus breaking apart and undergoing nuclear decay and (b) a quantum wire attached to leads acting as electron reservoirs.

5.2 Organization

The derivation of the main mathematical framework used throughout this part of the thesis, the effective non-Hermitian Hamiltonian, is presented in Chapter 6. Dicke superradiance

in quantum optics is described briefly in this chapter. It is shown that the phenomenon of superradiance is a generic feature of all open quantum systems. The conditions under which superradiance occurs are discussed in detail. In this chapter we closely follow the approach used in [93, 99].

Chapters 7, 8 and 9 consider various physical systems which are all studied within the effective Hamiltonian framework. The problem of quantum transport through two different topologies is considered in Chapter 7. In the first section, signal transmission is studied through a one-dimensional chain with a single qubit attached to its center. In the second case, a two-channel quantum wire is considered. For both cases, transition to superradiance and its effect on transport properties are discussed in detail.

Chapter 8 proposes a novel solid state charge qubit suitable for performing quantum operations. The system consists of a one-dimensional wire with a pair of qubits embedded at its center. It is shown that the system supports collective states localized in the left and right sides of the wire and therefore, as a whole, performs as a single qubit. Here, the superradiant states effectively protect the remaining internal states from decaying into the continuum and hence increase the lifetime of the qubit. Furthermore, environmental noise is introduced by considering random Gaussian fluctuations of electronic energies. The interplay between decoherence and superradiance is studied by solving the stochastic Liouville equation. It is shown that, in addition to increasing the lifetime, the emergence of the superradiant states increases the qubit coherence.

In Chapter 9 we consider one-dimensional structures of plasmonic metallic nanospheres. For a single sphere, solving the Maxwell equations results in quasi-stationary eigenmodes. It is shown that systems of two or more coupled spheres can be described by the effective non-Hermitian Hamiltonian matrix, even though our treatment of this problem is entirely

classical. This allows us to predict the occurrence of superradiance phenomena in systems of plasmonic spheres. In particular, when two spheres couple through a single continuum channel and the effect of coherent interaction between the spheres becomes noticeable, the eigenmodes of the system fall into two distinct categories; superradiant states with enhanced radiation and dark states with extremely suppressed radiation properties. The transmission through plasmonic waveguides, one-dimensional chains with an arbitrary number of spheres, is also considered. Similar to the quantum transport problem, superradiance enhances energy transport through the plasmonic waveguides. Part 4 includes the conclusion and future directions.

For want of a better term, a gas which is radiating strongly because of coherence will be called 'superradiant'.

Robert Henry Dicke

Chapter 6

The Effective non-Hermitian Hamiltonian

6.1 Derivation-Feshbach Projection Formalism

Consider a quantum system described by the Hamiltonian H_0 and its discrete set of eigenvectors $|i\rangle$ that interacts with its surrounding environment. The environment is thermodynamically large and is characterized by infinitely many channels with continuous energy spectrum $|c; E\rangle$. The total Hamiltonian H is then the sum of the Hamiltonians of the system, the environment and their interaction.

Let us divide the Hilbert space of this problem into two subspaces with the help of projection operators $\mathcal{Q}$ and $\mathcal{P}$. The operator $\mathcal{Q}$ only acts on the subspace of the closed system and the operator $\mathcal{P}$ acts on the environment only. Without loss of generality, one can further assume that the projections are orthogonal, therefore $\mathcal{P} + \mathcal{Q} = 1$ and $\mathcal{P}\mathcal{Q} = \mathcal{Q}\mathcal{P} = 0$.

The total Hamiltonian H is then decomposed into $H = H_{\mathcal{QQ}} + H_{\mathcal{QP}} + H_{\mathcal{PQ}} + H_{\mathcal{PP}}$, where $H_{\mathcal{QQ}} = \mathcal{Q}H\mathcal{Q}$, $H_{\mathcal{QP}} = \mathcal{Q}H\mathcal{P}$, $H_{\mathcal{PQ}} = \mathcal{P}H\mathcal{Q}$ and $H_{\mathcal{PP}} = \mathcal{P}H\mathcal{P}$. The effective Hamiltonian is achieved by projecting the stationary wave function in the Sschrödinger equation, $H\Psi = E\Psi$, into the subspace of the closed system

$$\mathscr{H}_{\text{eff}}(E)\mathcal{Q}\Psi = E\mathcal{Q}\Psi, \tag{6.1}$$

where

$$\mathscr{H}_{\text{eff}}(E) = H_{\mathcal{QQ}} + H_{\mathcal{QP}}\frac{1}{E - H_{\mathcal{PP}}}H_{\mathcal{PQ}}. \tag{6.2}$$

The first term in the right-hand side of (6.2) is the Hamiltonian of the closed system $\mathcal{Q}H\mathcal{Q} = H_0$. The second term in (6.2), that incorporates the interaction with the environment, has a simple interpretation. The operator $H_{\mathcal{PQ}}$ takes the particle out of the system to the environment, where it propagates through the environment via $(E - H_{\mathcal{PP}})^{-1}$, and finally returns back to the system through $H_{\mathcal{QP}}$. This term can be further simplified by calculating the matrix element between two intrinsic states of the closed system $|i\rangle$ and $|j\rangle$

$$\langle i|H_{\mathcal{QP}}\frac{1}{E - H_{\mathcal{PP}}}H_{\mathcal{PQ}}\,|j\rangle = \sum_c \int dE' \frac{A_i^c(E')A_j^{c*}(E')}{E - E' + i0}, \tag{6.3}$$

where $A_i^c(E)$ is the transition amplitude from continuum channel $|c; E\rangle$ to internal state $|i\rangle$; $A_i^c(E) = \langle i|H_{\mathcal{QP}}\,|c; E\rangle$. The shift in the energy, $E \to E + i0$, is required in order to avoid the singularity on the real energy axis. The transition amplitudes are in general energy dependent; the channel c is open only if the running energy is greater than the channel energy threshold and closed otherwise. Using the Sokhotski-Plemelj theorem, the integral in

(6.3) can be decomposed into Hermitian and anti-Hermitian parts

$$\sum_c \int dE' \frac{A_i^c(E')A_j^{c*}(E')}{E - E' + i0} = \tag{6.4}$$

$$\sum_c \mathcal{P}.\mathcal{V}. \int dE' \frac{A_i^c(E')A_j^{c*}(E')}{E - E'} - i\pi \sum_{c_{\text{open}}} A_i^c(E)A_j^{c*}(E),$$

where $\mathcal{P}.\mathcal{V}.$ denotes the Cauchy principal value. Accordingly, two operators are defined; $\Delta(E)$, corresponding to the Hermitian component in (6.4) with matrix elements

$$\Delta_{ij}(E) = \sum_c \mathcal{P}.\mathcal{V}. \int dE' \frac{A_i^c(E')A_j^{c*}(E')}{E - E'}, \tag{6.5}$$

and $W(E)$ corresponding to the anti-Hermitian component in (6.4), with matrix elements

$$W_{ij}(E) = 2\pi \sum_{c_{\text{open}}} A_i^c(E)A_j^{c*}(E). \tag{6.6}$$

Thus, in operator form, the *energy-dependent* effective Hamiltonian is

$$\mathscr{H}_{\text{eff}}(E) = H_0 + \Delta(E) - \frac{i}{2} W(E). \tag{6.7}$$

The two terms, $\Delta(E)$ and $W(E)$, also known as the *self energy*, completely take the effect of the interaction with the environment into account. The Hermitian part, $\Delta(E)$, renormalizes the energies of the closed system. The summation in (6.5) runs over all continuum channels, open and closed, and therefore it takes into account *virtual* transitions to the environment. On the other hand $W(E)$, which is responsible for the decay width of the energy states of the effective Hamiltonian (6.7), only includes contributions from real transitions to the

continuum channels and hence it only runs over the channels open at a given energy.

In many situations, including the cases we are concerned with in this thesis, the energy interval of interest is relatively small and the transition amplitudes, $A_i^c(E)$, can be considered to be smooth functions of energy. Consequently, the energy dependence of the amplitudes can be neglected. Then the principal value integral in (6.5) vanishes and the effective Hamiltonian reduces to

$$\mathscr{H}_{\text{eff}} = H_0 - \frac{i}{2} W. \tag{6.8}$$

For the remainder of the thesis, the effective Hamiltonian (6.8) is used as the starting point for investigating various open systems.

6.2 The Superradiance Phase Transition

We now discuss the superradiance transition starting with the original idea predicted by Dicke more than half a century ago [97]. Dicke superradiance in quantum optics is described qualitatively. It is then argued that the phenomenon of superradiance is a general feature of open quantum systems. The existence of intrinsic states coupled to a few continuum channels can strongly affect the dynamics of the system. In this situation a phase transition can occur and broad superradiant states that acquire almost the entire available width can form. Consequently the remaining states become long-lived and trapped within the system.

6.2.1 Dicke Superradiance in Quantum Optics

It is well known that when a system of dilute gas is excited, for instance by a laser, the individual atoms or molecules of the gas release their energy due to the so-called spontaneous radiation phenomenon. This radiation is isotropic and incoherent and the intensity of

radiation, I, which exponentially decays with characteristic time τ_r, is proportional to the number of atoms N, $I \propto N$. This situation is graphically shown in Fig. 6.1.

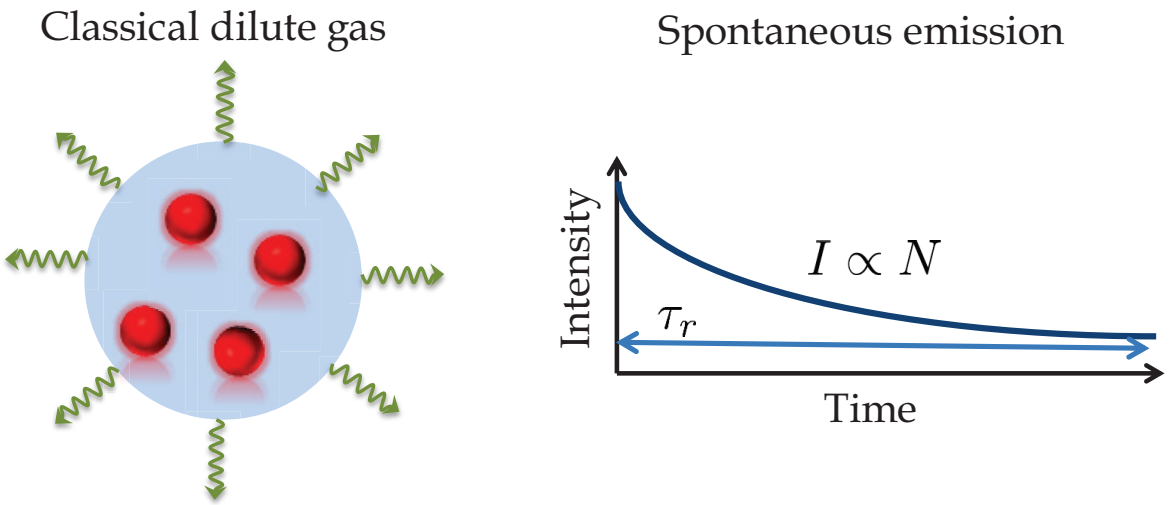

Figure 6.1: Spontanous emission of a dilute classical gas initially prepared in the excited state. The radiation is isotropic and the intensity is proportional to the number of atoms.

In 1954, Dicke predicted the phenomenon of coherent spontaneous radiation. It was shown that a system with a relatively large number of two-level atoms that interact through the background radiation which has a much larger wavelength than the dimensions of the system, supports broad resonances. In his paper [97] Dicke coined the term *superradiant* for such states:

> "For want of a better term, a gas which is radiating strongly because of coherence will be called superradiant."

When the system is initially prepared in the many-body superradiant state, the emission is anisotropic and it occurs as a burst of radiation, indicating the small characteristic decay time, $\tau_{s.r.}$, of the state (See Fig. 6.2). Moreover, Dicke showed that the intensity of the radiation is proportional to the squared of the number of atoms: $I \propto N^2$. Dicke superradiant emission is graphically shown in Fig. 6.2.

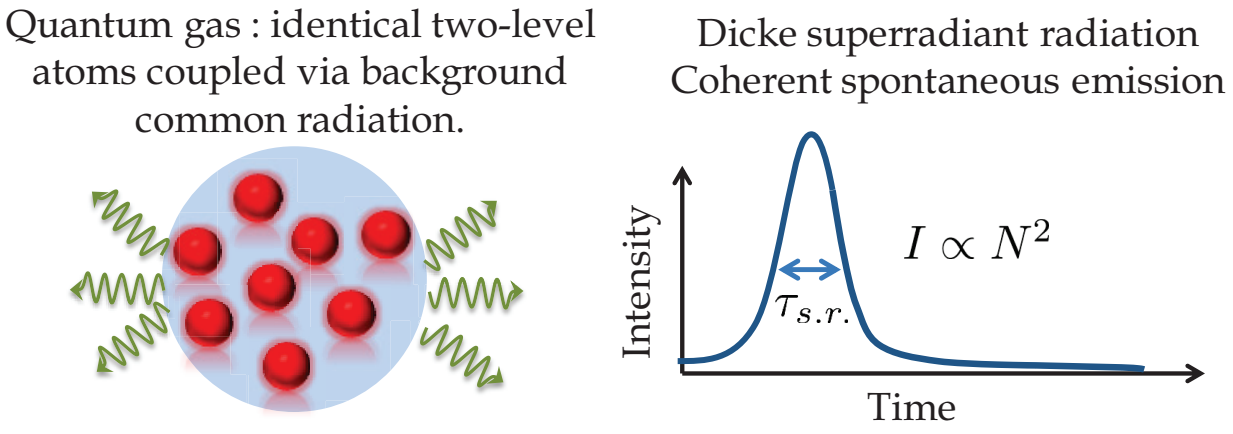

Figure 6.2: Dicke coherent spontanous radiation. The radiation is directional and the intensity is proportional to the squared of the number of atoms.

6.2.2 Superradiance in Open Systems

As mentioned, the phenomenon of superradiance is a generic feature of open quantum system. In order to see this, it helps to consider the statistics of the *quasi-stationary* eigenenergies of the effective Hamiltonian (6.8)

$$\mathscr{E}_r = E_r - \frac{i}{2}\Gamma_r, \tag{6.9}$$

where Γ_r is the width of the state and related to the lifetime by $\tau_r = \hbar/\Gamma_r$. The positiveness of Γ_r is guaranteed by the Cholesky factorized form of W in (6.6) which makes W a positive definite matrix. We define the quantity ξ that parameterizes the strength of interaction with the external world, thus

$$\mathscr{H}_{\text{eff}} = H_0 - \frac{i}{2}\xi\, W. \tag{6.10}$$

Because the framework is exact and no approximation was used, ξ can take arbitrarily small values representing weak interactions or extremely large values representing strong interactions with the external world. For weak interactions, when ξ is small, the anti-

Hermitian component, W is a perturbation to H_0. The complex eigenenergies are then narrow resonances with an almost uniform width distribution [89, 99]. In the opposite limit of strong interaction, the anti-Hermitian component becomes the dominant term and H_0 is the perturbation. It is clear from (6.6) that the rank of W is equal to the number of open channels which is normally much smaller than the number of intrinsic states of the closed system. Therefore a few states become giant resonances that steal the entire width and the remaining states become long-lived and effectively decoupled from the environment. Due to the resemblance of this phenomenon to the Dicke superradiance in quantum optics, we term the broad, short-lived resonances as superradiant states and the narrow, short-lived resonances as subradiant states. It was shown in [93, 99] that the superradiance *phase transition* occurs when $\langle\Gamma\rangle/D \approx 1$, where $\langle\Gamma\rangle$ is the average widths of the energies in (6.9), and D is the mean level spacing of the closed system.

6.3 Scattering Matrix and Transmission

The non-Hermitian Hamiltonian formalism provides a suitable platform for studying scattering properties of open quantum systems. Consider process $a \to b$, where a particle enters from channel a, which is coupled to the intrinsic state of the closed system $|i\rangle$ with the coupling amplitude A_i^a, propagates through the system with possible virtual excursions to the continuum and back, and finally exits from the intrinsic state $|j\rangle$ to the decay channel b with the amplitude A_j^b. The amplitude of this process is given by [99]:

$$Z^{a\to b}(E) = \sum_{i,j} A_i^{b*} \left(\frac{1}{E - \mathcal{H}_{eff}}\right)_{ij} A_j^a. \tag{6.11}$$

It was shown in [93] that the corresponding scattering matrix, $S^{ba} = \delta^{ba} - iZ^{ba}$, is unitary [93] and the transmission coefficient is

$$T^{ba}(E) = \left| Z^{ba}(E) \right|^2 . \tag{6.12}$$

It might be convenient to perform the transformation to the (biorthogonal) basis $|r\rangle$ of eigenfunctions of the effective Hamiltonian. The complex energies $\mathscr{E}_r = E_r - (i/2)\Gamma_r$ correspond to the poles of the scattering matrix, while the process amplitude (6.11) still has factorized residues transformed to the eigenbasis,

$$Z^{ba}(E) = \sum_r \frac{\tilde{A}^b_r \tilde{A}^a_r}{E - \mathcal{E}_r}. \tag{6.13}$$

We can note parenthetically that this description can be treated as a simple superposition of interfering resonances only approximately, namely if the energy dependence of continuum amplitudes A^a_n is neglected as it is done in our consideration. In this approximation the time decay curve of a single isolated resonance $|r\rangle$ would be pure exponential with the width Γ_r.

It has today occurred to me that an amplifier using
semiconductors rather than vacuum is in principle possible.

William Shockley's Laboratory notebook, 29 Dec 1939

Chapter 7

Quantum Transport

7.1 Introduction

Thanks to the development of nanotechnology, the preparation of low-dimensional assemblies of nanoparticles becomes a routine experimental task [109]. This renews the attention to the study of quantum properties of relatively simple low-dimensional mesoscopic systems which reveal a rich physical behavior. In this context, the exactly solvable models as tight-binding one- or two-dimensional chains coupled to adatoms or impurities are of special interest [106, 110–112]. In light of this, quantum transport in two different nanostructure topologies are considered in this section.

7.2 Quantum Signal Transmission Through a Single-Qubit Chain

In what follows we consider a system with a two-level atom of an impurity (qubit) inserted into an open periodic chain. The model is simple enough to allow for the exact solution; at the same time the model turns out to be rich enough to demonstrate interesting physics of the signal transmission. An analytical consideration is supplemented by the detailed numerical study for the finite chains

We first consider a *closed* chain of $2N$ identical cells with the nearest neighbor hopping interaction. Two arms of the chain are connected through the central cell occupied by a two-level atom (qubit). We find the energy spectrum of the system that consists of a normal band of delocalized Bloch standing waves and two additional states outside the band corresponding to the excited and the ground states of the qubit. We study the evolution of the energy spectrum as a function of the chain-qubit coupling strength.

Next, we describe the energy spectrum of the *open* system coupled to the continuum through its edge states. The former stationary states acquire decay widths that change as a function of the coupling constants. The decay widths of the qubit states are small compared to those of the Bloch waves. The qubit states remain essentially localized at the qubit even when the coupling of the chain to the continuum becomes sufficiently strong to allow for the formation of super-radiant states.

In addition, we study the transmission through the chain as a function of the coupling parameters. In both limits of the edge continuum coupling being weak and strong compared to the coupling between the qubit levels, the resonances are well isolated all having narrow decay widths and perfect transmission at resonance energies. When both couplings are of

comparable strength, the resonances are overlapped and the transmission is below the perfect level. The results are summarized in the Discussion.

7.2.1 Closed Chain

7.2.1.1 Symmetric and Antisymmetric Modes

We consider a linear chain of $2N$ identical cells numbered as $n = -N, -(N-1), ..., -1$ and $n = 1, ..., N-1, N$, while the central cell, $n = 0$, is occupied by a qubit, a two-level atom with states $|0\rangle$ and $|e\rangle$, excitation energy $\epsilon_e - \epsilon_0 = \Delta$, and matrix element λ of the qubit excitation. The energy ϵ_0 is the level position in all cells; for simplicity we put the lower level of the isolated qubit at the same position. Introducing the hopping (tunneling) matrix element v between the neighboring cells, we come to the Hamiltonian of the closed chain:

$$H_{nn} = \epsilon_0, \quad H_{n,n+1} = H_{n+1,n} = v, \quad n = -N, ..., 0, ..., N; \tag{7.1}$$

$$H_{ee} = \Delta, \quad H_{0e} = H_{0e} = \lambda, \tag{7.2}$$

where all matrix elements can be considered as real.

Before introducing the coupling to the outside world, we briefly characterize the solution for the closed chain. A general stationary state $|E\rangle$ with energy E can be presented as a superposition

$$|E\rangle = \sum_{n=-N}^{N} c_n(E)|n\rangle + b(E)|e\rangle. \tag{7.3}$$

The boundary conditions for the chain closed at the edges are $c_{-N-1} = c_{N+1} = 0$. The

coefficients of the superposition (7.3) satisfy the obvious equations:

$$(E-\epsilon_0)c_n - v(c_{n-1}+c_{n+1}) = 0, \quad n \neq 0, \tag{7.4}$$

$$(E-\epsilon_0)c_0 - v(c_{-1}+c_{+1}) = \lambda b, \tag{7.5}$$

$$(E-\Delta)b = \lambda c_0. \tag{7.6}$$

Eqs. (7.5) and (7.6) can be treated as boundary conditions for the two chains (left and right) implying that

$$c_0(E) = \frac{v(E-\Delta)}{(E-\epsilon_0)(E-\Delta)-\lambda^2}\,(c_{-1}+c_1). \tag{7.7}$$

Following the same procedure as for a single chain [99], see also Appendix in Ref. [103], we find that the solutions on both sides of the qubit have the form

$$c_n = \begin{cases} A\xi_+^n + B\xi_-^n, \ n<0; \\ A'\xi_+^n + B'\xi_-^n, \ n>0. \end{cases} \tag{7.8}$$

The amplitudes $\xi_\pm$ are given by

$$\xi_\pm = \frac{1}{2v}\left[E-\epsilon_0 \pm \sqrt{(E-\epsilon_0)^2-4v^2}\right], \tag{7.9}$$

and $\xi_+\xi_- = 1$. The edge conditions determine

$$B = -A\left(\frac{\xi_-}{\xi_+}\right)^{N+1}, \quad B' = -A'\left(\frac{\xi_+}{\xi_-}\right)^{N+1}. \tag{7.10}$$

The central point determines two classes of solutions. The *antisymmetric* states, $c_n +$

$c_{-n} = 0$, have $c_0 = 0$, so that these wave functions are decoupled from the excited qubit that lives on the excited level $E = \Delta$ (in this situation the qubit can be excited or deexcited only by an additional external coupling). Because of $c_0 = 0$ and interaction only between the neighboring cells, the two sides of the chain are also decoupled from each other so that such modes do not take part in the transport through the whole chain. The spectrum E_q of the antisymmetric states is determined by the roots of $\xi_-^{2N+2} = 1$ that can be parameterized by the even-number quantized quasimomentum q, or by the phase φ_q,

$$E_q = 2v\cos\varphi_q, \quad \varphi_q = \frac{\pi q}{2N+2}, \quad q \text{ even}, \tag{7.11}$$

and the local amplitudes (7.8) of the wave functions are

$$c_n(q) = i^q \sqrt{\frac{1}{N+1}}\,\sin(n\varphi_q). \tag{7.12}$$

The energies (7.11) are inside the Bloch band $(-2v, +2v)$.

The *symmetric* solutions, $c_1 = c_{-1}$, involve the qubit into dynamics and the corresponding roots are determined by

$$\xi_+^{2N+2} = \frac{\lambda^2 + (E-\Delta)\sqrt{(E-\epsilon_0)^2 - 4v^2}}{\lambda^2 - (E-\Delta)\sqrt{(E-\epsilon_0)^2 - 4v^2}}. \tag{7.13}$$

To derive this relation, it is convenient to use eq. (7.4) and connect the amplitude c_1, or c_{-1}, to the central amplitude c_0,

$$c_1 = c_0\,\frac{\xi_+^N - \xi_-^N}{\xi_+^{N+1} - \xi_-^{N+1}}. \tag{7.14}$$

With the qubit disconnected, $\lambda \to 0$, we have the missing in eq. (7.11) q-odd part of the band spectrum with the amplitudes (7.12) where $\sin(n\varphi_q)$ is changed to $\cos(n\varphi_q)$. Depending on the relative position of Δ with respect to the band width $2v$, there are two cases; below throughout the section we set $\epsilon_0 = 0$.

7.2.1.2 Case $\Delta > 2v$

In this case, the upper level is always outside the band, $E > 2v$; the lower level also leaves the band at a finite value of λ when $E < -2v$. The full spectrum of twelve energy levels for $N = 5$ is shown as a function of λ in Fig.7.1. The upper state starts at $E = \Delta$ and grows approximately linearly with λ. At small λ, this is the state with the excited qubit and only weak admixtures of intrinsic sites.

With increasing λ, the symmetric and antisymmetric states inside the band become degenerate, while the "excited" (upper) wave function is spread almost equally over two states of the qubit. The orthogonal combination of the excited and ground state of the qubit gives the lower state (at sufficiently large values of λ). In this limit the picture effectively is of Rabi oscillations between the qubit levels with only a small probability of hopping along the chain. The chain then is almost decoupled from the qubit. This evolution of the two wave functions is illustrated by Fig. 7.2.

7.2.1.3 Case $\Delta < 2v$

Here we consider the spectrum of the energy levels as a function of λ when the qubit excitation energy is inside the band ($\Delta < 2v$). The full spectrum of twelve energy levels for $N = 5$, $\Delta = 0.5$ is shown as a function of λ in Fig. 7.3. When $\lambda = 0$, all the energies are inside the band; with increasing λ, both the upper and lower energies move out of the band (as

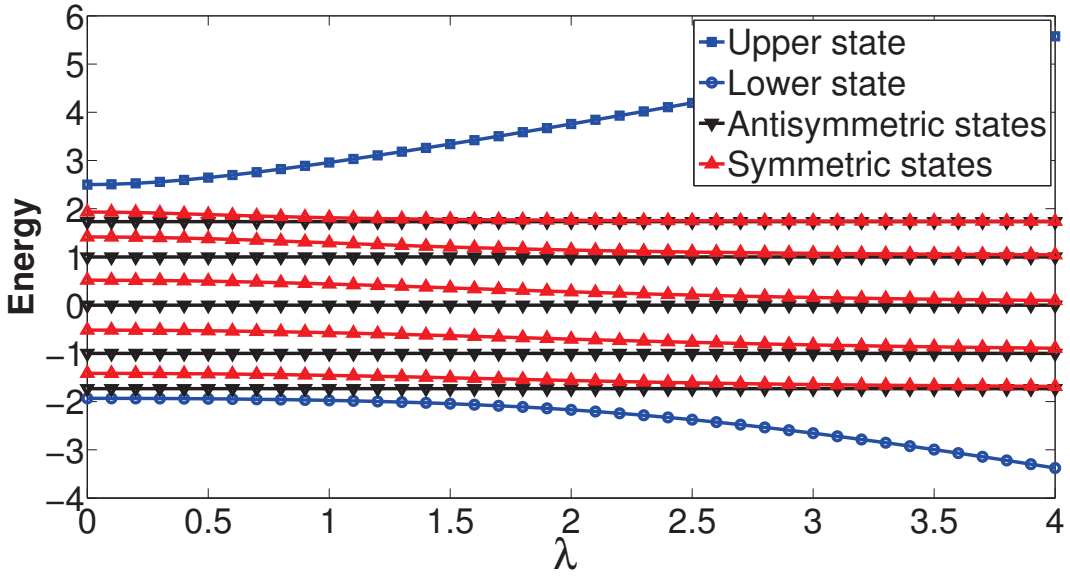

Figure 7.1: Energy levels for a system of the closed chain of eleven sites and the excited qubit state in the middle as a function of the qubit coupling strength λ; the hopping amplitude is set to $v = 1$, and the excitation energy of the qubit $\Delta = 2.5$.

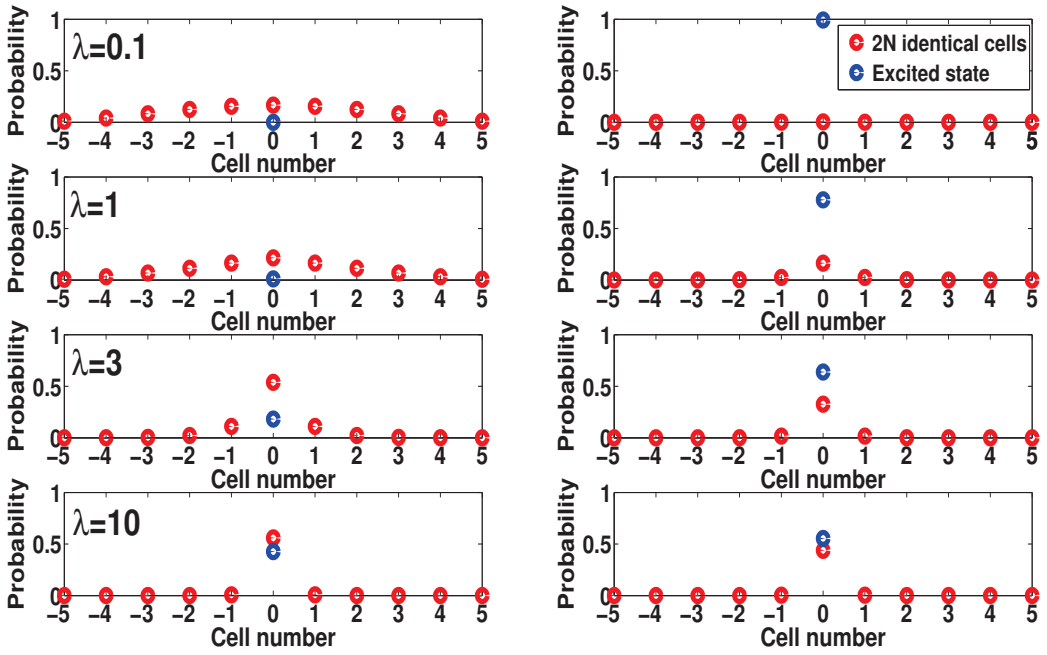

Figure 7.2: Squared components of the lower (left column) and upper (right column) eigenstates as a function of the qubit excitation strength λ, for a chain $N = 5$ and $v = 1$.

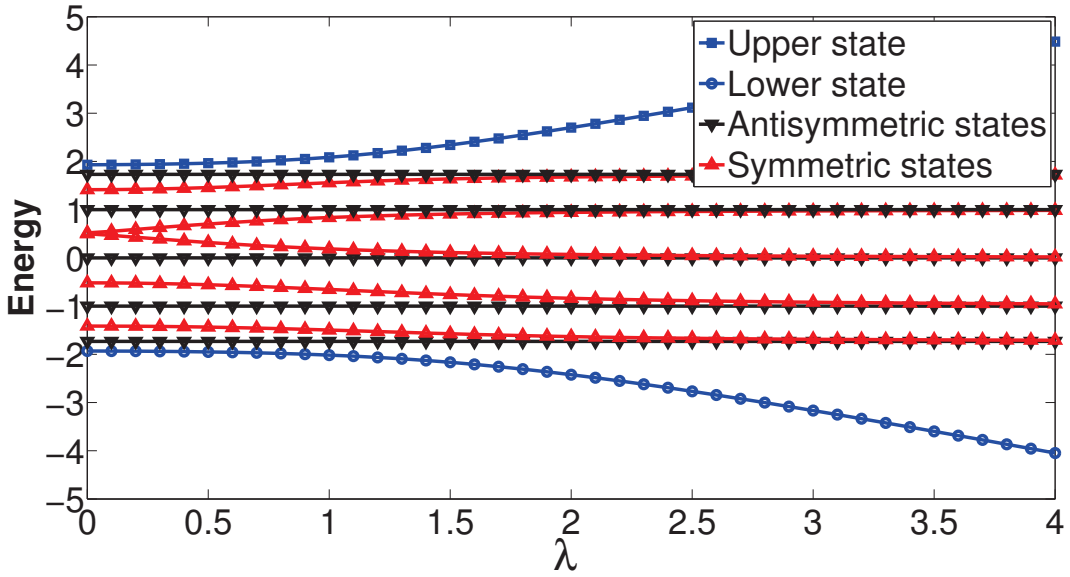

Figure 7.3: Energy levels for a system of the closed chain of eleven sites and the excited qubit state as a function of the qubit coupling strength λ; the hopping amplitude is set to $v = 1$, and the excitation energy of the qubit $\Delta = 0.5$.

before). As λ increases the symmetric states and the qubit level inside the band merge with corresponding antisymmetric states.

Fig. 7.4 shows the eigenstates corresponding to the lowest and highest eigenenergies, upper and lower wave functions. Unlike in the case B, when $\lambda = 0.1$, in the upper wave function there is a small admixture of the excited qubit state.

The special situation emerges if Δ is degenerate with the energy of one of the antisymmetric states. In this case, $c_0 = 0$, however b is not necessarily vanishing. Eq. (5) results in $c_1 + c_{-1} = -(\lambda/v)b$. As a consequence we obtain here two eigenstates which do not fall into the symmetric or anti-symmetric category. In Fig. 7.5 we show the two eigenstates for $N = 5$, $v = 1$, $\Delta = \sqrt{3}$. As λ increases the two state become localized either in the left chain or in the right chain.

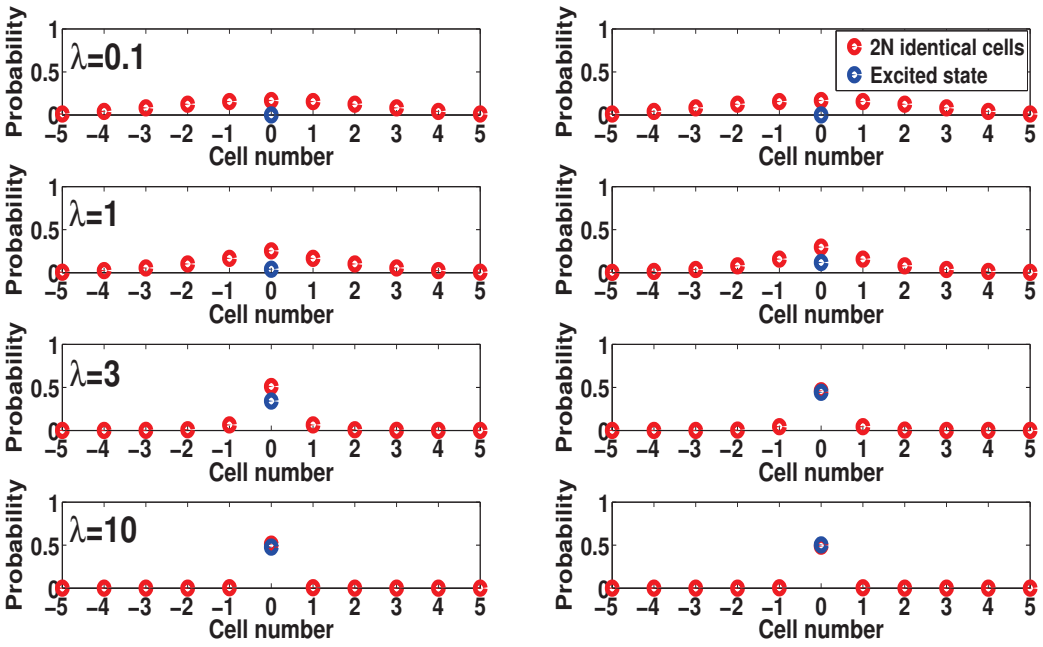

Figure 7.4: Squared components of the lower (left column) and upper (right column) of the wave functions as a function of the qubit excitation strength λ, for a chain $N = 5$, $\Delta = 0.5$ and $v = 1$.

7.2.1.4 Large N Chain

For two qubit levels outside of the band we can derive in case of large N a simple expression. For the upper qubit level, $E > 2v$, we always have $\xi_+ > \xi_-$. Hence, for large N we may neglect ξ_-^N in eq. (7.14) to obtain $c_1 = c_0/\xi_+ = c_0\xi_-$. Accordingly, for the lower qubit level, $E < -2v$, we may neglect ξ_+^N in eq. (7.14). This allows us to find from expressions (7.5) and (7.6) equations for the two levels genetically related to the qubit:

$$\sqrt{E^2 - 4v^2} = \pm\frac{\lambda^2}{E - \Delta}, \tag{7.15}$$

where plus (minus) corresponds to the upper (lower) qubit level.

The wave functions of these states are given by

$$|\Psi_{\mp}\rangle = B_{\mp}\left\{\sum_{-N}^{N}\xi_{\mp}^{|n|}\,|n\rangle + \frac{\lambda}{E-\Delta}\,|e\rangle\right\}, \tag{7.16}$$

where the normalization constant $B_{\mp}$ is defined by

$$B_{\mp}^2\left[1+\frac{\lambda^2}{(E-\Delta)^2}-4\frac{\varepsilon_{\mp}^2}{\varepsilon_{\mp}^2-1}\right]=1, \tag{7.17}$$

with the same identification of the signs.

In fact, the asymptotic expression (7.15) is good even for $N = 5$. For example, for $E/2v = 1.1$ we have the ratio $(\xi_-/\xi_+)^5 = 0.01$, while at $N = 10$ the ratio $(\xi_-/\xi_+)^{10}$ is of the order of 10^{-4}. Therefore, for the qubit levels positioned out of the band, the expression (7.15) is good for any $N \geq 5$ and for any value of Δ. As before, these two states move out of the band as λ increases. For the states inside the band, there are no simple expressions for large N. However, their behavior is similar to that shown in Fig.7.1: as λ increases all symmetric states merge with antisymmetric states.

7.2.2 Open Chain

Now we assume that the edge states are coupled to the outside world by ideal leads and the situation becomes identical with what can be described by the effective non-Hermitian Hamiltonian (6.8),

$$\mathscr{H}_{\text{eff}} = H - \frac{i}{2}W, \tag{7.18}$$

acting only in the intrinsic space of the closed system. The anti-Hermitian part W is given by equation (6.6). In our case, the only non-vanishing amplitudes are $A^L_{-N} = \sqrt{\gamma_L}$ and $A^R_N = \sqrt{\gamma_R}$ describing the coupling of the left (right) edge to the left (right) decay channel.

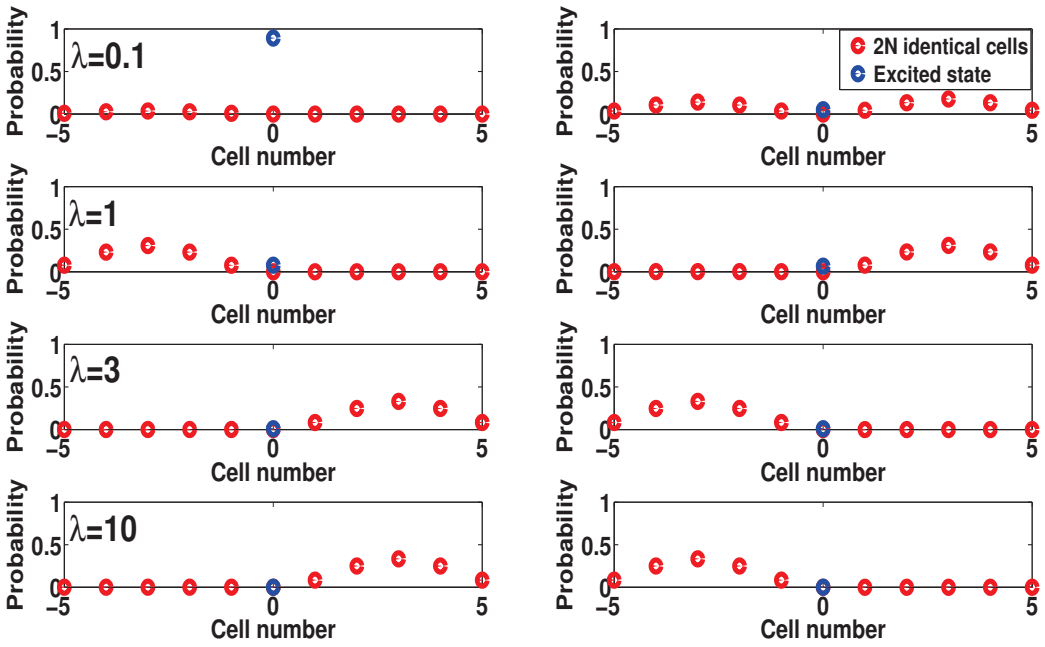

Figure 7.5: Squared components of two wave functions for degenerate level as a function of the qubit excitation strength λ, for a chain $N = 5$, $\Delta = \sqrt{3}$ and $v = 1$.

In the case of a linear chain we allow only left and right decays through the edge states (it would be also interesting to study the decoherence through the coupling with many "random" weak channels connected to the intrinsic sites). The factorized nature of the operator W (dictated essentially by requirements of unitarity of the scattering matrix in the channel space, see for example [113]), shows that this operator has only few non-zero eigenvalues their number being equal to the number of open channels. The corresponding eigenstates of W are obviously just the edge states directly coupled to the continuum. Therefore it is sufficient in our scheme to introduce two complex energies, ϵ_R and ϵ_L for the states at the edges, where $\epsilon_{L,R} = \epsilon_0 - (i/2)\gamma_{L,R}$. Such an open system without a qubit was analyzed in Refs. [99, 101, 103, 105]. In this approach the states directly coupled to the continuum play the role of doorways [114], and the remaining states can get their widths (finite lifetimes) only through their coupling to the doorways.

The typical situation for the chain without a qubit is evolving as a function of parameters $\gamma_{L,R}$ compared to the level spacing D in the closed system. At weak coupling, every intrinsic state becomes a resonance with a small decay width determined by the overlap of the Bloch state with the edges; the final width distribution has, for $\gamma_L = \gamma_R$, a maximum in the center of the band. In the limit of strong continuum coupling, we have a super-radiant situation when the central state in the spectrum accumulates almost the entire width while the remaining states become very long-lived (trapped). In the case of $\gamma_L \neq \gamma_R$ there occur two super-radiant transitions [103] with the maximum of the signal transmission in between. In the site representation, the super-radiant states with energies in the center of the band are concentrated at the edges [99]. This picture survives also the possible presence of disorder in the intrinsic wells [101].

The results for the chain with the qubit are illustrated by the series of graphs, where the chain consists of 5+1+5=11 cells with the qubit in the middle, altogether 12 intrinsic states. Here we diagonalize the effective Hamiltonian in the *doorway representation*: the continuum coupling occurs only at the edges which serve as doorways, and the matrix elements of the anti-Hermitian part of the effective Hamiltonian (7.18), which couples the states $|q\rangle$ with the outside world, are given in the band representation by

$$W_{qq'} = \gamma_L c_{-N}(q) c_{-N}(q') + \gamma_R c_N(q) c_N(q'). \tag{7.19}$$

Fig. 7.6 shows the evolution (as a function of λ) of the resonance energies for the case of weak continuum coupling, $\gamma_L = \gamma_R = 0.1$ (the scale is fixed by the band width, $v = 1$). At small λ and $\Delta > 2$, we have the parabolic distribution of widths with the maximum at the center of the band, as known from previous studies [99,101], and the decoupled excited qubit

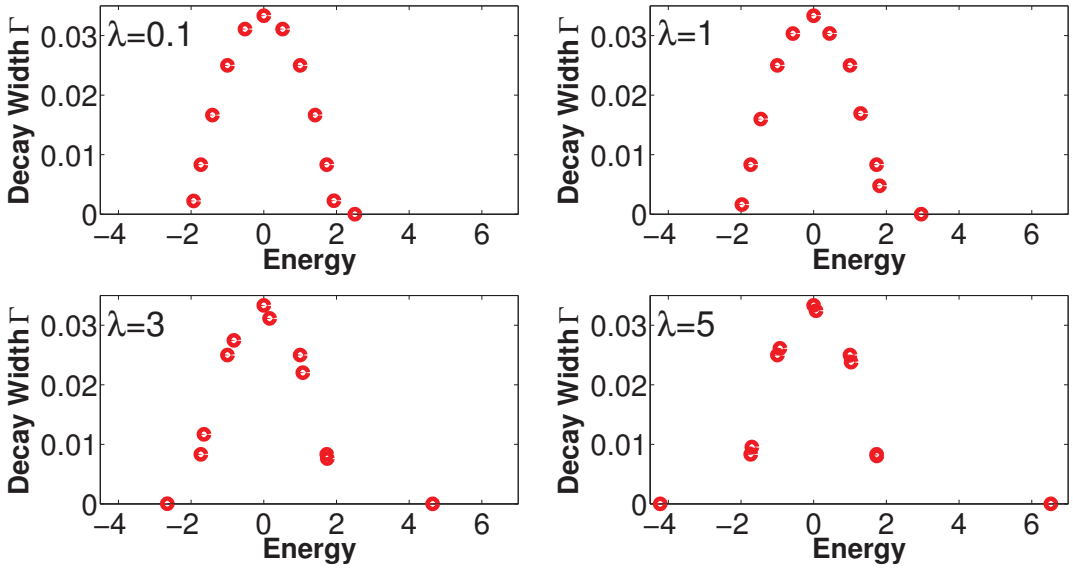

Figure 7.6: Resonance complex energies (eigenvalues of the effective Hamiltonian for weak continuum coupling, $\gamma = 0.1$) evolve as a function of the qubit excitation strength λ. Two qubit states are effectively decoupled from the chain and move along the real energy axis.

state above the band with zero width. As λ increases, the symmetric and antisymmetric states merge becoming effectively decoupled from the qubit. The upper qubit state and emerging outside the band the lower qubit state are still almost stationary (Rabi regime). They are moving along the real energy axis being repelled by the band.

The situation changes when we come to the strong continuum coupling, Fig. 7.7. Here we again follow the evolution as a function of λ but at $\gamma = 20$. At small $\lambda = 0.1$, the two coinciding super-radiant states are formed in the center of the band (here we keep $\gamma_L = \gamma_R$), and the remaining ten states are trapped, effectively returning to the non-overlap regime (the left lower plot shows, at a much smaller width scale, the parabolic width distribution). With increase of λ, the super-radiant states survive, while the qubit states again are repelled by the band along the real energy axis having still very small widths.

It is instructive to take a look of the width evolution as a function of the continuum coupling strength γ. The typical process is presented by Fig. 7.8, where the trajectories of

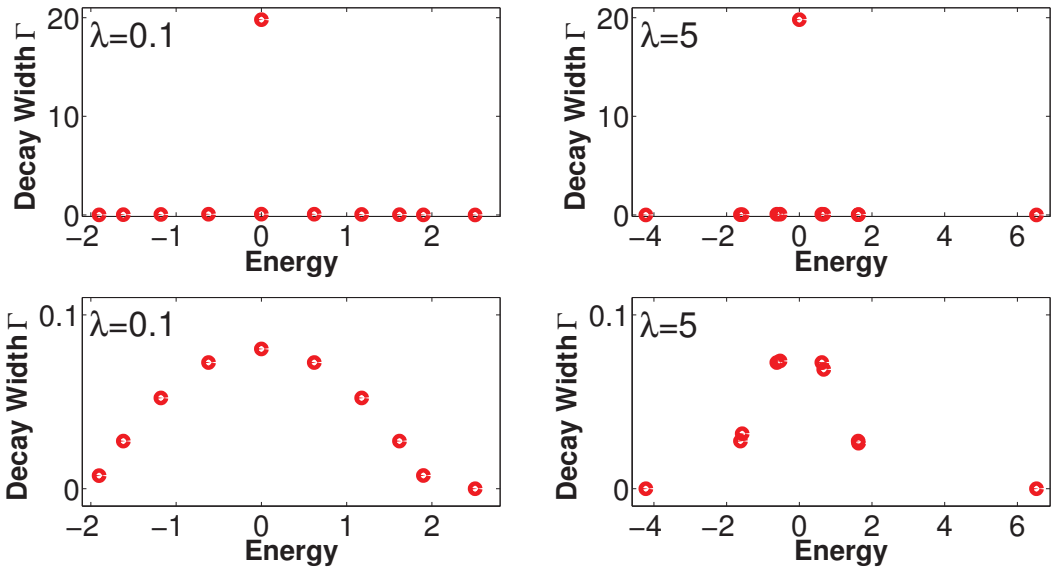

Figure 7.7: Resonance complex energies (eigenvalues of the effective Hamiltonian for strong continuum coupling, $\gamma = 20$) show segregation of two super-radiant states in the middle of the band from ten trapped states which include the strongly localized states of the qubit.

all twelve complex poles in the lower half of the complex plane are shown. In the limit of very weak continuum coupling, part (a) of this figure, the width distribution is parabolic, being proportional, as a function of real energy, to the group velocity of the band states. It is transformed with increase of γ. All widths, except for the super-radiant states in the center of the energy band, turn back after reaching their maximum values. Their corresponding trajectories are almost symmetric with respect to their maxima which is typical for the phenomenon of super-radiance in a space of fixed dimension. Indeed, after the segregation of the super-radiant state(s), the remaining trapped states are essentially in the same situation as they were in the beginning of the process; this symmetry for the finite dimension of intrinsic space is a characteristic feature [103] that appears also in the statistical distribution of neutron widths for thermal-energy neutron resonances [115]. Part (b) of the figure selects, on a detailed energy scale, the complex-plane evolution of the excited qubit state that becomes extremely long-lived. The details of interference between neighboring resonances were also

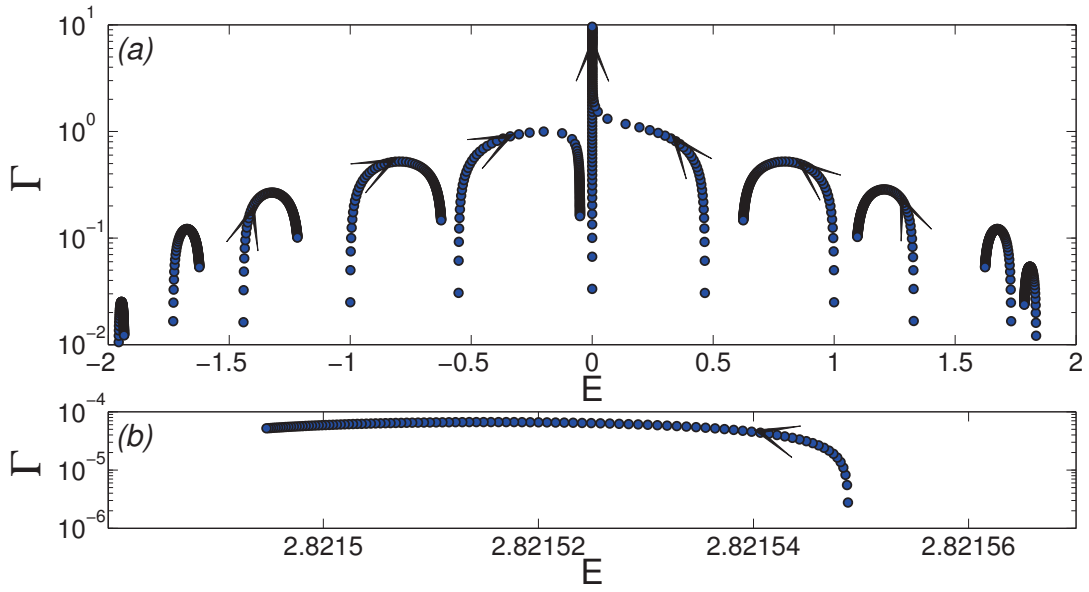

Figure 7.8: Complex-plane trajectories of eigenstates of the effective Hamiltonian; the parameter values are $v = 1,\ \lambda = 0.8,\ \Delta = 2.5$. The arrows show the direction of the evolution as γ changes from 0 to 10. Panel (a) shows the behavior of 12 states in the chain while panel (b) singles out the state genetically connected to the excited qubit state located outside the band.

discussed repeatedly in the context of the electron conduction in nano-scale systems, see for example [116].

It was noticed long ago [117] that, in the description of an open system with the aid of the effective Hamiltonian, the Hermitian and non-Hermitian parts of the interaction act in the opposite way. The real (Hermitian) perturbation repels the levels but, through the mixing mechanism, attracts the widths of unstable states. Contrary to that, the imaginary (non-Hermitian) interaction through the continuum repels the widths (the road to superradiance and trapping) but attracts real energies of resonances. This attraction is seen in Fig. 7.9 for a larger value of λ: as the continuum coupling γ increases along the road to super-radiance, the real energies of the poles move to the middle of the band, where the super-radiant states are located.

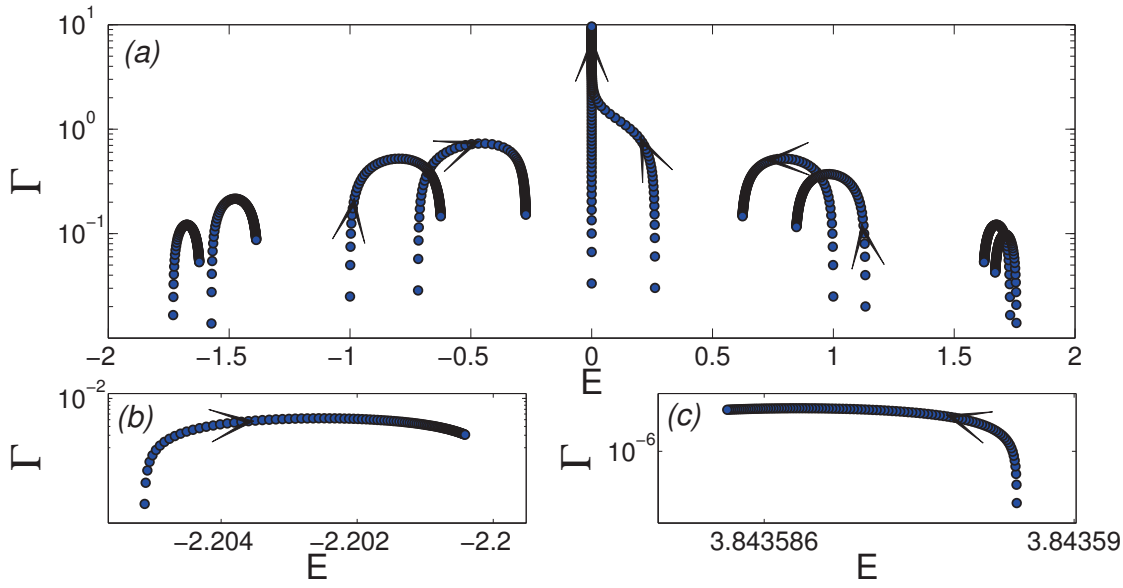

Figure 7.9: Complex-plane trajectories of eigenstates of the effective Hamiltonian; the parameters values are $v = 1,\ \lambda = 2.1,\ \Delta = 2.5$. Ten states, including the super-radiant at the edges of the chain, are moved closer inside the band, panel (a), two states mainly localized at the qubit have energies outside the band and essentially interact only with each other having a large lifetime with respect to tunneling through the chain, panels (b) and (c) .

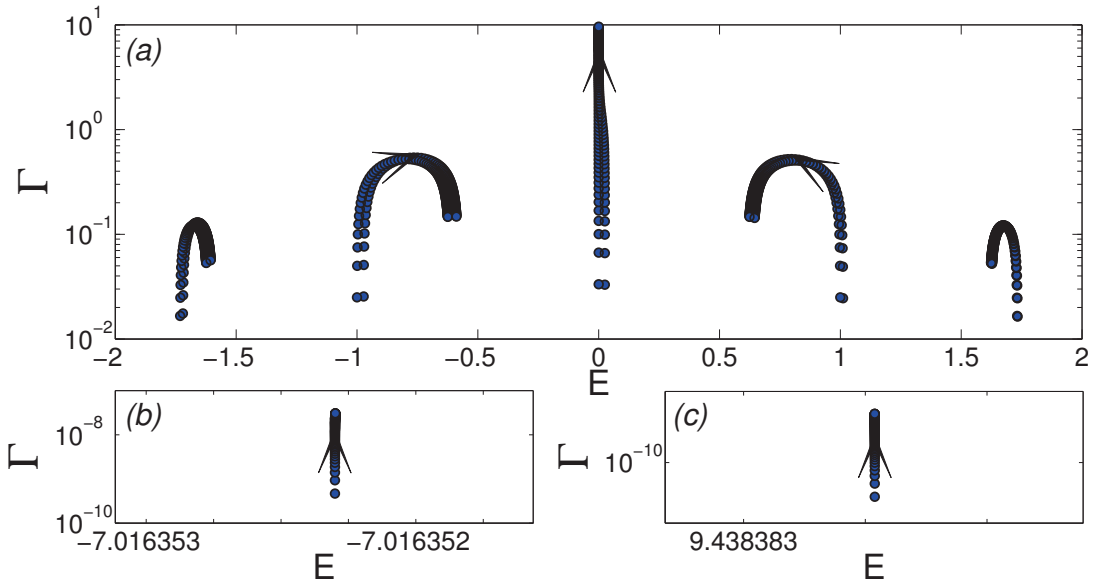

Figure 7.10: Complex-plane trajectories of eigenstates of the effective Hamiltonian; the parameters values are $v = 1,\ \lambda = 8,\ \Delta = 2.5$. Ten states, including the super-radiant at the edges of the chain, are moved closer inside the band, panel (a). The qubit states, the ground state, (b), and the excited state, (c), are essentially decoupled.

Finally, the limit of very strong coupling between the qubit levels is shown in Fig. 7.10 where $\lambda = 8$. With increasing continuum coupling γ, as antisymmetric and symmetric roots merge, we see, panel (a), the evolution of pairs of states (ten of them inside the band including the super-radiant ones). The time arrow of this evolution is again in the direction of attraction for the real energies of resonances. The qubit states, the ground state, (b), and the excited state, (c), are essentially decoupled. They do not shift and only gradually increase their (still small) decay widths as γ increases.

Next we briefly consider the case when qubit energy Δ is inside the band. In Fig. 7.11 we show the resonance complex energies for $\Delta = 0.5$ and for weak continuum coupling, $\gamma = 0.1$, as a function of the qubit excitation strength λ. We have already seen that at small λ there are two eigenstates with eigenenergies close to $\Delta = 0.5$. Their decay width is smaller since there is a strong contribution from the excited qubit state to these two.

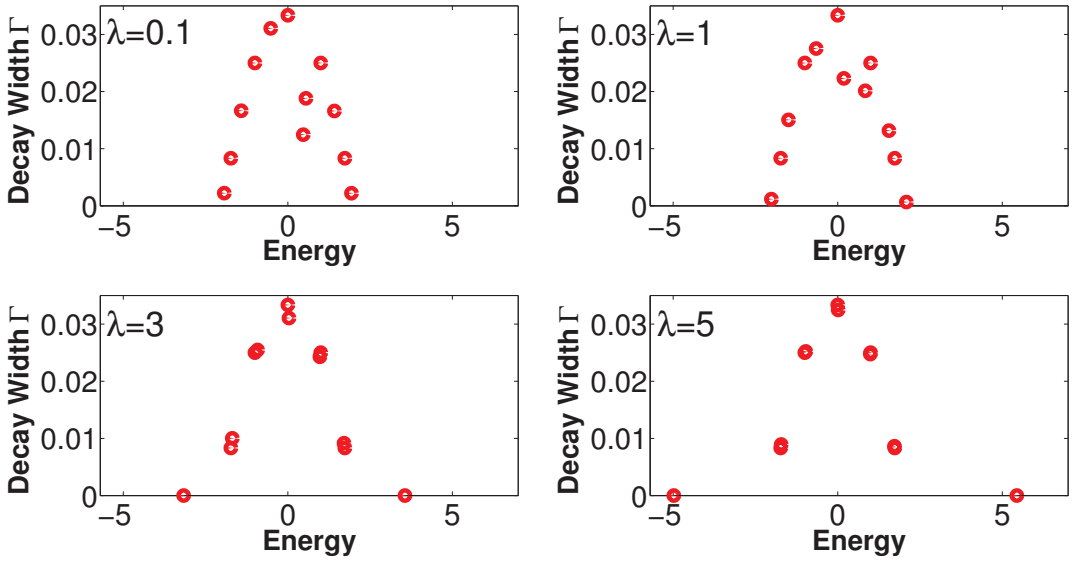

Figure 7.11: Resonance complex energies (eigenvalues of the effective Hamiltonian) for $\Delta = 0.5$ and for weak continuum coupling, $\gamma = 0.1$ as a function of the qubit excitation strength λ.

As λ increases, the eigenenergies inside the band merge,so that the two qubit states are effectively decoupled from the chain moving along the real energy axis. Resonance complex energies for strong continuum coupling $\gamma = 20$ are shown in Fig. 7.12 for $\Delta = 0.5$. Here the situation is qualitatively identical with that in Fig. 7.7. At small $\lambda = 0.1$, the two coinciding super-radiant states are formed in the center of the band, and the remaining ten states are trapped. With the increase of λ, the superradiant states survive, while the qubit states again are repelled by the band along the real energy axis having still very small widths.

7.2.3 Transmission Through The Chain

Here we briefly consider the transmission of an external signal through the chain with the inserted qubit, similarly to the consideration made earlier for the uniform chain or multi-dimensional lattices [103] and for the star graph [108]. As discussed earlier in Chapter 6, the

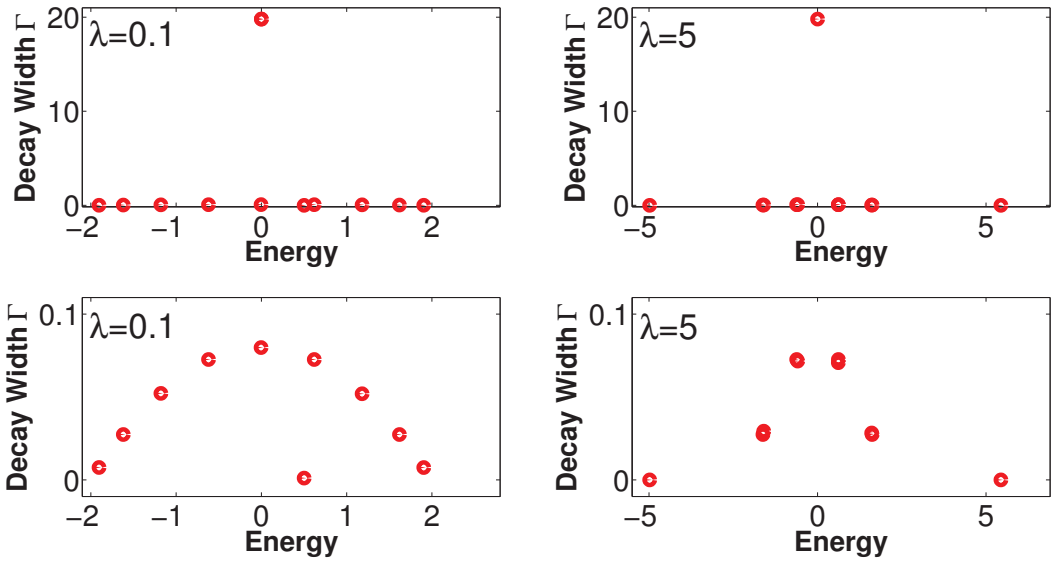

Figure 7.12: Resonance complex energies (eigenvalues of the effective Hamiltonian) for $\Delta = 0.5$ and for strong continuum coupling, $\gamma = 20$ as a function of the qubit excitation strength λ.

internal propagation of the signal of given energy E in the open system is described by the propagator

$$G(E) = \frac{1}{E - \mathscr{H}_{\text{eff}}}, \tag{7.20}$$

where $\mathscr{H}_{\text{eff}}$ is the effective Hamiltonian (7.18) with the imaginary part (6.6) that describes multiple excursions of the signal into continuum and back. Our simple geometry has two open channels, left and right (labeled in eq. (7.19) L and R). The full amplitude Z^{LR} and the transmission coefficient T^{LR} of the process between channels were given earlier by (6.11) and (6.12), respectively.

For the calculation of transmission we adopt the approach of Ref. [103]. For the open chain of Sec. 3, the transmission is determined by the edge couplings which we again assume here to be equal, $\gamma_L = \gamma_R = \gamma$. Similarly to Ref. [103], the transmission coefficient (6.12)

can be written as

$$T^{RL}(E) = T^{LR}(E) = \left| \frac{(\gamma/v^2)(E-\Delta)}{\prod_{r=1}^{2N+2}[(E-\mathcal{E}_r)/v]} \right|^2 . \tag{7.21}$$

Below we show the transmission results for the chain of $N = 5$ (twelve intrinsic states) and various combinations of the parameters. The resulting picture is determined by the counterplay of the trend to super-radiation and decoupling of the qubit.

Starting with the weak qubit excitation amplitude, Fig. 7.13 for $\lambda = 0.1$, we follow the evolution of the transmission as a function of the continuum coupling γ. At small $\gamma = 0.1$, panel (a), we see twelve isolated resonances all having narrow decay widths; one of them is outside the energy band as we discussed earlier. When γ is growing, panels (b) and (c), the resonances start overlapping. When two super-radiant states merge at $\gamma = 2.4$, panel (c), they disappear from the transmission spectrum, so that panel (d) for $\gamma = 4$ shows ten separated resonances. At each resonance the transmission is perfect, $T = 1$.

Next four panels, Fig. 7.14, correspond to the intermediate value $\lambda = 2$. Again the case of weak continuum coupling, panel (a), $\gamma = 0.1$, reveals twelve resonances; now the two states associated with the qubit are outside the energy band, while all resonances still show perfect transmission. At $\gamma = \lambda = 2$, panel (b), the competition between the transmission through the chain and Rabi dynamics of the qubit leads to an almost random pattern of overlapping resonances with transmission below perfect, similarly to Ericson fluctuations [107] or universal conductance fluctuations [118]. The relation between those well known pictures and necessary changes due to the effects of unitarity in exact theory were discussed in Ref. [102]. At large $\gamma \gg \lambda$, panels (c) and (d), the continuum coupling prevails leading to the narrow resonances coming from trapped intrinsic states.

Finally, the large value of the qubit excitation strength, $\lambda = 5$, changes the transmission

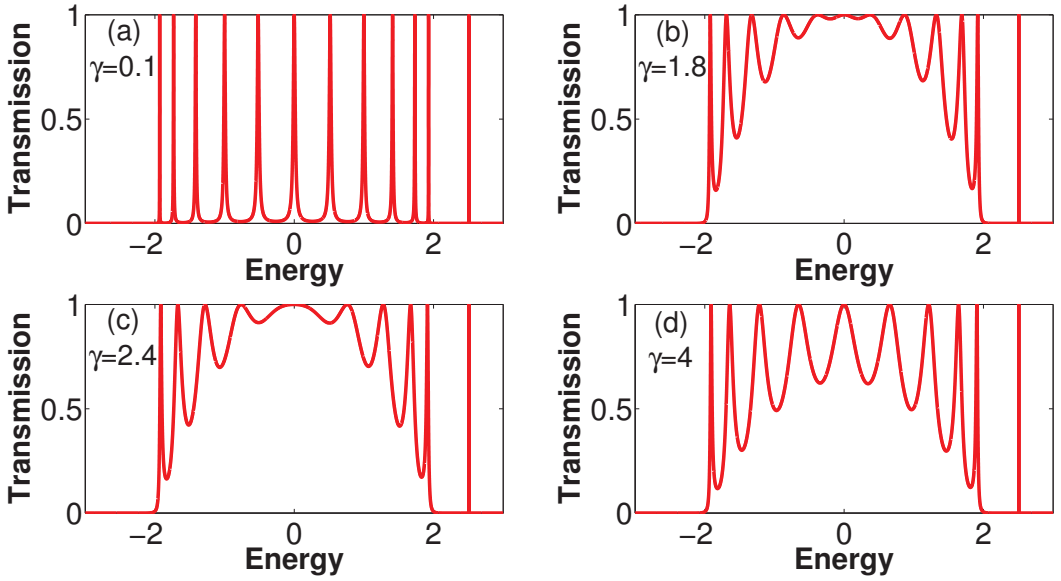

Figure 7.13: Evolution of the transmission for small $\lambda = 0.1$ as a function of the continuum coupling parameter $\gamma_L = \gamma_R = \gamma$, from 12 isolated resonances (one outside the energy band) through overlap and super-radiance to ten resonances corresponding to trapped states. As earlier, $\Delta = 2.5,\ v = 1$.

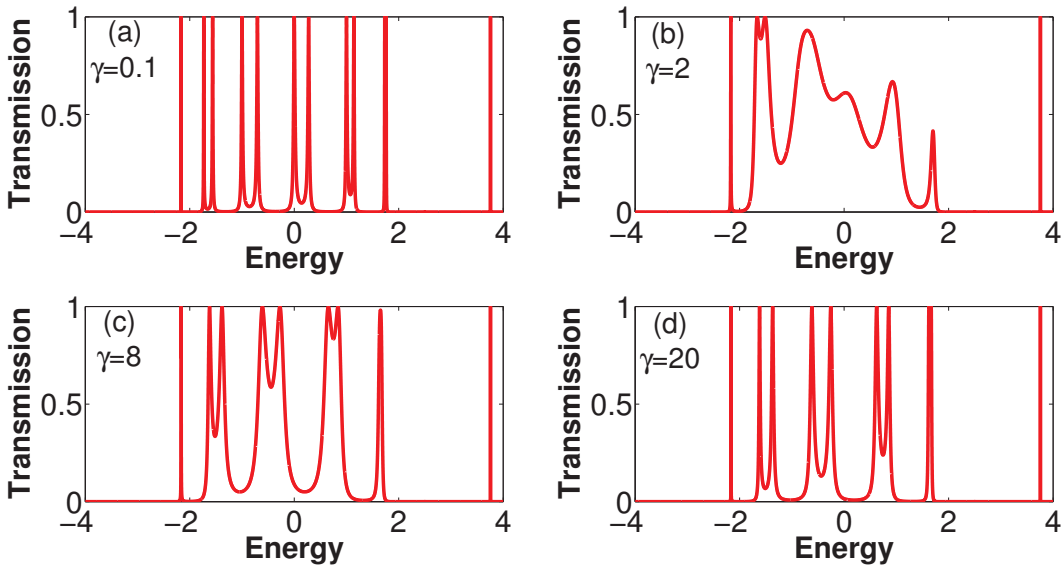

Figure 7.14: The same as Fig. 7.13, with $\lambda = 2$.

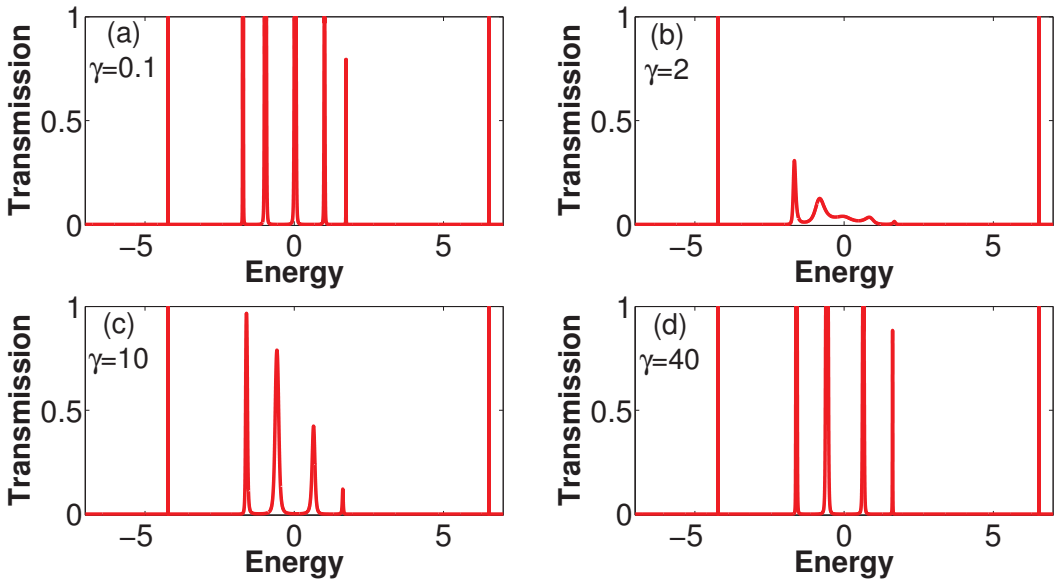

Figure 7.15: The same as Fig. 7.13, with $\lambda = 5$.

picture at not very large γ, Fig. 7.15. At small continuum coupling, $\gamma \ll \lambda$, panel (a), the two states associated with the qubit produce two resonances outside the band, with transmission equal to 1. At $\gamma = 2$, panel (b), we observe some kind of an intrinsic resonance between propagation and internal oscillations which, along with the emergence of superradiance, almost kills the transmission at other energies within the band. With further growth of γ, panels (c) and (d), the perfect transmission through trapped states, including those associated with the qubit, is gradually restored. This abundance of possible regimes opens the way to various applications.

At the conclusion of this section we show the transmission across the chain for the case when Δ is inside the band, Fig. 7.16, and for the case of large N, Fig. 7.17.

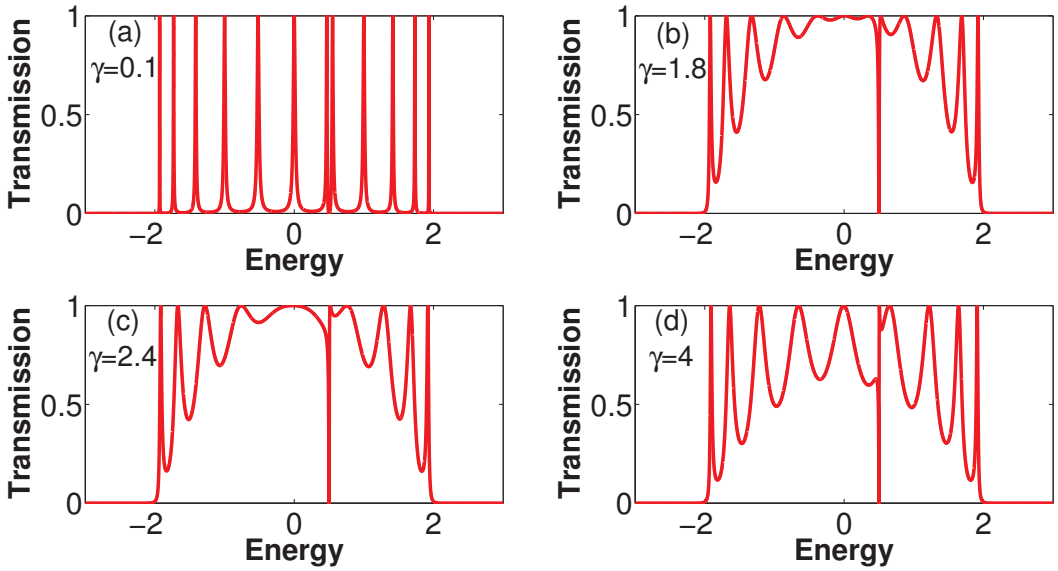

Figure 7.16: Transmission through the chain for $N = 5$, $\lambda = 0.1$, $\Delta = 0.5$ as function of continuum coupling γ

.

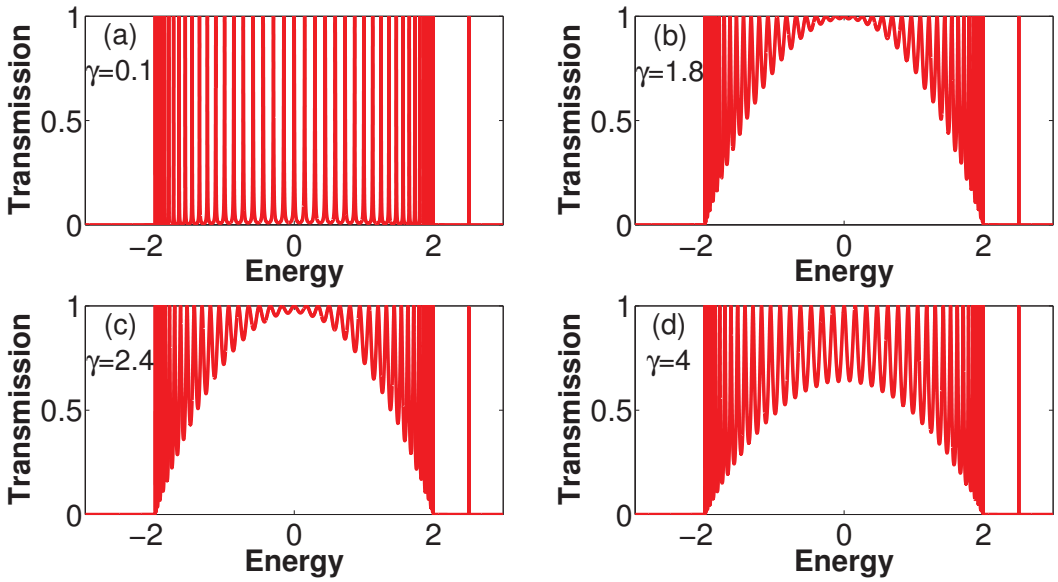

Figure 7.17: Transmission through the chain for $N = 20$, $\lambda = 0.1$, $\Delta = 2.5$ as function of continuum coupling γ

.

7.2.4 Discussion

Using the formalism of the effective non-Hermitian Hamiltonian, we studied a model of quantum signal transmission through a linear periodic chain with a qubit placed at the center. For the closed chain, the intrinsic eigenstates form two classes, antisymmetric that includes standing waves with the excluded center site and two independent subchains, and symmetric that reveals the qubit dynamics with two additional eigenstates. When the system is coupled to the environment at its entrance and exit points, we have found the spectrum of quasistationary states characterized by complex energies and finite lifetimes. Two of those states are genetically related to the ground and excited state of the qubit with real energy outside the Bloch band.

The most interesting feature is the stability of states related to the qubit, small decay widths and correspondingly long lifetimes. Further, these states are only weakly perturbed when the coupling of the chain to the continuum becomes strong. In the limit of strong coupling, the qubit states and remaining trapped Bloch states are practically shielded from the external world by the two superradiant states localized at the edges of the chain. The stability of the qubit states and the possibility to switch on and off the access to them suggests that the simple configuration considered above may serve as a building block of a quantum computer.

We discussed also the transmission through the chain as a function of the coupling strength to the continuum. In the limits of weak and strong continuum coupling (as compared to the excitation amplitude of the qubit) the chain reveals well separated narrow resonances with perfect transmission at corresponding energy. In the intermediate regime, when the continuum coupling and the excitation strength of the qubit are comparable, the

resonances overlap with the transmission below the perfect level.

There are many possibilities to enrich this prototypical model. For a realistic situation, for example a chain of quantum dots, one should carefully determine the lifetimes of the qubit states. The geometry of the system can be made more complicated in various ways including the transition to more-dimensional schemes. More qubits and more branches can be added approaching a complicated network. Another direction is to include electron-phonon interactions in order to consider vibrational effects [122]. It would be also interesting to extend the ideology of an open quantum system to the study of coherent photon transport in continuous waveguides [119] and circuit quantum electrodynamics [95, 120, 121].

7.3 Two-Channel Quantum Wire

In this section, we study superradiance and its effect on transport properties in a quantum wire with a different geometry: a one-dimensional chain of two level systems where the edges are coupled to the outside world presented by a continuum of channels. The two-channel wire has served as a model in [123] where superconductivity in ladder structures was studied and in [110] where a two-dimensional chain was coupled to an adatom. This specific system was not earlier analyzed from the viewpoint of superradiance.

The steps taken to attack this problem are in general similar to the previous section. First, we consider the isolated wire, a closed chain of N identical two-level cells with the nearest neighbor hopping interaction between the ground and excited states of neighboring cells. A closed form solution describes the two energy bands of the system. Several symmetries associated with the eigenvectors of the system are explained as well. Similar to the single qubit chain case, the system is then opened through the coupling of the left and right

edges of the chain to the continuum. As a result of the coupling the eigenenergies acquire an imaginary part. The evolution of the complex energies as a function of the coupling strength is studied in detail. The superradiance transition emerges as in the previous case. It is shown that the width is uniformly distributed at weak coupling. However, the picture changes at strong couplings: the states are not uniformly broadened. The superradiant states, their number being equal to the number of intrinsic doorway states directly coupled to the continuum, are greatly broadened while the remaining states acquire only small widths. Next, the transport properties of the system are studied. It is shown that the transition between the weak and the strong coupling regimes i.e. the superradiance transition, greatly influences the scattering properties of the system, particularly the transmission coefficient. Energy-dependent coupling to the continuum due to the presence of the decay threshold is considered as well. It is shown that superradiance plays a significant role, even when the energy levels are in proximity to their cutoff thresholds.

7.3.1 The Isolated Two-Channel Wire

The wire of the model consists of a periodic chain of N identical two-level cells. The energy levels of the ground state $|n, g\rangle$ and the excited state $|n, e\rangle$ of each cell are ϵ and $\epsilon + \Delta$, respectively. The matrix element for excitation between the ground and excited state of each cell is denoted λ, and the hopping amplitudes between the neighboring ground and excited states are v_1 and v_2, respectively. Fig. 7.18 shows a schematic of the system under study.

The Hamiltonian of the closed chain is

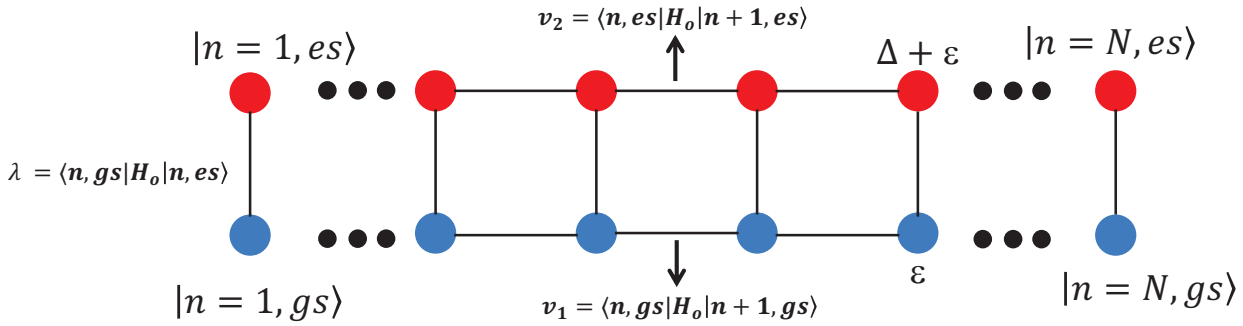

Figure 7.18: Schematic of the two-channel wire.

$$H_0 = \sum_{n=1}^{N} \Big\{ \frac{\epsilon}{2} |n,g\rangle \langle n,g| + \frac{\epsilon + \Delta}{2} |n,e\rangle \langle n,e| + \lambda |n,g\rangle \langle n,e| + v_1 |n,g\rangle \langle n-1,g| + v_2 |n,e\rangle \langle n-1,e| + h.c. \Big\}. \tag{7.22}$$

In order to diagonalize the Hamiltonian a stationary state with energy E is considered as a superposition of localized states,

$$|q\rangle = \sum_{n=1}^{N} \Big[a_n(E) |n,g\rangle + c_n(E) |n,e\rangle \Big]. \tag{7.23}$$

The Schrödinger equation with the Hamiltonian given in eq. (7.22) determines a set of two coupled linear recurrence equations for the amplitudes a_n and c_n:

$$(\epsilon + \Delta)c_n + \lambda a_n + v_2(c_{n-1} + c_{n+1}) = Ec_n, \quad n = 1, 2, .., N, \tag{7.24}$$

$$\epsilon a_n + \lambda c_n + v_1(a_{n-1} + a_{n+1}) = Ea_n, \quad n = 1, 2, .., N. \tag{7.25}$$

Ordinary decoupling of the equations would lead to a fifth order recurrence relation. However, the decoupled equations can be simplified with the realization of a symmetry resulting from the parallel ladder structure of the two-channel wire:

$$c_n = m(E)a_n. \tag{7.26}$$

Rewriting eq. (7.24) using eq. (7.26) results in a second order difference equation:

$$\left\{(\epsilon + \Delta) + \frac{\lambda}{m}\right\} c_n + v_2(c_{n-1} + c_{n+1}) = Ec_n. \tag{7.27}$$

The solution to this equation, after applying the boundary condition $c_{n=0} = c_{n=N+1} = 0$, is a standing wave with the quasimomentum q,

$$c_n = A(-1)^n \sin(n\phi_q), \quad \phi_q = \frac{\pi q}{N+1}. \tag{7.28}$$

One can find the energy levels of the system using eqs. (7.26), (7.28), and the original set of the two recurrence relations. The eigenenergies are solutions to the following quadratic equation:

$$(\epsilon + \Delta) + \frac{\lambda^2}{E - \epsilon + 2v_1 \cos\phi_q} - 2v_2 \cos\phi_q = E. \tag{7.29}$$

Hence the energy levels are

$$E_q^{\pm} = \frac{1}{2}\Big[-\alpha_q \pm \sqrt{\alpha_q^2 - 4\beta_q}\Big],$$
$$\alpha_q = 2v_1\cos\phi_q - \epsilon + 2v_2\cos\phi_q - (\epsilon+\Delta),$$
$$\beta_q = -2\epsilon v_2\cos\phi_q + 4v_1v_2\cos^2\phi_q$$
$$-\lambda^2 + (\epsilon+\Delta)(\epsilon - 2v_1\cos\phi_q). \tag{7.30}$$

The coefficient $m(E)$ is found simultaneously:

$$m_q^{\pm}(E) = \frac{E_q^{\pm} - \epsilon + 2v_1\cos\phi_q}{\lambda}. \tag{7.31}$$

Finally, the normalization of the eigenvectors results in

$$c_n^{q,\pm}(E) = (-1)^n\sqrt{\tfrac{2}{N+1}}\,\frac{m_q^{\pm}}{\sqrt{1+(m_q^{\pm})^2}}\sin(n\phi_q),$$
$$a_n^{q,\pm}(E) = \frac{c_n^{q,\pm}(E)}{m_q^{\pm}}, \quad q = 1, 2, ..., N. \tag{7.32}$$

Similar to the single-qubit wire case, the eigenvectors can be classified into two categories: symmetric and anti-symmetric states with respect to the center of the wire. From the equation for the energy levels, eq. (7.29), it is easy to establish an extra symmetry associated with the eigenvectors,

$$E_q^+E_q^- - (\epsilon + 2v_1\cos\phi_q)(E_q^+ + E_q^-) + (\epsilon + 2v_1\cos\phi_q)^2 = -\lambda^2, \tag{7.33}$$

and use eq. (7.33) to show that

$$\frac{|m_q^-|}{\sqrt{1+(m_q^-)^2}} = \frac{1}{\sqrt{1+(m_q^+)^2}}. \tag{7.34}$$

As a result, for a fixed state q,

$$|c_n^{q,\pm}| = |a_n^{q,\mp}|, \quad n = 1, 2, ..., N. \tag{7.35}$$

Fig. 7.19 shows the energy levels of the two bands as functions of the coupling between the ground and the excited states (λ) for a system with $N = 5$. As expected, the energy plot is similar to a typical semiconductor band structure; the bands repel each other when the excitation amplitude λ grows.

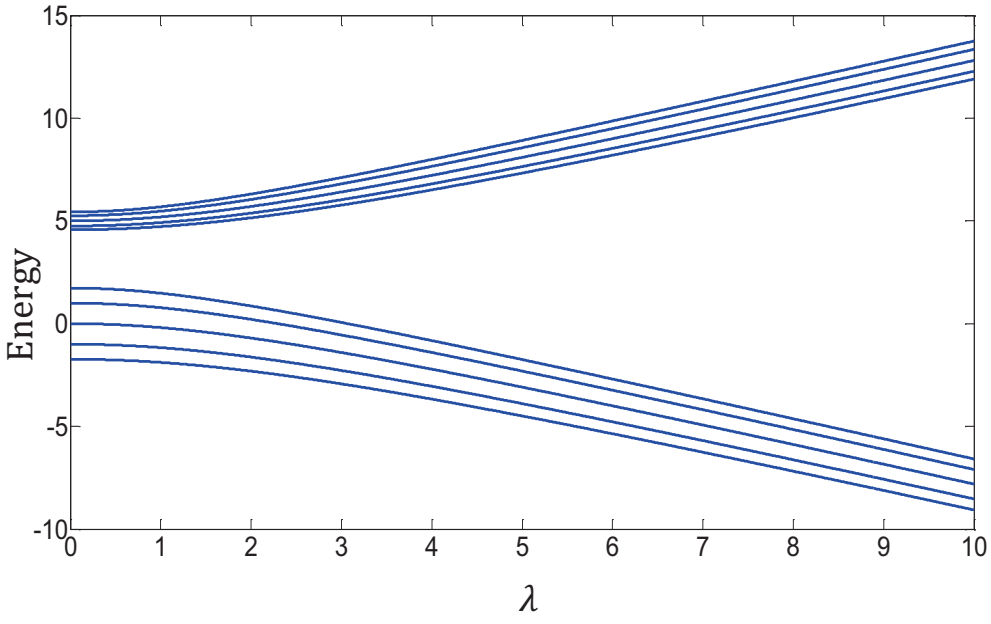

Figure 7.19: Energy levels of a two-band wire as a function of the coupling between the ground and excited states of each cell, the parameters of the wire are: $N = 5, \epsilon = 0, \Delta = 5, v_1 = 1$ and $v_2 = 2$.

7.3.2 Coupling to the Continuum and Superradiance

Now we open the system coupling the excited states at the edges to the ideal leads which are characterized by a continuum of states. This situation can be described by the effective Hamiltonian (6.8).

We assume that the left, $|n=1,e\rangle$, and the right, $|n=N,e\rangle$, edge state are each coupled to one channel in the continuum. Correspondingly, the squares of the coupling amplitudes determine the partial widths γ^L and γ^R of the left and right edge states decoupled from the chain,

$$\begin{aligned} A^{c=\text{left}}_{n=1,e} &= \sqrt{\gamma^L}, \\ A^{c=\text{right}}_{n=N,e} &= \sqrt{\gamma^R}. \end{aligned} \tag{7.36}$$

In the basis of unperturbed chain states, the operator W has only two matrix elements,

$$W_{|n=1,e\rangle,|n=1,e\rangle} = \gamma^L, \quad W_{|n=N,e\rangle,|n=N,e\rangle} = \gamma^R. \tag{7.37}$$

In order to diagonalize the effective Hamiltonian, W is transformed into the eigenvector basis of the closed system, $|q,\pm\rangle$.

$$W_{|q,\pm\rangle,|q',\pm\rangle} = \gamma^L c^{q,\pm}_{n=1} c^{q',\pm}_{n=1} + \gamma^R c^{q,\pm}_{n=N} c^{q',\pm}_{n=N}, \tag{7.38}$$

where $c^{q,\pm}_n$ are given in eq. (7.32). The effective Hamiltonian can now be diagonalized which

leads to the following secular equation for the complex energies ε:

$$\Omega(\varepsilon) \equiv 1 + iP_+(\varepsilon)(\gamma^L + \gamma^R) + \gamma^L\gamma^R(P_-^2(\varepsilon) - P_+^2(\varepsilon)) = 0, \tag{7.39}$$

where $P_+(\varepsilon)$ and $P_-(\varepsilon)$ are defined as

$$P_+(\varepsilon) = \frac{1}{N+1}\sum_{q,\pm}(1)^q \frac{\sin^2\phi_q m_q^{\pm}}{(\varepsilon - E_q^{\pm})(1 + (m_q^{\pm})^2)}$$

and

$$P_-(\varepsilon) = \frac{1}{N+1}\sum_{q,\pm}(-1)^q \frac{\sin^2\phi_q m_q^{\pm}}{(\varepsilon - E_q^{\pm})(1 + (m_q^{\pm})^2)}.$$

Fig. 7.20 shows the resonance complex energies $E - (i/2)\Gamma$ of our system with N=5, when the two ends are symmetrically coupled to the continuum, $\gamma^L = \gamma^R = \gamma$. At weak coupling, when γ=0.1, all eigenenergies gain small decay width Γ due to interaction with the environment. Further increase of γ initially results in the increase of the decay widths for all resonances as illustrated in the upper right panel (γ = 1). The complex pole dynamics changes at larger values of γ (see [93] and references therein). At a critical point, when $\gamma/D \simeq$1, where D is the mean level spacing of the energy levels of H_0, the system undergoes a superradiance transition. Beyond this point the decay widths do not monotonically increase with the increase of γ. In fact, only some states (superradiant) continue to increase their decay widths while the remaining states become long-lived (trapped) states. This phenomenon is illustrated in the lower left panel of Fig. 7.20, where γ=10 and the two super-radiant states, in accordance with the number of open channels, have obtained larger decay widths compared to the other states. The picture remains similar at larger γ.

At γ=20, the lower right panel, the two overlapping super-radiant states are shown in the smaller window. Note that the number of superradiant states is always equal to the number of continuum channels coupled to the wire; it is also important to notice the different vertical scales on these panels.

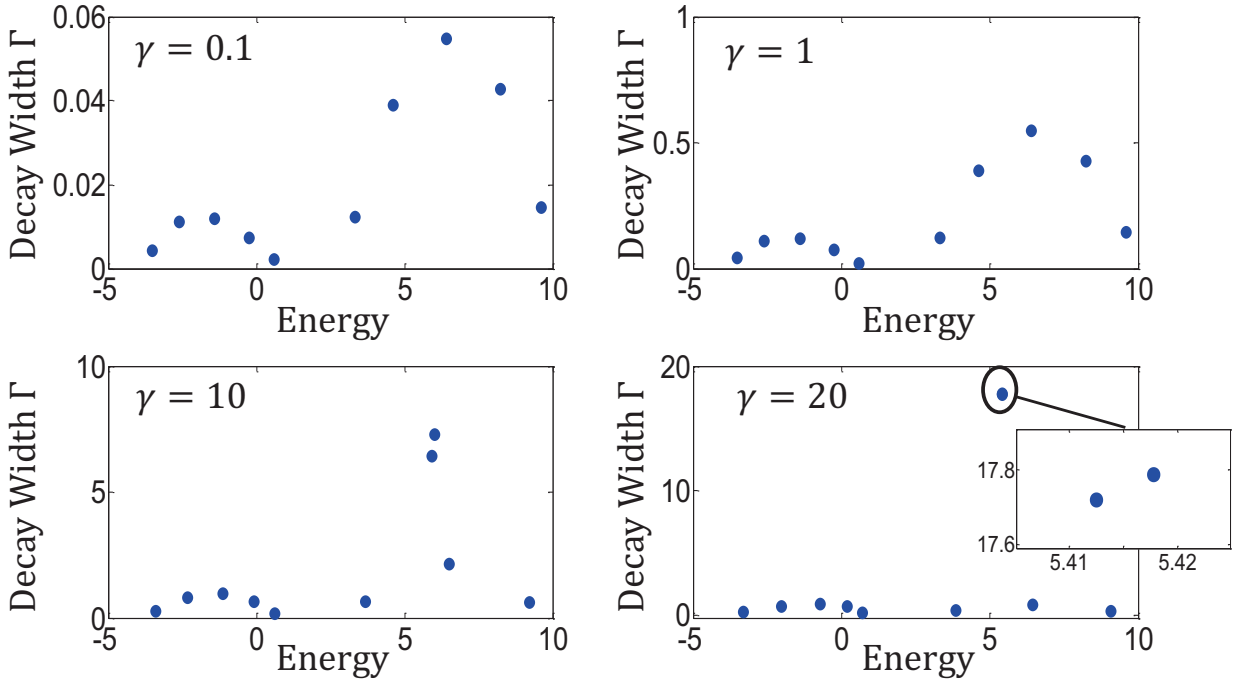

Figure 7.20: Complex eigenenergies for different values of the coupling strength to the continuum, γ. The parameters of the wire are: $N = 5, \epsilon = 0, \Delta = 5, \lambda = 3, v_1 = 1$ and $v_2 = 2$.

It is instructive to consider the evolution of the resonances in the complex plane as γ increases. This is depicted in Fig. 7.21.

7.3.3 Transmission Through The Wire

Scattering properties of the two-channel quantum wire, in particular transmission of a signal through the wire at weak, intermediate and strong coupling regimes, are considered in this section. This concerns the features which could be the most significant for any practical

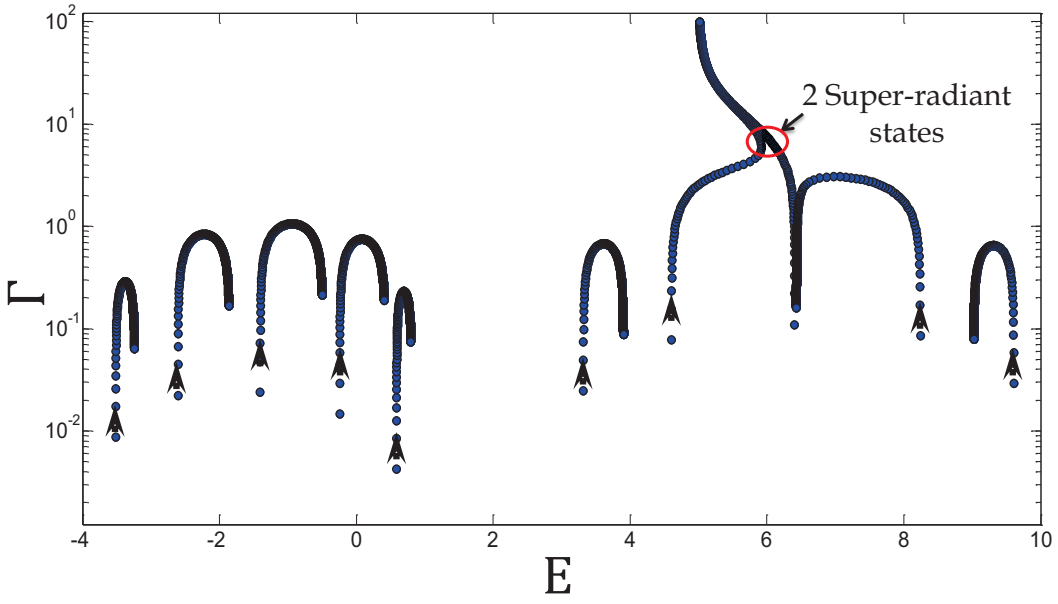

Figure 7.21: Evolution of the energies in the complex plane. Up to the critical point all the decay widths increase as γ increases. A superradiant transition occurs as γ exceeds the critical value. After passing the critical point, the decay width of the two superradiant states increases with the increase of γ, whereas the decay width of the other eight states decreases. The parameters of the wire are similar to the one in Fig . 7.20. The arrows show the direction of the evolution as γ varies from 0 to 100.

application.

The transmission coefficient is calculated according to eqn. (6.12). Of course, one can also look at the reflection channels; the reflectivity coefficient is $R = 1 - T$, since the form of the anti-Hermitian part (6.6) preserves the unitarity of the scattering matrix. the transmission coefficient $T^{L\leftrightarrow R}(E)$ is depicted for different values of γ, Fig. 7.22. At small γ, the perfect transmission, $T = 1$, occurs at narrow resonances. With increasing the coupling, the resonances broaden and start to overlap. At the super-radiance transition, the maximum transmission is achieved as a result of the broadening of the states, the case of γ=4. With further increase of γ there are only three resonances left in the upper band, the two super-radiant states are out of the picture since they are extremely broaden (γ=100). Note that the resonances become narrow as the trapped states lose their widths.

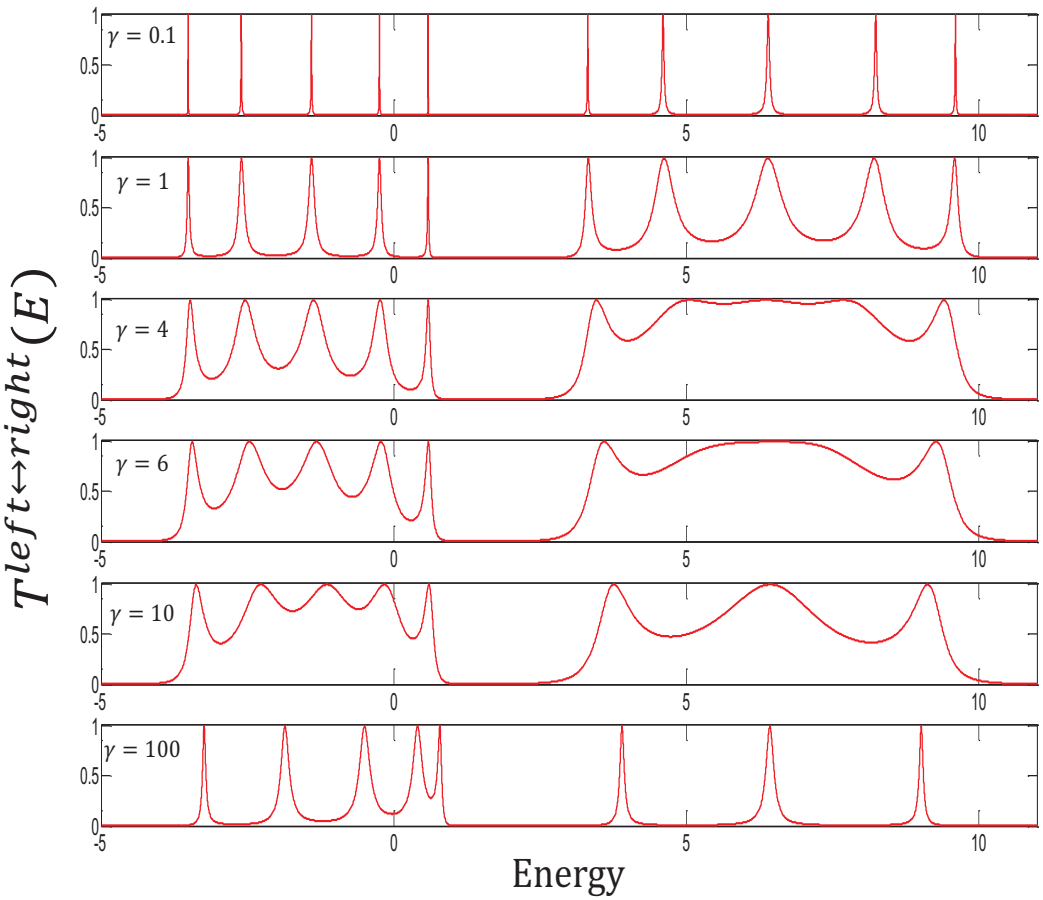

Figure 7.22: Transmission through the two-channel wire for different values of γ. The parameters of the wire are similar to those in Fig . 7.20.

7.3.4 Energy-Dependent Coupling

In previous sections it was assumed that the matrix elements of the effective Hamiltonian do not depend on the running energy E. The energy dependence appeared only due to the resonance denominators. Here we briefly address a more realistic situation with energy-dependent coupling to the continuum. This dependence arises inevitably when the energy of an experiment is in the proximity of thresholds of the continuum channels (separation energy in nuclei or the work function in solids). As a result, one should consider the energy dependency of the coupling amplitudes. When a simple case of the s-wave form dependence

is considered, the coupling amplitudes can be taken as

$$A^L_{n=1,e}(E) = \alpha^L \Theta(E - E^L_c)\sqrt{E - E^L_c}$$
$$A^R_{n=N,e}(E) = \alpha^R \Theta(E - E^R_c)\sqrt{E - E^R_c}, \tag{7.40}$$

where α^L and α^R are the strengths of the coupling to the left and to the right edge, respectively. In general these coefficients could be different; similar to the previous section we assume a symmetric coupling to the continuum, hence $\alpha^L = \alpha^R = \alpha$. E^L_c and E^R_c are the cutoff energies of the continuum coupling also assumed to be the same, E_c, for both channels. Θ is the step function, which guarantees that the system is decoupled from the environment at energy below threshold.

Fig. 7.23 shows the complex energies of the same system when the cutoff threshold E_c is approximately located in between the two bands of the isolated wire. Note that the superradiant transition still occurs as the coupling strength α increases. The four states with energy below threshold do not acquire any width being decoupled from the environment. The four trapped states above threshold initially gain width as α increases, however, beyond the superradiant transition, when α=2, they become long-lived states. On the lower right panel the two overlapping super-radiant states with the large decay width are shown in a smaller window.

In Fig. 7.24 we show the transmission coefficients for different values of the strength coupling α. It is clear that the states below threshold do not participate in the transport of the signal. Similar to the energy-independent case, Fig. 7.22, the transmission increases in the super-radiant transition when the resonances start overlapping.

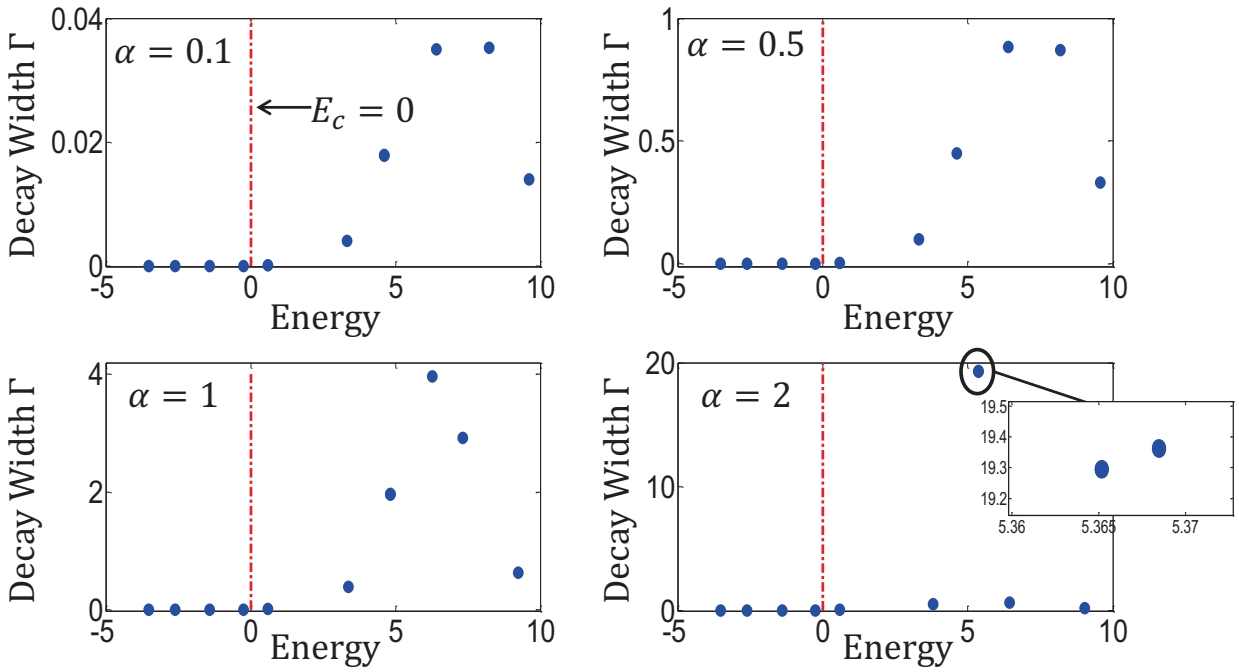

Figure 7.23: Complex energies in the case of energy-dependent couplings for different values of the coupling strength, α. The cutoff threshold is shown with a vertical line, E_c=0. The wire parameters are the same as in Fig . 7.20.

7.3.5 Discussion

The effective non-Hermitian Hamiltonian was used to study an open quantum wire of two-level atoms. The dynamics of the states when the wire is coupled to the continuum undergo dramatic change as the strength of the coupling to the continuum varies crossing the super-radiant segregation point separating the broad (short-lived) states from long-lived (trapped) states. It was demonstrated that the width distribution of the states significantly alters transport properties of the wire. Maximum transmission is achieved at the super-radiance transition. The future studies should include the practically important current-voltage characteristic of a quantum wire in different coupling regimes. This can be done considering the wire connected with reservoirs of electrons with different changeable chemical potentials.

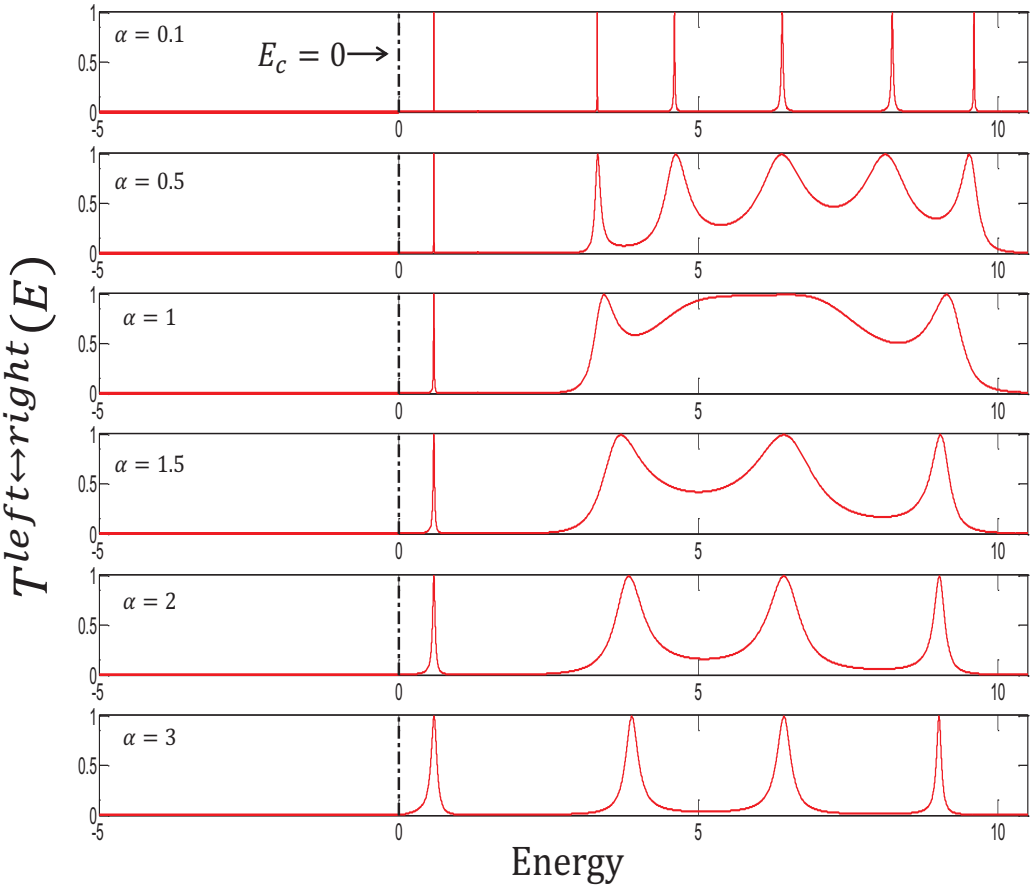

Figure 7.24: Transmission through the two-channel wire with energy-dependent couplings for different values of the coupling strength, α. The cutoff threshold located between the two bands is shown with a red vertical line, E_c=0. The wire parameters are the same as in Fig. 7.20.

Nanotechnology will let us build computers that are incredibly powerful. We'll have more power in the volume of a sugar cube than exists in the entire world today.

Ralph Merkle

Chapter 8

Solid State Quantum Computing

8.1 Introduction

Despite great theoretical advances in the field of quantum information, the best system to realize the underlying physical layer of quantum computers is still a matter of debate. The problem arises with the most fundamental element of the quantum computer, a single qubit. Ideally, error-free qubits are desired due to the fact that unknown quantum states cannot be replicated without loss of information, a consequence of the so-called no-cloning theorem. Even with advances in error correcting codes and fault-tolerant quantum computing, we still require qubits which are inherently resistive to noise and decoherence and therefore have long life and coherence times capable of outlasting gate operation timespans.

Over the past two decades, many systems have been proposed for the physical implementation of a qubit. Some examples are photonic qubits in optical quantum computers [124, 125], collective spin states in nuclear magnetic resonance (NMR) systems [126–128],

electronic states in trapped ions [129–131], charge, flux or phase qubits in superconducting circuits [132–135], electronic states on the surface of superfluid helium [136, 137] and electronic charge or spin in solid state systems [138–140]. For a comprehensive review and discussion of advantages and disadvantages of various qubit implementations see [142].

Recently, solid-state based quantum components have sparked great interest, mainly due to their scalability. In addition, the accumulated knowledge in nano-circuit fabrication, along with existing infrastructure, can be combined to more easily realize nano-scale integrated quantum computers [141].

In any physical implementation, it is critical to consider not only the system of interest but also the constituents that the system interacts with once placed in a greater final design. In the case of solid-state based quantum computing systems, the qubits interact with devices for writing and reading information in and out, such as leads and charge detectors. These devices can be modeled as a continuum due to the large density of states they possess. Consequently, one has to deal with an *open* mesoscopic quantum system where the intrinsic states are coupled to the external world through a number of channels. Similarly to a nuclear or molecular reaction, each channel is characterized by the energy of the final states and their quantum numbers. The channels have energy thresholds when the coupling opens connecting the system to the environment. Such situations require a correct unified treatment of the discrete bound states and the continuum.

As demonstrated earlier, a convenient framework for such problems is given by the effective non-Hermitian Hamiltonian approach introduced by Feshbach [91]. The description is non-perturbative and formally exact, treating the dynamics of systems with weak, intermediate and strong couplings to the environment on equal footing. This framework is quite flexible and can be adjusted to various types of problems ranging from nuclear reactions [99, 145] to

electronic transport in mesoscopic physics [108, 146] and quantum optics [147]. An overview of the approach and some of its results can be found in [93]. To stress the large spectrum of applications using this approach we note its utilization in plasmonic antenna arrays [95] and biological light harvesting complexes [96].

Earlier in Chapter 7, a simple system of a quantum wire with a two-level atom (qubit) inserted in the middle was considered using the effective Hamiltonian [148]. The qubit was used to regulate transport in the wire. In fact, insertion of qubits in various systems was found to be useful in different applications. For instance, in [149], a charge detector is proposed consisting of a qubit attached to a quantum wire. In this section we consider a similar system; a quantum wire with two embedded qubits which, as a whole, behave like a single qubit.

We first introduce a *closed* one-dimensional chain of $2N$ identical sites with hoping between adjacent cells. The center of the chain is occupied by an *asynchronized* pair of two-level atoms: the couplings between the ground states and excited states of the two qubits are inversely proportional. The band structure of the system consists of delocalized states extended over the chain and additional states outside the Bloch band confined to the central qubits. Depending on the coupling strengths within the qubits, the states inside the band are localized in the left arm, the right arm, or evenly distributed across the entire chain. Consequently the system acts as a *distributed* charge qubit with collective right and left states.

Next the *open* system with the edge sites coupled to the continuum is considered. The continuum represents ideal leads or charge detectors attached to the edges. Due to the interaction with the leads the energy states acquire decay widths influenced by the continuum coupling in a non-trivial manner. At sufficiently strong coupling, protective superradiant

edge states are formed. These states steal the entire width and hence prevent the remaining states from decaying into the environment.

Finally, we perform a numerical study on the effect of noise and investigate the phenomenon of decoherence. The noise in the environment is modeled by a random Gaussian process. The situation is described by the stochastic Liouville equation that determines the evolution of the density matrix. It is shown that the formation of superradiant states can maximize the coherence time of the distributed qubit system.

8.2 Closed System

The proposed system consists of a nano-wire with a pair of two-level atoms embedded at its center. The wire is considered to be a one-dimensional chain of $2N$ identical sites numbered as $n = -N, -(N-1), ..., -1$ and $n = 1, ..., N-1, N$. The chain is modeled by a tight-binding Hamiltonian with coupling between adjacent neighbors:

$$H_{\mathrm{W}} = \sum_{\substack{n=-N \\ n\neq 0}}^{N} \epsilon_0 c_n^\dagger c_n + \sum_{n,n'} \nu\big(c_n^\dagger c_{n'} + c_{n'}^\dagger c_n\big), \tag{8.1}$$

where ϵ_0 is the on-site energy, ν is the hopping integral, and $c_n^\dagger$ and c_n are creation and annihilation operators at site $|n\rangle$, respectively. The typical value for ν is within the range of 1-100 μeV in quantum dot systems [140, 143, 144]. The second sum in the Hamiltonian (8.1) runs over the nearest neighboring cells only.

Two asynchronized qubits are symmetrically connected to the center of the wire. The left

qubit with excited state $|e_L\rangle$ and energy level δ_L is connected to site $|-1\rangle$ with Hamiltonian

$$H_Q^L = \delta_L c_L^\dagger c_L + \lambda\big(c_L^\dagger c_{-1} + c_{-1}^\dagger c_L\big), \tag{8.2}$$

where λ is the matrix element of the qubit excitation and $c_L^\dagger$ and c_L are creation and annihilation operators for the left qubit excited state, respectively. Similarly, the right qubit with excited state $|e_R\rangle$ and energy level δ_R is connected to site $|1\rangle$

$$H_Q^R = \delta_R c_R^\dagger c_R + \frac{\kappa}{\lambda}\big(c_R^\dagger c_1 + c_1^\dagger c_R\big). \tag{8.3}$$

Here, $c_R^\dagger$ and c_R create and annihilate an excitation in the qubit upper level, respectively. κ/λ is the coupling strength between the ground and excited states of the two-level atom. The left and right qubits are fully asynchronized, i.e. at strong coupling between the excited and ground states of the left qubit, the two states of the right qubit are weakly coupled and vice versa; κ is the asynchronization parameter. In practice this parameter can be tuned by introducing a local electric field and adjusting the field strength [150, 151].

The total Hamiltonian of the closed system is the sum

$$H_0 = H_{\mathrm{W}} + H_L^Q + H_R^Q. \tag{8.4}$$

A generic stationary wave function of the system with energy E is represented as

$$|\psi(E)\rangle = \sum_{\substack{n=-N \\ n\neq 0}}^{N} a_n(E)\,|n\rangle + b_L(E)\,|e_L\rangle + b_R(E)\,|e_R\rangle\,. \tag{8.5}$$

In order to fulfill the Schrödinger equation, the coefficients of the superposition in (8.5)

satisfy the linear three-term recurrence relation

$$(E-\epsilon_0)a_n-\nu(a_{n-1}+a_{n+1})=0, \qquad n\neq 0,\pm 1. \tag{8.6}$$

The discontinuities at ± 1 are due to the inserted qubits in the center. This naturally divides the chain into two regions, left and right. The solutions in the two sides of the chain are given by

$$a_n=\begin{cases} a_n^L=A_L\zeta_+^n+B_L\zeta_-^n, & -N\leq n<-1,\\ a_n^R=A_R\zeta_+^n+B_R\zeta_-^n, & 1<n\leq N, \end{cases} \tag{8.7}$$

where $\zeta_\pm$ are the roots of the characteristic polynomial of the recurrence relation,

$$\zeta_\pm=\frac{1}{2\nu}\Big[E-\epsilon_0\pm\sqrt{(E-\epsilon_0)^2-4\nu^2}\Big], \tag{8.8}$$

with the obvious property $\zeta_+\zeta_-=1$. The remaining equations resulting from solving the Schrödinger equation can be used as a boundary condition to connect the two regions in (8.7) in order to find the constants A_L, A_R, B_L and B_R. At $n=\pm 1$ we have

$$(E-\epsilon_0)a_{-1}-\nu(a_{-2}+a_1)=\lambda b_L, \tag{8.9}$$

$$(E-\epsilon_0)a_1-\nu(a_2+a_{-1})=\frac{\kappa}{\lambda}b_R, \tag{8.10}$$

$$(E-\delta_L)b_L=\lambda a_{-1}, \tag{8.11}$$

$$(E-\delta_R)b_R=\frac{\kappa}{\lambda}a_1. \tag{8.12}$$

For two important cases, the solution can be analytically obtained assuming, for simplic-

ity, that $\delta_L = \delta_R = \delta$. In the first case, when $\lambda \to 0$, the system supports states that are either fully localized in the right side or in the left side of the chain. In the second case we consider $\lambda^2 = \kappa$, where the excitation is equally distributed between the left and the right sides of the chain. The system is analogous to a qubit where the two states are extended over the entire left or right side of the wire, with λ serving as the coupling parameter, regulating the population in each side and enabling us to perform gate operations. In accordance, we adopt a special notation throughout the section. The stationary state (8.5) is denoted as

$$|\psi(E)\rangle = |L_\lambda(E)\rangle + |R_\lambda(E)\rangle\,, \tag{8.13}$$

where $|L_\lambda(E)\rangle$ contains the components of the wave function in the left side of the chain,

$$|L_\lambda(E)\rangle = \sum_{n=-N}^{-1} a_n^L(E)\,|n\rangle + b_L(E)\,|e_L\rangle\,, \tag{8.14}$$

while $|R_\lambda(E)\rangle$ contains the components in the right side,

$$|R_\lambda(E)\rangle = \sum_{n=1}^{N} a_n^R(E)\,|n\rangle + b_R(E)\,|e_R\rangle\,. \tag{8.15}$$

The subscript λ indicates that the left and right states are changed as λ takes different values.

8.2.1 Case $\lambda \to 0$

In the limit of very weak coupling between the two states in the left qubit, $\lambda \to 0$, the eigenstates of the system fall into two categories: states that are confined in the two central qubits and Bloch waves fully localized in the right or the left side of the chain. Since the

left qubit is decoupled from the chain, there exists a state with the only non-vanishing wave function component $b_L = 1$ and energy $E = \delta$. The right qubit states can be found using eqs. (8.10) and (8.12). The two states have energies

$$E = -\frac{\kappa}{\lambda} + \frac{1}{2}(\epsilon_0 + \delta) \text{ and } E = \frac{\kappa}{\lambda} + \frac{1}{2}(\epsilon_0 + \delta), \tag{8.16}$$

corresponding to eigenstates $a_1 = -b_R = 1/\sqrt{2}$ and $a_1 = b_R = 1/\sqrt{2}$, respectively.

The states of the second type are distributed over the wire, localized either in the left side between the sites $|-N\rangle$ and $|-1\rangle$, or in the right side between $|1\rangle$ and $|N\rangle$. According to (8.12), since $\kappa/\lambda_c \to \infty$, we have $a_1^R = 0$. This breaks the symmetrical structure of the wire, creating a longer chain on the left and leaving the right chain shorter, which is the key point in realizing a qubit structure using the proposed system. For the states in the left side (only $a_n^L \neq 0$), applying the boundary conditions $a_1^R = 0$ and $a_{-N-1}^L = 0$ to (8.7) provides an equation for energies, $\zeta_-^{2N+2} = 1$. Thus the energies can be parameterized by a positive even number, the quantized quasi-momentum k,

$$E_k^L = \epsilon_0 + 2\nu\cos\varphi_k^L, \quad \varphi_k^L = \frac{\pi k}{2N+2}, \quad k \text{ even}, \tag{8.17}$$

and the corresponding amplitudes (8.7) are of the Bloch-wave type,

$$a_n^L(k) = i^k\sqrt{\frac{2}{N+1}}\sin(n\varphi_k^L). \tag{8.18}$$

In what follows, according to (8.13), these states are denoted as $|L_0(E)\rangle$.

Similarly, for the states in the right side of the wire (only $a_n^R \neq 0$) with boundary

conditions $a_1^R = 0$ and $a_{N+1}^R = 0$ we have $\zeta_+^{2N} = 1$. Thus

$$E_k^R = \epsilon_0 + 2\nu \cos\varphi_k^R, \quad \varphi_k^R = \frac{\pi k}{2N}, \quad k \text{ even}, \tag{8.19}$$

with eigenfunctions

$$a_n^R(k) = i^k \sqrt{\frac{2}{N}} \sin(n\varphi_k^R). \tag{8.20}$$

These states are denoted as $|R_0(E)\rangle$.

As k varies, the energy states (8.17) and (8.19) consecutively alternate and come in pairs. In each pair, the higher energy state is extended in the left side and the lower level in the right side, being associated with wave functions $|L_0\rangle$ and $|R_0\rangle$, respectively. Clearly, in the extreme limit of $\lambda \to \infty$ we have the reverse situation. Since $a_{-1}^L = 0$, the right chain becomes longer and the upper energy state in each pair is localized in the right side of the chain and therefore can be denoted as $|R_\infty\rangle$. Consequently, the lower energy state is localized on the left which is indicated by $|L_\infty\rangle$.

8.2.2 Case $\lambda^2 = \kappa$

For finite values of λ the two sides of the chain are not decoupled and states are extended over the entire chain. The parameter λ therefore acts as a knob to control the population in the left and right regions. We now consider a special case of $\lambda^2 = \kappa$ where the population is equally divided between the two sides of the wire. Due to symmetry, there exist two types of eigenfunctions: fully symmetric states with $a_n^L = a_n^R$ and anti-symmetric states with $a_n^L = -a_n^R$. Using eqs. (8.9) and (8.11) or eqs. (8.10) and (8.12) we obtain an equation

for the energies,

$$\frac{\sin\left[(N+1)\phi\right]}{\sin(N\phi)} = \pm 1 + \frac{\kappa}{\nu(E-\delta)}, \tag{8.21}$$

where $\sin\phi = (1/2\nu)\sqrt{(E-\epsilon_0)^2 - 4\nu^2}$, with the positive (negative) sign corresponding to symmetric (anti-symmetric) states. Analogous to an equal superposition of the two states in a qubit, we denote the symmetric and anti-symmetric states as $(1/\sqrt{2})(|L_{\sqrt{\kappa}}\rangle + |R_{\sqrt{\kappa}}\rangle)$ and $(1/\sqrt{2})(|L_{\sqrt{\kappa}}\rangle - |R_{\sqrt{\kappa}}\rangle)$, respectively. The evolution with varying λ from zero to infinity and controlling the state of the qubit is graphically shown in Fig. 8.1 using the Bloch sphere. Assuming that at $\lambda = 0$ the state is localized on the left, $|L_0\rangle$, a 90° rotation ($\pi/2$ pulse) is performed by adiabatically moving λ to $\lambda = \sqrt{\kappa}$. Further increasing λ to extreme values localizes the particle in the right side of the chain, $|R_\infty\rangle$.

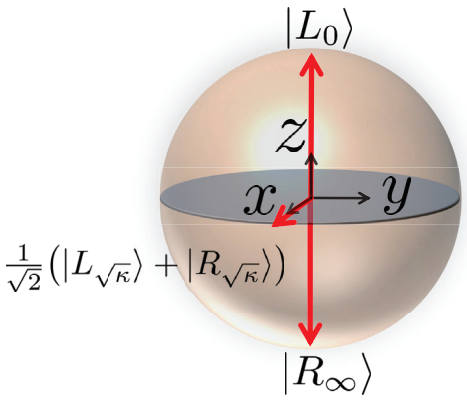

Figure 8.1: Graphical presentation of qubit rotation on the Bloch sphere. Gate operations can be performed by varying the value of λ. The initial state at $\lambda = 0$ is localized in the left side, $|L_0\rangle$. At $\lambda = \sqrt{\kappa}$ the state is 90° rotated becoming an equal superposition of the left and right states. When $\lambda \to \infty$, the state becomes localized on the right.

The complete band structure as a function of λ is shown in Fig. 8.2(a). The parameters of the system are $N = 10$, $\epsilon_0 = 0$, $\nu = 1$, $\delta = 2.5$ and $\kappa = 4$ (for the remainder of the section, ϵ_0 is set to zero and the scale is fixed by setting $\nu = 1$). The black curves correspond to states localized in the central qubits and the red curves are pairs of extended states over

the wire. Fig. 8.2(b) shows pair I in a smaller energy scale. It is clear that any rotation on the Bloch sphere can be performed by varying λ. The arrow indicates the avoided crossing point, when $\lambda = \sqrt{\kappa}$. The difference between two consecutive energy solutions of eq. (8.21) is the Rabi frequency, Ω, at which the population oscillates between the left and right sides of the chain.

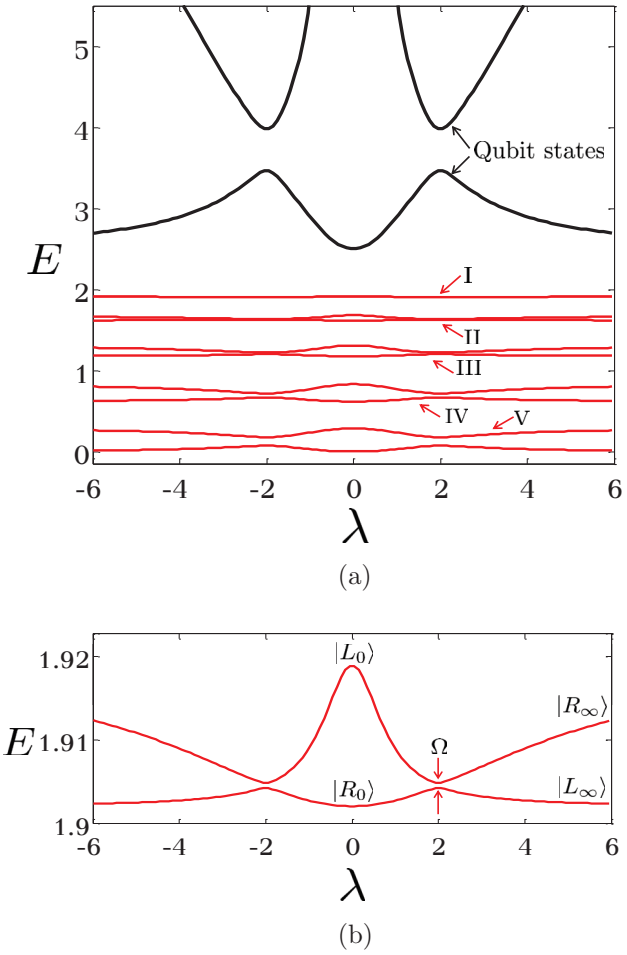

Figure 8.2: (a) Upper half of the band structure as a function of λ for a system with $N = 10$, $\epsilon_0 = 0$, $t = 1$, $\delta = 2.5$ and $\kappa = 4$. The black curves correspond to states localized in the central qubits and the red curves are pairs of Bloch waves. (b) A closer view of pair I as a function of λ.

The squared components of the wave function (8.5) of the upper and lower states in pair I as a function of λ are shown in Fig. 8.3. The figure only considers the components in the

chain and not those of the excited states of the central qubits (a_n's in the wave function (8.5)). At $\lambda = 0$ the upper and lower states are fully localized in the left and right sides, respectively. At $\lambda = \sqrt{\kappa} = 2$, both upper and lower states are in equal superpositions. As λ increases, the upper state quickly becomes localized in the right side. Similarly, the lower state develops into a localized state in the left.

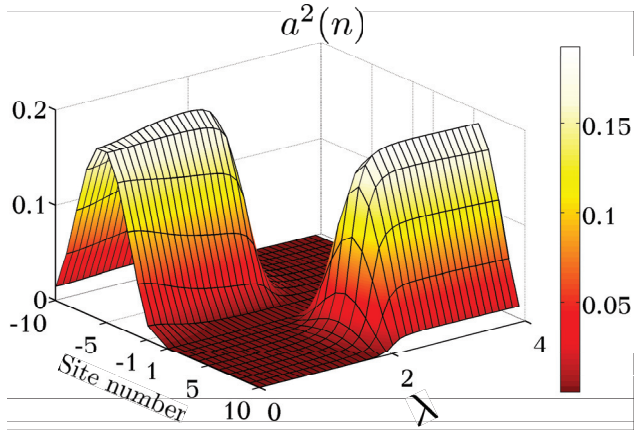

(a)

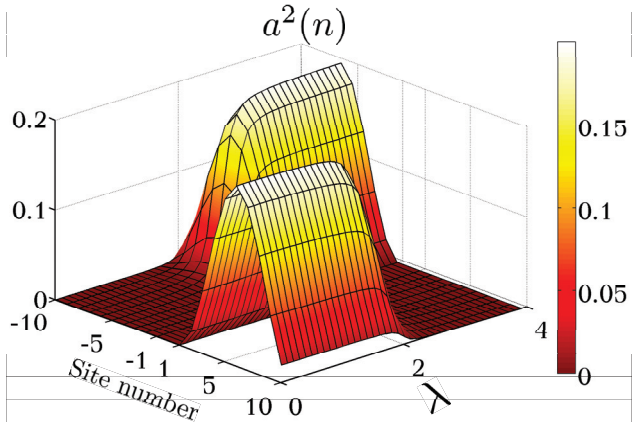

(b)

Figure 8.3: Evolution of the squared components of the (a) upper state and (b) lower state wave functions in pair one indicated in Fig. 8.2. Only the components in the chain are considered in the figure: amplitudes $a(n)$ in the wave function (8.5).

All pairs within the Bloch band in Fig. 8.2 possess a qubit structure and therefore can be considered for implementing a qubit. The wave function profile, however, varies for each pair. Fig. 8.4 shows the upper state wave function in pair III as λ takes different values.

The behavior is qualitatively the same as in pair I, when λ increases, the state evolves from being fully localized in the left to being fully localized in the right.

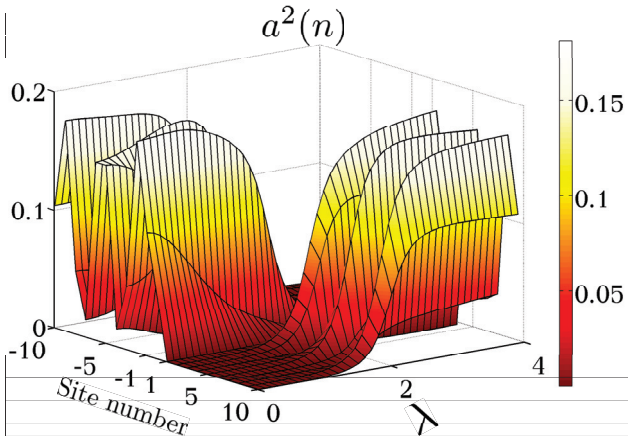

Figure 8.4: Evolution of the squared components of the upper state wave function in pair three indicated in Fig. 8.2. Only the components inside the chain are considered in this figure.

8.3 Open System - Superradiance and Emergence of Protecting Edge States

In this section we consider the open system with the two edge sites of the chain coupled to the external world. This represents the interaction of the system with devices such as charge detectors and leads connected to the two ends of the wire. We apply the non-Hermitian Hamiltonian technique discussed in Chapter 6 to the distributed qubit system.

We open our system by coupling the left-most and right-most sites ($|-N\rangle$ and $|N\rangle$) to ideal leads by the amplitudes A_{-N}^{cL} and A_{N}^{cR}, respectively. We further assume that the energy dependence of the amplitudes can be ignored and the couplings are symmetric, $A_{-N}^{L} = A_{N}^{R} = \sqrt{\gamma}$. Here γ is the parameter representing the interaction strength with the decay channels. The effective Hamiltonian (6.8), with H_0 being the Hamiltonian of the closed

system (8.4), thus fully describes the situation. Since the chain is only coupled through the edge sites, the operator W takes on a simple form: according to (6.6) the only non-zero matrix elements of this operator are

$$W_{-N,-N} = W_{N,N} = \gamma. \tag{8.22}$$

The behavior of the system is strongly influenced by the dimensionless parameter γ/D, where D is the mean energy level spacing of the closed system. A parametric study for a chain without qubits and a chain with a single qubit was performed in [105] and [148], respectively. In both cases, the typical picture was found to be as follows. At weak coupling to the environment, all intrinsic states acquire a small decay width. The width distribution among the states is almost uniform with the maximum at the center of the Bloch band. When γ grows, the distribution abruptly changes at $\gamma \simeq D$. Beyond this point, further increasing the coupling results in the segregation of states into long-lived narrow and short-lived broad resonances. As previously, in analogy to Dicke superradiance in quantum optics [97], we term these emergent giant resonances as superradiant states.

Adopting a similar approach to our system we consider a chain with 20 intrinsic cells ($N = 10$), a pair of asynchronized qubits attached at the center, and the two end sites coupled to the continuum. The results of this study are presented with a series of figures (in all figures the scale is fixed by setting $\nu = 1$).

In the first step we diagonalize the effective Hamiltonian,

$$\mathcal{H} \left| q \right\rangle = \mathcal{E}_q \left| q \right\rangle , \tag{8.23}$$

The trajectories of the energies $\mathcal{E}_q$ in the complex plane as a function of γ are shown in Fig. 8.5. The x and y axes represent the real and imaginary parts of the energies, respectively ($\mathcal{E}_q = E_q - (i/2)\Gamma_q$). The parameters of the system are $\delta = 2.5$, $\lambda = 0.01$, $\kappa = 4$. States within the band are shown in the top panel. Because λ is small, the states are fully localized in both sides of the chain. The five pairs indicated in the figure correspond to the pairs of the closed system shown in Fig. 8.2. The emergence of superradiant states is clear in the figure. At small values of γ all states are narrow resonances. The decay widths grow as γ increases. At the critical value of $\gamma \simeq 2.5$ the sharp superradiant transition occurs. Beyond this point, the superradiant states (pair V in the figure) become broad resonances, essentially protecting the remaining states from decaying into the continuum. The lower panel in the figure shows the states outside of the band. These states are localized in the central qubits and have extremely small decay widths. For these states, the shift in the real energy is negligible and therefore after the superradiance transition they trace back the same trajectories.

It was noticed in [152] that the real part of the effective Hamiltonian repels the levels while attracting the widths. On the contrary, the anti-Hermitian part attracts the real energies but repels the widths. This phenomenon can be seen in Fig. 8.5, where on the road to superradiance the energy levels are attracted to the center of the band.

The evolution of complex energies of the same system when $\lambda = 2$ is shown in Fig. 8.6. All pairs are now evenly distributed over the entire chain. The picture is qualitatively the same as in the previous case. The two superradiant states are again placed in the center of the band. At large values of coupling to the continuum, the superradiant states acquire the entire width, leaving the remaining states to be long-lived.

In order to better envision the protecting role of the superradiant states we compare the lifetime of a particle inside the chain for different initial conditions. In the first case, the

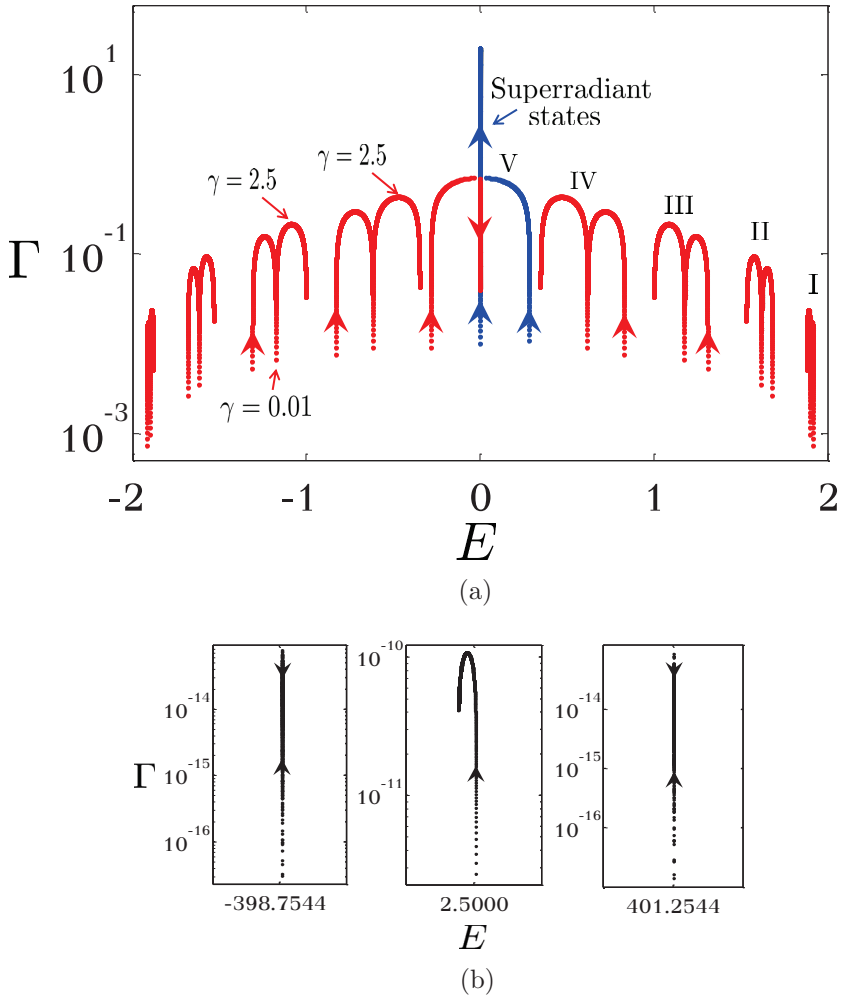

Figure 8.5: Evolution of complex eigenenergies as a function of coupling to the continuum for (a) states within the Bloch band and (b) states outside the band. The arrows indicate the direction in which γ evolves from 0.05 to 20 with 0.01 increments. The parameter values are $\delta = 2.5$, $\lambda = 0.01$ and $\kappa = 4$.

particle is initialized in the upper energy state of pair I shown in Fig. 8.6. In the second case, the initial state is that of the upper energy of pair V (superradiant pair) shown in the same figure. We calculate the survival probability $P(t)$ according to

$$P(t) = \sum_m \left| \langle m \, | \psi(t) \rangle \right|^2, \tag{8.24}$$

where $|m\rangle$'s are the intrinsic states of the closed system ($\{|n\rangle\}$, $|e_L\rangle$ and $|e_R\rangle$ in the wave

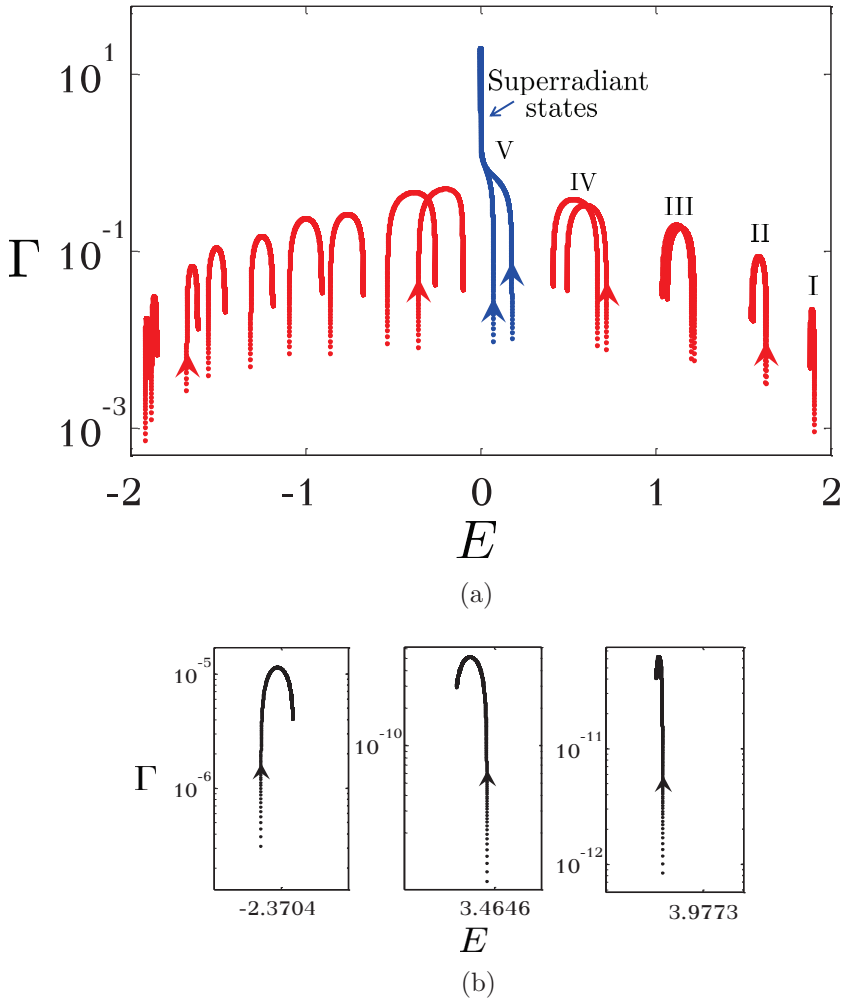

Figure 8.6: Evolution of the complex eigenenergies as a function of coupling to the continuum for (a) states within the Bloch band and (b) states outside the band. γ varies from 0.05 to 20 with 0.01 increments. The parameter values are $\delta = 2.5$, $\lambda = 2$ and $\kappa = 4$.

function (8.5)) and $\psi(t)$ is the result of quantum evolution,

$$\psi(t) = e^{-i\mathcal{H}_{\text{eff}}t}\psi_0, \tag{8.25}$$

where ψ_0 is the initial state. The initial state can be expanded in the biorthogonal space of

the eigenstates of the effective Hamiltonian (8.23), $\psi_0 = \sum_q c_q |q\rangle$. Consequently we have

$$P(t) = \Big| \sum_{m,q} c_q e^{-i\mathcal{E}_q t} \langle m|q\rangle \Big|^2. \tag{8.26}$$

The results for different values of the coupling constant γ are shown in Fig. 8.7. In panel (a) the particle was initialized in the upper state of the first energy pair in the band structure. Compared to the weak coupling case ($\gamma = 0.25$), at the superradiance transition ($\gamma = 2.5$) the lifetime is by an order of magnitude smaller, which makes the situation convenient for measurement and fast readout of the qubit system. At strong coupling and beyond the superradiance transition, when $\gamma = 25$, the lifetime increases and allows for storing information or performing operations on the qubit. Contrary to this, it is shown in panel (b) that the lifetime of a particle initialized in the superradiant state monotonically decreases as the coupling strength is increased. Consequently, other pairs in the band structure become protected from decaying into the leads.

Next we consider the band structure of the open system. Fig. 8.8 shows the upper half of the band structure when $\gamma = 3$. Here the y-axis gives the real part of energy. The picture is similar to the band structure of the closed system (Fig. 8.2) with all pairs slightly pushed towards the center of the band. In addition, pair V has now become a superradiant pair where the two states have short lifetimes and are insensitive to the parameter λ. Therefore the pair is no longer a suitable candidate for our qubit system and its role is solely protecting other pairs from decaying into continuum.

It is interesting to monitor the superradiant wave function profile in the chain as a function of γ. We again consider two cases here: $\lambda = 0.01$ and $\lambda = 2$. The two superradiant wave functions for the first case are shown in Fig. 8.9. For small values of γ the upper and

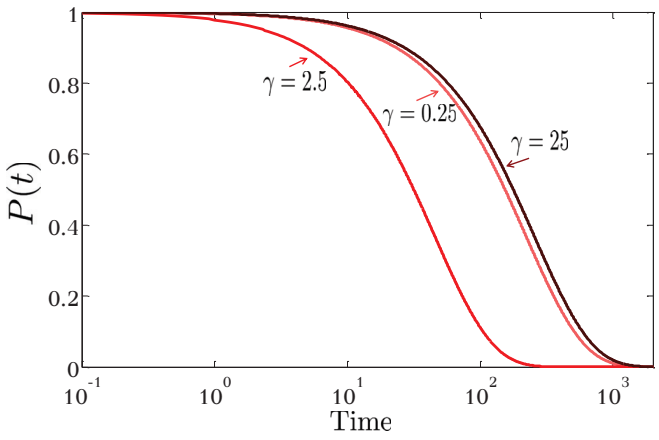

(a)

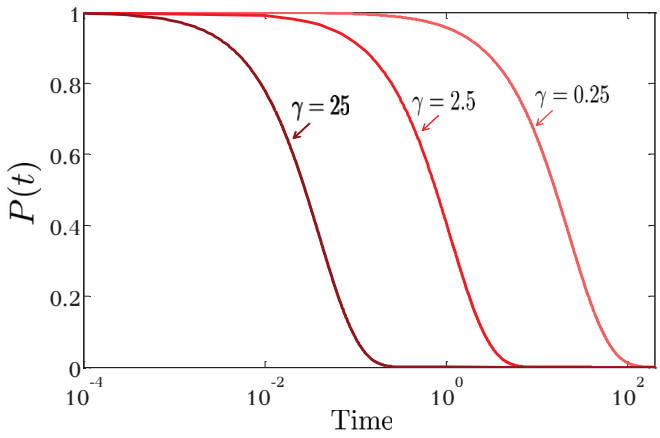

(b)

Figure 8.7: Lifetime for different values of coupling to the continuum γ for a particle initialized in (a) the upper state of pair I and (b) the upper state of pair V (superradiant pair) in Fig. 8.6. The parameter values are $\delta = 2.5$, $\lambda = 2$ and $\kappa = 4$.

lower states are Bloch waves confined to the left and the right sides of the chain, respectively. As γ increases, the states quickly become localized at the edges of the wire.

The wave functions for the second case, $\lambda = 2$, are shown in Fig. 8.10. The picture is similar to the previous case with the difference that, at weak coupling, the states are extended over the entire chain. It is apparent that at strong coupling the superradiant states become localized in the two edges [153].

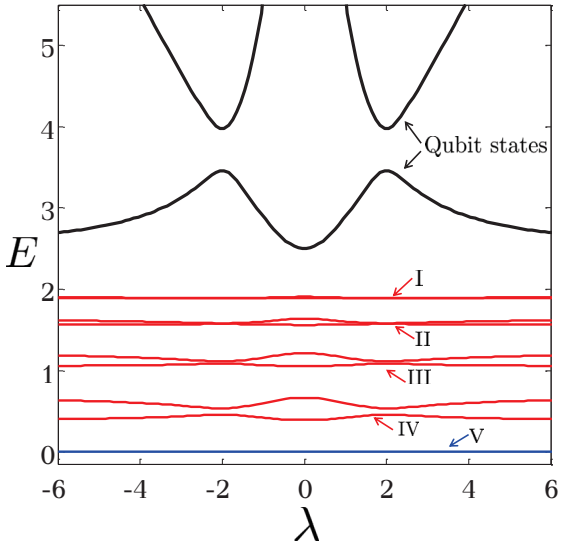

Figure 8.8: Upper half of the band structure as a function of λ for the open system with $\delta = 2.5$, $\kappa = 4$ and $\gamma = 3$. The black curves correspond to states localized in the central qubits and the red curves are pairs of Bloch waves.

8.4 Noise and Decoherence

So far, we have studied the system under ideal conditions i.e. assuming that all processes are fully coherent. In reality, due to the interaction with the surrounding the system is subject to perturbations that might destroy the phase relations of the components of a wave function (decoherence). Because superradiance is a direct consequence of quantum superposition and therefore a coherent phenomenon, we expect such fluctuations to have a great impact on the dynamics of the system.

In this section we study the interplay between superradiance and decoherence by considering a model originally introduced by Haken and Strobl [154]. The model has been extensively used for studying the role of dephasing in various physical situations such as radiative decay in molecular aggregates [155], quantum teleportation and the implementation of a quantum controlled-NOT gate [156]. The dephasing process is introduced by adding a

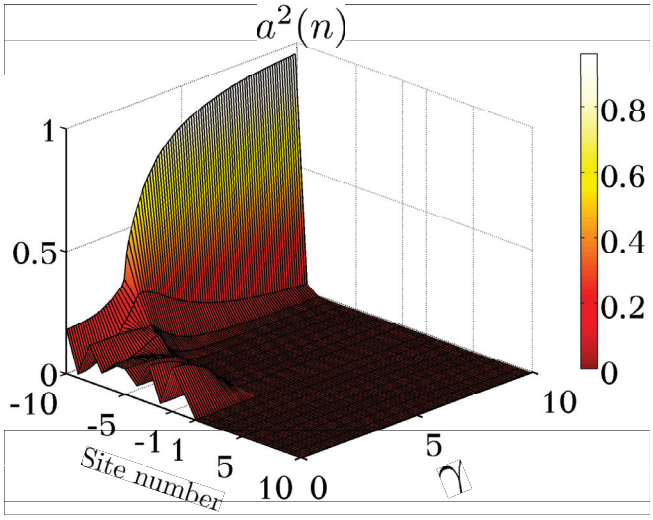

(a)

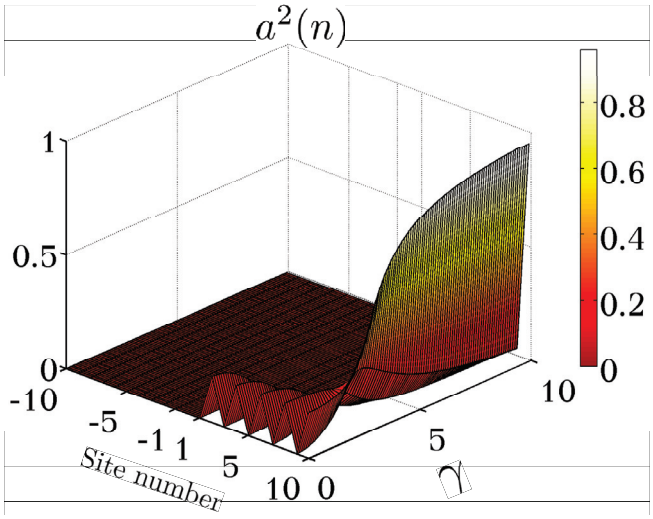

(b)

Figure 8.9: Evolution of the squared components of the wave functions for (a) upper and (b) lower superradiant states. The parameters are $\delta = 2.5$, $\kappa = 4$ and $\lambda = 0.01$. Only the components inside the chain are considered in the figure.

time-dependent Hamiltonian to the effective non-Hermitian Hamiltonian,

$$H_\phi(t) = \sum_{\substack{n=-N \\ n\neq 0}}^{N} \delta\epsilon_n(t) c_n^\dagger c_n + \delta\epsilon_L(t) c_L^\dagger c_L + \delta\epsilon_R(t) c_R^\dagger c_R, \tag{8.27}$$

where $\delta\epsilon(t)$ describe stochastic Gaussian processes representing rapid fluctuations of on-site

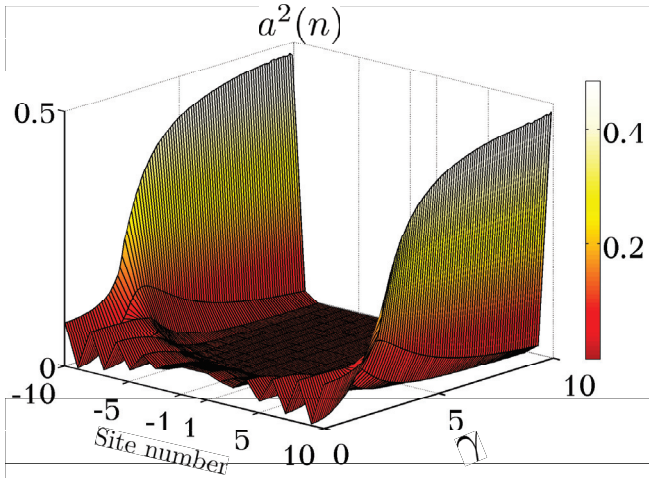

(a)

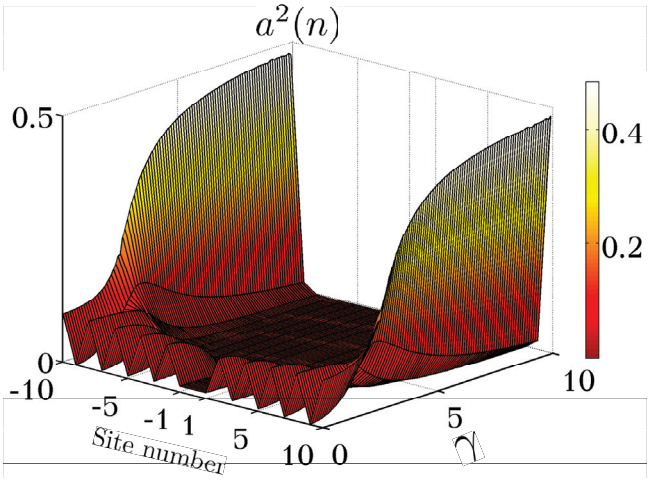

(b)

Figure 8.10: Evolution of the squared components of the wave functions for (a) upper and (b) lower superradiant states. The parameters are $\delta = 2.5$, $\kappa = 4$ and $\lambda = 2$. Only the components inside the chain are considered in the figure.

electronic energies with zero mean and delta-function correlations in time

$$\langle \delta\epsilon_i(t) \rangle = 0, \tag{8.28}$$

$$\langle \delta\epsilon_i(t)\delta\epsilon_j(t') \rangle = \alpha_\phi \delta_{i,j}\delta(t-t'). \tag{8.29}$$

Here α_ϕ is the parameter representing the dephasing strength; subscripts i and j run over

cell numbers, $n = -N, ..., -1, 1, ..., N$, as well as the excited states of the central qubits, L and R. The symbol $\langle\ \rangle$ denotes averaging over the statistical ensemble.

The evolution of the density matrix $\rho(t)$ is governed by the stochastic Liouville equation. In the site representation we have (see the appendix for derivation)

$$\frac{\partial}{\partial t}\langle\rho(t)\rangle_{i,j} = -i\big[\mathcal{H}_{\text{eff}}, \langle\rho(t)\rangle\big]_{i,j} - 2\alpha_\phi(1-\delta_{i,j})\langle\rho(t)\rangle_{i,j}. \tag{8.30}$$

Both superradiance and dephasing result in the decay of off-diagonal elements of the density matrix. As a measure of coherence, we define a new quantity, $\mathcal{R}(t)$, according to

$$\mathcal{R}(t) = \sum_{i\neq j}\langle\rho(t)\rangle_{i,j}. \tag{8.31}$$

Furthermore, we define the coherence time, τ_{coh}, as the time duration for which $\mathcal{R}(\tau_{\text{coh}}) = \mathcal{R}(0)/e$. Without coupling to the continuum, $\gamma = 0$, we have $\mathcal{R}(t) = \mathcal{R}(0)e^{-\alpha_\phi t}$ and $\tau_{\text{coh}} = \alpha_\phi^{-1}$. For an open system, $\gamma \neq 0$, the Liouville equation (8.30) was numerically solved using the ordinary differential equations package in Matlab. Here we consider three cases, $\alpha_\phi = 10^{-3}$, $\alpha_\phi = 10^{-2}$ and $\alpha_\phi = 10^{-1}$. For each case, the coherence time is calculated for systems with different numbers of sites. The initial density matrix in all calculations corresponds to the upper state in the highest energy pair inside the Bloch band (pair I in Fig. 8.8) when $\lambda^2 = \kappa$.

The results for the case of the weak dephasing strength, $\alpha_\phi = 10^{-3}$, are shown in Fig. 8.11. As expected, regardless of the site number, the coherence time is equal to $\tau_{\text{coh}} = 10^3$ when $\gamma = 0$. As γ increases, coherence time is governed by superradiance dynamics. At the transition to superradiance, the initial state achieves its maximum decay width and hence

τ_{coh} reaches its minimum due to fast decay into the continuum. However, the reduction in τ_{coh} is quite different for chains with varying numbers of sites. For larger chains, states have a smaller share of the total width and therefore longer lifetimes compared to shorter chains. Consequently, at the superradiance transition, longer chains have larger decoherence time. A similar type of resistance and robustness to noise with an increase in the number of sites was observed in nanoscale rings within light-harvesting systems [157]. At larger values of γ, the lifetime of the initial state increases which in turn increases τ_{coh}.

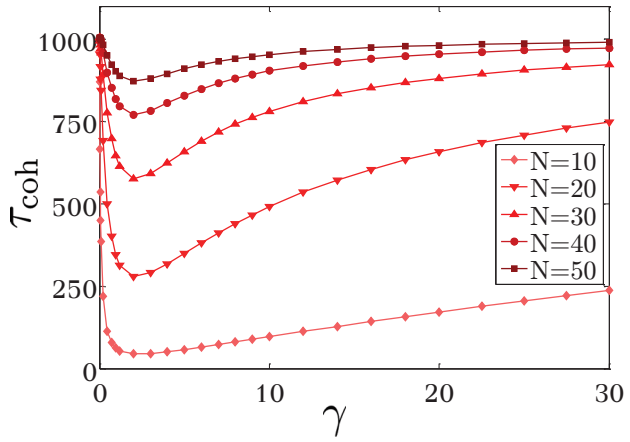

Figure 8.11: Coherence time as defined in (8.31) for systems with different numbers of cells when $\alpha_\phi = 10^{-3}$. The initial state is the upper state of the highest pair inside the Bloch band. Other parameters are $\lambda = \sqrt{\kappa} = 2$ and $\delta = 2.5$.

Fig. 8.12 shows the results for $\alpha_\phi = 10^{-2}$. The effect of superradiance is apparent only for systems with a smaller number of sites. For systems with $N = 10$ and $N = 20$, τ_{coh} is decreased due to the decay into the continuum (for smaller systems the lifetime of the initial state is shorter since there are less states that share the entire decay width).

The results associated with the case of $\alpha_\phi = 10^{-1}$, are presented in Fig. 8.13. The strong dephasing quickly dissipates the off-diagonal elements of the density matrix. This happens before the particle gets a chance to escape the wire and therefore the superradiance effect is suppressed by the dephasing phenomenon. As expected and demonstrated by the figures,

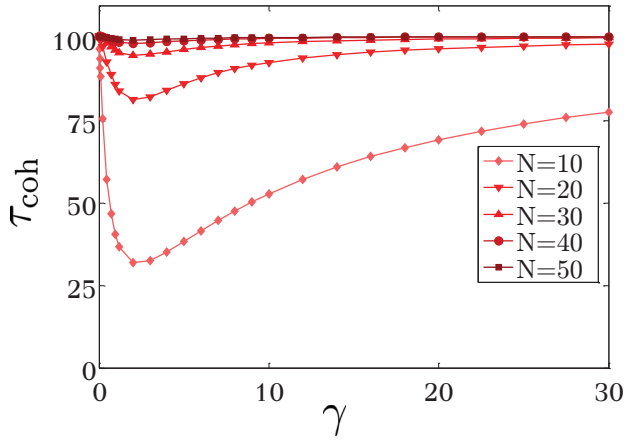

Figure 8.12: Coherence time of systems with different numbers of cells when $\alpha_\phi = 10^{-2}$. The initial state is the upper state of the highest pair inside the Bloch band.

superradiance survives only in the presence of relatively weak dephasing.

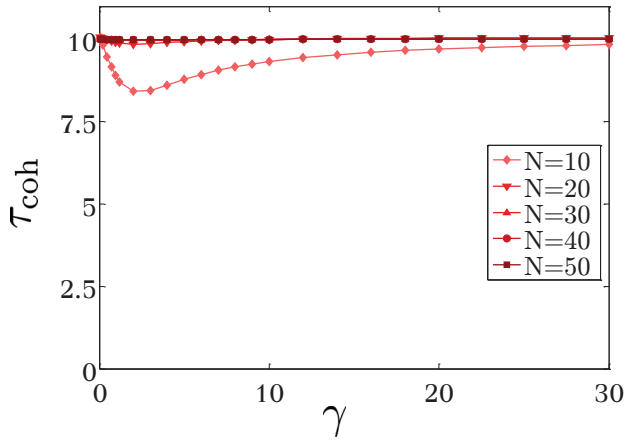

Figure 8.13: Coherence time of systems with different numbers of cells when $\alpha_\phi = 10^{-1}$. The initial state is the upper state of the highest pair inside the Bloch band.

8.5 Discussion

We proposed a novel solid-state based system for implementing a qubit. The system consists of a one-dimensional chain and a pair of two-level atoms inserted at its center where the couplings between their ground and excited states are inversely proportional. The energy eigenstates within the Bloch band exhibit a qubit-like behavior. The coupling between the

ground and excited states of the two central qubits can be used to perform gate operations and initialize the system in a given state. The effect of connecting the wire to ideal leads and charge detectors (coupling to the continuum) was discussed in detail by exploiting the non-Hermitian effective Hamiltonian approach. In the case of strong continuum coupling, two broad resonances localized at the edges of the wire are formed. These emerging superradiant edge states increase the lifetime of the remaining states making them suitable candidates for qubit implementation. The effect of ambient noise was included by considering the stochastic Liouville equation. The interplay between superradiance and decoherence was discussed for various dephasing strengths. Superradiant effects are prominent for weak dephasing strengths and fade away as the noise increases.

For the rest of my life I will reflect on what light is.

Albert Einstein

Chapter 9

Non-Hermitian Plasmonics Antennas and Waveguides

9.1 Introduction

Manipulation of light in nanometer scales via surface plasmonic resonances of metallic structures has attracted a great deal of attention over the past two decades [159]. Optical antennas capable of localizing light in sub-wavelength regions have resulted in a new generation of photonic devices with applications ranging from imaging [160–162] to biosensing [163, 164] and emission enhancement of photon sources [165–167]. In addition, plasmonics is ought to play an important role in the efficient reception and transport of optical energy in light harvesting devices [174]. Therefore, various waveguide structures are being investigated in order to control and further improve the propagation of light in micrometer length scales [172, 173].

More recently, it has been shown that surface plasmons can exhibit quantum interfer-

ence [168, 169]. This has sparked a great interest in studying the quantum properties of surface plasmons and exploiting plasmonic devices as potential building blocks of quantum computers and quantum circuits [170, 171].

It was previously suggested that plasmonic structures could be mapped to quantum systems governed by non-Hermitian Hamiltonians [95, 175]. In [95], the radiation properties of an array of optical dipole antennas are manipulated by altering the anti-Hermitian coupling strength between the elements of the array. However, due to the complexity of nano-dipole antennas and the lack of closed form expressions for the fields, the mapping to a non-Hermitian Hamiltonian was achieved via numerical simulation and curve fitting. In this section we consider systems of plasmonic nano-spheres using the effective Hamiltonian framework introduced in Chapter 6. This framework provides a general platform for studying different physical systems; it has been previously utilized in various problems ranging from quantum signal transmission in nano-structures [105, 148] to solid state quantum computing [90] and nuclear reactions [101, 114]. The description of plasmonic structures via the effective Hamiltonian is achieved due to the correspondence between the Feshbach formalism and the coupled mode theory of optical resonators. The effective non-Hermitian Hamiltonian approach allows us to translate phenomena already known in condensed matter and nuclear systems to the plasmonic system under study. One such example is the existence of superradiant and subradiant, or dark, states. In addition, the effective Hamiltonian framework can be readily used in order to calculate observables, such as the transmission coefficient through a plasmonic waveguide.

We first discuss the coupled mode formalism used for studying optical and plasmonic systems. The connection between the effective Hamiltonian and coupled mode theory is illustrated through simple two-level examples. We then consider a single plasmonic metallic

nanosphere. The wave equation is solved in order to find the natural resonant frequencies of the single sphere, and discuss the intrinsic radiative nature of nanospheres. This provides a basis for the consideration of two spheres via coupled mode theory. The signature of superradiance emerges when the interaction between adjacent optical nano antennas occurs through a single continuum channel, resulting in states with enhanced radiation and confined dark modes. The effect of these states on energy transmission through a one-dimensional chain of spheres is also considered, with applications to optical frequency nanoscale antennas and waveguide-like structures.

9.2 Coupled Mode Theory and The Non-Hermitian Hamiltonian

In this thesis, we employ the coupled mode theory in order to study systems of interacting plasmonic spheres. This method, is reminiscent of the time-dependent perturbation theory in quantum mechanics; it has been used for the investigation of coupled resonators in optical systems [176–178], wireless energy transfer loop antennas [179] and plasmonic structures including antennas [95, 179] and waveguides [180–182]. The coupled mode approach significantly simplifies the complexity of the problem: instead of solving the wave equation one needs to solve a system of linear algebraic equations. In addition, it provides a clear and intuitive picture of how interaction between the constituents of the system can dramatically change the dynamics.

The formulation provided in this thesis, similar to [183], is rather general. No specific boundary conditions are assumed and hence it is applicable to the system of coupled plasmonic nanoantennas discussed in the future sections.

Consider two non-magnetic dielectric resonators with relative dielectric constants $\epsilon_1(\vec{r})$ and $\epsilon_2(\vec{r})$. The resonators occupy a volume in space, V_1 and V_2, respectively. In addition, consider that the relative dielectric constants $\epsilon_1(\vec{r})$ and $\epsilon_2(\vec{r})$, are equal to unity for points outside of the first and second resonators, respectively. In a time harmonic scenario each resonator, when isolated, satisfies the wave equation

$$\vec{\nabla} \times \vec{\nabla} \times \vec{\mathcal{E}}_n^{\alpha}(\vec{r}) - \left(\frac{\omega_{\alpha,n}}{c}\right)^2 \epsilon_{\alpha}(\vec{r}) \vec{\mathcal{E}}_n^{\alpha}(\vec{r}) = 0, \tag{9.1}$$

where $\alpha = 1, 2$ denotes the resonator number and c is the speed of light in the background medium which is assumed to be the free space for simplicity. Due to the sharp discontinuity between the resonator and the background at the resonator boundaries, the modes are quantized and characterized by the integer number $n = 1, 2, 3, ...$ and their eigenfrequency $\omega_{\alpha,n}$. The modes of isolated resonators are normalized according to

$$\int_V \epsilon_{\alpha}(\vec{r}) \vec{\mathcal{E}}_m^{\alpha^*}(\vec{r}) . \vec{\mathcal{E}}_n^{\alpha}(\vec{r}) d^3r = \delta_{mn}, \tag{9.2}$$

where V is the total volume and m and n are the mode indices and δ_{mn} is the Kronecker delta. The normalization expression is of crucial importance and its form is dictated by the boundary conditions of the problem. For instance in [183] the normalization is similar to (9.2), however with no complex conjugation. As we will see, the normalization expression has to be modified when discussing spherical plasmonic particles in the following sections. For now, without loss of generality, we assume that the normalization rule is given by the general dot product definition provided in (9.2) with the integration volume being all space, as this is usually the case in electromagnetic textbooks.

Next we assume that, for a system of two coupled resonators, the total electric field, $\vec{\mathcal{E}}(\vec{r})$, can be written as a superposition of a finite number of individual modes of the two resonators:

$$\vec{\mathcal{E}}(\vec{r}) = \sum_{n=1}^{N} \Big[a_1(n)\vec{\mathcal{E}}_n^1(\vec{r}) + a_2(n)\vec{\mathcal{E}}_n^2(\vec{r}) \Big], \tag{9.3}$$

where N is the total number of modes. The total electric field satisfies the wave equation

$$\vec{\nabla} \times \vec{\nabla} \times \vec{\mathcal{E}}_n(\vec{r}) - \Big(\frac{\omega_n}{c}\Big)^2 \epsilon(\vec{r})\ \vec{\mathcal{E}}_n(\vec{r}) = 0, \tag{9.4}$$

where ω_n are the eigenfrequencies of the coupled system and $\epsilon(\vec{r})$ is the dielectric constant at a given point, $\vec{r}$, when both resonators are simultaneously present. The function $\epsilon(\vec{r})$ is equal to $\epsilon_1(\vec{r})$ and $\epsilon_2(\vec{r})$ for points inside the first and second resonator, respectively, and is equal to unity otherwise. Plugging the ansatz (9.3) into the wave equation (9.4) and using its linearity and (9.1) we arrive at

$$\begin{aligned} &\sum_{n=1}^{N} \Big[a_1(n)\big(\omega_{1,n}\big)^2 \epsilon_1(\vec{r})\vec{\mathcal{E}}_n^1(\vec{r}) + a_2(n)\big(\omega_{2,n}\big)^2 \epsilon_2(\vec{r})\vec{\mathcal{E}}_n^2(\vec{r}) \Big] \\ &\qquad = \omega_n^2 \epsilon(\vec{r}) \sum_{n=1}^{N} \Big[a_1(n)\vec{\mathcal{E}}_n^1(\vec{r}) + a_2(n)\vec{\mathcal{E}}_n^2(\vec{r}) \Big]. \end{aligned} \tag{9.5}$$

Using the normalization rule (9.2) to project (9.5) onto $\vec{\mathcal{E}}_m^1(\vec{r})$ and $\vec{\mathcal{E}}_m^2(\vec{r})$ for all values of m: $m = 1, 2, .., N$, we obtain a system of $2N$ linear equations. In the matrix form

$$\begin{pmatrix} \boldsymbol{T^{11}} & \boldsymbol{T^{12}} \\ \boldsymbol{T^{21}} & \boldsymbol{T^{22}} \end{pmatrix} \begin{pmatrix} \boldsymbol{\Omega_1^2} & \mathbf{0} \\ \mathbf{0} & \boldsymbol{\Omega_2^2} \end{pmatrix} \begin{bmatrix} \vec{A}_1 \\ \vec{A}_2 \end{bmatrix} = \omega^2 \begin{pmatrix} \boldsymbol{L^{11}} & \boldsymbol{L^{12}} \\ \boldsymbol{L^{21}} & \boldsymbol{L^{22}} \end{pmatrix} \begin{bmatrix} \vec{A}_1 \\ \vec{A}_2 \end{bmatrix}, \tag{9.6}$$

where $\vec{A}_1$ and $\vec{A}_2$ are $N \times 1$ vectors of the coefficients $a_1(n)$ and $a_2(n)$ in the ansatz (9.3),

respectively. $\mathbf{\Omega_1}$ and $\mathbf{\Omega_2}$ are $N \times N$ diagonal matrices containing the eigenfrequencies of the isolated resonators with matrix elements

$$\big(\Omega_\alpha\big)_{mn} = \omega_{\alpha,n}\ \delta_{mn} \tag{9.7}$$

where as previously $\alpha = 1, 2$. The matrix elements of the four square $N \times N$ matrices $\boldsymbol{T^{\alpha\beta}}$, where $\alpha, \beta = 1, 2$, are given by

$$T^{\alpha\beta}_{mn} = \int_V \epsilon_\beta(\vec{r})\vec{\mathcal{E}}^{\alpha^*}_m(\vec{r}).\vec{\mathcal{E}}^{\beta}_n(\vec{r})d^3r. \tag{9.8}$$

According to (9.2), $\boldsymbol{T^{11}}$ and $\boldsymbol{T^{22}}$ are equal to the identity matrix $\mathbf{1}$. Finally the elements of the matrices $\boldsymbol{L^{\alpha,\beta}}$ are given by

$$L^{\alpha\beta}_{mn} = \int_V \epsilon(\vec{r})\vec{\mathcal{E}}^{\alpha^*}_m(\vec{r}).\vec{\mathcal{E}}^{\beta}_n(\vec{r})d^3r. \tag{9.9}$$

Because the dielectric function $\epsilon(\vec{r})$ is the sum of the two dielectric function, the matrix elements $L^{12}_{m,n}$ and $T^{12}_{m,n}$ are related via

$$L^{12}_{mn} = T^{12}_{mn} + \int_{V_1} \big(\epsilon_1(\vec{r}) - 1\big)\vec{\mathcal{E}}^{1^*}_m(\vec{r}).\vec{\mathcal{E}}^{2}_n(\vec{r})d^3r, \tag{9.10}$$

where the integration is carried out over the volume of the first resonator, V_1 only. Accordingly, we define the matrix $\boldsymbol{K^{12}}$ with matrix elements

$$K^{12}_{mn} = \int_{V_1} \big(\epsilon_1(\vec{r}) - 1\big)\vec{\mathcal{E}}^{1^*}_m(\vec{r}).\vec{\mathcal{E}}^{2}_n(\vec{r})d^3r. \tag{9.11}$$

Therefore

$$\boldsymbol{L^{12}} = \boldsymbol{T^{12}} + \boldsymbol{K^{12}}. \tag{9.12}$$

Similarly L^{21}_{mn} is related to T^{21}_{mn} as

$$L^{21}_{mn} = T^{21}_{mn} + \int_{V_2} \big(\epsilon_2(\vec{r}) - 1\big)\vec{\mathcal{E}}^{2^*}_m(\vec{r}).\vec{\mathcal{E}}^{1}_n(\vec{r})d^3r. \tag{9.13}$$

Correspondingly $\boldsymbol{K^{21}}$ is defined with matrix elements

$$K^{21}_{mn} = \int_{V_2} \big(\epsilon_2(\vec{r}) - 1\big)\vec{\mathcal{E}}^{2^*}_m(\vec{r}).\vec{\mathcal{E}}^{1}_n(\vec{r})d^3r. \tag{9.14}$$

Hence

$$\boldsymbol{L^{21}} = \boldsymbol{T^{21}} + \boldsymbol{K^{21}}. \tag{9.15}$$

In order to simplify (9.6), we accept a number of approximations that are commonly used in studying systems of weakly coupled resonators [184–186]. We assume that the diagonal matrix elements in (9.9) are approximately equal to unity, i.e. $L^{11}_{m,n} = L^{22}_{m,n} \approx 1$ and therefore $\boldsymbol{L^{11}} = \boldsymbol{L^{22}} \approx \mathbf{1}$. This is justified due to the strong field confinement within the dielectric regions. Furthermore, we assume that the coupling is weak and therefore the coupling elements in (9.10) satisfy the condition $T^{12}_{mn}T^{21}_{m'n'} \ll 1$. Using these approximations along with (9.12) and (9.15), the coupled mode equation (9.6) reduces to

$$\begin{pmatrix} \mathbf{1} & -\boldsymbol{K^{12}} \\ -\boldsymbol{K^{21}} & \mathbf{1} \end{pmatrix} \begin{pmatrix} \boldsymbol{\Omega^2_{11}} & \mathbf{0} \\ \mathbf{0} & \boldsymbol{\Omega^2_{22}} \end{pmatrix} \begin{bmatrix} \vec{A}_1 \\ \vec{A}_2 \end{bmatrix} = \omega^2 \begin{bmatrix} \vec{A}_1 \\ \vec{A}_2 \end{bmatrix}. \tag{9.16}$$

It is also helpful to linearize the system of equations (9.16). This can be done by noting that

the eigenmodes of the isolated resonators are not far apart and are clustered around their mean value [187], i.e. $\omega \approx \omega_{\alpha,n}$. Under this approximation ω and $\omega_{\alpha,n}$ satisfy the following

$$\omega^2 - \big(\omega_{\alpha,n}\big)^2 \approx 2\omega_{\alpha,n}(\omega - \omega_{\alpha,n}). \tag{9.17}$$

This brings us to the final form of the coupled mode equations

$$\begin{pmatrix} \mathbf{1} & -\frac{1}{2}\boldsymbol{K^{12}} \\ -\frac{1}{2}\boldsymbol{K^{21}} & \mathbf{1} \end{pmatrix} \begin{pmatrix} \mathbf{\Omega_{11}} & \mathbf{0} \\ \mathbf{0} & \mathbf{\Omega_{22}} \end{pmatrix} \begin{bmatrix} \vec{A}_1 \\ \vec{A}_2 \end{bmatrix} = \omega \begin{bmatrix} \vec{A}_1 \\ \vec{A}_2 \end{bmatrix}. \tag{9.18}$$

In the simplest situation when the two resonators are identical and only one mode of an isolated resonator is considered, the electric field of the coupled system can be expressed as $\vec{\mathcal{E}}(\vec{r}) = a_1\vec{\mathcal{E}}^1(\vec{r}) + a_2\vec{\mathcal{E}}^1(\vec{r})$. According to (9.18) the coupled mode equations are then given by

$$\begin{aligned} \omega_0 a_1 + \kappa\ a_2 &= \omega a_1, \\ \omega_0 a_2 + \kappa^* a_1 &= \omega a_2, \end{aligned} \tag{9.19}$$

where ω_0 is the eigenfrequency of the isolated resonators. Using (9.11) and (9.18), κ is given by

$$\kappa = -\frac{1}{2}\omega_0 \int_{\mathrm{V}_1} \big(\epsilon_1(\vec{r}) - 1\big)\vec{\mathcal{E}}^{1^*}(\vec{r}).\vec{\mathcal{E}}^2(\vec{r})d^3r. \tag{9.20}$$

The coupling coefficient κ has a simple interpretation: it is the interaction energy between the field generated by the second resonator and the dipole moment of the first resonator averaged over one period. The complex conjugation of the coupling coefficient in (9.19) is dictated by the energy conservation, assuming there is no loss or gain in the system [187].

The eigenfrequencies of the coupled system, which are guaranteed to be real due to the Hermitian form of the equations in (9.19), are

$$\omega_{\pm} = \omega_0 \pm |\kappa|, \tag{9.21}$$

where the frequencies of the coupled system, ω_+ and ω_-, correspond to the symmetric eigenstate with $a_1 = a_2 = 1/\sqrt{2}$ and the anti-symmetric eigenstate with $a_1 = -a_2 = 1/\sqrt{2}$, respectively.

One can readily see the similarity between the coupled mode theory and the quantum theory as both are a theory of waves. Equation (9.19) is the Schrödinger equation for a two-level system (a qubit). In quantum mechanical language, ω_0 is the energy of the *unperturbed* states and the off-diagonal matrix element κ represents the interaction strength between the two states which is responsible for the level repulsion and avoided crossing of the final *mixed* states.

An interesting dynamic of the two-level system is the so-called Rabi oscillation. Let the system at time $t = 0$ be prepared in the unperturbed state with energy ω_1. Then the probability $P(t)$ to find the system in the same state at time t is [188]

$$P(t) = 1 - 4\frac{|\kappa|^2}{\omega_R^2}\sin^2\Big(\frac{\omega_R t}{2}\Big), \tag{9.22}$$

where $\omega_R = \omega_+ - \omega_- = 2|\kappa|$ is the Rabi frequency of the excitation oscillating back and forth between the two levels. Because the unperturbed energies of the two states are equal, the probability goes through the minimum, $P = 0$, which indicates that the excitation can be completely transferred, leaving no residue in the initial state. The Rabi oscillation was

predicted in systems of optical waveguides [189] and in coupled ring resonators [190].

We now focus on a more realistic case: two coupled identical dielectric resonators where in general, due to damping and leakage of the resonators, the energy is no longer conserved. Therefore the governing equations need not be Hermitian. In the case of open systems one has to modify the normalization expression (9.2) which leads to an altered expression for κ. The coupling coefficient in this case is similar to (9.20) but with no complex conjugation (see [183] for detail). The coupled equations (9.19) are modified to a more general form

$$\begin{aligned} \omega_0 a_1 + \kappa a_2 &= \omega a_1 \\ \omega_0 a_2 + \kappa a_1 &= \omega a_2, \end{aligned} \tag{9.23}$$

where ω_0 can now be complex: $\omega_0 = \eta_0 - i\gamma_0/2$ representing loss and radiation. Similarly, κ is in general complex as well: $\kappa = \kappa' - i\kappa''$ where κ' and κ'' are real numbers. The right hand side of the coupled equations (9.23) can then be written as the summation of two matrices, a Hermitian matrix, H_0', and an anti-Hermitian matrix W':

$$\begin{pmatrix} \omega_0 & \kappa \\ \kappa & \omega_0 \end{pmatrix} = H_0' - \frac{i}{2} W', \tag{9.24}$$

where

$$H_0' = \begin{pmatrix} \eta_0 & \kappa' \\ \kappa' & \eta_0 \end{pmatrix} \tag{9.25}$$

and

$$W' = \begin{pmatrix} \gamma_0 & 2\kappa'' \\ 2\kappa'' & \gamma_0 \end{pmatrix}. \tag{9.26}$$

The similarity between the coupled mode theory and the effective non-Hermitian Hamiltonian formalism becomes apparent by comparing (6.8) and (9.24). The problem of two coupled dielectric resonators is mapped to a two level quantum system where in general each level is coupled to an independent continuum channel. This is because in general the rank of W' is 2, therefore, according to (6.6), one requires two independent open channels to construct the anti-Hermitian matrix W'. In the particular case when $\gamma_0 = \pm 2\kappa''$, the rank of W' is equal to unity, therefore the superradiance condition is fulfilled and only one open channel is required to construct the matrix W'. In this case, the effective Hamiltonian has two distinct eigenvalues, a purely real eigenvalue or the subradiant state , reminiscent of dark modes in open quantum systems, with eigenfrequency $\eta_0 - \kappa'$, and a complex eigenvalue with enhanced radiation properties and eigenfrequency $\eta_0 + \kappa' - i\gamma_0$, which is the superradiant state.

9.3 A Single Metallic Sphere

In this section we consider a single isolated metallic sphere embedded in a homogeneous background dielectric material. The problem is treated classically by solving Maxwell equations. In the absence of external sources and assuming a harmonic time dependence of the form

$$\vec{\mathbb{E}}(\vec{r}, t) = e^{i\omega t}\vec{\mathcal{E}}(\vec{r}), \tag{9.27}$$

the governing equation is the well known Helmholtz equation

$$\nabla^2\vec{\mathcal{E}}(\vec{r}) - k^2\vec{\mathcal{E}}(\vec{r}) = 0. \tag{9.28}$$

The wave number k is defined for the interior and exterior regions of the plasmonic sphere according to

$$k = \begin{cases} k_{\text{in}} = \frac{\omega}{c}\sqrt{\epsilon_{\text{in}}} & r \leq a, \\ k_{\text{out}} = \frac{\omega}{c}\sqrt{\epsilon_{\text{out}}} & r > a, \end{cases} \tag{9.29}$$

where c is the speed of light in vacuum and a is the radius of the sphere which is located at the origin of the coordinate system. The relative dielectric constants of the metallic sphere and the background medium are denoted by ϵ_{in} and ϵ_{out}, respectively. Plasmonic structures are usually made of noble metals, such as gold and silver, with face-centered cubic lattice type or alkali metals, such as sodium and potassium, with body-centered cubic crystal structures. Due to their symmetric crystal lattice types, they are isotropic to light and their relative permittivity is characterized by a scalar. This dielectric constant is well described by the Drude-Sommerfeld model

$$\epsilon_{\text{in}}(\omega) = \epsilon_{\infty} - \frac{\omega_p^2}{\omega^2 - i\omega\gamma_s}, \tag{9.30}$$

where ω_p is the plasma frequency which is defined by the electron effective mass m^*, the vacuum permittivity ϵ_0, electron charge e, and electron density n; $\omega_p^2 = ne^2/\epsilon_0 m^*$. The loss within the dielectric material due to various processes, such as electron-phonon interaction, impurities and scattering, is incorporated into the relaxation rate γ_s. The negative sign of this term in the denominator is dictated by the phase convention adopted in (9.27). The phenomenological parameter ϵ_{∞} accounts for the contribution of the bound electrons to the polarization of the dielectric material. For typical metals the plasma frequency, ω_p, ranges from 3 to 15 eV (700-3600 THz) which mainly falls into the ultraviolet spectrum [191–195].

The damping rate γ_s is much smaller than the plasma frequency, $\gamma_s \ll \omega_p$, being of the order $10^{-2} - 10^{-1}$ eV (2.4-24 THz). Finally, the correction term ϵ_∞ typically ranges from 1 to 10 [196]. In an ideal electron gas, $\epsilon_\infty = 1$ and $\gamma_s = 0$, therefore the dielectric function (9.30) reduces to $\epsilon_{\text{in}}(\omega) = 1 - \omega_p^2/\omega^2$. Below the plasma frequency the dielectric function is negative and the field can not penetrate inside the metal. For frequencies larger than the plasma frequency however, the dielectric constant become positive and the fields can penetrate the metal.

Using the spherical coordinate system, the solutions of the Helmholtz equation (9.28) for the plasmonic sphere can be divided into two categories: transverse magnetic (TM) modes with vanishing radial magnetic field and transverse electric (TE) modes with no radial electric field component. In this work we consider the TM modes only. The components of the electric field are given by [197]:

$$\begin{aligned}
\mathcal{E}_r &= \zeta\ C(r;a)\ell(\ell+1)\frac{f_\ell(kr)}{\epsilon(r)kr}Y_\ell^m(\theta,\phi),\\
\mathcal{E}_\theta &= \zeta\ C(r;a)\frac{1}{\epsilon(r)kr}\frac{\partial}{\partial(kr)}\Big(krf_\ell(kr)\Big)\frac{\partial}{\partial\theta}Y_\ell^m(\theta,\phi),\\
\mathcal{E}_\phi &= \zeta\ C(r;a)\frac{1}{\epsilon(r)kr}\frac{\partial}{\partial(kr)}\Big(krf_\ell(kr)\Big)\frac{1}{\sin\theta}\frac{\partial}{\partial\phi}Y_\ell^m(\theta,\phi),
\end{aligned} \tag{9.31}$$

where ζ is the normalization constant discussed in detail in the next section. The dielectric constant is equal to ϵ_{in} and ϵ_{out} for $r \leq a$ and $r > a$, respectively. $Y_\ell^m(\theta,\phi)$ is a spherical harmonics with $\ell = 0, 1, 2, ...$ and $m = 0, \pm1, \pm2, ..., \pm\ell$. The case of $\ell = 0$ results in the trivial solution. The first non-trivial solution corresponds to the dipole mode, $\ell = 1$. The function $f_\ell(kr)$ is equal to the spherical Bessel function of the first kind and the spherical

Hankel function of the second kind, for $r \leq a$ and $r > a$, respectively.

$$f_\ell(kr) = \begin{cases} j_\ell(k_{\text{in}} r) & r \leq a, \\ h_\ell^{(2)}(k_{\text{out}} r) & r > a. \end{cases} \tag{9.32}$$

The Bessel function $j_\ell(k_{\text{in}} r)$ represent standing waves within the plasmonic sphere while, noting the phase convention (9.27), the Hankel function $h_\ell^{(2)}(k_{\text{out}} r)$ describes radially outward traveling waves which satisfy the Sommerfeld radiation boundary condition. The coefficient $C(r; a)$ guarantees that the boundary conditions are satisfied at the boundary of the sphere (see [198] for details)

$$C(r; a) = \begin{cases} \left[\ j_\ell(k_{\text{in}} a)\right]^{-1} & r \leq a, \\ \left[\ h_\ell^{(2)}(k_{\text{out}} a)\right]^{-1} & r > a. \end{cases} \tag{9.33}$$

Matching the interior and the exterior fields leads to the characteristic equation of the discrete eigenfrequencies of the system:

$$\epsilon_{\text{in}} \left[1 + k_{\text{out}} a \, \frac{h_\ell^{(2)'}(k_{\text{out}} a)}{h_\ell^{(2)}(k_{\text{out}} a)}\right] = \epsilon_{\text{out}} \left[1 + k_{\text{in}} a \, \frac{j_\ell'(k_{\text{in}} a)}{j_\ell(k_{\text{in}} a)}\right]. \tag{9.34}$$

Here, the prime denotes differentiation with respect to the argument of the function, i.e. $j_\ell'(k_{\text{in}} r) = \partial j_\ell(k_{\text{in}} r)/\partial(k_{\text{in}} r)$. For a given radius, different modes can be labeled by ℓ: $\omega_{0,\ell}$, where the subscript 0 denotes isolated single spheres. In case of small spherical particles, when $ka \ll 1$, considering the dipole mode $\ell = 1$, the spherical Bessel and Hankel functions can be approximated by their leading order terms: $j_1(k_{\text{in}} a) \sim k_{\text{in}} a/3$ and $h_1^{(2)}(k_{\text{out}} a) \sim i(k_{\text{out}} a)^{-2}$. Therefore the characteristic equation (9.34) reduces to $\epsilon_{\text{in}} = -2\epsilon_{\text{out}}$ which leads

to the well known resonance frequency of $\omega = \omega_p/\sqrt{3}$ for an ideal electron gas with $\epsilon_\infty = 1$ and $\gamma_s = 0$.

Next, we numerically solve eq. (9.34) for a silver sphere with a free space background. The parameters of the Drude-Sommerfeld model for silver are [196]: the plasma frequency $\omega_p = 8.9$ eV, the damping rate $\gamma_s = 0.1$ eV, and $\epsilon_\infty = 5$. The eigenfrequencies are always complex, which indicates the radiative nature of the nanospheres [199]. The real and imaginary components of the eigenfrequencies as a function of radius and for various values of $\ell = 1, 2, 3, 4$, are shown in Fig. 9.1. The real part is the frequency required to excite a mode, for instance with a laser, and the imaginary component is the associated width of the mode. For all the modes, as expected, the real component decreases monotonically as the radius increases. To see the capability of the plasmonic sphere to manipulate light in sub-wavelength dimensions consider the dipole resonance ($\ell = 1$) for a 50 nm sphere. The resonance frequency is about 3 eV corresponding to a free space wavelength of approximately 413 nm which is an order of magnitude larger than the radius of the sphere. The imaginary part of the eigenfrequencies consists of both non-radiative and radiative components, $\mathrm{Im}(\omega_{0,\ell}) = \gamma^{\mathrm{nrad}} + \gamma_\ell^{\mathrm{rad}}$. The non-radiative damping is associated with the loss within the plasmonic sphere. It was discussed in [199] that the non-radiative component can approximately be considered size-independent and is of equal value for all different modes, $\gamma^{\mathrm{nrad}} = (1/2)\gamma_s$. It is therefore clear from Fig. 9.1(b) that the dipole is the most radiative mode. For $\ell = 1$, initially the sphere becomes more radiative as the radius increases. However, larger spheres have less pronounced radiation properties. For all higher order modes, the imaginary part grows as the radius increases.

The electric field patterns of a silver sphere with a radius of 40 nm and various values of ℓ are shown in Fig. 9.2. The field values are in logarithmic scale being normalized to

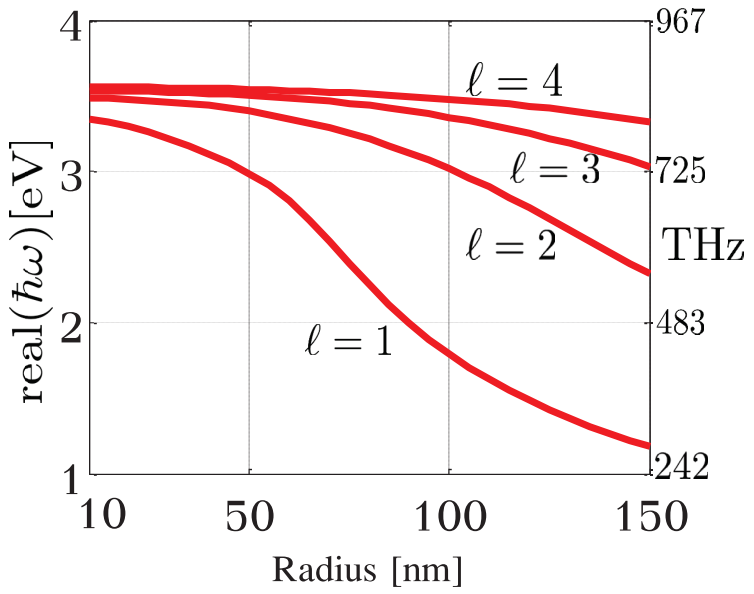

(a)

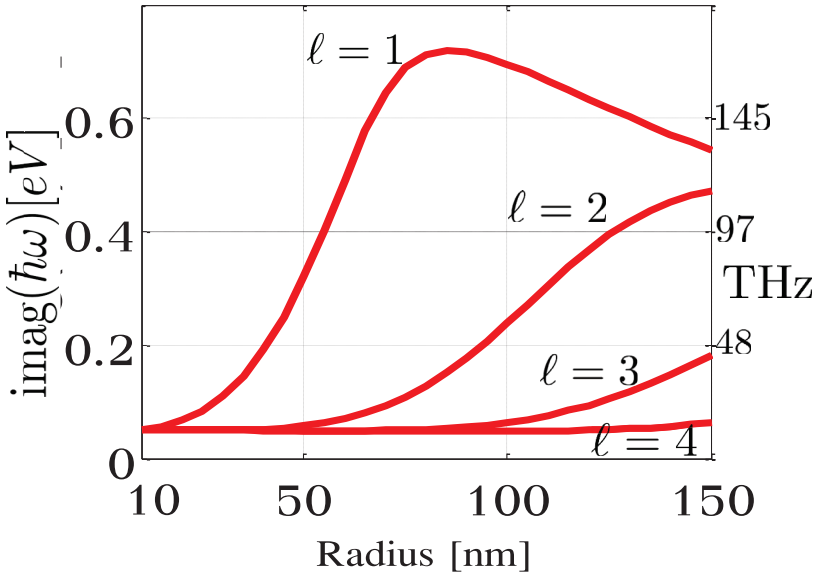

(b)

Figure 9.1: Eigenfrequencies for a metallic silver sphere with free space background as a function of radius for various ℓ values (a) real part and (b) imaginary part. The left and right axes represent values in units of eV and THz, respectively.

the maximum of the electric field. As the ℓ value increases the fields become more tightly bound to the surface of the sphere. This becomes important when we consider the coupling between two spheres in the next section.

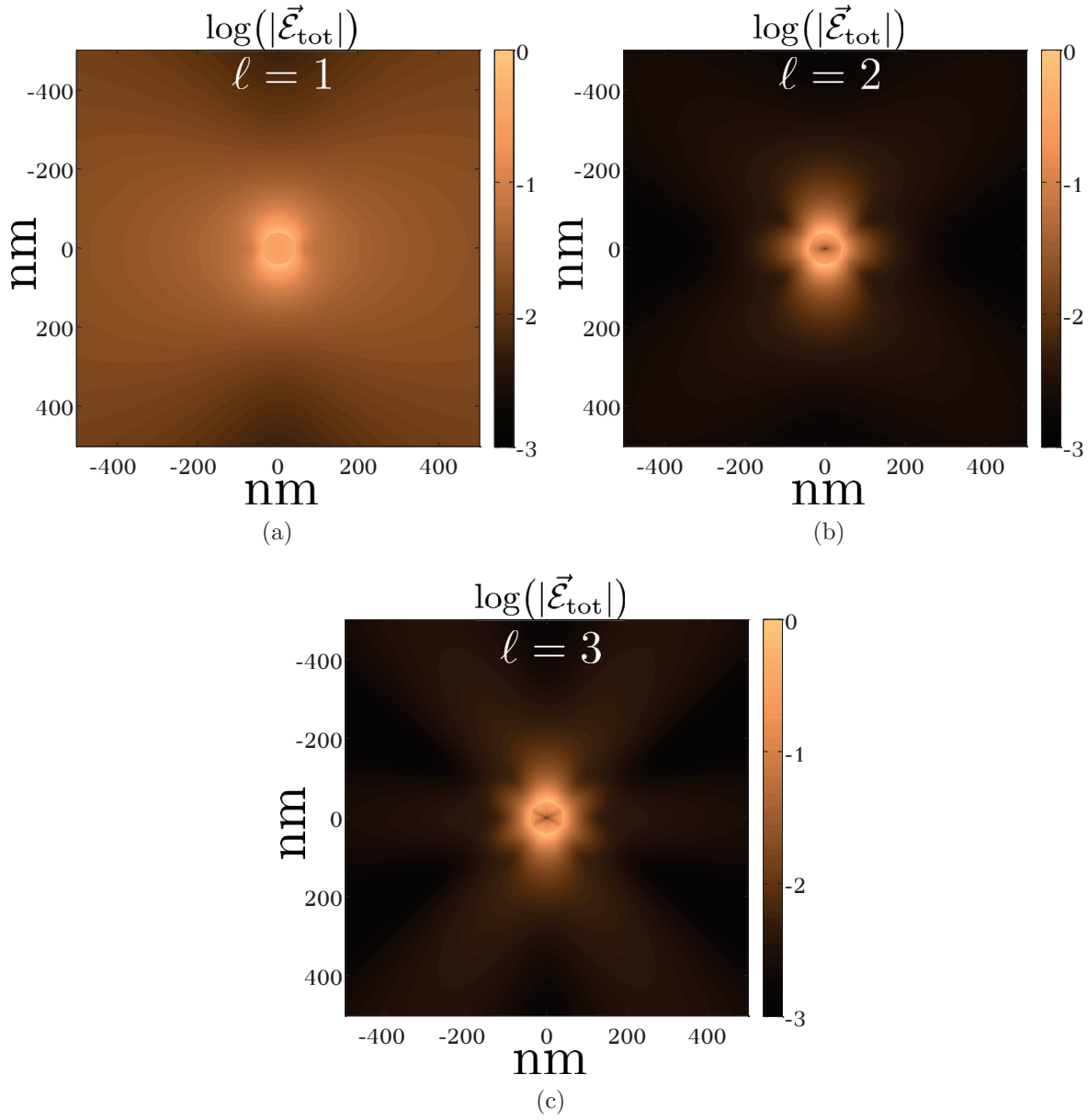

(a) (b) (c)

Figure 9.2: Electric field patterns of a silver sphere with a radius of 40 nm for (a) dipole mode, $\ell = 1$, (b) quadrupole mode, $\ell = 2$, and (c) octupole mode, $\ell = 3$. The values are normalized to the maximum of the electric field. The projection m is equal to zero for all three plots.

It is also instructive to look at the electric field pattern for the dipole mode. Fig. 9.3 represents the electric field pattern in polar coordinates for various radial distances from the center of the sphere. The black arrow represents the dipole orientation. In all six figures, ρ is the radial distance, perpendicular to the dipole axis and z is the direction along the dipole.

The blue line represents the relative field strength at a given polar angle. Furthermore, the field strength is normalized to the maximum value of the electric field. Fig. 9.3(a) shows the pattern right at the surface of the plasmonic sphere, $r/a = 1$. Closer to the surface of the sphere the fields reach the maximum along the direction of the dipole. At $r/a = 3$ and $r/a = 5$ the patterns are almost omnidirectional (see Figs. 9.3(b) and (c)). The well known doughnut shape radiation pattern of the dipole only emerges in the far field. This is shown in Figs. 9.3(d), (e) and (f).

The eigenmodes and plasmonic resonances of single metallic nanospheres of various sizes and the effect of different background dielectrics have been considered in detail in [201] for gold nanoparticles and in [200] for alkali metals such as sodium, lithium and Cesium; see [199] for a more detail description of the size dependency properties of nanospheres. Below we consider the case of two identical plasmonic spheres and discuss the coupling between them and the eigenmodes of the system.

9.4 Superradiant and Dark States in System of Two Coupled Spheres

We now consider the case of two coupled metallic spheres within the coupled mode theory framework discussed earlier. The interaction between the spheres can greatly alter the radiation properties of the system and result in resonance frequencies profoundly different from those for the isolated spheres. Here, we limit our consideration to the dipole modes only. This is justified by the earlier discussion that the dipole mode is the most radiative mode and also has the longest range compared to higher multipolarities. The isolated frequencies discussed in the previous section serve as the diagonal elements in the coupled mode

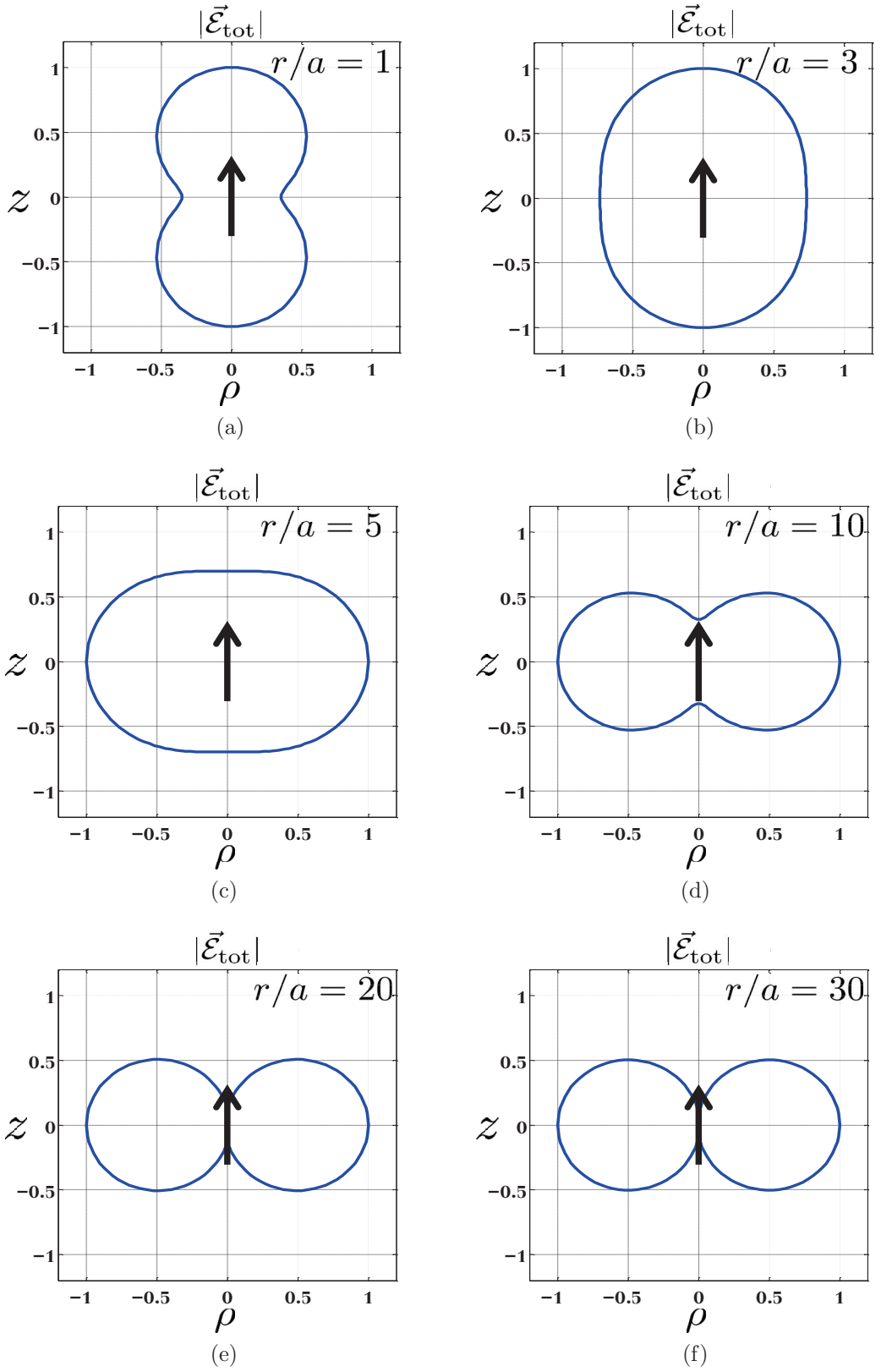

Figure 9.3: Electric field pattern for (a) $r/a = 1$, (b) $r/a = 3$, (c) $r/a = 5$, (d) $r/a = 10$, (e) $r/a = 20$, and (f) $r/a = 30$. ρ is the radial distance and z is the direction along the dipole. The values are normalized with respect to the maximum of the electric field.

matrix (9.24). The real and imaginary components of the dipole eigen mode are the diagonal elements of the Hermitian (9.25) and the anti-Hermitian (9.26) matrices, respectively. The coupling between two modes, κ, makes up the off-diagonal matrix elements of the final matrix (9.24).

However, a difficulty arises due to the normalization of the single sphere modes. In the far field region, $k_{\text{out}}r \gg 1$, the spherical Hankel functions behave asymptotically as

$$h_\ell^{(2)}(k_{\text{out}}r) \approx (i)^{\ell+1}\frac{e^{-ik_{\text{out}}r}}{k_{\text{out}}r}. \tag{9.35}$$

Because of the complex nature of the eigenfrequencies, the asymptotic form of the fields given by (9.35) grows exponentially in space as $r \to \infty$. This growth is however compensated by the exponential decay in time in the complete expression of the field (9.27) when the time dependency is considered. As a result the amplitude of the wave front of the total field (9.27) reaching any point in the asymptotic region is proportional to $1/r$, as it is expected. Nevertheless, the modes (9.31) should be properly normalized. The correct normalization of such modes was discussed in [202–204] for one-dimensional problems. The generalization to three dimensions by three different methods is discussed in [205], [206], and [207]. However, in [208], it was shown that all three expressions are compatible.

The normalization condition is given by [208]:

$$\int_V \sigma(\vec{r},\omega)\vec{\mathcal{E}}(\vec{r}).\vec{\mathcal{E}}(\vec{r})d^3r + \frac{i\epsilon_{\text{out}}}{2k}\int_{\partial V}\vec{\mathcal{E}}(\vec{r}).\vec{\mathcal{E}}(\vec{r})d^2r = 1 \tag{9.36}$$

where V is the integration volume and ∂V is its surface. The integration volume is assumed to be sufficiently large, so the fields at its surface are accurately approximated by asymptotic

expressions of the spherical Hankel function provided in (9.35). The modified dielectric function $\sigma(\vec{r},\omega)$ which incorporates the dispersiveness of the medium is given, according to [209] as

$$\sigma(\vec{r},\omega) = \frac{1}{2\omega}\frac{\partial}{\partial\omega}\Big(\omega^2\epsilon(\vec{r},\omega)\Big). \tag{9.37}$$

Contrary to the normalization discussed earlier, the dot-product in (9.36) does not require any complex conjugation of the fields. It is therefore easier to use the so-called tesseral harmonics instead of the conventional spherical harmonics in the field expression (9.31). The tesseral harmonics (sometimes also called real spherical harmonics) are nothing but even and odd superpositions of the traditional spherical harmonics, see Appendix C. The normalization condition (9.36) defines the constant ζ in the field expressions (9.31) up to a phase. It is shown in Appendix B that assuming the volume of integration as a sphere, the volume and surface terms in the normalization expression can be evaluated explicitly. It is furthermore proved in the same appendix that the condition (9.36) reduces to:

$$I\big[j_\ell(k_{\text{in}}a)\big] - I\big[h_\ell^{(2)}(k_{\text{out}}a)\big] = 1, \tag{9.38}$$

where the functional $I\big[f_\ell(kr)\big]$ is given by (B.5)

$$I\big[f_\ell(kr)\big] = \sigma(\vec{r},\omega)\ \xi^2\ C^2(r;a)\frac{\ell(\ell+1)}{k^2}\bigg[rf_\ell^2(kr) + kr^2 f_\ell(kr)f_\ell'(kr) \tag{9.39}$$

$$+\frac{k^2r^3}{2}\Big(f_\ell^2(kr) - f_{\ell-1}(kr)f_{\ell+1}(kr)\Big)\bigg]. \tag{9.40}$$

Once the normalization constant ζ is found the coupling between two modes can be

calculated according to

$$\kappa = -\frac{1}{2}\omega_0 \int_{V_1} \big(\epsilon_1(\vec{r}) - 1\big)\vec{\mathcal{E}}^1(\vec{r}).\vec{\mathcal{E}}^2(\vec{r})d^3r, \tag{9.41}$$

where V_1 is again the volume of sphere 1. Contrary to (9.20), the fields from both spheres are treated on equal footing and no complex conjugation is required due to the normalization definition (9.36).

In what follows we show the eigenfrequencies of a system of two coupled spheres with different sizes and for different separation distances. The coupling κ is calculated numerically and the coupled mode matrix is constructed and diagonalized. In the first case two identical silver spheres with radii of 10 nm are considered and the eigenfrequencies of the system are calculated for two different dipole orientations and as a function of the separation distance between the spheres. It is important to note that due to the symmetry of the dipole modes, dipoles with perpendicular orientations do not couple. Therefore we consider two orthogonal orientations only.

Fig. 9.4(a) shows the case where the two dipoles are parallel (vertical orientation). Both the real and imaginary components of the eigenfrequencies are plotted as a function of the separation d between the two spheres normalized by the sphere radius a. The maximum coupling occurs when the two spheres are in contact with one another which in turn results in the largest deviation from the unperturbed frequency of a single sphere (dotted black lines). As the separation increases, the coupling decreases and the two eigenfrequencies approach the unperturbed eigenmode. A similar phenomenon is seen for the case of two dipoles in Fig. 9.4(b) (horizontal orientation). However, for a specific separation distance between the spheres, the splitting of the two eigen modes is larger compared to the previous

case. This is because, as shown in the previous section, the electric field is maximum along the dipole direction in the near field (see Fig. 9.3). Consequently, this orientation results in larger coupling coefficients between the spheres.

According to our findings in the previous section, silver spheres with larger diameters are more radiative. It is therefore desirable to look at the case of coupling between larger spheres since the coupling is stronger. Fig. 9.5 shows the eigenfrequencies of a system of two silver spheres with radii of 40 nm. We only consider the case of the horizontal dipole orientation when that the coupling coefficient is larger. The difference between the superradiant and subradiant states is more pronounced in this case. At $d/a \approx 3$ there is a distinct difference between the imaginary components of the two eigen modes. Similar to the previous case, the two eigen frequencies approach the unperturbed resonance as the separation distance increases.

According to our calculations, an exact dark mode does not exist for a system of two silver plasmonics dipoles. Therefore a numerical search over the parameters of the Drude-Sommerfeld dielectric function (9.30) was performed in order to find material properties for which two plasmonic spheres can support a dark mode. Fig. 9.6 shows the eigenfrequencies of a system of two spheres with Drude-Sommerfeld parameters of $\epsilon_\infty = 1$, $\omega_p = 10.918$ eV and $\gamma_s = 0$. At $d/a \approx 3.5$, the rank of the anti-Hermitian part of the coupled mode matrix is almost unity indicating that the interaction between the two spheres occurs through a single continuum channel. Consequently, the imaginary component of the subradiant mode is extremely small, in the order of 10^{-3} eV. This is indicated with a black circle in the figure.

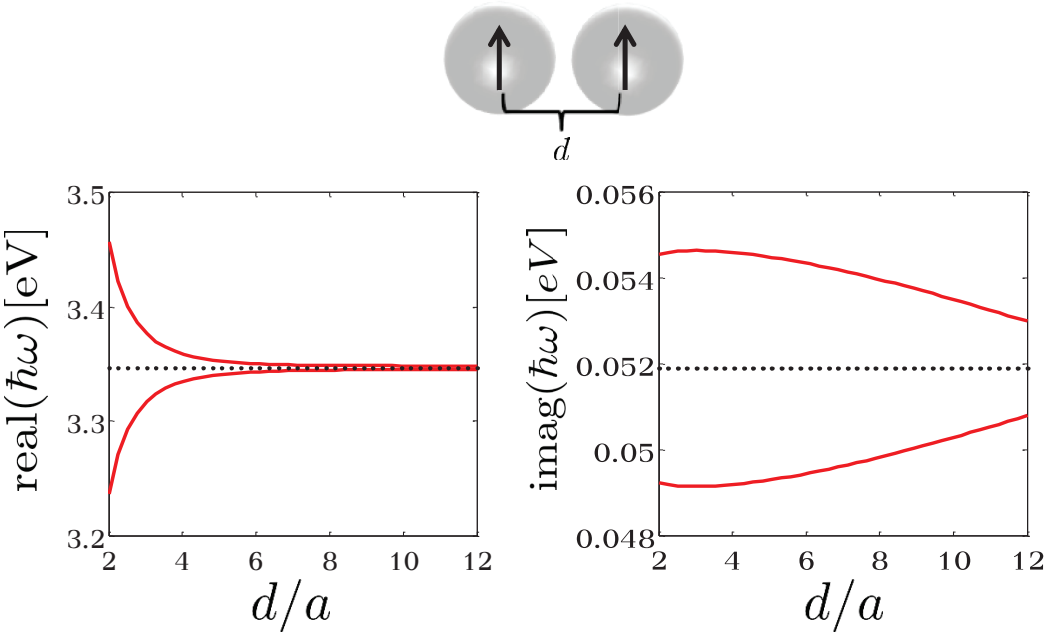

(a)

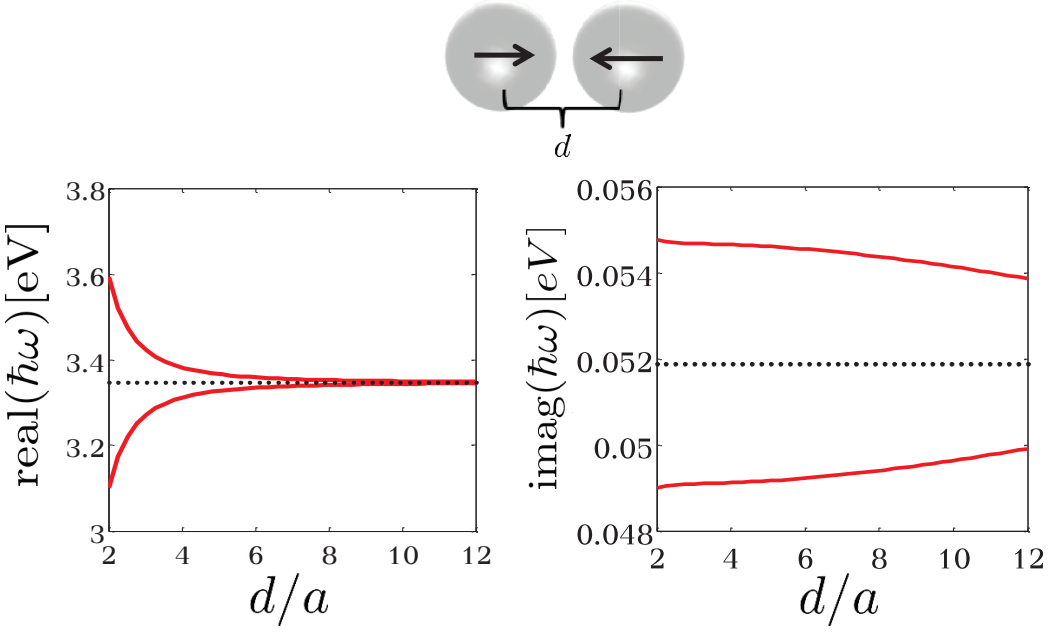

(b)

Figure 9.4: Real and imaginary components of the eigenfrequencies of a system of two coupled identical silver spheres with (a) vertical and (b) horizontal dipole orientations. The radii of the spheres are 10 nm. d is the center-to-center separation and a is the radius of the spheres. The black dotted lines represent the unperturbed eigenfrequency of a single sphere.

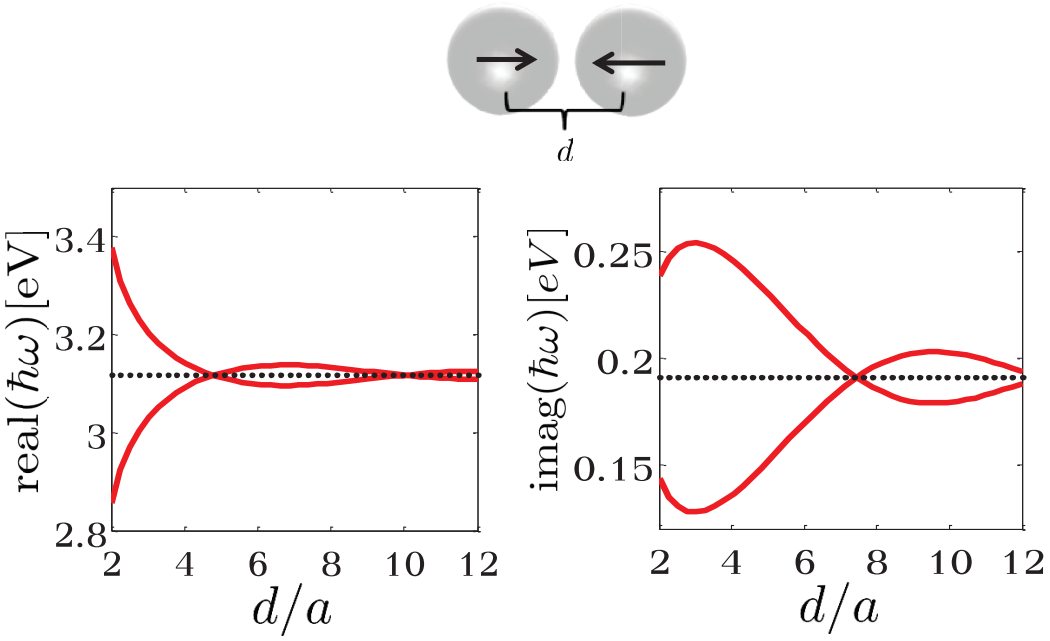

Figure 9.5: Real and imaginary components of the eigenfrequencies of a system of two coupled identical silver spheres with horizontal dipole orientation. The radii of the spheres are 40 nm. d is the center-to-center separation and a is the radius of the spheres. The black dotted lines represent the unperturbed eigenfrequency of a single sphere.

9.5 Plasmonic Waveguide

We now consider the signal transmission through a plasmonic waveguide, namely a one-dimensional chain of identical spheres. It is assumed that the two edges of the waveguide are connected to an instrument capable of exciting the system of spheres with frequency ω_e and measuring the electric field intensity. Fig. 9.7 depicts the schematic of the plasmonic waveguide and the two probes symmetrically coupled to the edges of the chain with coupling constants γ_e. Similar to the tight binding model of crystals in condensed matter physics, it is further assumed that each sphere in the chain only interacts with its nearest neighbor.

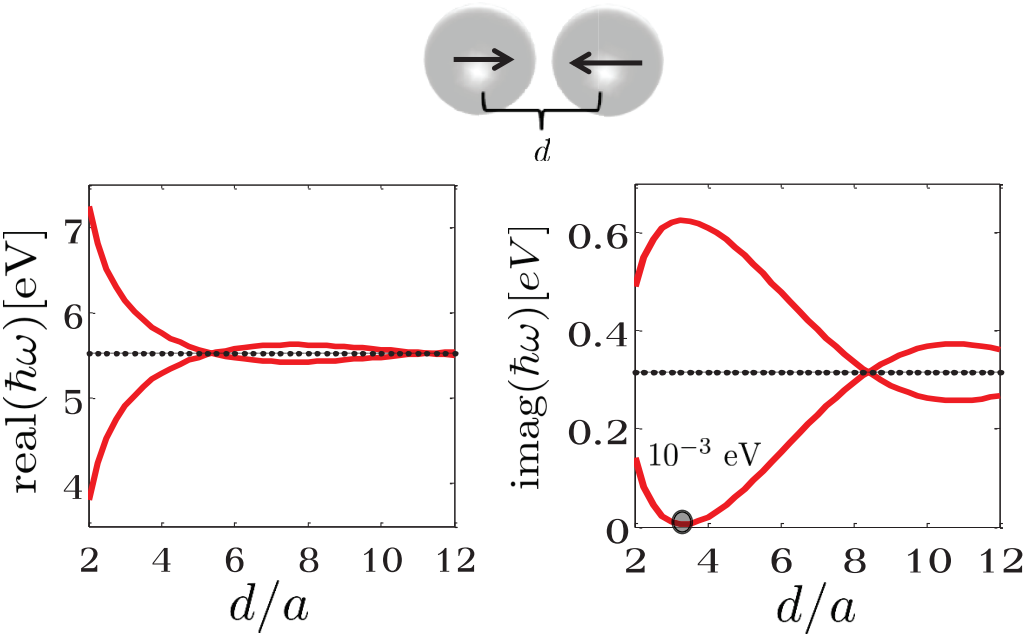

Figure 9.6: Real and imaginary components of the eigenfrequencies of a system of two coupled identical spheres with horizontal dipole orientation. The material properties of the sphere are: $\epsilon_\infty = 1$, $\omega_p = 10.918$ eV and $\gamma_s = 0$. The radii of the spheres are 20 nm. d is the center to center separation and a is the radii of the spheres. The black dotted lines represent the unperturbed eigenfrequency of a single sphere.

This system can be modeled with the effective non-Hermitian Hamiltonian (6.8)

$$\mathscr{H}_{\text{eff}} = \begin{bmatrix} \frac{i}{2}\gamma_e + \omega_0 & \kappa & 0 & \dots & 0 & 0 \\ \kappa & \omega_0 & \kappa & \dots & 0 & 0 \\ 0 & \kappa & \omega_0 & \kappa & \dots & 0 \\ \vdots & \vdots & \vdots & \ddots & \vdots & \vdots \\ 0 & 0 & 0 & \dots & \kappa & \frac{i}{2}\gamma_e + \omega_0 \end{bmatrix}, \tag{9.42}$$

where ω_0 is the unperturbed dipole frequency of the spheres, and κ is the coupling coefficient (9.41) between adjacent dipoles. It is important to mention that the addition of the anti-Hermition matrix elements, $\frac{i}{2}\gamma_e$, with a positive sign is due to the phase convention adopted

earlier in (9.27).

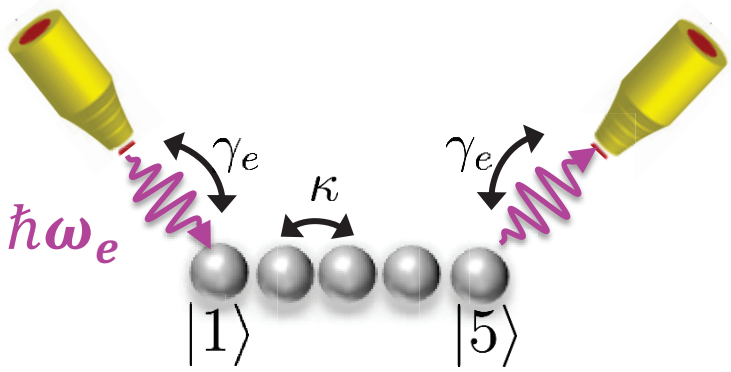

Figure 9.7: Schematics of a plasmonic waveguide; a one-dimensional chain of five silver spheres with nearest neighbor coupling κ. The two edges are symmetrically coupled to continuum, the excitation source with frequency ω_e, with coupling coefficient γ_e.

Through its coupling to the two probes, the system can undergo an additional superradiance phase transition, other than that discussed in the previous section. This is illustrated by considering two different plasmonic waveguides. In both cases, according to our findings in the last section, in order to maximize the coupling between the neighboring sites the spheres are in contact with one another and the dipole orientation of the spheres is considered to be along the waveguide (horizontal orientation). In the first case, a chain of five silver spheres with radii of 10 nm is considered (Fig. 9.7). The resulting effective Hamiltonian (9.42) describing the system is a 5x5 square matrix with diagonal elements, $\omega_0 = 3.3468 + i0.0519$ eV, and off-diagonal matrix elements $\kappa = -0.2459 + i0.0029$ eV. The continuum coupling coefficient γ_e is treated as a variable that changes from small, $\gamma_e = 0.01$ eV, to extreme values $\gamma_e = 10$ eV. The evolution of the complex eigenvalues of the effective Hamiltonian as the coupling to the continuum varies is shown in Fig. 9.8(a). At small values of γ_e all the eigenvalues acquire a small width through the coupling to the continuum. The widths of the complex eigenmodes almost uniformly increase as the system is more strongly coupled

to the continuum. However, the situation changes dramatically at $\gamma_e \approx 1$. The eigenvalues have reached their maximum width and, with further increasing γ_e, the system undergoes a phase transition (superradiance transition) when the eigenmodes become segregated into two distinct categories: superradiant and subradiant states. At strong coupling, the two superradiant states, their number being equal to the number of continuum channels (two probes), steal the entire available width of the system and leave the remaining states as narrow resonances.

The second waveguide differs only in the size of the spheres which have radii of 40 nm. In this case, the diagonal unperturbed frequencies are $\omega_0 = 3.1172 + i0.1910$ eV and the off-diagonal coupling coefficients are $\kappa = -0.2606 + i0.0475$ eV. The continuum coupling γ_e is again varied from $\gamma_e = 0.01$ eV to $\gamma = 10$ eV, and the complex eigenvalues are plotted in Fig. 9.8(b). In general the picture is similar to the previous case. The superradiant transition can be clearly seen as the coupling γ_e increases to extreme values.

We now study the propagation of a signal through the two waveguides using the transmission coefficient (6.12). Using (6.11) and (6.12) we arrive at the following expression for the transmission coefficient

$$T(\hbar\omega_e) = \left| \frac{\gamma_e/\kappa}{\prod_{r=1}^{N} \left[(\hbar\omega_e - \hbar\omega_r)/\kappa\right]} \right|^2, \tag{9.43}$$

where ω_r are the complex frequencies of the effective Hamiltonian (9.42) and N is its dimension.

Transmission as a function of the excitation frequency, ω_e, is shown in Fig. 9.9 for the waveguide with 10 nm spheres. At weak coupling to the continuum, $\gamma_e = 0.03$ eV, Fig. 9.9(a), the five resonances are distinguishable. However, the resonances are not well

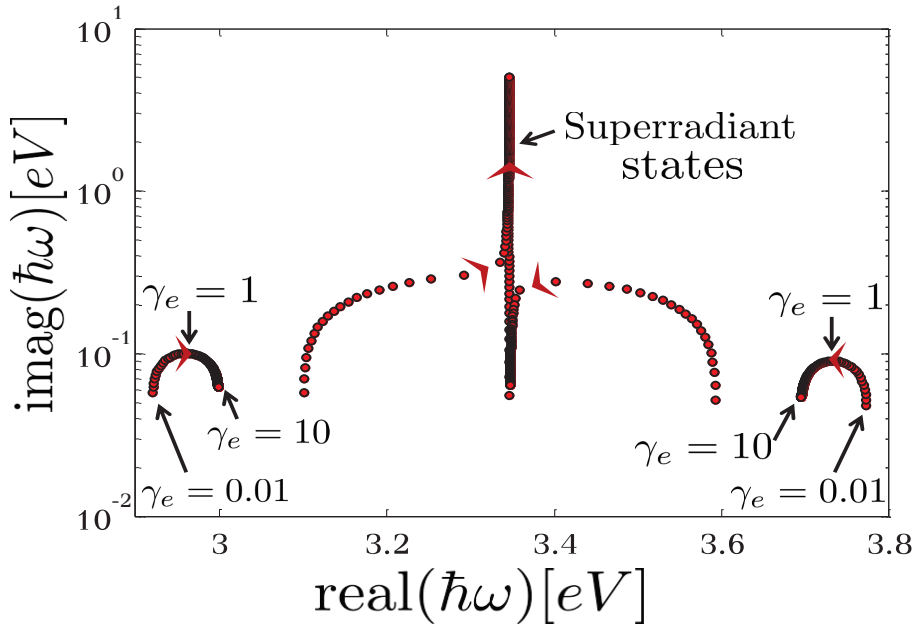

(a)

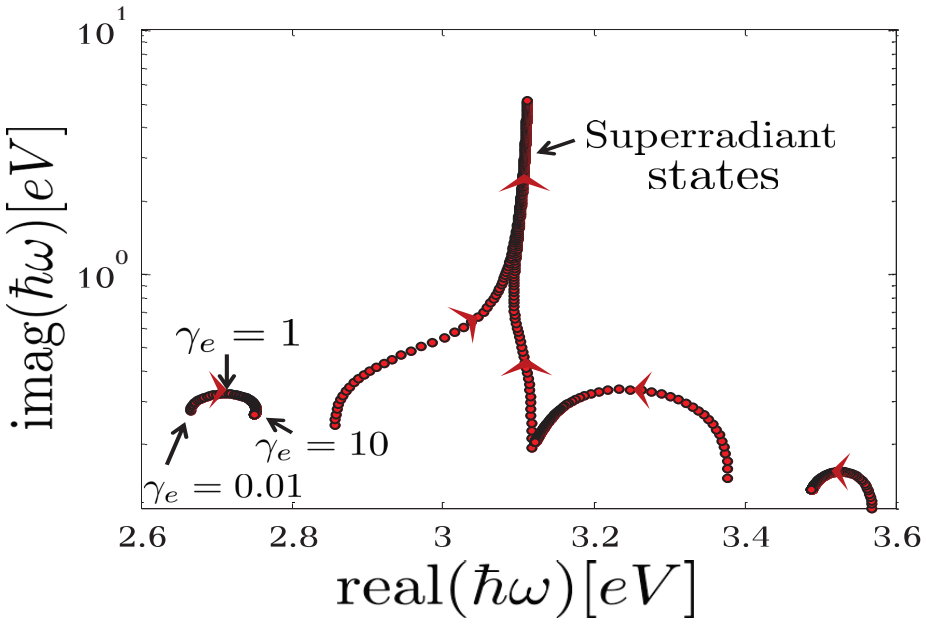

(b)

Figure 9.8: Complex-plane trajetories of the effective Hamiltonian for a one-dimensional chain of five identical silver spheres with radii of (a) 10 nm and (b) 40 nm. The spheres are in contact with one another and the dipoles are oriented along the waveguide. The arrows show the direction of the evolution as γ_e changes from 0.01 eV to 10 eV.

separated due to the complex coupling coefficient between spheres, κ, which provide the eigenvalues of the effective Hamiltonian an initial width even for the closed system ($\gamma_e = 0$). The case of intermediate coupling when $\gamma_e = 0.55$ eV is shown in Fig. 9.9(b). This is when the system is on the road to superradiance transition and all the eigenvalues of the Hamiltonian have large widths. Consequently, the resonances overlap and the transmission is dramatically enhanced. The case of strong couplings, Fig. 9.9(c), has a picture similar to that of the weak coupling case. However, only three resonances are remained. The two giant superradiant states do not participate in signal transmission and transmission is greatly suppressed due to the small width of the remaining subradiant states.

We follow the same steps of weak, intermediate and strong coupling to continuum in order to study transmission through the waveguide with 40 nm spheres. Due to larger coupling, κ, between adjacent spheres the eigenvalues of the effective Hamiltonian poses a relatively large initial width even for small coupling to the continuum. Therefore, contrary to the previous case, the resonances overlap and are not separated even at weak coupling, Fig. 9.10(a). Similar to before, the transmission is greatly enhanced at the superradiance transition, and at extreme couplings, we are back to suppressed transmission.

9.6 Discussion

We studied the resonant frequencies of plasmonic spherical nanoantennas by solving the full wave equation. These eigenfrequencies are always complex due to radiation and damping. Utilizing the non-Hermitian effective Hamiltonian framework, it was shown that a system of coupled two spheres can have modes with distinct properties; a superradiant mode with enhanced radiation and a dark mode with extremely damped radiation.

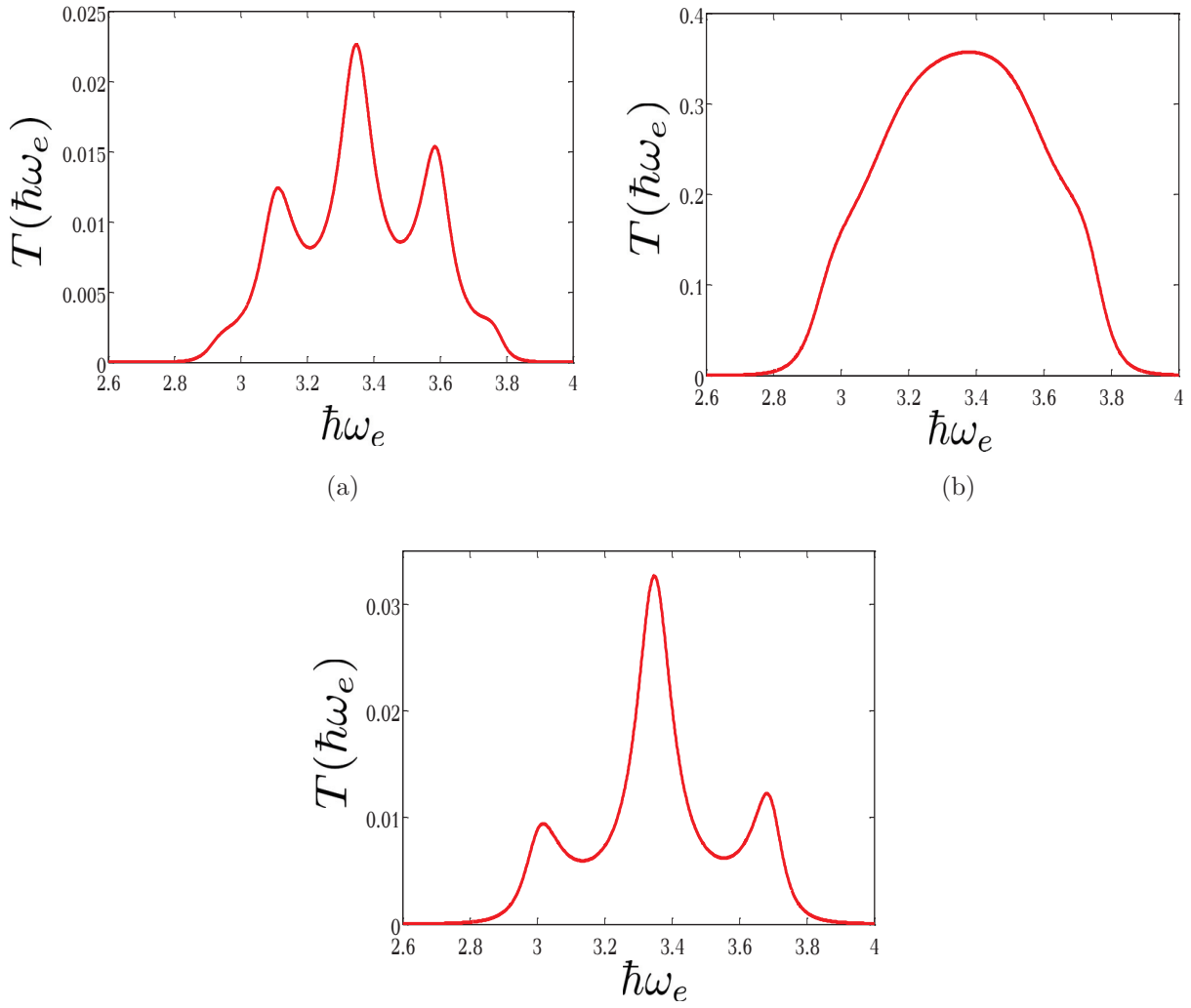

Figure 9.9: Transmission through a one-dimensional chain of five identical spheres with radii of 10 nm as a function of excitation source frequency ω_e for (a) γ_e =0.03 eV, (b) γ_e =0.55 eV, and (c) γ_e =10 eV.

Signal transmission through one dimensional chains was also considered. The coupling of the edge spheres to the continuum can drastically change transport properties of the system. A different superradiant transition arises through this interaction. Transmission is greatly enhanced at this transition.

A possible direction to improve the accuracy of the results is to modify the Drude-Sommerfeld model by including terms that take into account surface scattering effects. It

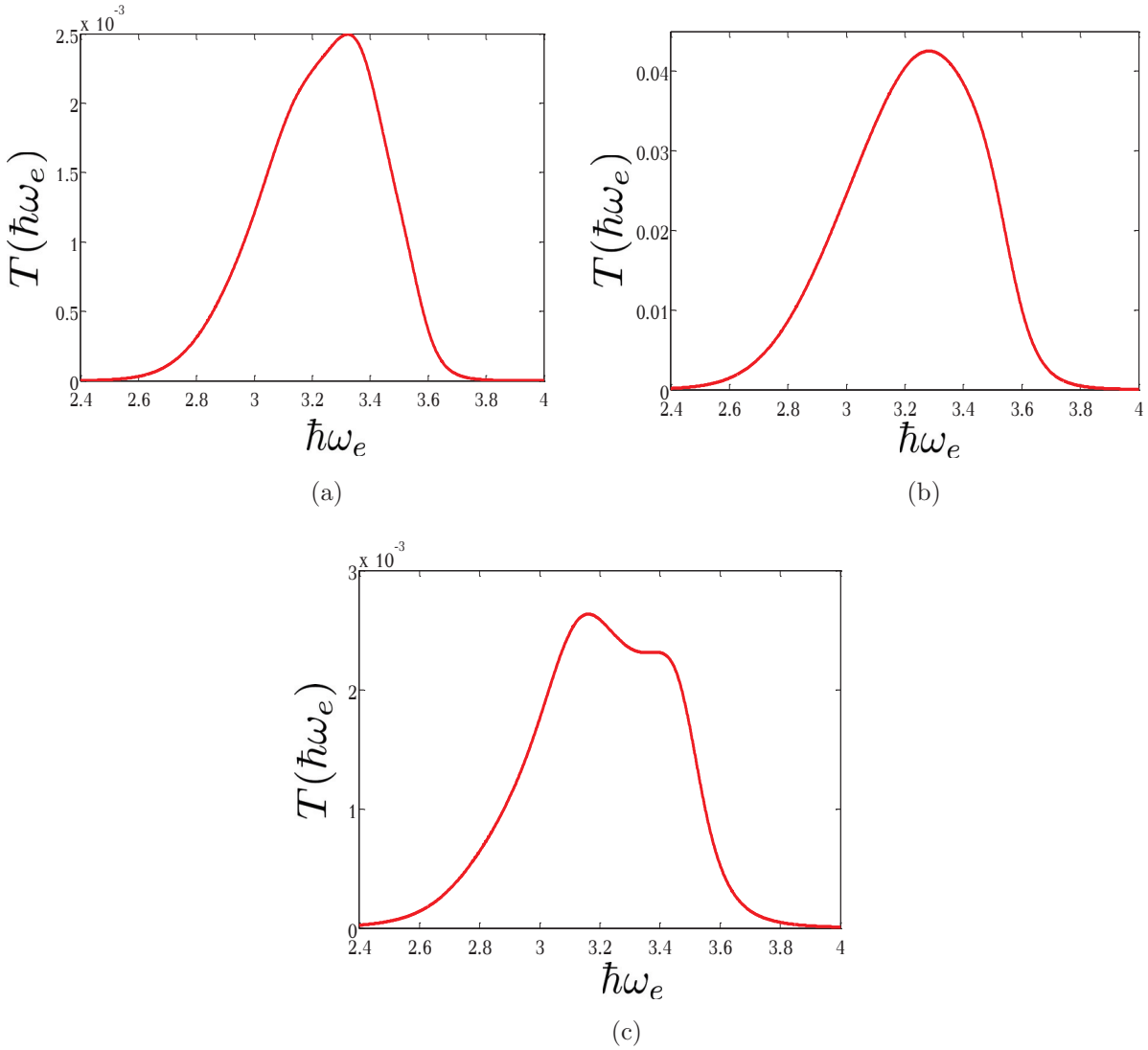

Figure 9.10: Transmission through a one-dimensional chain of five identical spheres with radii of 40 nm as a function of excitation source frequency ω_e for (a) γ_e =0.05 eV, (b) γ_e =0.7 eV, and (c) γ_e =10 eV.

would be interesting to study the contribution of surface scattering to the total damping and radiation of the nanospheres. Another possibility is to consider higher order modes and their effect on the eigenfrequencies of the coupled system. These are left for the future.

Part 4

Conclusion and Future Work

To achieve great things, two things are needed; a plan, and not quite enough time.

Leonard Bernstein

Chapter 10

Conclusion

10.1 Summary

10.1.1 The Novel Microwave Imaging System

In the first part of this thesis, a novel microwave imaging system was proposed. The primary component of the system is a tunable reflectarray antenna with high beam steering capabilities. The unit cell of the array operates at two frequency bands and requires only one varactor diode to dynamically alter the phase of the scattered field. This significantly reduces the manufacturing cost of the array compared to more complicated designs that require multiple varactors. The unit cell was evaluated using both full-wave simulations and equivalent circuit modeling. The equivalent circuit provides a simple description of the unit cell in terms of passive circuit components and requires far less computation time compared to the full wave simulations. The 10x10 reflectarray built using the proposed unit cell shows excellent steering capabilities. The beam can be deflected up to $\pm 60^{\circ}$ in both frequency

bands. This steering range has not yet been reported in literature.

The inclusion of the beam scanning array in the proposed microwave imaging system significantly reduces cost and operational complexities compared to traditional setups. In conventional systems, the region of interest is enclosed by a costly array of transceiver antennas which additionally requires a complicated switching circuitry. Our design eliminates the need for multiple antennas and the involved circuitry. In addition, there is no constraint on the size of the object under test. Consequently, the inspection of large objects such as airplane wings and wind turbine blades would be achievable.

A prototype of the imaging system was built and experimentally verified. Using the time reversal signal processing technique, the system was able to detect and locate cylindrical targets of different sizes and positions. The system was also used for NDE applications aimed at detecting different types of anomalies in dielectric materials. Specifically, two types of anomalies were considered in the thesis: defects and metallic impurities. It was demonstrated that the system was capable of accurately detecting both defects and impurities.

10.1.2 Superradiance in Open Quantum Systems

In the second part of the thesis the following three problems,

1. quantum transport through one-dimensional nanostructures,

2. quantum computation with a novel solid state charge qubit and,

3. plasmonic nanoantennas and waveguides,

were investigated within the framework of the non-Hermitian Hamiltonian. This approach provides an alternative to popular methods such as the Feynman diagrammatic techniques

and the master equation approach that are commonly used for studying open quantum systems. Not only is the suggested method less complex, it also reveals new physics, namely the sharp redistribution of decay widths and the emergence of short-lived "superradiant" states for sufficiently strong coupling to the continuum. The effects of the emergence of superradiant states on the properties of the system and various observables were discussed in detail for all three problems. It was shown that quantum signal transmission is greatly enhanced at the superradiance transition. The superradiance phenomenon is also responsible for the longer lifetime and protection of the internal states of the proposed qubit against noise and decoherence. Finally, the superradiance transition provided a tool to manipulate light via plasmonic structures and control the properties of nanoantennas and waveguide. These findings can have a significant impact on the future of the semiconductor, quantum computation, and imaging industries. Transistors could be engineered to be more power efficient. Noise-resistant solid state qubits could maintain coherence much longer than gate operation times and plasmonic field enhancement via superradiance in sub-wavelength dimensions could improve imaging resolution and sensing capabilities.

10.2 Future Work

10.2.1 The Novel Microwave Imaging System

One possible direction to improve the capability of the proposed system is to leverage the 3D beam steering ability of the reflectarray. This can be achieved by controlling individual unit cells of the array as opposed to entire columns in the two dimensional case. Therefore, while the prototype was used in a 2D setup, it can be readily extended to 3D applications. One can also increase the beam steering range and go beyond $\pm 60^{\circ}$ and achieve larger gain

values by extending the surface area of the reflectarray and increasing the number of unit cells.

Another possible improvement to the existing system would be to enhance the image reconstruction technique. Though time reversal signal processing is fast, robust, and simple, one drawback is the need for prior knowledge of a healthy sample, which is unavailable in many cases. A potential solution would be to utilize more advanced reconstruction algorithms such as limited angle tomographic techniques [87, 88, 211, 212]. This would allow for a reconstruction of target spatial profiles, moving beyond mere defect detection. Moreover, the system can be easily scaled to operate in other frequency bands to detect targets and defects with smaller or larger dimensions. It therefore has a range of potential applications such as medical imaging, defect detection in extended composite materials, et cetera. These are left for future studies.

10.2.2 Superradiance in Open Quantum Systems

With regard to the quantum transport problem and the models discussed in this thesis, there are many possibilities to enrich the prototypical models. For a realistic situation, for example a chain of quantum dots, one should carefully determine the lifetimes of the qubit states. The geometry of the system can be made more complicated in various ways including the transition to more-dimensional schemes. More qubits and more branches can be added approaching a complicated network. It would be also interesting to extend the ideology of an open quantum system to the study of coherent photon transport in continuous waveguides and circuit quantum electrodynamics.

Another possibility is the inclusion of vibrational modes [122] and their coupling to electrons. In many physical systems such as bio and DNA molecules electron-phonon interaction

plays a significant role in the transport properties. The same can be considered for the proposed qubit. More accurate calculations of lifetime and decoherence can be made by explicitly considering the interaction between electrons and phonons instead of the assumptian made in this thesis, i.e. random gaussian noise.

The results found in the plasmonic problem need to be verified against exact numerical solutions. Even though the coupled mode theory is intensively used within the optic and plasmonic community it is necessary to verify the results against numerics since the coupled mode framework is essentially a perturbation theory. It is also important to consider higher order modes in the perturbation expansion. These are left for the future.

APPENDICES

Appendix A

The Stochastic Liouville Equation

Here we provide a simple derivation of the stochastic Liouville equation using perturbation theory. The case considered here is a special case of the more general model where the presence of phonons was accounted for by a heat bath affecting the electrons in a stochastic fashion. Similarly, we include the vibrational effects, which lead to dephasing, by the addition of the time-dependent Hamiltonian (8.27). Fluctuations of electronic energies are modeled using Gaussian processes with the standard stochastic properties (8.28) and (8.29). The total Hamiltonian is then $H = \mathcal{H} + H_\phi$ and the evolution of the density operator is governed by the von Neumann equation,

$$\dot{\rho} = -i[H, \rho]. \tag{A.1}$$

Next we define superoperators $\mathcal{L}_{\text{eff}}$ and $\mathcal{L}_\phi$ according to

$$\mathcal{L}_{\text{eff}}\rho = [\mathcal{H}, \rho], \tag{A.2}$$

$$\mathcal{L}_\phi\rho = [H_\phi, \rho]. \tag{A.3}$$

The von Neumann equation (A.1) in terms of the superoperators reads

$$\dot{\rho} = -i\mathcal{L}\rho = -i(\mathcal{L}_{\text{eff}} + \mathcal{L}_\phi)\rho. \tag{A.4}$$

Using

$$\rho^I(t) = e^{i\mathcal{L}_{\text{eff}}t}\rho(t), \tag{A.5}$$

$$\mathcal{L}_\phi^I = e^{i\mathcal{L}_{\text{eff}}t}\mathcal{L}_\phi e^{-i\mathcal{L}_{\text{eff}}t}, \tag{A.6}$$

the time evolution equation, (A.4), transforms to the interaction picture,

$$\frac{\partial}{\partial t}\rho^I(t) = -i\mathcal{L}_\phi^I\rho^I. \tag{A.7}$$

The solution of eq. (A.7) up to the second order in the perturbation expansion is

$$\begin{aligned}\rho^I(t) =&\rho^I(0) - i\int_0^t dt'\mathcal{L}_\phi^I(t')\rho^I(0)\\ &+ i^2\int_0^t dt'\int_0^{t'} dt''\mathcal{L}_\phi^I(t')\mathcal{L}_\phi^I(t'')\rho^I(0).\end{aligned} \tag{A.8}$$

This formal solution only makes sense after averaging over the ensemble. Using the properties of the bath given in eqs. (8.28) and (8.29) we have

$$\langle\rho^I(t)\rangle = \rho^I(0) - \int_0^t dt'\int_0^{t'} dt''\langle\mathcal{L}_\phi^I(t')\mathcal{L}_\phi^I(t'')\rangle\rho^I(0). \tag{A.9}$$

Differentiating (A.9) we arrive at the equation of motion for $\langle\rho^I(t)\rangle$,

$$\frac{\partial}{\partial t}\langle\rho^I(t)\rangle = -\int_0^t dt'\langle\mathcal{L}_\phi^I(t)\mathcal{L}_\phi^I(t')\rangle\langle\rho^I(t)\rangle. \tag{A.10}$$

In obtaining (A.10) it was assumed that the bath memory is short compared to the time scales of the density operator. Therefore $\rho^I(0)$ was replaced by $\langle\rho^I(t)\rangle$. Evaluating the

integral with the help of (8.29) and using the definition provided in (A.2) we arrive at

$$\frac{\partial}{\partial t}\langle\rho^I(t)\rangle = -\alpha_\phi \sum_j \Big[(c_j^I)^\dagger c_j^I, \big[(c_j^I)^\dagger c_j^I, \langle\rho^I(t)\rangle\big]\Big], \tag{A.11}$$

where j runs over cells, $n = -N, ..., -1, 1, ..., N$, as well as the excited states of the central qubits, L and R. Going back to the Schrödinger picture we have

$$\frac{\partial}{\partial t}\langle\rho(t)\rangle = -i\mathcal{L}_{\text{eff}}\langle\rho(t)\rangle - \alpha_\phi \sum_j \Big[c_j^\dagger c_j, \big[c_j^\dagger c_j, \langle\rho(t)\rangle\big]\Big]. \tag{A.12}$$

Finally, by calculating the matrix element of the density operator in the site representation, we arrive at the expression given in (8.30),

$$\frac{\partial}{\partial t}\langle\rho(t)\rangle_{i,j} = -i\big[\mathcal{H}_{\text{eff}}, \langle\rho(t)\rangle\big]_{i,j} - 2\alpha_\phi(1-\delta_{i,j})\langle\rho(t)\rangle_{i,j}. \tag{A.13}$$

Even though we have used perturbation expansion to derive the above stochastic Liouville equation, the final result is exact [158] due to the Markovian character of the random process, eqs. (8.28) and (8.29).

Appendix B

Quasi Normal Modes Normalization

In this appendix we explicitly normalize the fields of a plasmonic sphere by evaluating the normalization expression (9.36)

$$\int_V \sigma(\vec{r},\omega)\vec{\mathcal{E}}(\vec{r}).\vec{\mathcal{E}}(\vec{r})d^3r + \frac{i\epsilon_{\text{out}}}{2k}\int_{\partial V}\vec{\mathcal{E}}(\vec{r}).\vec{\mathcal{E}}(\vec{r})d^2r = 1. \tag{B.1}$$

Due to the homogeneity of the sphere dielectric function ϵ_{in}, and the surrounding background ϵ_{out}, the modified dielectric function $\sigma(\omega)$ given in (9.37) is only a function of frequency and can be taken out of the integral. In what fallows we first evaluate the volume term in (B.1) assuming the normalization volume itself is a sphere with a radius R where $a \ll R$. We first consider the volume term. Using the field expressions given in (9.31) the volume term of the normalization (9.36) is expressed as

$$\sigma(\omega)\int_V \vec{\mathcal{E}}(\vec{r}).\vec{\mathcal{E}}(\vec{r})d^3r = \sigma(\omega)\ \zeta^2\ \int_0^R drr^2\ C^2(r;a)\Bigg\{\big(\ell(\ell+1)\big)^2\bigg(\frac{f_\ell(kr)}{kr}\bigg)^2\int d\Omega\bigg(Y_\ell^m(\theta,\phi)\bigg)^2$$
$$+\bigg(\frac{1}{kr}\frac{\partial}{\partial(kr)}\big(krf_\ell(kr)\big)\bigg)^2\int d\Omega\bigg[\bigg(\frac{\partial}{\partial\theta}Y_\ell^m(\theta,\phi)\bigg)^2+\frac{1}{sin^2\theta}\bigg(\frac{\partial}{\partial\phi}Y_\ell^m(\theta,\phi)\bigg)^2\bigg]\Bigg\}, \tag{B.2}$$

where $d\Omega = \sin\theta d\theta d\phi$ is the solid angle differential in spherical coordinates. The integrals involving spherical harmonics can be evaluated by using the orthogonality relation of the

tesseral harmonics and identity (C.2) in Appendix C. Thus, (B.2) reduces to

$$\sigma(\omega)\int_V \vec{\mathcal{E}}(\vec{r}).\vec{\mathcal{E}}(\vec{r})d^3r = \\ \sigma(\omega)\ \zeta^2\ \ell(\ell+1)\int_0^R drr^2\ C^2(r;a)\Bigg\{\ell(\ell+1)\bigg(\frac{f_\ell(kr)}{kr}\bigg)^2+\bigg(\frac{1}{kr}\frac{\partial}{\partial(kr)}\big(krf_\ell(kr)\big)\bigg)^2\Bigg\}. \tag{B.3}$$

Due to the disconitiouty of the function $f_\ell(kr)$ and the coefficients $C(r;a)$ at the surface of the plasmonic sphere [see eqn. (9.33)], the radial integral in (B.3) has to be divided into two terms: $\int_0^R = \int_0^a + \int_a^R$. Each term can be evaluated with the help of (C.3) and (C.5). This brings us to the final expression for the volume term of the normalization

$$\sigma(\omega)\int_V \vec{\mathcal{E}}(\vec{r}).\vec{\mathcal{E}}(\vec{r})d^3r = I\big[j_\ell(k_{\text{in}}a)\big] - I\big[h_\ell^{(2)}(k_{\text{out}}a)\big] + I\big[h_\ell^{(2)}(k_{\text{out}}R)\big], \tag{B.4}$$

where the functional $I\big[f_\ell(kr)\big]$ is defined as

$$I\big[f_\ell(kr)\big] = \tag{B.5}$$
$$\sigma(\omega)\ \zeta^2\ C^2(r;a)\frac{\ell(\ell+1)}{k^2}\bigg[rf_\ell^2(kr)+kr^2f_\ell(kr)f_\ell^{'}(kr)+\frac{k^2r^3}{2}\Big(f_\ell^2(kr)-f_{\ell-1}(kr)f_{\ell+1}(kr)\Big)\bigg].$$

As before, $f_\ell^{'}(kr)$ implies differentiation with respect to the argument i.e. $\frac{\partial}{\partial(kr)}f_\ell(kr)$. Note that in evaluating the first term of the right hand side of (B.4), $I\big[j_\ell(k_{\text{in}}a)\big]$, one has to use all the parameters corresponding to the region interior to the plasmonic sphere. i.e. $\epsilon_{\text{in}}(\omega)$, k_{in} and $C(r;a)$ for $r \leq a$ as it is defined in (9.33). Accordingly, the same applies to the second and third terms, $I\big[h_\ell^{(2)}(k_{\text{out}}a)\big]$ and $I\big[h_\ell^{(2)}(k_{\text{out}}R)\big]$, for which one has to use the parameters corresponding to the background material.

Next we show that the last term in the right hand side of (B.4), $I\big[h_\ell^{(2)}(k_{\rm out}R)\big]$, exactly cancels out with the surface term in (9.36). Therefore, as expected, the normalization condition becomes independent of the integration volume. Because the integration sphere was assumed to be sufficiently large, asymptotic expressions can be used to evaluate both these terms. The spherical Hankel functions at large radial distances have the following asymptotic form

$$h_\ell^{(2)}(kr) \sim i^{(\ell+1)}\frac{e^{-ikr}}{kr}\left(1 - i\frac{\ell(\ell+1)}{2kr}\right). \tag{B.6}$$

The last term in the right hand side of (B.5) can therefoe be approximated as

$$I\big[h_\ell^{(2)}(k_{\rm out}R)\big] \approx \frac{-i\epsilon_{\rm out}}{2k}C^2(r;a)(-)^{\ell+1}e^{-2ik_{\rm out}R}. \tag{B.7}$$

We now consider the surface term of the normalization condition (9.36). Considering that in the far field the dominant terms are $\mathcal{E}_\theta$ and $\mathcal{E}_\phi$ and using the asymptotic form of the spherical Hankel function (B.6), the leading order of the surface term is

$$\frac{i\epsilon_{\rm out}}{2k}\int_{\partial V}\vec{\mathcal{E}}(\vec{r}).\vec{\mathcal{E}}(\vec{r})d^2r \approx \frac{i\epsilon_{\rm out}}{2k^3}C^2(r;a)(-)^{\ell+1}e^{-2ik_{\rm out}R} \tag{B.8}$$

It is clear that the surface term (B.8) and (B.7) of the volume term cancel out. With this, the normalization condition (B.1) reduces to

$$I\big[j_\ell(k_{\rm in}a)\big] - I\big[h_\ell^{(2)}(k_{\rm out}a)\big] = 1, \tag{B.9}$$

which provide us the coefficient ζ in (9.31).

Appendix C

Tesseral Harmonics and Spherical Functions Identities

This appendix contains the definition of tesseral harmonics and a list of identities that are used throughout Chapter 9.

The tesseral harmonic are linear superpositions of the complex spherical harmonics with same ℓ and opposite sign m values. Therefore the azimuthal dependency of the functions are in the form of $\sin(m\phi)$ and $\cos(m\phi)$ instead of the usual exponential form $e^{im\phi}$. They are defined as [210]:

$$Y_\ell^m(\theta,\phi) = \begin{cases} \sqrt{\frac{2\ell+1}{2\pi}\frac{(\ell-|m|)!}{(\ell+|m|)!}}P_\ell^{|m|}(\cos\theta)\sin(|m|\phi) & m<0 \\ \sqrt{\frac{2\ell+1}{4\pi}}P_\ell^m & m=0 \\ \sqrt{\frac{2\ell+1}{2\pi}\frac{(\ell-m)!}{(\ell+m)!}}P_\ell^m(\cos\theta)\cos(m\phi) & m>0 \end{cases} \tag{C.1}$$

where P_ℓ^m are the associated Legendre polynomials. The tesseral harmonics satisfy the same orthogonality relation as the complex spherical harmonics.

The tesseral harmonics also satisfy the following identity

$$\int d\Omega \left\{ \left(\frac{\partial}{\partial \theta} Y_\ell^m(\theta,\phi) \right)^2 + \frac{1}{\sin^2\theta} \left(\frac{\partial}{\partial \phi} Y_\ell^m(\theta,\phi) \right)^2 \right\} =$$

$$\ell(\ell+1). \tag{C.2}$$

This can be proven by starting with the fact that the harmonics fulfill the identity $r^2\nabla^2 Y_\ell^m(\theta,\phi) = -\ell(\ell+1)Y_\ell^m(\theta,\phi)$. One can then get to (C.2), by calculating the matrix element of the operator $r^2\nabla^2$ and using integration by parts.

A useful identity of the spherical Bessel and Hankel functions is the following

$$\int dr \left\{ \ell(\ell+1) f_\ell^2(kr) + \left(\frac{\partial}{\partial(kr)} kr f_\ell(kr) \right)^2 \right\} =$$

$$r f_\ell^2(kr) + kr^2 f_\ell(kr) f_\ell'(kr) + k^2 \int dr r^2 f_\ell^2(kr). \tag{C.3}$$

where as previously $f_\ell'(kr)$ implies differentiation with respect to the argument. The equality can be proven by using integration by parts and the spherical Bessel differential equation to get

$$\ell(\ell+1) f_\ell^2(kr) = k^2 r^2 f_\ell(kr) f_\ell''(kr) + 2kr f_\ell(kr) f_\ell'(kr) + k^2 r^2 f_\ell^2(kr), \tag{C.4}$$

and

$$\int dr r^2 f_\ell^2(kr) = \frac{r^3}{2} \left(f_\ell^2(kr) - f_{\ell-1}(kr) f_{\ell+1}(kr) \right). \tag{C.5}$$

BIBLIOGRAPHY

BIBLIOGRAPHY

[1] J. H. Scatliff and P. J. Morris, "From Röntgen to magnetic resonance imaging: the history of medical imaging," *N. C. Med. J.*, vol. 75, no. 2, pp. 111-113, Mar. 2014.

[2] M. Yu. Tretyakov, V. V. Parshin, M. A. Koshelev, A. P. Shkaev, and A. F. Krupnov, "Extension of the range of resonator scanning spectrometer into submillimeter band and some perspectives of its further developments," *J. Mol. Spectrosc.*, vol. 238, no. 1, pp. 91-97, Apr. 2006.

[3] D. J. Vondran, "Making connections beyond 110 GHz," *Microwave J.*, vol. 56, no. 2, pp. 22-42, Feb. 2013.

[4] G. N. Bindu, S. J. Abraham, A. Lonappan, V. Thomas, C. K. Aanandan, and K. T. Mathew, "Active microwave imaging for breast cancer detection," *Progress In Electromagnetics Research*, Vol. 58, 149-169, 2006.

[5] Z. Liu, H. Ukida, P. Ramuhalli, and K. Niel *Integrated Imaging and Vision Techniques for Industrial Inspection* , Springer, London, 2015.

[6] American Cancer Society, Inc., Atlanta, GA,"Cancer facts & figures," 2015

[7] E. C. Fear, P. M. Meaney, and M. A. Stuchly, "Microwaves for breast cancer?," *IEEE Potentials*, Vol. 22, No. 1, 12–18, 2003.

[8] M. Lazebnik, D. Popovic, L. McCartney, C. B. Watkins, M. J. Lindstrom, J. Harter, S. Sewall, T. Ogilvie, A. Magliocco, T. M. Breslin, W. Temple, D. Mew, J. H. Booske, M. Okoniewski, and S. C. Hagness, "A large-scale study of the ultrawideband microwave dielectric properties of normal, benign and malignant breast tissues obtained from cancer surgeries," *Phys. Med. Biol.*, Vol. 52, No. 20, 6093–6115, 2007.

[9] P. C. Johns and M. J. Yaffe, "X-ray characterisation of normal and neoplastic breast tissues," *Phys. Med. Biol.*, Vol. 32, No. 6, 675–696, 1986.

[10] M. J. Yaffe, "Mammographic density. Measurement of mammographic density," *Breast Cancer Res.*, Vol. 10, No 209, 1–10, 2008.

[11] F. T. D'Astous and F. S. Foster, "Frequency dependent of ultrasound attenuation and backscatter in breast tissue," *Ultrasound Med. Biol.*, Vol. 12, No 10, 795–808, 1986.

[12] S. Kharkovsky and R. Zoughi, "Microwave and millimeter wave nondestructive testing and evaluation - overview and recent advances," *IEEE Instrum. Meas. Mag.*, Vol. 10, No. 2, 26–38, 2007.

[13] P. M. Meaney, M. W. Fanning, D. Li, S. P. Poplack and K. D. Paulsen, "A clinical prototype for active microwave imaging of the breast," *IEEE Trans. Microw. Theory Techn.*, Vol. 48, No. 11, 1805–1808, 2000.

[14] A. Qing and C. K. Lee, "Microwave imaging of parallel perfectly conducting cylinders using real-coded genetic algorithm coupled with newton-kantorivitch method," *Progress In Electromagnetics Research*, Vol. 28, 275–294, 2000.

[15] A. H. Golnabi, P. M. Meaney, S. D. Geimer, and K. D. Paulsen, "Comparison of no-prior and soft-prior regularization in biomedical microwave imaging," *J. Med. Phys.*, Vol. 36, 159–170, 2011.

[16] M. Ostadrahimi, P. Mojtabai, S. Noghanian, J. LoVetri, and L. Shafai, "A multiprobe-per-collector modulated scatterer technique for microwave tomography," *IEEE Antennas Wireless Propag. Lett.*, Vol. 10, 1445–1448, 2011.

[17] C. Gilmore, A. Zakaria, S. Pistorius, and J. LoVetri, "Microwave imaging of human forearms: pilot study and image enhancement," *Int. J. Biomed. Imaging*, Vol. 2013, 673027, 2013.

[18] N. R. Epstein, P. M. Meaney, and K. D. Paulsen, "3D parallel-detection microwave tomography for clinical breast imaging," *Rev. Sci. Instrum.*, Vol. 85, 124704, 2014.

[19] K. Arunachalam, L. Udpa, and S. Udpa, "Microwave imaging of penetrable scatterers using deformable mirror," *IEEE Trans. Magn.*, Vol. 43, No. 4, 1805–1808, 2007.

[20] K. Arunachalam, L. Udpa, and S. Udpa, "A computational investigation of microwave breast imaging using deformable reflector," *IEEE Trans. Biomed. Eng.*, Vol. 55, No. 2, 554–562, 2008.

[21] K. Arunachalam, "Investigation of a deformable mirror microwave imaging and therapy technique for breast cancer," *Doctoral dissertation*, Michigan State University, East Lansing, Michigan,USA, 2006.

[22] D. G. Berry, R. G. Malech, and W. A. Kennedy, "The reflectarray antenna," *IEEE Trans. Antennas Propag.*, vol. 11, no. 6, pp. 645-651, Nov. 1963.

[23] R. D. Javor, X. D. W, and K. Chang, "Beam steering of a microstrip flat reflectarray antenna," in *Proc. Int. Symp. Antennas Propag. AP-S Digest.*, 1994, pp. 956-959.

[24] D. M. Pozar and T. A. Metzler, "Analysis of reflectarray antenna using microstrip patches of variable size," *Electron. Lett.*, vol. 29, no. 8, pp. 657-658, Apr. 1993.

[25] A. Kelkar, "FLAPS: conformal phased reflecting surfaces," in *Proc. IEEE National Radar Conf.*, 1991, pp. 58-62.

[26] J. Huang and R. J. Pogorzelski, "A Ka-band microstrip reflectarray with elements having variable rotation angles," *IEEE Trans. Antennas Propag.*, vol. 46, no. 5, pp. 650-656, May. 1998.

[27] J. A. Encinar, "Design of a dual freqeuncy reflectarray using microstrip stacked patches of variable size," *Electron. Lett.*, vol. 32, no. 12, pp. 1049-1050, Jun. 1996.

[28] J. Huang, C. Han, and K. Chang, "A cassegrain offset-fed dual-band reflectarray," in *Proc. Int. Symp. Antennas Propag.*, 2006, pp. 2439-2442.

[29] M. Inam and M. Y. Ismail, "Integration of PIN diodes with slot embedded patch elements for active reflectarray antenna design," in *Proc. Int. Symp. Telecommunication Technologies*, 2012, pp. 151-155.

[30] O. Bayraktar, O. A. Civi, and T. Akin, "Beam switching reflectarray monolithically integrated with RF MEMS switches," *IEEE Trans. Antennas Propag.*, vol. 60, no. 2, pp. 854-862, Feb. 2012.

[31] W. Hu, R. Cahill, J. A. Encinar, R. Dickie, H. Gamble, V. Fusco, and Norman Grant, "Design and measurment of reconfigurble millimeter wave reflectarray cells with nematic liquid crystal," *IEEE Trans. Antennas Propag.*, vol. 56, no. 10, pp. 3112-3117, Oct. 2008.

[32] R. R. Romanofsky, "Advances in scanning reflectarray antennas based on ferroelectric thin-film phase shifters for deep-space communications," in *Proc. IEEE*, 2007, vol. 95, no. 10, pp. 1968-1975.

[33] E. Carrasco, M. Tamagnone, and J. Perruisseau-Carrier, "Tunable graphene reflective cells for THz reflectarrays and generalized law of reflection," *Appl. Phys. Lett.*, vol. 102, no. 104103, 2013.

[34] S. V. Hum and J. Perruisseau-Carrier, "Reconfigurable reflectarray and Array lenses for dynamic antenna beam control: a review," *IEEE Trans. Antennas Propag.*, vol. 62, no. 1, pp. 183-198, Jan. 2014.

[35] C. Guclu, J. Perruisseau-Carrier, and O. A. Civi, "Proof of concept of a dual-band circularly-polarized RF MEMS beam-switching reflectarray," in *IEEE Trans. Antennas Propag.*, vol. 60, no. 11, pp. 5451-5455, Nov. 2012.

[36] H. Moghadas, M. Daneshmand, P. Mousavi, M. R. Chaharmir, and J. Shaker, "Orthogonally-polarized dual-band MEMS-tunable double-slotted unit cell for reflectarray applications," in *Proc. Int. Symp. Antennas Propag.*, 2012, pp. 1-2.

[37] C. Mias and J. H. Yap, "A varactor-tunable high impedance surface with a resistive-limped-element biasing grid," *IEEE Trans. Antennas Propag.*, vol. 55, no. 7, pp. 1955-1962, Jul. 2007.

[38] S. V. Hum, M. Okoniewski, and R. J. Davies, "Modeling and design of electronically tunable reflectarrays," *IEEE Trans. Antennas Propag.*, vol. 55, no. 8, pp. 2200-2210, Aug. 2007.

[39] D. Rodrigo, L. Jofre, and J. Perruisseau-Carrier, "Unit cell for frequency-tunable beam-scanning reflectarray," *IEEE Trans. Antennas Propag.*, vol. 61, no. 12, pp. 5992-5999, Dec. 2013.

[40] A. Tayebi, J. Tang, P. Roy Paladhi, L. Udpa, and S. Udpa, "A microwave tomography system using a tunable mirror for beam steering," in *Proc. 40th Annual Review of Progress in Quantitative Nondestructive Evaluation, AIP Conf. Proc.*, 2014, vol. 1581, no. 1, pp. 1537-1543.

[41] A. Tayebi, J. Tang, P. Roy Paladhi, L. Udpa, and S. Udpa, "Design and development of an electrically-controlled beam steering mirror for microwave tomography," in *Proc. 41th Annual Review of Progress in Quantitative Nondestructive Evaluation, AIP Conf. Proc.*, 2015, vol. 1650, no. 1, pp. 501-508.

[42] J. Tang, A. Tayebi, S. Udpa, E. J. Rothwell, and A. Temme, "A dual-band tunable reflectarray," in *Proc. Antennas and Propagation Society International Symposium*, 2014, pp. 1033-1034.

[43] D. Cadoret, A. Laisne, M. Milon, R. Gillard, and H. Legay, "FDTD analysis of reflectarray radiating cells," in*Proc. Int. Conf. Wireless Communications and Applied Computational Electromag.*, 2005, pp. 853-856.

[44] I. Bardi, R. Remski, D. Perry, and Z. Cendes, "Plane wave scattering from frequency-selective surfaces by the finite-element method," *IEEE Trans. Antennas Magn.*, vol. 38, no. 2, pp. 641-644, Mar. 2002.

[45] S. A. Schelkunoff, "The impedance concept and its application to problems of reflection, shielding and power absorption," *Bell System Technical Journal*, vol. 17, Issue 1, pp. 17 - 48, 1938.

[46] J. Huang and J. A. Encinar, *Relectarray Antennas*, Hoboken-Piscataway, NJ, USA: Wiley-IEEE Press, 2007.

[47] H. Rajagopalan and Y. Rahmat-Samii, "Reflectarray antennas: an intuitive explanation of reflection phase behavior," in *Proc. General Assembly and Scientific Symp., 2011 XXXth URSI*, 2011, pp. 1-4.

[48] B. O. Zhu, K. Chen, N. Jia, L. Sun, J. Zhao, T. Jiang, and Y. Feng, "Dynamic control of electromagnetic wave propagation with equivalent principle inspired tunable metasurface," *Nature, scientific reports*, vol. 4, no. 4971, May. 2014.

[49] X. F. Luo, P. T. Teo, A. Qing, and C. K. Lee, "Design of double-square-loop freqeuncy-selective surfaces using differential evolution strategy coupled with equivalent-circuit model," *Microwave and Optical Technology Lett.,*, vol. 44, no. 2, pp. 159-162, Jun. 2005.

[50] M. G. Bray and D. H. Werner, "A novel design approach for an independently tunable dual-band EBG AMC surface," in *Proc. Int. Symp. Antennas Propag.*, 2004, pp. 289-292.

[51] N. Marcuvitz, *Waveguide Handbook*, New York, NY, USA: Dover Publications Inc., 1950.

[52] R. J. Langley and E. A. Parker, "Equivalent circuit model for arrays of square loops," *Electron. Lett.*, vol.18, no. 7, pp. 294-296, Apr. 1982.

[53] C. K. Lee, and R. J. Langley, "Equivalent circuit models For frequency selective surfaces at oblique angles of incidence," in *Proc. Microw. Antennas Prop.*, 1985, vol. 132, no. 6, pp. 395-399.

[54] R. J. Langley, and E. A. Parker, "Double square frequency selective surfaces and their equivalent circuit," *Electron. Lett.*, vol.19, no. 17, pp. 675-667, Aug. 1983.

[55] A. Campos, R. Moreira, and J. Trindade, "A comparison between the equivalent circuit model and moment method to analyze FSS," in *Int. Microw. Optoelectronics Conf.*, 2009, pp. 760-765.

[56] B. A. Munk, *Frequency Selective Surfaces: Theory and Design*, USA: Wiley , 2000.

[57] F. Costa, C. Amabile, A. Monorchio, and E. Prati, "Waveguide dielectric permittivity measurement technique based on resonant FSS filters," *IEEE Microw. Wireless Compon. Lett.*, vol.21, no. 5, pp. 273-275, May. 2011.

[58] P. W. Hannan and A. Balfour, "Simulation of a phased-array antenna in waveguide," *IEEE Trans. Antennas Propag.*, vol. 13, issue 3, pp. 342-353, May. 1965.

[59] B. T. Perry, E. J. Rothwell, and L. C. Kempel, "A comparison of the measured pulse response of layered materials using time- and frequency-domain systems," *IEEE Antennas Propag. Magazine*, vol. 49, no. 5, pp. 117-123, Oct. 2007.

[60] M. Bertero, and P. Boccacci, "Introduction to inverse problems in imaging", Institute of Physics Publishing, London, 1998.

[61] S. I. Kabanikhin "Definitions and examples of inverse and ill-posed problems", J. Inv. Ill-Posed Problems, vol. 16, no. 4, pp. 317357, 2008.

[62] A. Devaney, "A filtered backpropagation algorithm for diffraction tomography," *Ultrasonic imaging*, vol. 4, no. 4, pp. 336–350, 1982.

[63] A. Devaney, "A computer simulation study of diffraction tomography," *IEEE Trans. Biomed. Eng,*, no. 7, pp. 377–386, 1983.

[64] A. C. Kak and M. Slaney, "Tomographic imaging with diffracting sources," in *Principles of Computerized Tomographic Imaging*. IEEE press, New York, 1988.

[65] A. J. Devaney, "Generalized projection-slice theorem for fan beam diffraction tomography," *Ultrasonic imaging*, vol. 7, no. 3, pp. 264–275, 1985.

[66] S. Pan and A. C. Kak, "A computational study of reconstruction algorithms for diffraction tomography: Interpolation versus filtered-backpropagation," *IEEE Trans. Acoustics, Speech and Signal Proc,*, vol. 31, no. 5, pp. 1262–1275, 1983.

[67] W. Tabbara, *et al.*, "Diffraction tomography: contribution to the analysis of some applications in microwaves and ultrasonics," *Inverse Problems*, vol. 4, no. 2, p. 305, 1988.

[68] X. Pan and M. A. Anastasio, "Minimal-scan filtered backpropagation algorithms for diffraction tomography," *JOSA A*, vol. 16, no. 12, pp. 2896–2903, 1999.

[69] X. Pan, "Unified reconstruction theory for diffraction tomography, with consideration of noise control," *JOSA A*, vol. 15, no. 9, pp. 2312–2326, 1998.

[70] M. A. Anastasio and X. Pan, "Full-and minimal-scan reconstruction algorithms for fan-beam diffraction tomography," *Applied optics*, vol. 40, no. 20, pp. 3334–3345, 2001.

[71] X. Pan and M. A. Anastasio, "On a limited-view reconstruction problem in diffraction tomography," *IEEE Trans. Med. Imag.,*, vol. 21, no. 4, pp. 413–416, 2002.

[72] L. Bellomo, S. Pioch, M. Saillard, and E. Spano, "Time reversal experiments in the microwave range: description of the radar and results," *Progress In Electromagnetics Research*, Vol. 104, 427–448, 2010.

[73] W. Zhang, A. Hoorfar, and L. Li, "Through-the-wall target localization with time reversal music method," *Progress In Electromagnetics Research*, Vol. 106, 75–89, 2010.

[74] M. Razavian, M. H. Hosseini, and R. Safian, "Time-reversal microwave imaging based on random configuration of transmitters or receivers," *Progress In Electromagnetics Research B*, Vol. 56, 235-250, 2013.

[75] P. Kosmas, and M. Rappaport, "Time reversal with FDTD method for microwave breast cancer detection," *IEEE Trans. Microw. Theory Techn.*, Vol. 49, No. 7, 2317–2323, 2005.

[76] S. Reyes-Rodríguez, N. Lei, B. Crowgey, L. Udpa, and S. S. Udpa, "Time reversal and microwave techniques for solving inverse problem in non-destructive evaluation," *NDT & E Int.*, Vol. 62, 106–114, 2014.

[77] L. El Sahmarany, L. Berry, N. Ravot, F. Auzanneau, and P. Bonnet, "Time reversal for soft faults diagnosis in wire networks," *Progress In Electromagnetics Research M*, Vol. 53, 45–58, 2013.

[78] K. S. Yee, "Numerical solution of the initial boundary value problems involving Maxwells equations in isotropic media", *IEEE Trans. Antennas Propag.*, vol. 14, no. 3, pp. 302–307, 1996.

[79] A. B. Gorji, and B. Zakeri "An improved time-reversal based target localization for through-wall microwave imaging", *Journal of Electrical and Computer Engineering Innovations*, vol. 1, no. 2, pp. 89–97, 2013.

[80] S. Zachary, D. Kingsland, R. Lee, and J. Lee, "A Perfectly Matched Anisotropic Absorber forUse as an Absorbing Boundary Condition, *IEEE Trans. Ant. Prop.*, vol. 43, no. 12, pp. 14601463, 1995.

[81] A. Tayebi, J. Tang, P. Roy Paladhi, L. Udpa, S. Udpa and E. J. Rothwell "Dynamic beam shaping using a dual-band electronically tunable reflectarray antenna," *IEEE Trans. Antennas Propag*, vol. 63, no. 10, pp. 4534–4539, 2015.

[82] N. Maaref, P. Millot, X. Ferriieres, C. Pichot, and O. Picon "Through-the-wall target localization with time reversal music method," *Progress In Electromagnetics Research*, vol. 106, pp. 75–89, 2010.

[83] B. Riddle, J. Baker-Jarvis, and J. Krupka, "Complex permittivity measurements of common plastics over variable temperatures," *IEEE Trans. Microw. Theory Techn.*, vol. 51, no. 3, pp. 727–733, 2003.

[84] M. Born and E. Wolf, "Principles of Optics," *Academic Press, New York*, 1970.

[85] M. Peichl, T. Albers, and S. Dill, "Detection of small impurities in bulk material by MMW radar," *16th Int. Radar Symp.*, Dresden, pp. 294-299, 2015.

[86] A. Tayebi, P. Roy Paladhi, L. Udpa, and S. Udpa, "A novel time reversal based microwave imaging system," *Progress In Electromagnetics Research C.*, vol. 62, pp. 139–147, 2016.

[87] P. Roy Paladhi, A. Sinha, A. Tayebi, L. Udpa, and S. Udpa, "Class of backpropagation techniques for limited-angle reconstruction in microwave tomography," *AIP Conf. Proc.*, vol. 1650, pp. 509–518, 2015.

[88] P. Roy Paladhi, A. K. Sinha, A. Tayebi, L. Udpa, and A. Tamburrino "Data redundancy in diffraction tomography," *Int. Rev. Prog. Appl. Comput. Electrom. (ACES)*, pp. 1–2, 2015.

[89] V. Zelevinsky and A. Volya, "Chaotic features of nuclear structure and dynamics: selected topics," *Phys. Scripta*, vol. 91, no. 3, pp. 033006, 2016.

[90] A. Tayebi, T. N. Hoatson, J. Wang, and V. Zelevinsky, "Environment-protected solid-state-based distributed charge qubit," *Phys. Rev. B*, vol. 94, no.23, pp. 235150, 2016.

[91] H. Feshbach, "Unified theory of nuclear reactions," *Ann. Phys. (N.Y.)*, vol. 5, no. 4, pp. 357–390, 1958; vol. 19, no.4, pp. 287–313, 1962.

[92] C. Mahaux and H.A. Weidenmüeller, "Shell Model Approach to Nuclear Reactions," North Holland, Amsterdam, 1969.

[93] N. Auerbach and V. Zelevinsky, "Super-radiant dynamics, doorways and resonances in nuclei and other open mesoscopic systems," *Rep. Prog. Phys.*, vol. 74, no. 10, pp. 106301-106310, 2011.

[94] K. Sasada and N. Hatano, "Quantum interference effect of resonant transport in nanoscale systems," *Physica E*, vol. 29, no.3, pp. 609–613, 2005.

[95] S. Zhang, Z. Ye, Y. Wang, Y. Park, G. Bartal, M. Mrejen, X. Yin, and X. Zhang, "Anti-Hermitian Plasmon Coupling of an Array of Gold Thin-Film Antennas for Controlling Light at the Nanoscale," *Phys. Rev. Lett.*, vol. 109, no. 19, pp. 193902-193906, 2012.

[96] G. L. Celardo, F. Borgonovi, M. Merkli, V. I. Tsifrinovich and G. P. Berman, "Superradiance Transition in Photosynthetic Light-Harvesting Complexes," *J. Phys. Chem. C*, vol. 116, no. 42, pp. 122105-22111, 2012.

[97] R.H. Dicke, "Coherence in Spontaneous Radiation Processes," *Phys. Rev.*, vol.93, no. 1, pp. 99–110, 1954.

[98] ed. M. G. Benedict, "Super-radiance: Multiatomic Coherent Emission," Taylor and Francis, New York, 1996.

[99] V. V. Sokolov and V. G. Zelevinsky, "Collective dynamics of unstable quantum states," *Ann. Phys. (N.Y.)*, vol. 216, no. 2, pp. 323-350, 1992.

[100] A. Volya and V. Zelevinsky, "Exploring quantum dynamics in an open many-body system: transition to superradiance," *J. Opt. B Quantum Semiclassical Opt.*, vol. 5, no. 3, pp. 450 , 2003.

[101] A. Volya and V. Zelevinsky, "Nuclei and Mesoscopic Physics," *AIP Conf. Proc., Nuclei and Mesoscopic Physics: WNMP*, vol. 777, pp. 229, 2004, ed. by V. Zelevinsky (AIP, Melville, 2005)

[102] S. Sorathia, F. M. Izrailev, G. L. Celardo, V. G. Zelevinsky, and G. P. Berman, "Internal chaos in an open quantum system: From Ericson to conductance fluctuations," *EPL*, vol. 88, no. 2, pp. 27003, 2009.

[103] G. L. Celardo, A. M. Smith, S. Sorathia, V. G. Zelevinsky, R. A. Sen'kov, and L. Kaplan, "Transport through nanostructures with asymmetric coupling to the leads," *Phys. Rev. B*, vol. 82, no.16, pp. 165437–165448, 2010.

[104] S. Sorathia, F. M. Izrailev, V. G. Zelevinsky, and G. L. Celardo, "From closed to open one-dimensional Anderson model: Transport versus spectral statistics," *Phys. Rev. E*, vol. 86, no.1, pp. 011142–011148, 2012.

[105] G. L. Celardo and L. Kaplan,, "Superradiance transition in one-dimensional nanostructures: An effective non-Hermitian Hamiltonian formalism," *Phys. Rev. B*, vol. 79, no. 15, pp. 155108-155116, 2009.

[106] S. Longhi, "Nonexponential Decay Via Tunneling in Tight-Binding Lattices and the Optical Zeno Effect," *Phys. Rev. Lett.*, vol. 97, no. 1, pp. 110402–110405, 2006.

[107] T. Ericson, "A theory of fluctuations in nuclear cross sections," Ann. Phys. (N.Y.), vol. 23, no. 3, pp. 390-414, 1963.

[108] A. Ziletti, F. Borgonovi, G. L. Celardo, F. M. Izrailev, L. Kaplan, and V. G. Zelevinsky, "Coherent transport in multibranch quantum circuitss," *Phys. Rev. B*, vol. 85, no. 2, pp. 052201-052205, 2012.

[109] Z. Tang and N. A. Kotov, "One-dimensional assemblies of nanoparticles: preparation, properties, and promise," *Adv. Mater.*, vol. 17, no. 8, pp.951-962, 2005.

[110] H. Nakamura, N. Hatano, S. Garmon, and T. Petrosky, "Quasibound states in the continuum in a two channel quantum wire with an adatom," *Phys. Rev. Lett.*, vol. 99, no. 21, pp. 210404–210407, 2007.

[111] A. D. Dente, R. A. Bustos-Marun, and H. M. Pastawski, "Dynamical regimes of a quantum SWAP gate beyond the Fermi golden rule," *Phys. Rev. A*, vol. 78, no. 6, pp. 062116-062125, 2008.

[112] S. Garmon, T. Petrosky, L. Simine, and D. Segal, "Amplification of non-Markovian decay due to bound state absorption into continuum," *Fortschr. Phys.*, vol. 61, no. 2–3, pp. 261–275, 2013.

[113] L. Durand, "S-matrix treatment of many overlapping resonances," *Phys. Rev. D*, vol. 14, no. 11, pp. 3174–3185 (1976).

[114] N. Auerbach and V. Zelevinsky, "Doorway states in nuclear reactions as a manifestation of the "super-radiant" mechanism," *Nucl. Phys.*, vol. A781, pp. 67–80, 2007.

[115] G. Shchedrin and V. Zelevinsky, "Resonance width distribution for open quantum systems," *Phys. Rev. C*, vol. 86, no.4, pp. 044602–044608, 2012.

[116] K. Sasada and N. Hatano, "Quantum interference effect of resonant transport in nanoscale systems," *Physica E*, vol. 29, pp. 609–613, 2005.

[117] P. von Brentano, "On the mixing of two bound and unbound levels: Energy repulsion and width attraction," *Phys. Rep.*, vol. 264, no. 1–5, pp. 57–66, 1996.

[118] C. W. J. Beenakker, "Random-matrix theory of quantum transport," *Rev. Mod. Phys.*, vol. 69, no. 3, pp. 731–808, 1997.

[119] J. T. Shen and S. Fan, "Coherent photon transport from spontaneous emission in one-dimensional waveguides," *Optics Lett.*, vol. 30, no. 15, pp. 2001–2003, 2005.

[120] J. -Q. Liao, Z. R. Gong, L. Zhou, Y. -X. Liu, C. P. Sun, and F. Nori, "Controlling the transport of single photons by tuning the frequency of either one or two cavities in an array of coupled cavities," *Phys. Rev. A*, vol. 81, no. 4, pp. 042304-042313, 2010.

[121] M. Delanty, S. Rebic, and J. Twamley, "Superradiance and phase multistability in circuit quantum electrodynamics," *New J. Phys.*, vol. 13, no. 5, pp. 053032, 2011.

[122] A. Tayebi and V. Zelevinsky, "The Holstein polaron problem revisited," *Journal of Physics A: Mathematical and Theoretical*, vol. 49, no. 25, pp. 255004, 2016.

[123] E. Dagotto, J. Riera and D. Scalapino, "Superconductivity in ladders and coupled planes," *Phys. Rev. B*, vol. 45, no.10, pp. 5744–5747, 1992.

[124] J. L. O'Brien, "Optical Quantum Computing," *Science*, vol. 318, no. 5856, pp. 15671570, 2007.

[125] P. Kok, W. J. Munro, K. Nemoto, T. C. Ralph, J. P. Dowling, and G. J. Milburn, "Linear optical quantum computing with photonic qubits," *Rev. Mod. Phys.*, vol. 79, no. 1, pp. 135-174, 2007.

[126] W. S. Warren, "The Usefulness of NMR Quantum Computing," *Science*, vol. 277, no. 5332, pp. 1688-1690, 1997.

[127] H. J. Mamin, M. Kim, M. H. Sherwood, C. T. Rettner, K. Ohno, D. D. Awschalom, and D. Rugar, "Nanoscale Nuclear Magnetic Resonance with a Nitrogen-Vacancy Spin Sensor," *Science*, vol. 339, no. 6119, pp. 557-560, 2013.

[128] N. Xu, J. Zhu, D. Lu, X. Zhou, X. Peng, and J. Du, "Quantum Factorization of 143 on a Dipolar-Coupling Nuclear Magnetic Resonance System," *Phys. Rev. Lett.*, vol. 108, no. 13, pp. 130501-130506, 2012.

[129] H. Häffner, C.F. Roos, and R. Blatt, "Quantum computing with trapped ions," *Phys. Rep.*, vol. 469, no. 4, pp. 155-203, 2008.

[130] D. Kielpinski, C. Monroe, and D. J. Wineland, "Architecture for a large-scale ion-trap quantum computer," *Nature*, vol. 417, pp. 709-711, 2002.

[131] C. Monroe and D. J. Kim, "Scaling the Ion Trap Quantum Processor," *Science*, vol. 339, no. 6124, pp. 1164-1169, 2013.

[132] M. H. Devoret and R. J. Schoelkopf, "Superconducting Circuits for Quantum Information: An Outlook," *Science*, vol. 339, no. 6124, pp. 1169-1174, 2013.

[133] E. Flurin, N. Roch, J. D. Pillet, F. Mallet, and B. Huard, "Superconducting Quantum Node for Entanglement and Storage of Microwave Radiation," *Phys. Rev. Lett.*, vol. 114, no. 9, pp. 090503-090507, 2015.

[134] T. Douce, M. Stern, N. Zagury, P. Bertet, and P. Milman, "Coupling a single nitrogen-vacancy center to a superconducting flux qubit in the far-off-resonance regime," *Phys. Rev. A*, vol. 92, no. 5, pp. 052335-052342, 2015.

[135] E. Lucero, R. Barends, Y. Chen, J. Kelly, M. Mariantoni, A. Megrant, P. O'Malley, D. Sank, A. Vainsencher, J. Wenner, T. White, Y. Yin, A. N. Cleland, and J. M.Martinis, "Computing prime factors with a Josephson phase qubit quantum processor," *Nat. Phys.*, vol. 8, pp. 719-723, 2012.

[136] P. M. Platzman and M. I. Dykman, "Quantum Computing with Electrons Floating on Liquid Helium," *Science*, vol. 282, no. 5422, pp. 1967-1969, 1999.

[137] M. I. Dykman, P. M. Platzman, and P. Seddighrad, "Qubits with electrons on liquid helium," *Phys. Rev. B*, vol. 67, no. 15, pp. 155402-155416, 2003.

[138] M. Yamamoto, S. Takada, C. Bauerle, K. Watanabe, A. D. Wieck, and S. Tarucha, "Electrical control of a solid-state flying qubit," *Nat. Nano.*, vol. 7, pp. 247-251, 2012.

[139] K. D. Petersson, J. R. Petta, H. Lu,and A. C. Gossard, "Quantum Coherence in a One-Electron Semiconductor Charge Qubit," *Phys. Rev. Lett.*, vol. 105, no. 24, pp. 246804-246807, 2010.

[140] T. Hayashi, T. Fujisawa, H. D. Cheong, Y. H. Jeong, and Y. Hirayama, "Coherent Manipulation of Electronic States in a Double Quantum Dot," *Phys. Rev. Lett.*, vol. 91, no. 22, pp. 226804-226807, 2003.

[141] A. Ardavan, M. Austwick, S. C. Benjamin, G. A. D. Briggs, T. J. S. Denni s, A. Ferguson, D. G. Hasko, M. Kanai, A. N. Khlobystov, B. W. Lovett, G. W. Morley, R. A. Oliver, D. G. Pettifor, K. Porfyrakis, J. H. Reina, J. H. Rice, J. D. Smith, R. A. Taylor, D. A. Williams, C. Adelmann, H. Mariette, and R. J. Hamers, "Nanoscale solid-state quantum computing," *Phil. Trans. R. Soc. A Math Phys. Eng. Sci.*, vol. 361, no. 1808, pp. 1473-1485, 2003.

[142] M. Pavičić, "Companion to quantum computation and communication," Wiley-VCH, Darmstadt, 2013.

[143] D. Y. Baines, T. Meunier, D. Mailly, A. D. Wieck, C. Bäuerle, L. Saminadayar, P. S. Cornaglia, G. Usaj, C. A. Balseiro, and D. Feinberg, "Transport through side-coupled double quantum dots: From weak to strong interdot coupling," *Phys. Rev. B*, vol. 85, no. 19, pp. 195117-195117, 2012.

[144] S. Fringes, C. Volk, B. Terrs, J. Dauber, S. Engels, S. Trellenkamp, and C. Stampfer, "Tunable capacitive inter-dot coupling in a bilayer graphene double quantum dot," *Phys. Status Solidi C*, vol. 9, no. 2, pp. 169-174, 2012.

[145] V. V. Sokolov and V. G. Zelevinsky, "Dynamics and statistics of unstable quantum states," *Nucl. Phys. A*, vol. 504, no. 3, pp. 562-588, 1989.

[146] A. Tayebi and V. Zelevinsky, "Superradiance in a two-channel quantum wire," AIP Conf. Proc., vol. 1619, no. 1, pp. 162-170, 2014.

[147] Ya. S. Greenberg and A. A. Shtygashev, "Non-Hermitian Hamiltonian approach to the microwave transmission through a one-dimensional qubit chain," *Phys. Rev. A*, vol. 92, no. 6, pp. 063835-063849, 2015.

[148] Y. S. Greenberg, C. Merrigan, A. Tayebi, V. Zelevinsky, "Quantum signal transmission through a single-qubit chain," *Eur. Phys. J. B*, vol. 86, no. 9, pp. 1-10, 2013.

[149] T. Kwapiński and R. Taranko, "Quantum wire as a charge-qubit detector," *Phys. Rev. A*, vol. 86, no. 5, pp. 052338-052346, 2012.

[150] C. B. Simmons, M. Thalakulam, B. M. Rosemeyer, B. J. Van Bael, E. K. Sackmann, D. E. Savage, M. G. Lagally, R. Joynt, Mark Friesen, S. N. Coppersmith, M. A. Eriksson,

"Charge Sensing and Controllable Tunnel Coupling in a Si/SiGe Double Quantum Dot," *Nano Lett.*, vol. 9, no. 9, pp. 3234-3238, 2009.

[151] L. DiCarlo, H. J. Lynch, A. C. Johnson, L. I. Childress, K. Crockett, C. M. Marcus, M. P. Hanson, and A. C. Gossard, "Differential Charge Sensing and Charge Delocalization in a Tunable Double Quantum Dot," *Phys. Rev. Lett.*, vol. 92, no. 22, pp. 226801-226804, 2004.

[152] P. von Brentano, "On the mixing of two bound and unbound levels: Energy repulsion and width attraction," *Phys. Rep.*, vol. 264, no. 1, pp. 57-66, 1996.

[153] A. Volya and V. Zelevinsky, "Superradiance and open quantum systems," *AIP Conf. Proc.*, vol. 777, no. 1, pp. 229-249, 2005.

[154] H. Haken and G. Strobl, "An exactly solvable model for coherent and incoherent exciton motion," *Z. Phys.*, vol. 262, no. 2, pp. 135-148, 1973.

[155] J. Grad, G. Hernandez, and S. Mukamel, "Radiative decay and energy transfer in molecular aggregates: The role of intermolecular dephasing," *Phys. Rev. A*, vol. 37, no. 10, pp. 3835-3846, 1988.

[156] Y. C. Cheng and R. J. Silbey, "Stochastic Liouville equation approach for the effect of noise in quantum computations," *Phys. Rev. A*, vol. 69, no. 5, pp. 052325–052339, 2004.

[157] G. Celardo, P. Poli, L. Lussardi, and F Borgonovi, "Cooperative robustness to dephasing: Single-exciton superradiance in a nanoscale ring to model natural light-harvesting systems," *Phys. Rev. B*, vol. 90, no. 8, pp. 085142–085149, 2014.

[158] P. Reineker, "Exciton dynamics in molecular crystals and aggregates," Springer, Berlin-Heidelb, 1982.

[159] Editorial, "Surface plasmon resurrection," *Nat. Photon.*, vol. 6, no. 11, pp. 707-707, 2012.

[160] X. Chen, N. C. Lindquist, D. J. Klemme, P. Nagpal, D. J. Norris, and S. Oh, "Split-Wedge Antennas with Sub-5 nm Gaps for Plasmonic Nanofocusing," *Nano Lett.*, vol. 16, no. 12, pp. 7849-7856, 2016.

[161] B. Ji, J. Qin, H. Tao, Z. Hao, and J. Lin, "Subwavelength imaging and control of ultrafast optical near-field under resonant- and off-resonant excitation of bowtie nanostructures," *New J. Phys.*, vol. 18, no. 9, pp. 093046, 2016.

[162] I. Maouli, A. Taguchi, Y. Saito, S. Kawata, and P. Verma, "Optical antennas for tunable enhancement in tip-enhanced Raman spectroscopy imaging," *Appl. Phys. Expr.*, vol. 8, no. 3, pp. 032401, 2015.

[163] K. V. Sreekanth, Y. Alapan, M. ElKabbash, E. Ilker, M. Hinczewski, U. A. Gurkan, A. De Luca, G. Strangi, "Extreme sensitivity biosensing platform based on hyperbolic metamaterials ," *Nat. Mater.*, vol. 15, no. 6, pp. 621–627, 2016.

[164] H. T. Ngo, H. Wang, A. M. Fales, and T. Vo-Dinh, "Plasmonic SERS biosensing nanochips for DNA detection," *Anal. Bioanal. Chem.*, vol. 408, no. 7, pp. 1773–1781, 2016.

[165] J. Straubel, R. Filter, C. Rockstuhl, and K. Słowik, "Plasmonic nanoantenna based triggered single-photon source," *Phys. Rev. B*, vol. 93, no. 19, pp. 195412–195422, 2016.

[166] T. Braun, V. Baumann, O. Iff, S. Hfling, C. Schneider, and M. Kamp, "Enhanced single photon emission from positioned InP/GaInP quantum dots coupled to a confined Tamm-plasmon mode," *Appl. Phys. Lett.*, vol. 106, no. 4, pp. 041113–041116, 2015.

[167] O. Demichel, M. Petit, S. Viarbitskaya, R. Mjard, F. de Fornel, E. Hertz, F. Billard, A. Bouhelier, and B Cluzel, "Dynamics, Efficiency, and Energy Distribution of Nonlinear Plasmon-Assisted Generation of Hot Carriers," *ACS Photonics*, vol. 3, no. 5, pp. 791–795, 2016.

[168] J. S. Fakonas, H. Lee, Y. A. Kelaita, and H. A. Atwater , "Extreme sensitivity biosensing platform based on hyperbolic metamaterials," *Nat. Photon.*, vol. 8, no. 4, pp. 317–320, 2014.

[169] S. D. Gupta and G. S. Agarwal, "Two-photon quantum interference in plasmonics: theory and applications," *Opt. Lett.*, vol. 39, no. 2, pp. 390–393, 2014.

[170] M. S. Tame, K. R. McEnery, S. K. Ozdemir, J. Lee, S. A. Maier, and M. S. Kim, "Quantum plasmonics," *Nat. Phys.*, vol. 9, no. 6, pp. 329–340, 2013.

[171] N. P. de Leon, M. D. Lukin, and H. Park, "Quantum plasmonic circuits," *IEEE J. Sel. Top. Quantum Electron.*, vol. 18, no. 6, pp. 1781–1801, 2012.

[172] E. Pisano, V. Coello, C. E. Garcia-Ortiz, Y. Chen, J. Beermann, and S. I. Bozhevolnyi, "Plasmonic channel waveguides in random arrays of metallic nanoparticles," *Opt. Express*, vol. 24, no. 15, pp. 17080–17089, 2016.

[173] I. L. Rasskazov, S. V. Karpov, and V. A. Markel, "Waveguiding properties of short linear chains of nonspherical metal nanoparticles," *J. Opt. Soc. Am. B*, vol. 31, no. 12, pp. 2981–2989, 2016.

[174] J. G. Smith, J. A. Faucheaux, and P. K. Jain, "Plasmon resonances for solar energy harvesting: A mechanistic outlook," *Nano Today*, vol. 10, no. 1, pp. 67–80, 2015.

[175] H. Alaeian and J. A. Dionne, "Non-Hermitian nanophotonic and plasmonic waveguides," *Phys. Rev. B*, vol. 89, no. 7, pp. 075136–075144, 2014.

[176] L. Verslegers, Z. Yu, Z. Ruan, P. B. Catrysse, and S. Fan, "From Electromagnetically Induced Transparency to Superscattering with a Single Structure: A Coupled-Mode Theory for Doubly Resonant Structures," *Phys. Rev. Lett.*, vol. 108, no. 8, pp. 083902–083906, 2012.

[177] N. V. Alexeeva, I. V. Barashenkov, K. Rayanov, and S. Flach, "Actively coupled optical waveguides," *Phys. Rev. A*, vol. 89, no. 1, pp. 013848–013852, 2014.

[178] L. Feng, Y. Xu, W. S. Fegadolli, M. Lu, J. E. B. Oliveira, V. R. Almeida, Y. Chen, and A. Scherer, "Experimental demonstration of a unidirectional reflectionless parity-time metamaterial at optical frequencies," *Nat. Mater.*, vol. 12, no. 2, pp. 108–113, 2012.

[179] A. Karalis, J. D. Joannopoulos, and M. Soljačić, "Efficient wireless non-radiative mid-range energy transfer," *Ann. of Phys.*, vol. 323, no. 1, pp. 34–48, 2008.

[180] A. A. Sukhorukov, A. S. Solntsev, S. S. Kruk, D. N. Neshev, and Y. S. Kivshar, "Nonlinear coupled-mode theory for periodic plasmonic waveguides and metamaterials with loss and gain," *Opt. Lett.*, vol. 39, no. 3, pp. 462–465, 2014.

[181] P. T. Bowen and D. R. Smith, "Coupled-mode theory for film-coupled plasmonic nanocubes," *Phys. Rev. B*, vol. 90, no. 19, pp. 195402–195413, 2014.

[182] M. Aning, Y. Li, and X. Zhang, "Coupled Mode Theory for Surface Plasmon Polariton Waveguides," *Plasmonics*, vol. 8, no. 2, pp. 769–777, 2013.

[183] B. Vial and Y. Hao, "A coupling model for quasi-normal modes of photonic resonators," *J. Opt.*, vol. 18, no. 11, pp. 115004, 2016.

[184] S. Y. Elnaggar, R. J. Tervo, and S. M. Mattar, "General expressions and physical origin of the coupling coefficient of arbitrary tuned coupled electromagnetic resonators," *J. Appl. Phys.*, vol. 118, no. 19, pp. 194901, 2015.

[185] S. Y. Elnaggar, R. Tervo, and S. M. Mattar, "Coupled modes, frequencies and fields of a dielectric resonator and a cavity using coupled mode theory," *J. Magn. Reson.*, vol. 238, pp. 1–7, 2014.

[186] S. Y. Elnaggar, R. J. Tervo, and S. M. Mattar, "Energy Coupled Mode Theory for Electromagnetic Resonators," *IEEE Trans. Micro. Theory Tech.*, vol. 63, no. 7, pp. 2115–2123, 2015.

[187] H. A. Haus and W. Huang, "Coupled-mode theory," *Proc. IEEE*, vol. 79, no. 10, pp. 1505–1518, 1991.

[188] V. Zelevinsky, "Quantum Physics Volume 1 : From Basics to Symmetries and Perturbations," Wiley–VCH, Weinheim, 2011.

[189] K. G. Makris, D. N. Christodoulides, O. Peleg, M. Segev, and D. Kip, "Optical transitions and Rabi oscillations in waveguide arrays," *Optoelectron. Lett.*, vol. 11, no. 5, pp. 342–347, 2015.

[190] A. F. A. Noorden, K. Chaudhary, M. Bahadoran, M. S. Aziz, M. A. Jalil, O. C. Tiong, J. Ali, and P. Yupapin, "Rabi oscillation generation in the microring resonator system with double-series ring resonators," *Opt. Express*, vol. 16, no. 14, pp. 10309–10314, 2008.

[191] M. G. Blaber, M. D. Arnold, and M. J. Ford, "Search for the Ideal Plasmonic Nanoshell: The Effects of Surface Scattering and Alternatives to Gold and Silver," *J. Phys. Chem. C*, vol. 113, no. 8, pp. 3041–3045, 2009.

[192] N. K. Grady, N. J. Halas, and P. Nordlander, "Influence of dielectric function properties on the optical response of plasmon resonant metallic nanoparticles," *Chem. Phys. Lett.*, vol. 399, no. 1–3, pp. 167–171, 2004.

[193] M. A. Ordal, Robert J. Bell, R. W. Alexander, L. L. Long, and M. R. Querry, "Optical properties of fourteen metals in the infrared and far infrared: Al, Co, Cu, Au, Fe, Pb, Mo, Ni, Pd, Pt, Ag, Ti, V, and W.," *Appl. Opt.*, vol. 24, no. 24, pp. 4493–4499, 1985.

[194] E. J. Zeman and G. C. Schatz, "An accurate electromagnetic theory study of surface enhancement factors for silver, gold, copper, lithium, sodium, aluminum, gallium, indium, zinc, and cadmium," *J. Phys. Chem.*, vol. 91, no. 3, pp. 634–643, 1987.

[195] H. van der Lem and A. Moroz, "Towards two-dimensional complete photonic bandgap structures below infrared wavelengths," *J. of Opt. A: Pure Appl. Opt.*, vol. 2, no. 5, pp. 395, 2000.

[196] H. U.Yang, J. D'Archangel, M. L. Sundheimer, E. Tucker, G. D. Boreman and M. B. Raschke, "Optical dielectric function of silver," *Phys. Rev. B*, vol. 91, no. 23, pp. 235137–235147, 2015.

[197] R. F. Harrington, "Time-Harmonic Electromagnetic Fields," Wiley-IEEE Press, New York, 2001.

[198] K. Kolwas, A. Derkachova, and S. Demianiuk, "The smallest free-electron sphere sustaining multipolar surface plasmon oscillation," *Computat. Mater. Sci.*, vol. 35, no. 3, pp. 337–341, 2006.

[199] K. Kolwas and A. Derkachova, "Damping rates of surface plasmons for particles of size from nano- to micrometers; reduction of the nonradiative decay ," *J. Quant. Spectrosc. Radiat. Transfer*, vol. 114, pp. 45–55, 2013.

[200] A. Derkachova and K. Kolwas, "Size dependence of multipolar plasmon resonance frequenciesand damping rates in simple metal spherical nanoparticles," Eur. Phys. J. Spec. Top., vol. 144, no. 1, pp. 93–99, 2007.

[201] A. Derkachova, K. Kolwas, and I. Demchenko, "Dielectric Function for Gold in Plasmonics Applications: Size Dependence of Plasmon Resonance Frequencies and Damping Rates for Nanospheres," *Plasmonics*, vol. 11, no. 3, pp. 941–951, 2016.

[202] P. T. Leung, S. Y. Liu, and K. Young, "Completeness and orthogonality of quasinormal modes in leaky optical cavities," Phys. Rev. A, vol. 49, no. 4, pp. 3057–3067, 1994.

[203] P. T. Leung, S. Y. Liu, and K. Young, "Completeness and time-independent perturbation of the quasinormal modes of an absorptive and leaky cavity," *Phys. Rev. A*, vol. 49, no. 5, pp. 3982–3989, 1994.

[204] P. T. Leung and K. M. Pang, "Completeness and time-independent perturbation of morphology-dependent resonances in dielectric spheres," *J. Opt. Soc. Am. B*, vol. 13, no. 5, pp. 805–817, 1996.

[205] C. Sauvan, J. P. Hugonin, I. S. Maksymov, and P. Lalanne, "Theory of the Spontaneous Optical Emission of Nanosize Photonic and Plasmon Resonators," *Phys. Rev. Lett.*, vol. 110, no. 23, pp. 237401–237405, 2013.

[206] P. T. Kristensen and S. Hughes, "Modes and Mode Volumes of Leaky Optical Cavities and Plasmonic Nanoresonators," *ACS Photonics*, vol. 1, no. 1, pp. 2–10, 2014.

[207] M. B. Doost, W. Langbein, and E. A. Muljarov, "Resonant-state expansion applied to three-dimensional open optical systems," *Phys. Rev. A*, vol. 90, no. 1, pp. 013834–013847, 2014.

[208] P. T. Kristensen, R. Ge and S. Hughes, "Normalization of quasinormal modes in leaky optical cavities and plasmonic resonators," *Phys. Rev. A*, vol. 92, no. 5, pp. 053810–053818, 2015.

[209] R. Ruppin, "Electromagnetic energy density in a dispersive and absorptive material," *Phys. Lett. A*, vol. 299, no. 2, pp. 309–312, 2015.

[210] W. E. Byerly, "An Elementary Treatise on Fourier's Series: and Spherical, Cylindrical, and Ellipsoidal Harmonics, with Applications to Problems in Mathematical Physics," Dover, New York, 1959.

[211] P. Roy Paladhi, A. Tayebi, P. Banerjee, L. Udpa, and S. Udpa, "Image reconstruction from highly sparse and limited angular diffraction tomography using compressed sensing approach," *Progress In Electromagnetics Research*, vol. 158, pp. 21–36, 2017.

[212] P. Roy Paladhi, A. Sinha, A. Tayebi, L. Udpa, and S. S. Udpa, "Improved backpropagation algorithms by exploiting data redundancy in limited-angle diffraction tomography," *Progress In Electromagnetics Research B*, vol. 66, pp. 1–13, 2016.